

https://dspace.org/

The effect of physical properties on the reflection seismic method: implications for shale gas exploration in the main Karoo Basin, South Africa

Coetzee, Jonise

2018

https://hdl.handle.net/10539/26953

Coetzee, Jonise (2018) Integration of seismic attributes and physical property measurements to study hydrocarbon reservoirs, offshore Orange Basin and Main Karoo Basin, South Africa, University of the Witwatersrand, Johannesburg, https://hdl.handle.net/10539/26953

Downloaded from a DSpace repository. https://dspace.org/

The effect of physical properties on the reflection seismic method: Implications for shale gas exploration in the Main Karoo Basin, South Africa

By

Jonise Coetzee

A dissertation submitted to the
Faculty of Science, University of the Witwatersrand
in fulfilment of the requirements for the degree of

Master of Science

Supervisors: Dr Musa Manzi, Dr Ergong Zhang and Prof Susan Webb

School of Geosciences
August 2018



UNIVERSITY OF THE
WITWATERSRAND,
JOHANNESBURG

Declaration

I declare that this dissertation is my own, unaided work. It is being submitted for the Degree of Master of Science at the University of the Witwatersrand, Johannesburg. It has not been submitted before for any degree or examination in any other university.

Jonise Coetzee: 

17th day of August 2018, at The University of the Witwatersrand, Johannesburg.

Abstract

The Main Karoo Basin of South Africa is being investigated for its shale gas potential. The presence of a possibly large hydrocarbon deposit (i.e., shale layer of the Whitehill Formation) is still underexplored. The reflection seismic method, amongst other geophysical methods, could yield more certainty and information about the geology at the subsurface of the basin. For the application of the reflection seismic technique to be successful, it is crucial to investigate and understand the physical properties (e.g., seismic velocities, bulk density and porosity) associated with hydrocarbons and their host rocks. To provide guidelines for future seismic surveys in the Main Karoo Basin, this study aims to determine the physical properties of Karoo Basin rocks and to better understand the nature of the seismic reflectivity of the hydrocarbon deposit (mainly shale unit), its underlying and overlying rock units. This was achieved by conducting laboratory experiments to measure P-wave (Vp) and S-wave (Vs) velocities at ultrasonic frequencies on drill-core samples as a function of stress and bulk density. The core samples were taken from the deep (~2.5 km) Karoo borehole (KWV borehole) that penetrated the entire Beaufort Group, the Fort Brown, Whitehill and Prince Albert Formations of the Ecca Group, and the Dwyka Group in the Main Karoo Basin.This study further investigates the influence of mineralogy, stress, fractures and mineral alignment on the seismic velocities of the rocks.

The shale samples collected from borehole KWV (15 in total) exhibit average P-wave and S-wave velocities of 3859 m/s and 2116 m/s, respectively. The shale samples have an average bulk density of 2.74 g/cm^3 and porosity of 1.66 %. On average, sandstone samples (10 in total) exhibit an average Vp of 4904 m/s, Vs of 2623 m/s, bulk density of 2.68 g/cm^3 and porosity of 1.12%. The shale and sandstone samples exhibit higher seismic velocities than typical soft rocks; which may be attributed to the presence of pyrite content in these samples. However the bulk densities of these samples fall within the published range of typical shale and sandstone samples. Twelve dolerite samples show average Vp and Vs values of 5105 m/s and 2718 m/s, respectively. The average bulk density and porosity for dolerite is 2.95 g/cm^3 and 1.65%, respectively. No correlation exists between the bulk density and P-wave velocities of the samples from borehole KWV.

The seismic velocities of all samples tend to increase as a function of uniaxial stress, indicating a possible closure of pore spaces, macro- and micro-fractures. The velocity-stress dependence behaviour varies considerably, depending on the rock type. No correlations were observed between the bulk density, depths and porosities of the samples. A sandstone exhibits a seismic anisotropy of 5.9%, while two shale samples exhibit seismic anisotropy of

5.8% and 11.4%, respectively. The fast seismic velocity is along the direction of the mineral SPO and micro-fracture line orientations.

The synthetic seismogram indicates that significant reflection coefficients (Rc) occur at most stratigraphic contacts (e.g., Rc~ 15% for shale-sandstone contact at the top of the Whitehill Formation of the lower Ecca Group), implying that these horizons, at least in terms of acoustic impedance contrasts, are favourable targets for surface reflection seismic surveys. The observed relationship between seismic velocities, mineralogy, fractures, mineral alignment and stress has particularly important implications (e.g., velocity analysis for seismic processing and time-to-depth conversion of the seismic data) for the design of future deep seismic surveys that may be used for future shale gas exploration.

Acknowledgements

I would like to acknowledge all the support and advice that I received from my main supervisor Dr Musa Manzi, throughout my MSc. I am sincerely grateful for all your moral and academic support, and for never doubting my ability to finish my MSc. To my co-supervisor, Dr Ergong Zhang, I am extremely grateful that you gave me so much of your time and knowledge in the last stretch of finishing this MSc. I am happy to call you a friend after this process. To Prof Susan Webb, thank you for always adding new ideas to this work, and for all your advice on any issues that I had with any research. I am very honoured to have worked with world-class scientists.

To Stephanie Scheiber-Enslin, thank you for always being willing to read through my work, all your inputs were invaluable. Michael Westgate, your help and support in all the programming aspects of this research was a massive help, and I will be forever grateful to you. I would also like to sincerely thank Julie Bourdeau for your willingness to assist me with any petrography-related work. To Andrew Carpede, thank you for all your assistance in cutting my samples, and for always being willing to help when I needed you. You made my days in the laboratory less lonely.

I would also like to express my gratitude to CIMERA for financing my MSc, and for all the opportunities that came with it. I am very grateful for the conferences that I could attend in the last two years. I would also like to acknowledge the DST-NRF for the financial support (Grant # UID23) to establish the MIXRAD micro-focus X-ray tomography facility at Necsa. I would also like to acknowledge Mr Kobus Hoffman of the RADTOM section for his contribution towards the research.

I am extremely grateful to Tania and Thinus van der Merwe for all your support. Thank you for always saving me from Excel, and Tania especially for the late nights when you did not give up on helping me. I will always be grateful to you that you opened your doors for me when I needed a place to stay during the last months of my MSc.

To my fiancé, Marnus, you were my rock throughout this process. I can always count on you for anything, and nothing is ever too much effort for you.

And last, but certainly not least, where do I even begin to thank my parents. This has been a long journey of studying, travelling and moving around. You supported and loved me in all my endeavours every single day, and I am tremendously grateful for all your moral and financial support.

Table of Contents

Declaration....ii
Abstract....iii
Acknowledgements....v
Table of Contents....vi
List of Figures....ix
List of Tables....xxiv
Table of Abbreviations....xxv
1. Introduction....1
1.1. Objectives of the study....4
1.2. Chapter descriptions....4
2. Geological overview of the Main Karoo Basin, South Africa....6
3. Geophysical log....11
4. Reflection seismics and physical properties....16
4.1. Elastic moduli and acoustic impedance....16
4.2. Factors affecting seismic velocities....19
4.2.1. Porosity, mineralogy and bulk density....19
4.2.2. Seismic velocities at elevated uniaxial stress....19
4.2.3. Seismic anisotropy....20
5. Methodology....22
5.1. Sampling....23
5.2. Seismic velocity measurements....25
5.2.1. Sample preparation....25
5.2.2. P- and S-wave velocity measurements....26
5.2.3. Signal processing....28
5.2.4. Measuring seismic velocities under uniaxial stress....29
5.3. Bulk density measurements....29
5.4. Porosity measurements....30
5.5. Fracture analysis....31

5.5.1. Sample preparation 32
5.5.2. Micro x-ray tomography 32
5.6. Petrography 34
5.7. Seismic anisotropy 34
5.8. Construction of synthetic seismograms 35
5.9. Error propagation 36
6. Results 38
6.1. Sampling 38
6.2. Seismic velocities 54
6.2.1. P- and S-waves 54
6.2.2. Signal processing 59
6.2.3. Uniaxial stress 61
6.3. Bulk density 70
6.4. Porosity 73
6.5. Fracture analysis 76
6.5.1. Micro x-ray tomography 76
6.6. Petrography 91
6.7. Anisotropy 97
6.8. Synthetic seismogram 99
7. Data integration and discussion 105
7.1. Sources of error 105
7.2. Seismic velocities, bulk density, porosity 107
7.3. Seismic velocities at elevated axial stress 112
7.4. Seismic anisotropy 118
7.5. Implications for seismic reflectivity 120
8. Conclusions 122
Recommendations 123
References 124
A. Appendix A – Seismic velocities 130

B. Appendix B – Signal processing..... 157
C. Appendix C – Uniaxial stress 168
D. Appendix D – MATLAB code..... 182

List of Figures

Figure 1.1: A geology map of the study area, indicating the position of borehole KWV relative to Willowvale and Durban, in the Eastern Cape Province of South Africa. Insert map shows the Figure location relative to the basin (red outline) and southern Africa. (SACS, 1980) 3
Figure 2.1: A stratigraphic log with a simplified lithology log down to a depth of 2352.4 m of borehole KWV. The stratigraphy of the Beaufort, Ecca and Dwyka groups are also indicated (CIMERA, n.d.). 8
Figure 2.2: Map indicating the different hydrocarbon potentials of the Ecca Group shales. The position of the 29°S latitude is indicated, as well as the location of the KWV borehole (Modified from Cole, 2011). 10
Figure 3.1: Log of seismic velocity, density and radioactivity geophysical responses in borehole KWV (CIMERA, n.d.). 12
Figure 3.2: Interpreted version of geophysical log. The red ellipse indicates the response for dolerite, while the yellow and black ellipses show the responses for sandstone and shale, respectively. The legend is the same as the legend in Figure 3.1. 14
Figure 4.1: Schematic seismic reflection ray paths over a horizontal interface. There is an impedance contrast at the contact between Z1 and Z2 (Manzi, 2013). 18
Figure 4.2: Velocity versus density plot for economic minerals, sedimentary rocks, felsic rocks, mafic rocks and ultramafic rocks. Sulphide mineralisation is also indicated (modified after Dentith and Mudge, 2014). 21
Figure 5.1: Flowchart summarizing all main steps taken during the course of the study. 22
Figure 5.2: The main steps taken to prepare samples for the pulse transmission technique. a) Samples were cut to a length of ~80 mm. b) The edges of the samples were lapped so that they would be smooth and parallel to one another. c) The final result of the sample preparations (sample W30). 25
Figure 5.3: The main steps and components of the pulse transmission technique. a) The sample placed between the receiver and the transmitter. This is the setup for measuring the seismic velocities of the sample under atmospheric stress b) The setup in a) is placed in a uniaxial stress applying system c) The applied stress is indicated on this wheel by the red needle, in units of MPa d) The setup as shown in b), connected to the pulse generator and oscilloscope e) The pressure applying rotary wheel. 26
Figure 5.4: A schematic image of the output wave on the oscilloscope, indicating the position of the P-wave (1), the first S-wave arrival (2) and the peak of the S-wave. The horizontal axis is time and the vertical axis is the amplitude of the waveform (Qixian and Bungey, 1996). .. 27
Figure 5.5: A single waveform output from the oscilloscope for a sandstone sample (sample W1). The locations of the first P- and S-wave arrivals are indicated on the waveform. 28

Figure 5.6: Method of obtaining the densities and porosities of the samples. a) Scale used to measure weight, and ultimately density, of samples. b) Laboratory Archimedes setup. 30
Figure 5.7: The setup of micro x-ray scans. The sample is placed within the cone of x-rays, between the radiation source and the detector (Adapted from Hoffman and De Beer, 2012). 32
Figure 5.8: Micro x-ray machine at NECSA, South Africa (Hoffman and De Beer, 2012) 33
Figure 5.9: Schematic representation of the a) y-direction and b) x-direction of the samples that were used to measure seismic velocity anisotropy. Micro-fractures in the sample are represented by yellow lines running parallel to the long axis of the sample. 35
Figure 5.10: Steps taken in the construction of a synthetic seismogram (Dentith and Mudge 2014). 35
Figure 5.11: TWT plotted against measured depth (MD) of SOEKOR seismic data (Scheiber-Enslin et al., 2014). The measured depth (MD) and the TWT of the Whitehill Formation are plotted (MD_TWT_Wh). Interval velocities (Fatti and du Toit, 1970) and a sonic velocity log from well WE1/66 (Fatti, 1987) are also plotted. 36
Figure 6.1: Sample W1, image and descriptions. This sample is a weakly weathered greyish white sandstone. It has green ripple mark textures with flaser bedding. 38
Figure 6.2: Sample W2, image and descriptions. The sample is a grey mudstone. 38
Figure 6.3: Sample W3, image and descriptions. This sample is a grey-green mudstone with dark grey to black rounded shale particles from 2 mm to 10 mm. The size of the particles increases towards base. 39
Figure 6.4: Sample W4, image and descriptions. The sample is a grey sandstone with darker grey interbedded shale. Shale bedding is well defined by dark and light banding of 1 mm to 3 mm thick. The sandstone has strong ripple mark textures with flaser bedding. The bedding dips 60°. 39
Figure 6.5: Sample W5, image and descriptions. This sample is a grey to dark grey shale with well-defined bedding, which is indicated by dark and light interbeds 2 mm to 5 mm thick. The bedding dips 60° 39
Figure 6.6: Sample W6, image and descriptions. The sample is a grey sandstone with well-defined bedding indicated by darker grey layers 2 mm to 6 mm thick. 40
Figure 6.7: Sample W7, image and descriptions. The sample is a medium-grained dolerite. 40
Figure 6.8: Sample W8, image and descriptions. The sample is a light grey, fine grained sandstone. It is upward-grading, with lenticular lamination. 40
Figure 6.9: Sample W9, image and descriptions. The sample is a dark grey to black, very fine grained shale. It has well-defined bedding, which appears as 2 mm to 10 mm thick, dark grey to black and lighter grey interbeds of laminated shale. 41

Figure 6.10: Sample W10, image and descriptions. The sample is a dark grey, fine grained sandstone with bedding dipping 5° to 7°. 41
Figure 6.11: Sample W11, image and descriptions. The sample is a dark grey to black shale, laminated with well-defined bedding defined by dark and light grey interbeds. 41
Figure 6.12: Sample W12, image and descriptions. The sample is a light green dolerite with a phaneritic texture. The lower and upper contacts are very fine-grained crystalline. 42
Figure 6.13: Sample W13, image and descriptions. The sample is a light grey, very fine-grained sandstone. It is laminated, with interbeds of shale. 42
Figure 6.14: Sample W14, image and descriptions. The sample is a dark grey shale with grey silty interbeds that are 2 mm to 5 mm thick. 42
Figure 6.15: Sample W15, image and descriptions. The sample is a grey, massive shale. .. 43
Figure 6.16: Sample W16, image and descriptions. The sample is a greenish grey, coarse-grained dolerite. 43
Figure 6.17: Sample W17, image and descriptions. The sample is a massive black shale with poorly-defined bedding. It has occasional grey, very fine grained sandstone interbeds, of 5 mm thickness. 43
Figure 6.18: Sample W18, image and descriptions. The sample is a massive, light grey medium grained sandstone. It has very weak bedding definitions in places. 44
Figure 6.19: Sample W19, image and descriptions. The sample is a black carbonaceous shale with occasional light grey, medium grained sandstone interbeds. 44
Figure 6.20: Sample W20, image and descriptions. The sample is a black carbonaceous shale with weak bedding that is defined by occasional dark grey beds, of 1 mm to 2 mm thickness. 44
Figure 6.21: Sample W21, image and descriptions. The sample is a light grey, very fine grained sandstone. It has well-defined bedding indicated by brownish grey, very fine grained interbeds. 45
Figure 6.22: Sample W22, image and descriptions. The sample is a grey green, medium-grained dolerite. 45
Figure 6.23: Sample W23, image and descriptions. The sample is a grey, medium grained sandstone with well-defined bedding. It has upward-grading sequences and ripple marking in places. 45
Figure 6.24: Sample W24, image and descriptions. The sample is a black carbonaceous shale with sandstone interbeds that are 2 mm to 10 mm thick. 46
Figure 6.25: Sample W25, image and descriptions. The sample is a light grey, massive shale with lighter grey speckling throughout. It has dark grey, rusty and well-bedded layers. 46

Figure 6.26: Sample W26, image and descriptions. The sample is a grey green, medium- to coarse-grained dolerite. 46
Figure 6.27: Sample W27, image and descriptions. The sample is a grey green, fine- to medium-grained dolerite. It has a sharp horizontal basal contact. 47
Figure 6.28: Sample W28, image and descriptions. The sample is a black, massive carbonaceous shale with occasional thin, grey and fine-grained sandstone interbeds. 47
Figure 6.29: Sample W29, image and descriptions. The sample is a light grey to grey, fine-grained massive sandstone. 47
Figure 6.30: Sample W30, image and descriptions. The sample is a grey, fine grained sandstone with rhythmic upward-grading cycles from light grey, fine grained sandstone to dark grey, very fine grained sandstone. It has strongly bleached zones throughout. 48
Figure 6.31: Sample W31, image and descriptions. The sample is a grey green, very coarse-grained dolerite with traces of magnetite. 48
Figure 6.32: Sample W32, image and descriptions. The sample is a grey green, fine- to medium-grained dolerite. It has patches of very coarse-grained dolerite with traces of magnetite. 48
Figure 6.33: Sample W33, image and descriptions. The sample is a grey green, fine-grained dolerite. 49
Figure 6.34: Sample W34, image and descriptions. The sample is a grey green to dark green, fine- to medium-grained dolerite. It has occasional near vertical calcite and quartz veins with hornblende at contacts. 49
Figure 6.35: Sample W35, image and descriptions. The sample is a fine- to medium-grained sandstone with dark grey to black, very fine to silty sandstone interbeds. Its bedding thickness varies from 5 mm to 30 mm. It has occasional faint rusty sections. 49
Figure 6.36: Sample W36, image and descriptions. The sample is a light grey to grey, very fine-grained sandstone with well-defined bedding. It has quartz veins with pyrrhotite. 50
Figure 6.37: Sample W37, image and descriptions. The sample is a grey green, very fine-grained dolerite with traces of magnetite. Its upper and lower contacts are irregular, but horizontal. 50
Figure 6.38: Sample W38, image and descriptions. The sample is a grey green, very fine-grained dolerite with traces of magnetite. Its upper and lower contacts are irregular, but horizontal. A fine-grained epidote alteration zone is present. 50
Figure 6.39: Sample W39, image and descriptions. The sample is a black, near massive carbonaceous shale. Its bedding is defined by thin, light grey, very fine-grained sandstone beds. It has disseminated pyrrhotite throughout and on its bedding planes. 51

Figure 6.40: Sample W40, image and descriptions. The sample is a black, near massive carbonaceous shale. It has a brecciated appearance with soft sediment deformation. It is highly pyritic, with very fine quartz veins. 51
Figure 6.41: Sample W41, image and descriptions. The sample is a black, well-bedded carbonaceous shale. Its bedding is defined by numerous disseminated pyrite bands on bedding plane. It has occasional grey to dark grey shale beds. 51
Figure 6.42: Sample W42, image and descriptions. The sample is a black, well-bedded carbonaceous shale. Its bedding defined is by numerous disseminated pyrite bands on bedding plane. It has occasional grey to dark grey shale beds. 52
Figure 6.43: Sample W43, image and descriptions. The sample is a dark grey with black shale. Its bedding is indicated in places by thin, lighter grey shale or sandstone beds. 52
Figure 6.44: Sample W44, image and descriptions. The sample is a dark grey with black shale. Its bedding is indicated in places by thin, lighter grey shale or sandstone beds. 52
Figure 6.45: Sample W45, image and descriptions. The sample is a massive, dark grey to black shale. It has no visible bedding. 53
Figure 6.46: Sample W46, image and descriptions. The sample is a grey, fine grained sandstone interbedded with dark grey to black shales. 53
Figure 6.47: Sample W47, image and descriptions. The sample is a grey, fine grained sandstone interbedded with dark grey to black shales. 53
Figure 6.48: Sample W48, image and descriptions. The sample is a grey, coarse grained matrix with rounded and occasional sub-angular sandstone and quartz fragments that are up to 70 mm in diameter. 54
Figure 6.49: Sample W49, image and descriptions. The sample is a grey, coarse grained matrix with rounded and occasional sub-angular sandstone and quartz fragments that are up to 70 mm in diameter. 54
Figure 6.50: The result of stacking multiple waveforms for a single mudstone sample versus a single waveform output of a sample (W2). Multiple waveform outputs from the oscilloscope for a mudstone sample (W2) were stacked to produce the red, smooth signal. 59
Figure 6.51: The result of stacking multiple waveforms for a single carbonaceous shale sample versus a single waveform output of a sample (W9). Multiple waveform outputs from the oscilloscope for a carbonaceous shale sample (W9) were stacked to produce the red, smooth signal. 60
Figure 6.52: The result of stacking multiple waveforms for a single carbonaceous shale sample versus a single waveform output of a sample (W19). Multiple waveform outputs from the oscilloscope for a carbonaceous shale sample (W19) were stacked to produce the red, smooth signal. 61

Figure 6.53: The effect of uniaxial stress on the P-wave velocity of sandstone samples from borehole KWV. The stress (x-axis) is divided into a number of phases. 63
Figure 6.54: The effect of uniaxial stress on the P-wave velocity of shale samples from borehole KWV. The stress (x-axis) is divided into a number of phases. 65
Figure 6.55: The effect of uniaxial stress on the P-wave velocity of carbonaceous shale samples from borehole KWV. The stress (x-axis) is divided into a number of phases. 66
Figure 6.56: The effect of uniaxial stress on the P-wave velocity of dolerite samples from borehole KWV. The stress (x-axis) is divided into a number of phases. 67
Figure 6.57: The effect of uniaxial stress on the P-wave velocity of rhythmite samples from borehole KWV. The stress (x-axis) is divided into a number of phases. 68
Figure 6.58: The effect of uniaxial stress on the P-wave velocity of tillite samples from borehole KWV. The stress (x-axis) is divided into a number of phases. 69
Figure 6.59: The total increase in P-wave velocities with uniaxial stress for all samples from borehole KWV. The initial (~ 0.1 MPa) and final (~ 80 MPa) P-wave velocities are plotted. . 69
Figure 6.60: The total increase in P-wave velocities with uniaxial stress for samples from borehole KWV. The samples with initial velocities below 2000 m/s are excluded in this plot, as these values are deduced to be unrealistic. 70
Figure 6.61: The relationship between the bulk density and the P-wave velocity for all the samples collected from borehole KWV. 73
Figure 6.62: The correlation between the density of the samples and the porosity of the samples. 76
Figure 6.63: The x-ray tomography results for the mudstone sample (Sample W2). A 3D image of the sample, as well as slices through the front and right of the sample is depicted in the image. In the 3D image, lighter and darker shades of grey represent relatively less and more dense sections of the sample. In the slices, bright colours represent low local density spots that are typical of pore spaces and fractures. 77
Figure 6.64: The x-ray tomography results for a sandstone sample (sample W8). A 3D image of the sample, as well as slices through the front and right of the sample is depicted in the image. In the 3D image, lighter and darker shades of grey represent relatively less and more dense sections of the sample. In the slices, bright colours represent low local density spots that are typical of pore spaces and fractures. The dark blue planes are location references for the slices. 78
Figure 6.65: The x-ray tomography results for a sandstone sample (sample W18). A 3D image of the sample, as well as slices through the front and right of the sample is depicted in the image. In the 3D image, lighter and darker shades of grey represent relatively less and more dense sections of the sample. In the slices, bright colours represent low local density spots

that are typical of pore spaces and fractures. The dark blue planes are location references for the slices. 79
Figure 6.66: The x-ray tomography results for a sandstone sample (sample W21). A 3D image of the sample, as well as slices through the front and right of the sample is depicted in the image. In the 3D image, lighter and darker shades of grey represent relatively less and more dense sections of the sample. In the slices, bright colours represent low local density spots that are typical of pore spaces and fractures. The dark blue planes are location references for the slices. 79
Figure 6.67: The x-ray tomography results for a sandstone sample (sample W36). A 3D image of the sample, as well as slices through the front and right of the sample is depicted in the image. In the 3D image, lighter and darker shades of grey represent relatively less and more dense sections of the sample. In the slices, bright colours represent low local density spots that are typical of pore spaces and fractures. The dark blue planes are location references for the slices. 80
Figure 6.68: The x-ray tomography results for a dolerite sample (sample W16). A 3D image of the sample, as well as slices through the front and right of the sample is depicted in the image. In the 3D image, lighter and darker shades of grey represent relatively less and more dense sections of the sample. In the slices, bright colours represent low local density spots that are typical of pore spaces and fractures. The dark blue planes are location references for the slices. 81
Figure 6.69: The x-ray tomography results for a dolerite sample (sample W26). A 3D image of the sample, as well as slices through the front and right of the sample is depicted in the image. In the 3D image, lighter and darker shades of grey represent relatively less and more dense sections of the sample. In the slices, bright colours represent low local density spots that are typical of pore spaces and fractures. The dark blue planes are location references for the slices. 81
Figure 6.70: The x-ray tomography results for a dolerite sample (sample W31). A 3D image of the sample, as well as slices through the front and right of the sample is depicted in the image. In the 3D image, lighter and darker shades of grey represent relatively less and more dense sections of the sample. In the slices, bright colours represent low local density spots that are typical of pore spaces and fractures. The dark blue planes are location references for the slices. 82
Figure 6.71: The x-ray tomography results for a dolerite sample (sample W33). A 3D image of the sample, as well as slices through the front and right of the sample is depicted in the image. In the 3D image, lighter and darker shades of grey represent relatively less and more dense sections of the sample. In the slices, bright colours represent low local density spots that are

typical of pore spaces and fractures. The dark blue planes are location references for the slices. 82
Figure 6.72: The x-ray tomography results for a dolerite sample (sample W34). A 3D image of the sample, as well as slices through the front and right of the sample is depicted in the image. In the 3D image, lighter and darker shades of grey represent relatively less and more dense sections of the sample. In the slices, bright colours represent low local density spots that are typical of pore spaces and fractures. The dark blue planes are location references for the slices. 83
Figure 6.73: The x-ray tomography results for a shale sample (W17). A 3D image of the sample, as well as slices through the front and right of the sample is depicted in the image. In the 3D image, lighter and darker shades of grey represent relatively less and more dense sections of the sample. In the slices, bright colours represent low local density spots that are typical of pore spaces and fractures. The dark blue planes are location references for the slices. 84
Figure 6.74: The x-ray tomography results for a shale sample (W43). A 3D image of the sample, as well as slices through the front and right of the sample is depicted in the image. In the 3D image, lighter and darker shades of grey represent relatively less and more dense sections of the sample. In the slices, bright colours represent low local density spots that are typical of pore spaces and fractures. The dark blue planes are location references for the slices. 84
Figure 6.75: The x-ray tomography results for a carbonaceous shale sample (W9). A 3D image of the sample, as well as slices through the front and right of the sample is depicted in the image. In the 3D image, lighter and darker shades of grey represent relatively less and more dense sections of the sample. In the slices, bright colours represent low local density spots that are typical of pore spaces and fractures. The dark blue planes are location references for the slices. 86
Figure 6.76: The x-ray tomography results for a carbonaceous shale sample (W19). A 3D image of the sample, as well as slices through the front and right of the sample is depicted in the image. In the 3D image, lighter and darker shades of grey represent relatively less and more dense sections of the sample. In the slices, bright colours represent low local density spots that are typical of pore spaces and fractures. The dark blue planes are location references for the slices. 86
Figure 6.77: The x-ray tomography results for a carbonaceous shale sample (W24). A 3D image of the sample, as well as slices through the front and right of the sample is depicted in the image. In the 3D image, lighter and darker shades of grey represent relatively less and more dense sections of the sample. In the slices, bright colours represent low local density

spots that are typical of pore spaces and fractures. The dark blue planes are location references for the slices. 87
Figure 6.78: The x-ray tomography results for a carbonaceous shale sample (W28). A 3D image of the sample, as well as slices through the front and right of the sample is depicted in the image. In the 3D image, lighter and darker shades of grey represent relatively less and more dense sections of the sample. In the slices, bright colours represent low local density spots that are typical of pore spaces and fractures. The dark blue planes are location references for the slices. 87
Figure 6.79: The x-ray tomography results for a carbonaceous shale sample (W39). A 3D image of the sample, as well as slices through the front and right of the sample is depicted in the image. In the 3D image, lighter and darker shades of grey represent relatively less and more dense sections of the sample. In the slices, bright colours represent low local density spots that are typical of pore spaces and fractures. The dark blue planes are location references for the slices. 88
Figure 6.80: The x-ray tomography results for a carbonaceous shale sample (W40). A 3D image of the sample, as well as slices through the front and right of the sample is depicted in the image. In the 3D image, lighter and darker shades of grey represent relatively less and more dense sections of the sample. In the slices, bright colours represent low local density spots that are typical of pore spaces and fractures. The dark blue planes are location references for the slices. 88
Figure 6.81: The x-ray tomography results for a carbonaceous shale sample (W42). A 3D image of the sample, as well as slices through the front and right of the sample is depicted in the image. In the 3D image, lighter and darker shades of grey represent relatively less and more dense sections of the sample. In the slices, bright colours represent low local density spots that are typical of pore spaces and fractures. The dark blue planes are location references for the slices. 89
Figure 6.82: The x-ray tomography results for a rhythmite sample (W30). A 3D image of the sample, as well as slices through the front and right of the sample is depicted in the image. In the 3D image, lighter and darker shades of grey represent relatively less and more dense sections of the sample. In the slices, bright colours represent low local density spots that are typical of pore spaces and fractures. The dark blue planes are location references for the slices. 89
Figure 6.83: The x-ray tomography results for a rhythmite sample (46). A 3D image of the sample, as well as slices through the front and right of the sample is depicted in the image. In the 3D image, lighter and darker shades of grey represent relatively less and more dense sections of the sample. In the slices, bright colours represent low local density spots that are

typical of pore spaces and fractures. The dark blue planes are location references for the slices. 90
Figure 6.84: The x-ray tomography results for a rhythmite sample (47). A 3D image of the sample, as well as slices through the front and right of the sample is depicted in the image. In the 3D image, lighter and darker shades of grey represent relatively less and more dense sections of the sample. In the slices, bright colours represent low local density spots that are typical of pore spaces and fractures. The dark blue planes are location references for the slices. 90
Figure 6.85: Thin section results for the mudstone sample (sample W2). a) is the microscopic image under plane polarized light (PPL), b) is the same image under cross polarized light (XPL) and c) is the sample under reflected light. 91
Figure 6.86: Thin section results for the sandstone sample (sample W8). a) is the microscopic image under plane polarized light (PPL) and b) is the same image under cross polarized light (XPL). 91
Figure 6.87: Thin section results for the shale sample (sample W17) under cross polarized light (XPL). 92
Figure 6.88: Thin section results for the sandstone sample (sample W18). a) is the microscopic image under plane polarized light (PPL) and b) is the same image under cross polarized light (XPL). 92
Figure 6.89: Thin section results for the sandstone sample (sample W21). a) is the microscopic image under plane polarized light (PPL) and b) is the same image under cross polarized light (XPL). 93
Figure 6.90: Thin section results for the carbonaceous shale sample (sample W24) under cross polarized light (XPL). 93
Figure 6.91: Thin section results for the shale sample (sample W25). a) is the microscopic image under plane polarized light (PPL) and b) is the same image under cross polarized light (XPL). 94
Figure 6.92: Thin section results for the rhythmite sample (sample W30). a) is the microscopic image under plane polarized light (PPL) and b) is the same image under cross polarized light (XPL). 94
Figure 6.93: Thin section results for the dolerite sample (sample W33). a) is the microscopic image under plane polarized light (PPL) and b) is the same image under cross polarized light (XPL). 95
Figure 6.94: Thin section results for the sandstone sample (sample W36). a) is the microscopic image under plane polarized light (PPL) and b) is the same image under cross polarized light (XPL). 95

Figure 6.95: Thin section results for the carbonaceous shale sample (sample W40). a) is the microscopic image under plane polarized light (PPL) and b) is the same image under cross polarized light (XPL). 96
Figure 6.96: Thin section results for the carbonaceous shale sample (sample W41). a) is the microscopic image under plane polarized light (PPL), b) is the same image under cross polarized light (XPL) and c) is the sample under reflected light. 96
Figure 6.97: Thin section results for the carbonaceous shale sample (sample W42). a) is the microscopic image under plane polarized light (PPL), b) is the same image under cross polarized light (XPL) and c) is the sample under reflected light. 96
Figure 6.98: The construction of a synthetic seismogram, where a) is a plot of the acoustic impedance, b) is the resulting reflection coefficient and c) is the synthetic seismogram and the lithology and stratigraphy of borehole KWV. 102
Figure 6.99: The synthetic seismograms for the (a) maximum and (b) minimum reflection coefficient. 103
Figure 6.100: The synthetic seismograms for the a) highest and b) lowest anisotropy values. 104
Figure 7.1: A summary of the average seismic velocities obtained in this study. 110
Figure 7.2: A comparison between the experimental P-wave velocity data at atmospheric stress and the P-wave velocity data from the geophysical log. 111
Figure 7.3: The summarised results of the average bulk density and porosity of all the samples from borehole KWV 111
Figure 7.4: The relationship between the porosity and bulk density of all the samples collected from borehole KWV 112
Figure 7.5: The relationship between the depth of sandstone samples from borehole KWV and the amount of stress required reach saturation velocity in the sandstone samples. 113
Figure 7.6: The relationship between the porosities of sandstone samples from borehole KWV and the total increase in P-wave velocities. 114
Figure 7.7: The relationship between the depth of shale samples from borehole KWV and the amount of stress required to each saturation velocity in the sandstone samples. 115
Figure 7.8: The relationship between the porosities of shale samples from borehole KWV and the total increase in P-wave velocities. 115
Figure 7.9: The relationship between the depth of dolerite samples from borehole KWV and the amount of stress required to reach saturation velocity in the sandstone samples. 116
Figure 7.10: The relationship between the porosities of dolerite samples from borehole KWV and the total increase in P-wave velocities. 116
Figure 7.11: A comparison between the experimental seismic velocity data under elevated axial stress and the P-wave velocity data from the geophysical log. 118

Figure 7.12: The P- and S-wave seismic anisotropies of samples based on seismic velocity measurements on samples in two orthogonal directions. 119
Figure A.1: The output waveform of sample W1. 132
Figure A.2: The output waveform of sample W2 132
Figure A.3: The output waveform of sample W3 133
Figure A.4: The output waveform of sample W4 133
Figure A.5: The output waveform of sample W5 134
Figure A.6: The output waveform of sample W6 134
Figure A.7: The output waveform of sample W7 135
Figure A.8: The output waveform of sample W8 135
Figure A.9: The output waveform of sample W9 136
Figure A.10: The output waveform of sample W10 136
Figure A.11: The output waveform of sample W11 137
Figure A.12: The output waveform of sample W12 137
Figure A.13: The output waveform of sample W13 138
Figure A.14: The output waveform of sample W14 138
Figure A.15: The output waveform of sample W15 139
Figure A.16: The output waveform of sample W16 139
Figure A.17: The output waveform of sample W17 140
Figure A.18: The output waveform of sample W18 140
Figure A.19: The output waveform of sample W19 141
Figure A.20: The output waveform of sample W20 141
Figure A.21: The output waveform of sample W21 142
Figure A.22: The output waveform of sample W22 142
Figure A.23: The output waveform of sample W23 143
Figure A.24: The output waveform of sample W24 143
Figure A.25: The output waveform of sample W25 144
Figure A.26: The output waveform of sample W26 144
Figure A.27: The output waveform of sample W27 145
Figure A.28: The output waveform of sample W28 145
Figure A.29: The output waveform of sample W29 146
Figure A.30: The output waveform of sample W30 146
Figure A.31: The output waveform of sample W31 147
Figure A.32: The output waveform of sample W32 147
Figure A.33: The output waveform of sample W33 148
Figure A.34: The output waveform of sample W34 148
Figure A.35: The output waveform of sample W35 149

Figure A.36: The output waveform of sample W36 149
Figure A.37: The output waveform of sample W37 150
Figure A.38: The output waveform of sample W38 150
Figure A.39: The output waveform of sample W39 151
Figure A.40: The output waveform of sample W40 151
Figure A.41: The output waveform of sample W41 152
Figure A.42: The output waveform of sample W42 152
Figure A.43: The output waveform of sample W43 153
Figure A.44: The output waveform of sample W44 153
Figure A.45: The output waveform of sample W45 154
Figure A.46: The output waveform of sample W46 154
Figure A.47: The output waveform of sample W47 155
Figure A.48: The output waveform of sample W48 155
Figure A.49: The output waveform of sample W49 156
Figure B.1: The results of stacking several output waveforms for sample W2 157
Figure B.2: The results of stacking several output waveforms for sample W8 157
Figure B.3: The results of stacking several output waveforms for sample W9 158
Figure B.4: The results of stacking several output waveforms for sample W16 158
Figure B.5: The results of stacking several output waveforms for sample W17 159
Figure B.6: The results of stacking several output waveforms for sample W18 159
Figure B.7: The results of stacking several output waveforms for sample W19 160
Figure B.8: The results of stacking several output waveforms for sample W24 160
Figure B.9: The results of stacking several output waveforms for sample W25 161
Figure B.10: The results of stacking several output waveforms for sample W26 161
Figure B.11: The results of stacking several output waveforms for sample W30 162
Figure B.12: The results of stacking several output waveforms for sample W31 162
Figure B.13: The results of stacking several output waveforms for sample W33 163
Figure B.14: The results of stacking several output waveforms for sample W34 163
Figure B.15: The results of stacking several output waveforms for sample W36 164
Figure B.16: The results of stacking several output waveforms for sample W39 164
Figure B.17: The results of stacking several output waveforms for sample W40 165
Figure B.18: The results of stacking several output waveforms for sample W41 165
Figure B.19: The results of stacking several output waveforms for sample W42 166
Figure B.20: The results of stacking several output waveforms for sample W46 166
Figure B.21: The results of stacking several output waveforms for sample W47 167
Figure C.1: The relationship between stress and seismic P-wave velocity of sample W5 (Shale) 168

Figure C.2: The relationship between stress and seismic P-wave velocity of sample W7 (Dolerite) 168
Figure C.3: The relationship between stress and seismic P-wave velocity of sample W8 (Sandstone) 169
Figure C.4: The relationship between stress and seismic P-wave velocity of sample W9 (Carbonaceous shale) 169
Figure C.5: The relationship between stress and seismic P-wave velocity of sample W10 (Sandstone) 170
Figure C.6: The relationship between stress and seismic P-wave velocity of sample W11 (Shale) 170
Figure C.7: The relationship between stress and seismic P-wave velocity of sample W13 (Sandstone) 171
Figure C.8: The relationship between stress and seismic P-wave velocity of sample W16 (Dolerite) 171
Figure C.9: The relationship between stress and seismic P-wave velocity of sample W17 (Black shale) 172
Figure C.10: The relationship between stress and seismic P-wave velocity of sample W18 (Sandstone) 172
Figure C.11: The relationship between stress and seismic P-wave velocity of sample W19 (Carbonaceous shale) 173
Figure C.12: The relationship between stress and seismic P-wave velocity of sample W21 (Sandstone) 173
Figure C.13: The relationship between stress and seismic P-wave velocity of sample W25 (Shale) 174
Figure C.14: The relationship between stress and seismic P-wave velocity of sample W26 (Dolerite) 174
Figure C.15: The relationship between stress and seismic P-wave velocity of sample W31 (Dolerite) 175
Figure C.16: The relationship between stress and seismic P-wave velocity of sample W33 (Dolerite) 175
Figure C.17: The relationship between stress and seismic P-wave velocity of sample W34 (Dolerite) 176
Figure C.18: The relationship between stress and seismic P-wave velocity of sample W37 (Dolerite) 176
Figure C.19: The relationship between stress and seismic P-wave velocity of sample W41 (Carbonaceous shale) 177

Figure C.20: The relationship between stress and seismic P-wave velocity of sample W42 (Carbonaceous shale) 177
Figure C.21: The relationship between stress and seismic P-wave velocity of sample W43 (Shale)..... 178
Figure C.22: The relationship between stress and seismic P-wave velocity of sample W44 (Shale)..... 178
Figure C.23: The relationship between stress and seismic P-wave velocity of sample W45 (Shale)..... 179
Figure C.24: The relationship between stress and seismic P-wave velocity of sample W46 (Rhythmite)..... 179
Figure C.25: The relationship between stress and seismic P-wave velocity of sample W47 (Rhythmite)..... 180
Figure C.26: The relationship between stress and seismic P-wave velocity of sample W48 (Tillite) 180
Figure C.27: The relationship between stress and seismic P-wave velocity of sample W49 (Tillite) 181

List of Tables

Table 3.1: The average values for bulk density and seismic velocity from the geophysical log for each sample from borehole KWV (CIMERA, n.d.). 15
Table 5.1: Summary of the stratigraphy and lithology of borehole KWV, with the location of samples indicated. The thicknesses of each unit are the same as indicated in Figure 2 (CIMERA, n.d.). 24
Table 5.2: The resolution and energy used to scan each sample during x-ray tomography. 33
Table 6.1: The lithology, stratigraphy and P- wave velocity for each sample from the KWV borehole. 57
Table 6.2: The lithology, stratigraphy and P- wave velocity for each sample from the KWV borehole. 58
Table 6.3: A summary of the effect of uniaxial stress on the P-wave velocity of each sample. The initial P-wave velocity (at 0 MPa), saturation P-wave velocity (at 80 MPa) and total increase in P-wave velocity is indicated. Initial velocities at 0 MPa are re-measured for each sample and are similar to values presented in Table 6.1. 62
Table 6.4: Bulk density results for the Karoo samples from the KWV borehole. 72
Table 6.5: Porosity results for Karoo samples from the KWV borehole. 75
Table 6.6: Seismic velocity results in two orthogonal directions, X and Y. The bulk anisotropy of the samples is also provided. The signals for sample W19 was too low to pick the arrival time of the S-wave. 98
Table 6.7: A comparison between the seismic anisotropy, micro-fracture orientation and mineral orientation of samples from borehole KWV. 99
Table 6.8: A summary of the seismic velocities, bulk densities, acoustic impedances and reflection coefficients of the samples from borehole KWV. 101
Table A.1: Data acquired to determine seismic velocities. P1 to P5 are the P-wave first arrival times for measurements 1 to 5 for each sample. 130
Table A.2: Data acquired to determine seismic velocities. S1 to S5 are the S-wave first arrival times for measurements 1 to 5 for each sample. 131

Table of Abbreviations

Abbreviation	Meaning
API	American Petroleum Institute
CFB	Cape Fold Belt
CIMERA	Centre for Excellence for Integrated Mineral and Energy Resource Analysis
CPO	Crystallographic Preferred Orientation
KWV	Willowvale borehole
MIXRAD	Micro-focus X-Ray Tomography Facility
NECSA	Nuclear Energy Corporation of South Africa
PPL	Plane Polarised Light
Rc	Reflection coefficient
SPO	Space Preferred Orientation
Tcf	Trillion cubic feet
TOC	Total Organic Carbon
TWT	Two-way travel time
Vp	P-wave velocity
Vs	S-wave velocity
VSP	Velocity Seismic Profile
XPL	Cross Polarised Light

1. Introduction

The presence of shale gas in the Main Karoo Basin of South Africa (Figure 1.1) has been under scrutiny the past few years. The basin has been estimated to contain 485 trillion cubic feet (Tcf) of shale gas (De Wit, 2011; Vermeulen, 2012; Geel et al., 2013; Warren, 2013). However, it has been clearly stated that this amount is only an estimate since the subsurface geology of the area is extremely variable and underexplored (Geel et al., 2013). Many factors are unknown when it comes to estimating the amount of shale gas in the Karoo Basin. Some of the factors include gas lost due to thermal degassing of the shale caused by dolerite intrusions, and tectonism relating to the formation of the Cape Fold Belt (Geel et al., 2013).

It is therefore crucial to investigate and provide a better understanding of the shale gas reservoirs in the Main Karoo Basin and their depths. Sparse borehole data have located the possible hydrocarbon reservoir in layers at depths greater than 1.5 km (Cole et al, 2011). These layers are from the lower Ecca Group of the Main Karoo Basin. Several reflection seismic surveys were conducted in the area, with more planned in the future for the exploration of shale gas. However, successful interpretation of the current and future seismic data is dependent on an understanding of the physical properties of the rocks. Physical property studies of rocks from the Main Karoo Basin may contribute to the geological and structural interpretation of the seismic profiles.

Physical property studies are an essential prerequisite to the design of any seismic survey. The objective of this research is to investigate physical properties that can influence the propagation and reflection of an elastic seismic wave through the rocks from the Main Karoo Basin. Ultrasonic seismic wave measurements (P- and S-wave velocities) were conducted on drill-core samples from the Main Karoo Basin under both atmospheric and uniaxial stress conditions. These results, together with the bulk density of the rocks, were used to establish the acoustic impedance of the drill-core samples, taken from different stratigraphic units of the deep (~2.5 km) Karoo borehole (KWV borehole), to determine whether the reflection coefficient (Rc) between the shale layer and the host rocks is large enough to produce seismic reflections. This should indicate whether the shale layer in the Main Karoo Basin can be imaged by the reflection seismic method. The study also investigated the effect that the mineralogy, bulk density, macro- and micro-fracture orientation, mineral alignment and stress may have on the seismic velocities of the rocks.

Previous studies on the Karoo Supergroup have looked into the shale gas potential of the lower Ecca Group (Cole et al, 2011), and the effect of dolerite intrusions on the shale gas

reservoir (Aarnes et al., 2011; Cole et al, 2011). However these studies, only focussed on the geological properties of the shale layer and did not extend their findings to the application of reflection seismic methods.

Regional reflection seismic surveys have previously been carried out in the Main Karoo Basin by Soekor (Fatti, 1987; Scheiber-Enslin et al., 2014). The strongest mapped regional seismic reflector of the Karoo Basin was the top of the Dwyka Group. This reflection was dubbed 'Old Faithful' and is 20 m thick with a P-wave velocity of 4200 m/s. Only weak reflectors were recorded above Old Faithful, due to small reflection coefficients between contrasting lithological rock layers. In the areas where dolerite intrusions are present, the quality of the data deteriorated (Scheiber-Enslin et al., 2014) because dolerites act as barriers that absorb and scatter the seismic energy. Reflection seismic surveys of a smaller scale have also been conducted in order to investigate the stratigraphy and geological structures of interest within the basin, for example, the 100 km line from Prince Albert to Slingersfontein near Beaufort West (Bräuer et al., 2007).

Physical properties such as seismic velocity, bulk density and porosity of Karoo Basin rocks have been investigated and reported by Baiyegunhi et al. (2014) and Fatti (1987). Bulk densities of 133 samples collected from Grahamstown to Queenstown were found to be between 2.50 g/cm^3 and 2.70 g/cm^3, with porosities ranging between 0.40% and 3.30 %. The bulk densities of 117 Karoo sandstone samples in the Eastern Cape range between 2.67 g/cm^3 and 2.77 g/cm^3. The bulk densities of 66 shale core samples from the same area range between 2.53 g/cm^3 and 2.76 g/cm^3 (Baiyegunhi et al., 2014). Fatti (1987) showed that sandstone samples collected from near East London had porosities less than 1%, with high seismic velocities (Vp = 5000 m/s) that slightly increase with depth. Fatti (1987) also observed that dolerite intrusions are characterized by higher seismic velocities (Vp = 6200 m/s) than the surrounding sediments in the basin. These results correlate well with the results by Bräuer et al. (2007) on similar rock types.

These seismic velocities correlate well with seismically-derived velocities reported by Bräuer et al. (2007). Bräuer et al. (2007) showed that the average P-wave velocities for Beaufort and Ecca Group rocks are between 4400 m/s and 5440 m/s, while the average S-wave velocities is 2600 m/s.

A previous physical property study on 118 cylindrical basalt samples from four different formations around Mahabaleshwar and Koyna in India have shown that the physical properties of the rocks varied significantly between formations (Prasanna Lakshmi et al., 2014). The

physical properties that were investigated in this study are the bulk density, porosity, P-wave and S-wave seismic velocities as well as Poisson's ratio.

It has been documented that the P-wave and S-wave velocities show a linear trend when plotted against porosity and clay content in shaly sandstones. Since porosity and clay content have larger effects on the S-wave velocity than the P-wave velocity, a high Vp/Vs ratio is indicative of a sample with a high porosity and/or clay content (Han et al., 1986). Han et al. (1986) also showed that the presence of clay in a specimen should significantly reduce the seismic velocity of the sample.

The Karoo Basin is still largely underexplored and many factors that directly influence the exploration and extraction of the shale gas, remain under investigated. This study should aid in the understanding of some of these factors, for example the effect that seismic velocity, density, mineralogy, porosity and micro-fracture orientation should have on reflection seismic exploration of the basin. More importantly, this study should also help to establish whether the reflection seismic method can be used to image the shale gas layer.

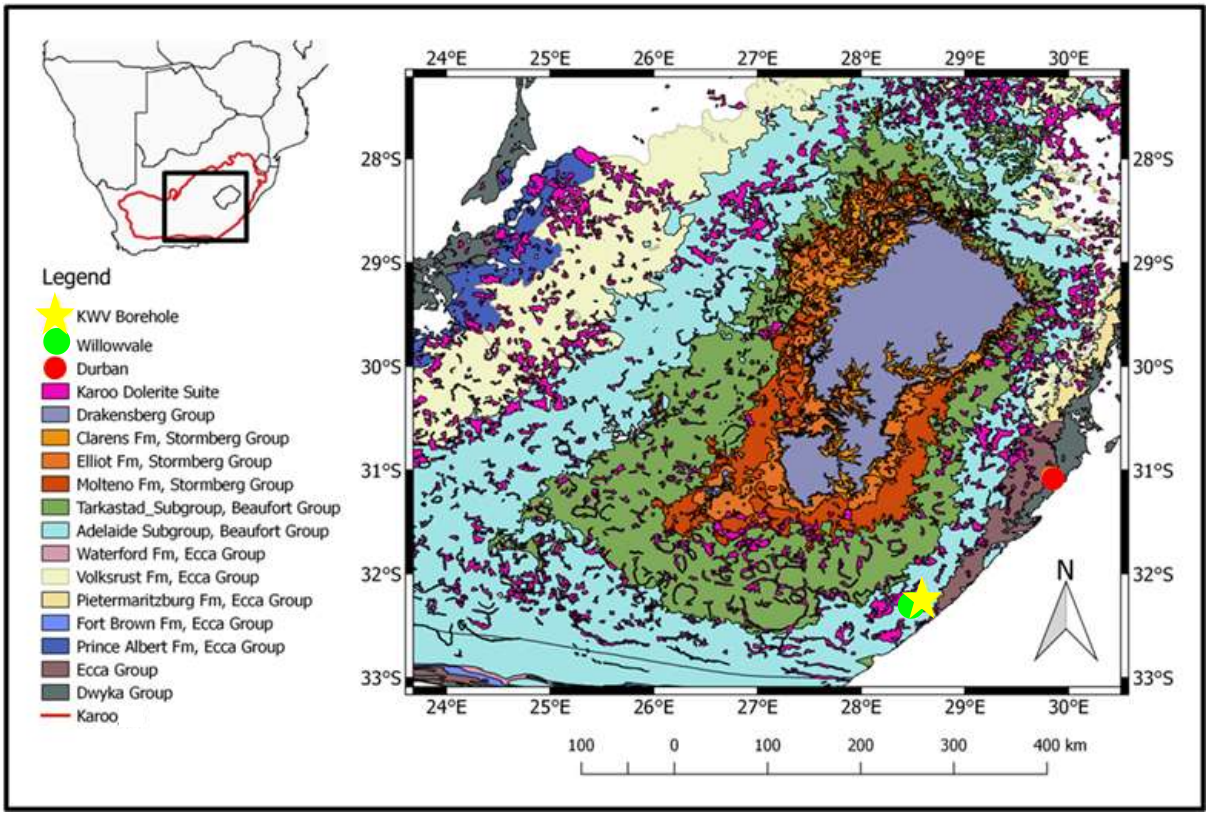

Figure 1.1: A geology map of the study area, indicating the position of borehole KWV relative to Willowvale and Durban, in the Eastern Cape Province of South Africa. Insert map shows the figure location relative to the basin (red outline) and southern Africa. **(SACS, 1980)**

1.1. Objectives of the study

The main objective of this study is to examine the feasibility of the reflection seismic method for hydrocarbon explorations in the Main Karoo Basin (Figure 1.1). The study is particularly focused on determining whether the seismic velocities and bulk densities of the Karoo Basin rocks can provide significant acoustic impedance contrasts that can produce strong seismic reflections at the stratigraphic interfaces of the Karoo borehole (KWV). Figure 2.1 provides the stratigraphic information of the Karoo borehole (KWV).

Another objective of the study is to establish the relationships between the seismic velocities and bulk densities of the Karoo rocks, and other physical and mineralogical features of the rocks. In particular, we seek answers to a number of questions:

- How does the mineralogy of the rock affect the bulk density and seismic velocity of the rock?
- How does the porosity of the rock affect the bulk density and seismic velocity of the rock?
- How does the presence of micro-fractures in the rock affect the bulk density and seismic velocity of the rock?
- Does the orientation of micro-fractures in the rock have any seismic velocity anisotropic effects in the rock?
- Does the preferred orientation of minerals in the rock have an effect on the seismic velocity anisotropy of the rock?

1.2. Chapter descriptions

Chapter 1 provides a brief literature review of physical property studies in the Main Karoo Basin of South Africa and the motivation for conducting this study. The chapter also provides the aim and objectives of this study as well as the layout of the thesis.

Chapter 2 reviews the main depositional processes of the Main Karoo Basin, and the resulting stratigraphy of the basin. The location of the study area, as well as the lithology and stratigraphy that was intersected by the borehole is provided. The literature review on the geology of the study area is also provided.

Chapter 3 provides the main results that were obtained from the geophysical log of the borehole.

Chapter 4 provides and discusses the fundamental basic principles of the reflection seismic method and its application to this study. The chapter also discusses the effects of physical rock properties and mineralogy on reflection seismics.

Chapter 5 provides the experimental and sampling procedure undertaken in this study and the description of all the samples. Chapters 6 and 7 provide and discuss all results obtained in this study. Finally, all conclusions drawn from this study are provided in Chapter 8.

2. Geological overview of the Main Karoo Basin, South Africa

The Main Karoo Basin covers about 300 000 km^2 of South Africa, which is almost two thirds of the country (Smith, 1990). The basin records rocks from the late Carboniferous to the mid-Jurassic periods. Its rocks were deposited in glacial- to dry desert-conditions (Cadle et al. 1993; Geel et al. 2013).

The Main Karoo Basin of South Africa was formed by complex geological and tectonic processes (Pysklywec and Mitrovica, 1999; Tankard et al., 2009; Wilson et al., 2014). South Africa was situated close to the south-western margin of Gondwana in the late Palaeozoic. The formation of the Karoo Supergroup of the Main Karoo Basin is closely related to the Cape Basin, which formed when the mantle was subsided in an extensional setting (Pysklywec and Mitrovica, 1999).

The Karoo Supergroup is also reported to have formed during a period of compressional tectonics linked to subduction that took place further south. Several compression phases resulted in the deformation of Cape sediments to form the Cape Fold Belt (CFB). Loading of the crust by the CFB resulted in the formation of a foreland basin during the late Carboniferous. It is debated whether this foreland basin is retro-arc with subduction to the north (Catuneanu et al., 1998) or due to continent-continent, arc collision or suturing, with subduction to the south (Lindeque et al., 2011). However, the size of the basin can only be accounted for by the additional widespread subsidence due to mantle flow (Pysklywec and Mitrovica, 1999; Tankard et al., 2009).

During compression, Gondwana was over the polar region resulting in a glacier-covered basin. Glacial blocks broke off and sediments were transported by the glaciers and deposited in the Karoo Basin (Pysklywec and Mitrovica, 1999).

Glacial deposits consequently accumulated in the Main Karoo Basin, initiating the deposition of the Dwyka Group. About 265 Ma ago, as Gondwana migrated away from the poles, the Karoo Basin was characterized by marine transgression across the basin (Pysklywec and Mitrovica, 1999). It was under shallow marine as well as deltaic conditions that resulted in the deposition of the Ecca Group. The organic muds of the Ecca Group formed when the Karoo Supergroup was the base of a vast anoxic lake. After millions of years of maturation, oil and gas formed from the lithified muds at approximately 250 Ma ago (Cole et al., 2011). Most of the oil and gas have since leaked out, yet pockets of ‘tight’ gas are still preserved in some of the shales.

The Ecca Group of the Karoo Supergroup is well-known for its shale gas reservoirs (Aarnes et al., 2011; Vermeulen, 2012; Warren, 2013). The deposit has been estimated to be as large as 485 Tcf, and at least 32 Tcf (Vermeulen, 2012), although precise estimates are presently unknown. The Whitehill and Prince Albert Formations of the lower Ecca Group are specifically targeted for shale gas exploration (De Wit, 2011). Bountiful dolerite intrusions north of 29°S caused a reduction in the organic carbon content of the shales in the target formations (Figure 2.2). This resulted in the conclusion that only the lower Ecca Group shales below a latitude of 29°S had the potential to produce dry gas, based on a comparison of the total organic carbon (TOC) content of the Ecca Group shales with that of dry gas containing shales elsewhere in the world (Figure 2.2) (Cole et al. 2011).

Another major stage of sedimentation in the Karoo Basin was due to fluvial systems that accumulated thick sedimentary sequences until the early Triassic (250 Ma). These sequences are presently known as the Beaufort Group. After the fluvial deposition, the basin underwent an episode of rapid uplift. This caused the environment to become erosional (Pysklywec and Mitrovica, 1999).

By this time the climate had warmed and was semi-arid with seasonal rainfall. Pulses of uplift resulted in coarser clastics in the Karoo Basin (Smith, 1990). This wedge of coarser sediments forms the Molteno Formation. The Molteno Formation comprises the basal part of the Stormberg Group and is of late Triassic (220 Ma) age (Johnson et al., 2006). Continued aridification led to the Elliot Formation being deposited on top of the Molteno Formation. This formation was deposited under playa-lake and wadi type environments. During the early Jurassic (190 Ma) the Clarens Formation was deposited under aeolian conditions (Smith, 1990).

It was during the Jurassic period that extrusive volcanic activity formed the Drakensberg Group (Smith, 1990). Sedimentation in the Karoo Basin was therefore terminated during the Jurassic period, with the influx of the Drakensberg lavas (Wilson et al., 2014; Pysklywec and Mitrovica, 1999).

The samples used in this study were provided by CIMERA (Centre of Excellence for Integrated Mineral and Energy Resource Analysis). The drill-core samples are from the Main Karoo Basin, specifically the Dwyka, Ecca and Beaufort Groups. These samples were acquired from borehole KWV, which is situated close to Willowvale, in the Eastern Cape Province (Figure 1.1).

The stratigraphic units that are intersected by KWV are the Adelaide Subgroup of the Beaufort Group, the Fort Brown, Ripon, Whitehill and Prince Albert Formations of the Ecca Group, and the Dwyka Group (Figure 2.1). The lithological units within each stratigraphic unit are also indicated.

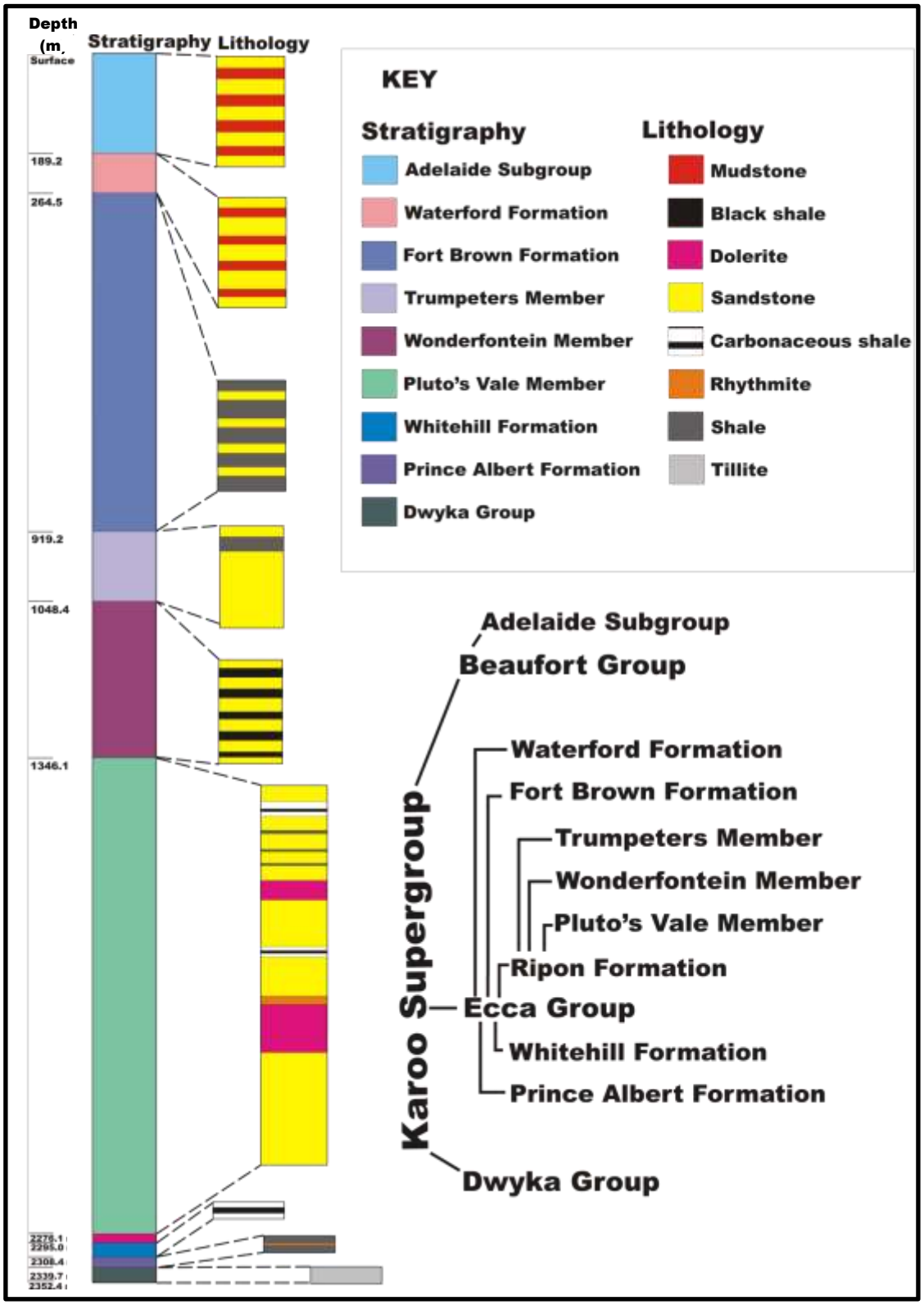

Figure 2.1: A stratigraphic log with a simplified lithology log down to a depth of 2352.4 m of borehole KWV. The stratigraphy of the Beaufort, Ecca and Dwyka groups are also indicated **(CIMERA, n.d.).**

The Adelaide Subgroup from the lower Beaufort Group outcrops at the KWV borehole site. This subgroup is composed of mudstone ranging in colour from green to grey and brown. It also consists of fine-grained sandstone lenses throughout the mudstone and siltstone (Smith, 1980; Johnson et al., 1996, Smith and Botha-Brink, 2011). The subgroup maximum thickness of the subgroup is 1000 m thick, however it is only 189 m thick at borehole KWV (Smith and Botha-Brink, 2011).

The Fort Brown Formation of the Ecca Group consists of prodelta mudstones as well as rhythmites, with minor amounts of sandstone, and reaches a thickness of 654.7 m. The underlying Ripon Formation has grey fine-grained sandstones with only minor mudstone (Geel et al., 2015). The Ripon Formation has a thickness of 1357 m.

The Whitehill Formation is characterized by black carbonaceous shales with quartzite, illite, muscovite, chlorite and pyrite. The shales at surface weather white due to the oxidation of the pyrite to gypsum and they also contain lenses of dolomite (Geel et al., 2013; Geel et al., 2015). Towards the south-central part of the basin the shales of the Whitehill Formation reach a maximum thickness of 30 m, but thins and pinches out from Hertzogville in the Free State to Coffee Bay in the Eastern Cape Province, such that only a thin layer (13.5 m) was intersected at borehole KWV. Even though the layer is relatively thin throughout the basin, high TOC contents (3% – 7%) have been measured on samples from Soekor boreholes for the Whitehill Formation in the southern part of the basin. These results indicated that this formation has a high potential to generate dry gas, including methane (Cole et al., 2011). However, the presence of dolerite within this formation indicates that the organic carbon might have been thermally transformed to produce carbon dioxide, methane and graphite. Thus dry gas should probably only occur in shales from the Whitehill Formation that lie south of a latitude of 29ºS (Figure 2.2).

The Prince Albert Formation underlies the Whitehill Formation and consists of mudstone and dark grey shale with small sandstone units. Dropstones from the underlying Dwyka Group are also found in this formation due to the gradational contact between the two groups (Johnson et al., 1996; Cole et al., 2011; Geel et al., 2013). The TOC values of the Prince Albert Formation ranges from 0.35% to 12.4%, with an average value of 2.4% (Cole et al., 2011). Dolerites have also intruded throughout the Prince Albert Formation. Although the dolerite-to-shale ratio is much less in this formation than in the Whitehill Formation (Cole et al., 2011) it is still expected that the shales from the Prince Albert Formation with a TOC content and depth sufficient to produce dry gas should occur below the 29ºS latitude line (Figure 2.2).

Due to the glacial deposition of the Dwyka Group, it is mainly made up of tillite and glacio-lacustrine shale. Fluvio-glacial sandstone, rhythmite and mudstone with dropstones are also present (Johnson et al., 1996). This group is at its thickest in the south, reaching 800 m in thickness near Beaufort West in the Western Cape Province, and thins out northwards until it pinches out at Newcastle in Kwazulu Natal (Cadle et al., 1993; Johnson et al., 1996). The Dwyka Group also contains some black shales, but they are sparse, with maximum thicknesses of 50 to 60 m. The TOC content of these shales averages at only 1.9% (Cole et al., 2011).

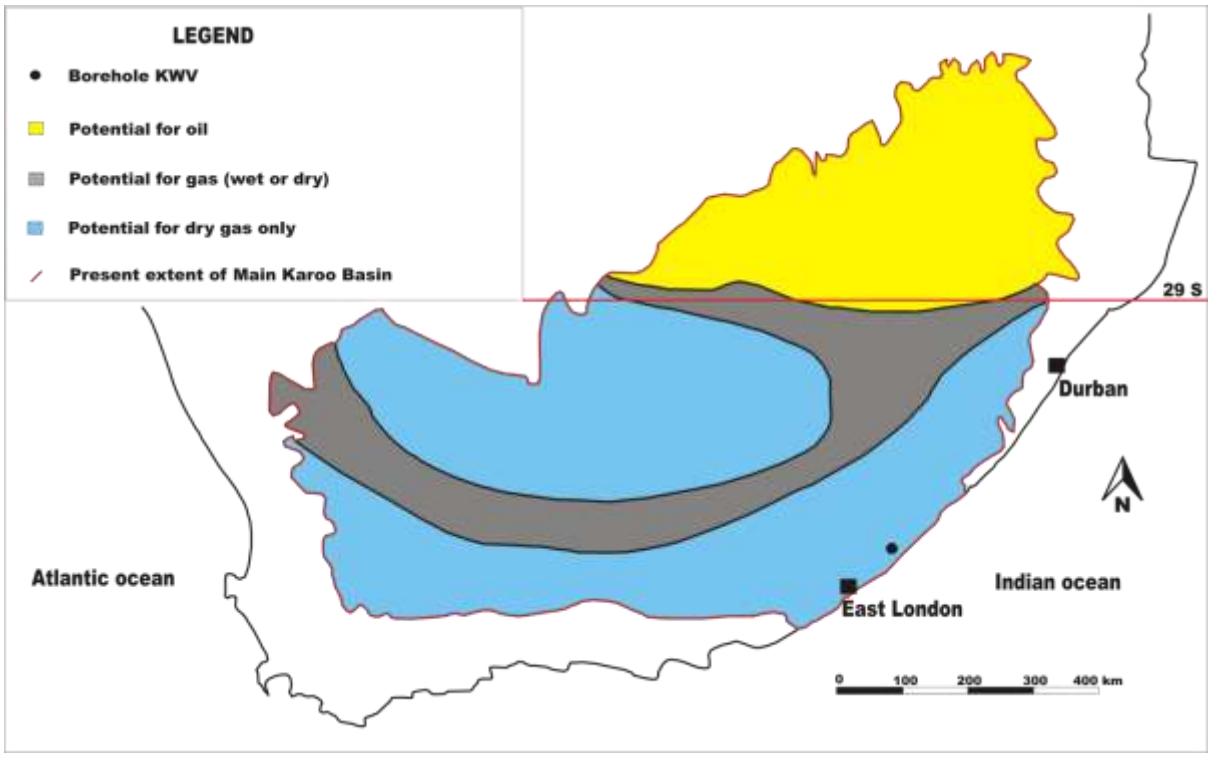

Figure 2.2: Map indicating the different hydrocarbon potentials of the Ecca Group shales. The position of the 29°S latitude is indicated, as well as the location of the KWV borehole (Modified from Cole, 2011).

3. Geophysical log

The KWV borehole was logged by Weatherford Slimline Services down to a depth of 2352.93 m. Variety of data were captured, from the temperature and diameter of the borehole, to the density, porosity and resistivity of the surrounding rocks.

The diameter of the borehole was measured to be 124 mm from the surface down to 288 m, 98 mm from 288 m down to 994 m and 79 mm from 994 m down to 2342 m. The temperature read between 29 ºC and 79 ºC, increasing with depth. Structures in the surrounding rocks were found to be shallowly dipping and striking in a north-west and south-west direction (CIMERA, n.d.). Figure 3.1 presents the lithology, seismic velocities, densities and gamma-ray responses from borehole KWV.

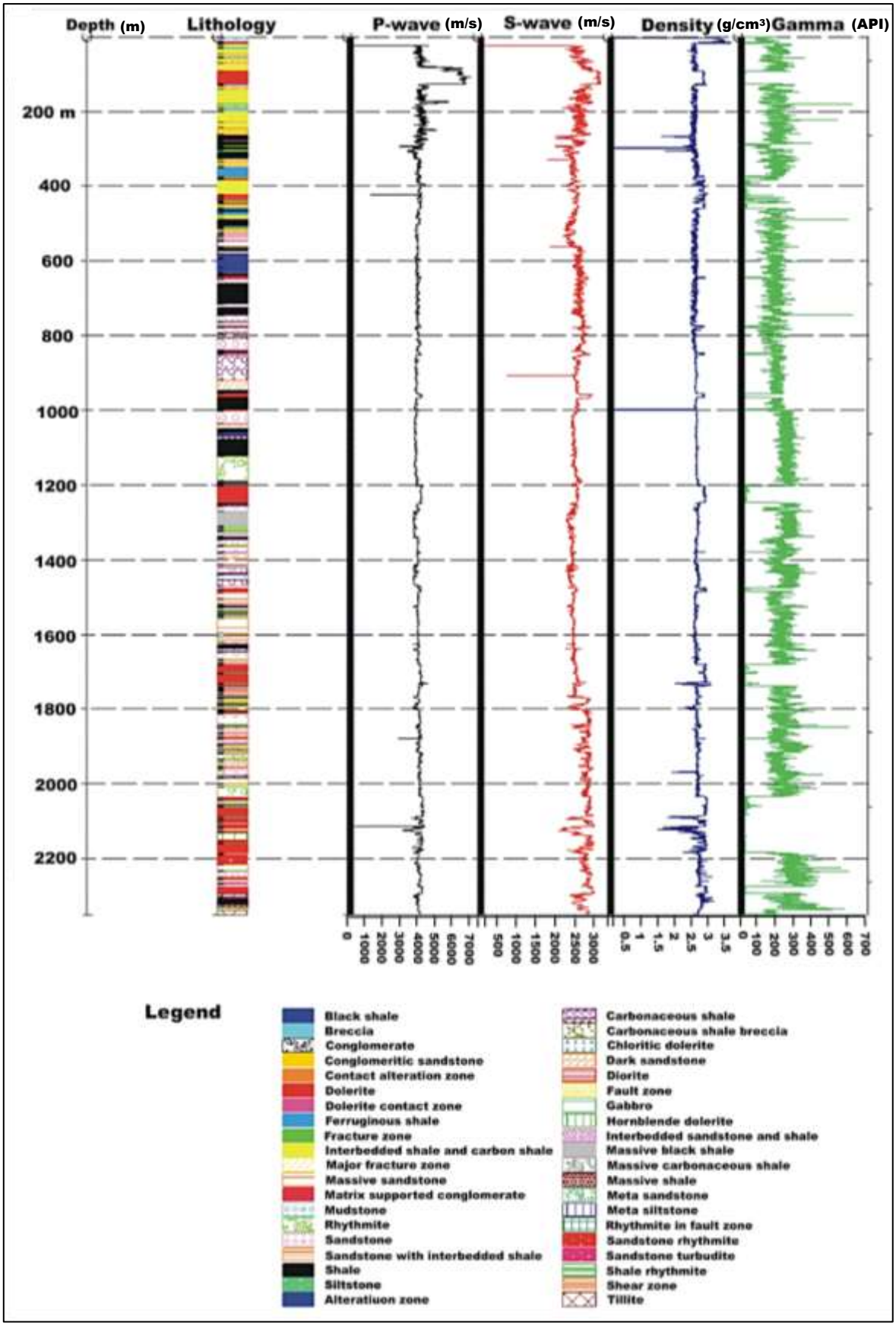

Figure 3.1: Log of seismic velocity, density and radioactivity geophysical responses in borehole KWV (CIMERA, n.d.).

The geophysical responses for different lithologies can be seen more clearly in Figure 3.2. Where dolerite was intercepted in the borehole, very low (<100 API) gamma ray readings are observed. This is possibly due to the very little radioactive material that is present in these rocks. The P- and S-wave velocities (Vp and Vs) are also higher where dolerite is present. Vp for dolerite above 200 m depth is approximately 6000 m/s, while it decreases to approximately 4500 m/s at a depth of 1200 m. The seismic velocities measured at greater depths are less accurate, since the borehole logs do not account for stress changes, i.e., the in situ conditions of the rocks are not taken into account.

Minor variations in geophysical responses are observed for shale and sandstone. Based on Figure 3.2, the P-wave and S-wave velocities for both rocks are very similar (Vp = 4000-4500 m/s, Vs = 2500-3000 m/s).

The average seismic velocities and bulk densities from the geophysical log for each sample that was collected from the borehole is provided in Table 3.11. The average seismic velocities from the geophysical log for all the sandstone samples are 4047 (± 96.26) m/s and 2603 (± 159.74) m/s for Vp and Vs, respectively. The average bulk density of these samples is 2.72 (± 0.25) g/cm^3. The average Vp for the shale samples are 3970 (± 97.43) m/s while the average Vs is 2547 (± 122.99) m/s. The average bulk density of the shale samples is 2.72 (± 0.7) g/cm^3. The average Vp and Vs values from the geophysical log, for all dolerite samples are 4213 (± 106.89) m/s and 2706 (± 178.99) m/s, respectively. The average bulk density of the dolerite samples is 2.86 (± 0.11) g/cm^3. In the case of the Rhythmite samples, the average Vp is 4178 (± 173.89) m/s and the average Vs is 2754 (± 176.02) m/s. The average bulk density of the Rhythmite samples is 2.82(± 0.13) g/cm^3. These values are compared to the experimental values to investigate the correlation between the two methods. Based on the geophysical log, the tillite samples exhibit average Vp and Vs values of 4174 (± 30.41) m/s and 2802 (± 54.62) m/s, respectively. The average bulk density of these samples is 2.73 (± 0.02) g/cm^3.

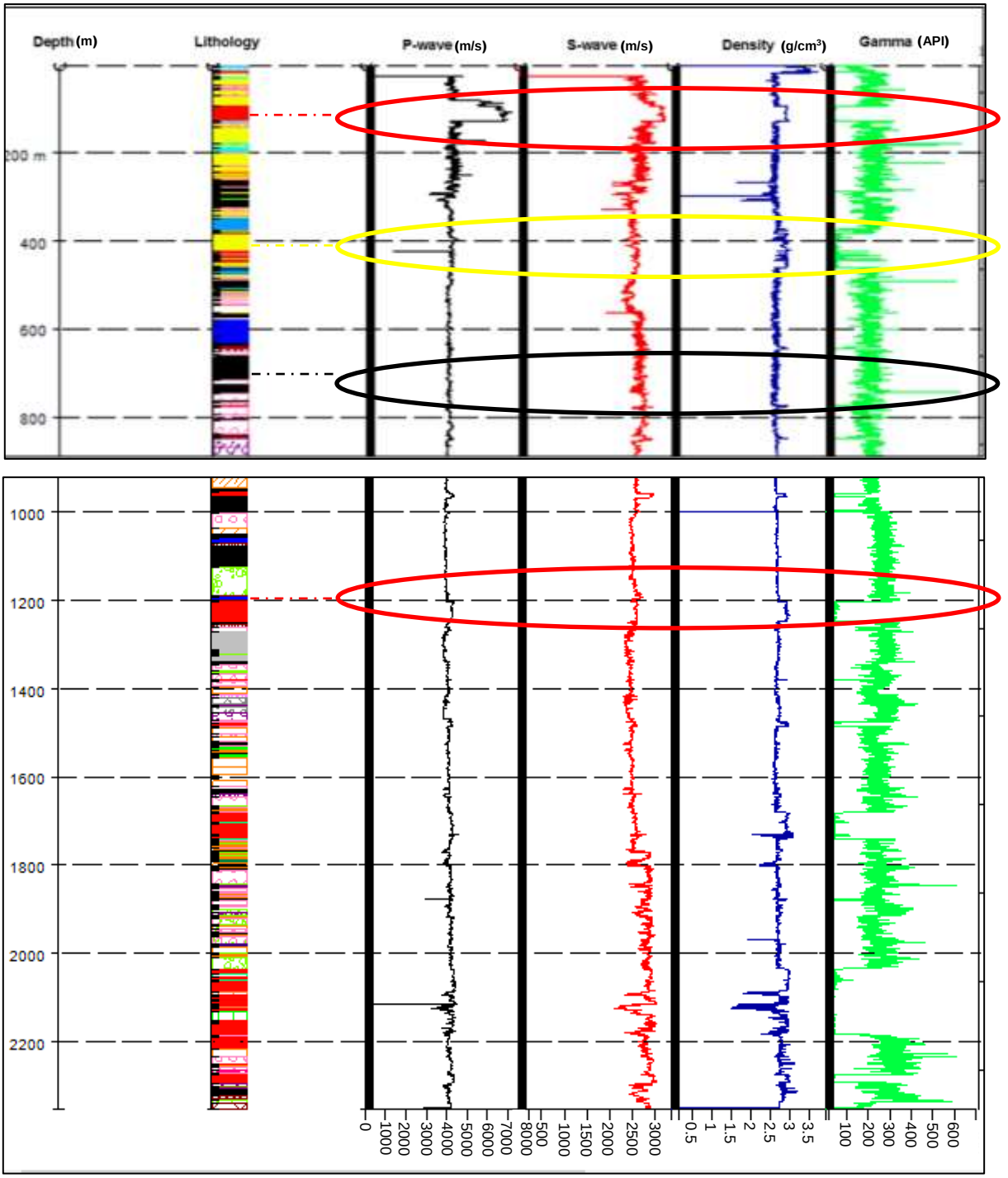

Figure 3.2: Interpreted version of geophysical log. The red ellipse indicates the response for dolerite, while the yellow and black ellipses show the responses for sandstone and shale, respectively. The legend is the same as the legend in Figure 3.1.

Table 3.1: The average values for bulk density and seismic velocity from the geophysical log for each sample from borehole KWV (CIMERA, n.d.).

Sample	Lithology	Density (g/cm^3)	P-wave velocity (m/s)	S-wave velocity (m/s)
W1	Sandstone	3.48 + 0.01	-	-
W2	Mudstone	2.59 + 0.04	4212 ± 58.18	2618 ± 29.72
W3	Breccia	2.64 + 0	4192 ± 56.44	2451 ± 27.23
W4	Sandstone interbedded shale	2.61 + 0.01	3985 ± 0.29	2597 ± 9.31
W5	Shale	2.69 + 0.01	3901 ± 15.52	2376 ± 8.28
W6	Sandstone	2.59 + 0.01	4036 ± 24.08	2506 ± 2.08
W7	Dolerite	2.9 + 0.01	4128 ± 0	2591 ± 0
W8	Sandstone	2.64 + 0.01	3979 ± 0	2581 ± 5.05
W9	Carbonaceous shale	2.64 + 0.01	3920 ± 7.18	2493 ± 0
W10	Dark sandstone	2.65 + 0	3964 ± 0	2513 ± 4.21
W11	Shale	2.64 + 0.01	4000 ± 0	2566 ± 0
W12	Dolerite	2.84 + 0.01	4245 ± 6.5	2936 ± 13.74
W13	Dark sandstone	2.64 + 0.01	3887 ± 5.21	2468 ± 5.27
W14	Shale	2.67 + 0.02	3957 ± 8.82	2476 ± 8.41
W15	Massive shale	2.71 + 0.01	3964 ± 0	2553 ± 0
W16	Dolerite	2.93 + 0.02	4282 ± 0	2566 ± 0
W17	Massive black shale	2.68 + 0.01	3808 ± 0	2323 ± 0
W18	Massive sandstone	2.64 + 0.01	4128 ± 0	2480 ± 5.16
W19	Massive carbonaceous shale	2.64 + 0	3860 ± 16.85	2487 ± 12.85
W20	Carbonaceous shale	2.74 + 0	3865 ± 0	2461 ± 0
W21	Sandstone	2.67 + 0.02	4084 ± 0	2483 ± 3
W22	Dolerite	2.92 + 0.01	4178 ± 9.08	2533 ± 8.82
W23	Sandstone	2.53 + 0.01	4000 ± 0	2504 ± 1.81
W24	Carbonaceous shale	2.66 + 0.01	4063 ± 0	2450 ± 0
W25	Massive shale	2.63 + 0.01	4063 ± 0	2480 ± 5.07
W26	Dolerite	2.89 + 0.01	4181 ± 10.08	2562 ± 10.63
W27		2.66 + 0.04	4299 ± 13.53	2566 ± 0
W28	Carbonaceous shale	2.76 + 0.01	4021 ± 0	2591 ± 11.45
W29	Massive sandstone	2.67 + 0.01	4218 ± 0	2913 ± 0
W30	Rhythmite	2.96 + 0.01	4379 ± 0	2913 ± 0
W31	Dolerite	2.95 + 0	4294 ± 11.12	2872 ± 7.17
W32		2.94 + 0.01	4403 ± 0	2897 ± 0
W33		2.95 + 0.02	4218 ± 0	2884 ± 4.98
W34		2.65 + 0.05	4036 ± 8.05	2444 ± 9.15
W35	Sandstone	2.75 + 0.01	4150 ± 0	2735 ± 0
W36		2.72 + 0.01	4087 ± 4.78	2860 ± 6.58
W37	Dolerite	2.88 + 0.01	4241 ± 0	2881 ± 0
W38		2.78 + 0.01	4045 ± 6.97	2744 ± 20.36
W39	Carbonaceous shale	2.8 + 0.03	3787 ± 4.79	2562 ± 13.29
W40		2.77 + 0.02	3964 ± 0	2591 ± 0
W41		2.74 + 0.01	4106 ± 0	2659 ± 5.89
W42		2.79 + 0.03	4027 ± 11	2699 ± 6.22
W43	Shale	2.8 + 0.01	4000 ± 0	2597 ± 5.75
W44		2.8 + 0.01	4021 ± 0	2617 ± 0
W45	Massive shale	2.8 + 0.01	4128 ± 0	2859 ± 7.08
W46	Rhythmite	2.79 + 0	4084 ± 0	2565 ± 2.51
W47		2.71 + 0.01	4072 ± 9.64	2785 ± 6.73
W48	Tillite	2.74 + 0.01	4152 ± 5.39	2838 ± 7.5
W49		2.71 + 0	4195 ± 0	2765 ± 1.73

4. Reflection seismics and physical properties

4.1. Elastic moduli and acoustic impedance

The seismic velocity and bulk density of a rock is controlled by the bulk modulus of the rock. Since the reflection seismic technique is dependent on waves reflected from discontinuities, the elastic properties (bulk modulus and Young's modulus) control the applicability of the technique (Dentith and Mudge, 2014; Park, 1997). For rocks at depth, the elastic moduli track the stress and strain conditions. The bulk modulus (κ) of a material is defined as the compressibility of the material, better described as the ratio of volumetric stress to volumetric strain,

$$\kappa = {P}/{\frac{\Delta V}{V}} \tag{1}$$

where *P* is the pressure (volumetric stress) and *V* is the volume. *ΔV* represents the change in volume.

The shear modulus (μ) is a measure of the shear strain affecting the material, and is defined by the ratio of shear stress to shear strain,

$$\mu = {\tau}/{\tan\theta} \tag{2}$$

where τ is the shear stress and tan θ is the shear strain.

Young's modulus (E) is the ratio of axial stress to axial strain, and is mathematically expressed as;

$$E = {\frac{F}{A}}/{\frac{\Delta l}{l}} \tag{3}$$

where *F* is the force applied to material, *A* is the cross-sectional area of material and l is the length of material. Young's modulus is a measure of the change in the length of the material, due to normal stresses acting in one direction (Vogt, 2009).

The last elastic modulus is the Poisson ratio (σ), which is a measure of the radial strain on a material subjected to uniaxial strain. It is expressed as the ratio of transverse strain to axial strain,

$$\sigma = {({\Delta r}/{r})}/{({\Delta l}/{l})} \tag{4}$$

where r is the radius of the material, Δr is the change in radius of the material, l is the length of material and Δl is the change in length of the material. The seismic velocity-bulk density relationship is strongly dependent upon stress and Poisson's ratio (Rybach and Buntebarth, 1982). Poisson's ratio plays an important part in reflection seismics since it can provide valuable constraints on crustal composition, which affects the compressional wave velocity (Christensen, 1996).

The elastic modulus can be used to calculate the speed of a seismic body wave through a material. A body wave is a type of seismic wave that moves through the subsurface of the Earth and constitutes the signal in seismic surveying (Dentith and Mudge, 2014). The mathematical expression of the speed of a seismic body wave through a material is given by:

$$V_{bodywave} = \sqrt{Elastic\ modulus / \rho} \quad (5)$$

where ρ is the bulk density of the material. A body wave is further divided into two waves. The P-wave is the compressional wave (longitudinal) and the S-wave is the shear wave (transverse). The P-wave has a higher velocity than the S-wave and always reaches the detector/sensor first. The amplitude of the S-wave is significantly higher than that of the P-wave (Punturo et al., 2005) in most solid media. Based on Equation 5, the equations for v_p and v_s then become:

$$v_p = \sqrt{(\kappa + 4/3\mu) / \rho} \quad (6)$$

$$v_s = \sqrt{\mu / \rho} \quad (7)$$

where μ is the shear modulus, κ is the bulk modulus and ρ is the bulk density of the material (Domenico, 1977). The propagation velocity of the P- and S-wave is calculated using Equation 8 (Birch, 1960):

$$v = \frac{x}{t} \quad (8)$$

where v is the velocity of the P- or S-wave, x is the distance that the wave travelled in time t (Gadallah and Fisher, 2009).

The velocity measurements that were obtained from the Karoo rocks are expected to obey Equations 5 to 7. If the velocity obtained from the drill-core samples is lower than expected, the elastic properties of the rocks should be able to address this difference.

In addition to measuring the physical properties of the borehole, these properties should be used to determine if reflection seismic surveys are feasible for shale gas exploration in the basin. Seismic wave propagation is dependent on physical properties such as bulk density and seismic wave velocities. To be able to map the shale layer using reflection seismic methods, there must be a significant acoustic impedance contrast between the shale and the host rocks (Figure 4.1).

Figure 4.1 illustrates the basic principles of the reflection seismic technique. Energy is injected into the Earth's surface. Reflected waves are received by an array of receivers at the surface. Whether a wave is reflected or not is controlled by various parameters. The most important parameter that influences the strength of the reflection is the contrast in acoustic impedance.

The acoustic impedance (z) is given by:

$$z = \rho \times V_p \tag{9}$$

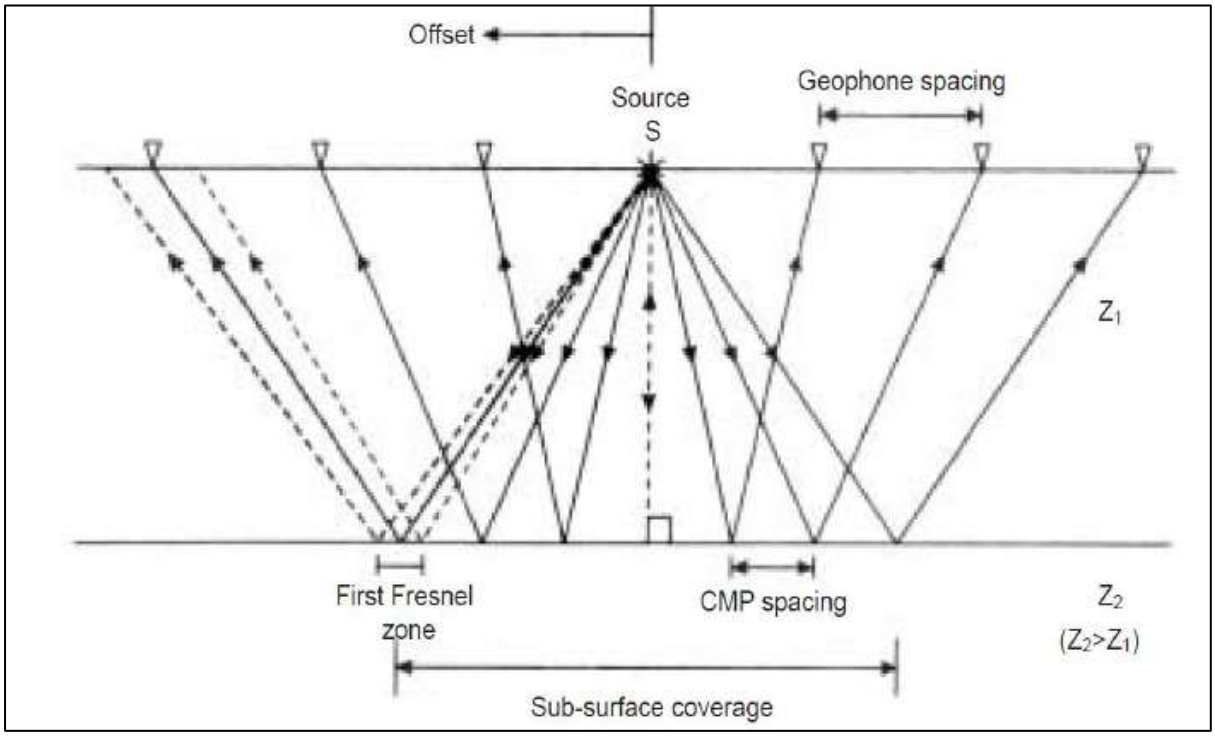

Figure 4.1: Schematic seismic reflection ray paths over a horizontal interface. There is an impedance contrast at the contact between Z1 and Z2 (Manzi, 2013).

The reflection coefficient (Rc) is the ratio of the amplitudes of the outgoing and incoming seismic waves caused by the acoustic impedances between adjacent rock layers. This parameter determines whether or not an incident seismic wave reflected at the interface between two layers can be detected by the surface seismic method. The reflection coefficient for normal incidence is given by:

$$Rc = \frac{z2 - z1}{z2 + z1} \quad (10)$$

where z1 and z2 are the acoustic impedances of layer one and layer two, respectively (Dentith and Mudge, 2014). The commonly-accepted criterion for a reflection is that the reflection coefficient at the contact between the layers should reflect at least 0.06 of the incident energy for the contrast to be detected by the reflection seismic method (Malehmir et al., 2013). Other factors influencing the reflection of a target are the size, depth and geometry of the target. The reflection coefficient was determined for different lithology types in the KWV borehole, e.g. a shale-dolerite and dolerite-sandstone contact, in order to establish whether the interfaces between the different lithological units can be detected by the reflection seismic method. It is therefore of vital importance to determine the physical properties of rocks in an area of interest ahead of carrying out a reflection seismic survey.

4.2. Factors affecting seismic velocities

Along with elastic properties, the bulk density and seismic velocity of rocks are affected by multiple factors such as porosity, stress and mineralogical parameters, as well as the presence of micro-fractures in the rock (Dentith and Mudge, 2014).

4.2.1. Porosity, mineralogy and bulk density

The effect of porosity on seismic velocity and bulk density are mainly dependent on the type of material occupying the pore spaces in the rock. This effect becomes significant when the porosity is 10 % or higher (Dentith and Mudge, 2014). Rocks filled with air or methane should have lower acoustic impedance than rocks filled with water. The effect of porosity on the acoustic wave velocities in sandstones have been previously investigated (Han et al., 1986). It has been shown that both the P- and S-wave velocities decrease linearly with the increase in porosity, however the P-wave velocity is affected more. It has also been shown that the presence of clay in sandstones significantly reduces the elastic moduli of the rocks, indicating that higher velocities are expected for rocks with a higher clay content. A study by Kassab and Weller (2013) also confirmed the inverse correlations between seismic wave velocities and porosity.

4.2.2. Seismic velocities at elevated uniaxial stress

Another physical parameter influencing the seismic velocity and bulk density of a rock is stress. According to Birch's law, with increasing stress the velocity of a seismic wave through a rock should also increase (Birch, 1960; Lin et al., 2005; Malehmir et al., 2013). According to Birch's law, the stress-velocity relationship should exhibit the renowned initial steep velocity

increase with elevated stress, typically illustrating the stress sensitivity of seismic wave velocities. The increases in seismic velocity are more rapid at shallower depths in the crust, since near-surface rocks are expected to be more porous than deeper rocks. With increasing confining stress, micro-fractures in the rocks are expected to close and the pore spaces are expected to decrease, thus leading to a linear relationship between velocity and stress. With the application of uniaxial stress to the rocks, an increase in seismic velocity was observed due to the closure of oriented micro-cracks (Punturo et al., 2005). When the seismic velocity stabilises, the saturation velocity is reached (Wyllie et al., 1958; Nkosi et al., 2016). At this stage the rocks become essentially crack-free (Ji et al., 2015). In this study, the effect that uniaxial stress has on the KWV samples was investigated in order to mimic the in situ conditions of the rocks.

4.2.3. Seismic anisotropy

The study of the seismic velocity anisotropy of Karoo Basin rocks is also important because it could affect the seismic reflections that may be observed in a seismic section (Malehmir et al., 2013). Seismic velocity anisotropy in rocks may be caused by different factors, such as the crystallographic preferred orientations of minerals (CPO), the shape preferred orientations of minerals (SPO) the orientations of plate-like minerals, aligned cracks or micro-fractures and compositional layering (Ivankina et al., 2017; Ji et al., 2015). The micro-fracture orientations in rocks from borehole KWV were mapped using micro x-ray computed tomography.

Studies by Ji et al. (2015) and Ivankina et al. (2017) show that seismic waves tend to propagate faster when they propagate parallel to the foliation plane of the minerals in a rock. The orientation of minerals present in the KWV samples was petrographically investigated to examine their effect on seismic anisotropy.

Seismic anisotropy of the rock samples are calculated using the following equation:

$$A = \frac{Vmax - Vmin}{Vmean} \times 100\% \qquad (11)$$

Where *Vmax* and *Vmin* are the maximum and minimum velocities measured for a sample, respectively, and *Vmean* is the mean velocity for the sample (Ji et al., 2015; Punturo et al., 2005.)

In cases where the porosity of a rock is less than 10 %, the effect of mineralogy on a rock's seismic velocity and bulk density becomes dominant. Any preferred orientations of minerals in a rock may also attribute to the seismic velocity anisotropy of the rock (Ivankina et al., 2017; Punturo et al., 2005). Since the rocks from the KWV borehole in the Karoo Basin are not

significantly porous, it is important to investigate the relationship between the minerals in the rocks and any anomalous seismic velocities and/or bulk densities. Of all the rock types included in Figure 4.2, sedimentary rocks have relatively lower bulk densities and seismic velocities than felsic rocks, mafic rocks and ultramafic rocks. It is evident from Figure 4.2 that felsic rocks containing large amounts of quartz and feldspars have similar densities to sedimentary rocks, but their seismic velocities are significantly higher. In general, there should be significant reflection coefficients between sedimentary rocks (e.g., shales and sandstones) and mafic rocks (e.g., dolerites). Since KWV samples from the Whitehill Formation contains disseminated pyrite, and samples from the Pluto's Vale Member and Whitehill Formation contains pyrrhotite, the effect of sulphide minerals on the seismic wave velocities and bulk densities of the rocks should also be considered. Most sulphide minerals, like pyrite, have a higher seismic velocity and density than its host rocks. However, the sulphide minerals sphalerite, chalcopyrite and pyrrhotite have lower seismic velocities and higher bulk densities than their host rocks (Dentith and Mudge, 2014).

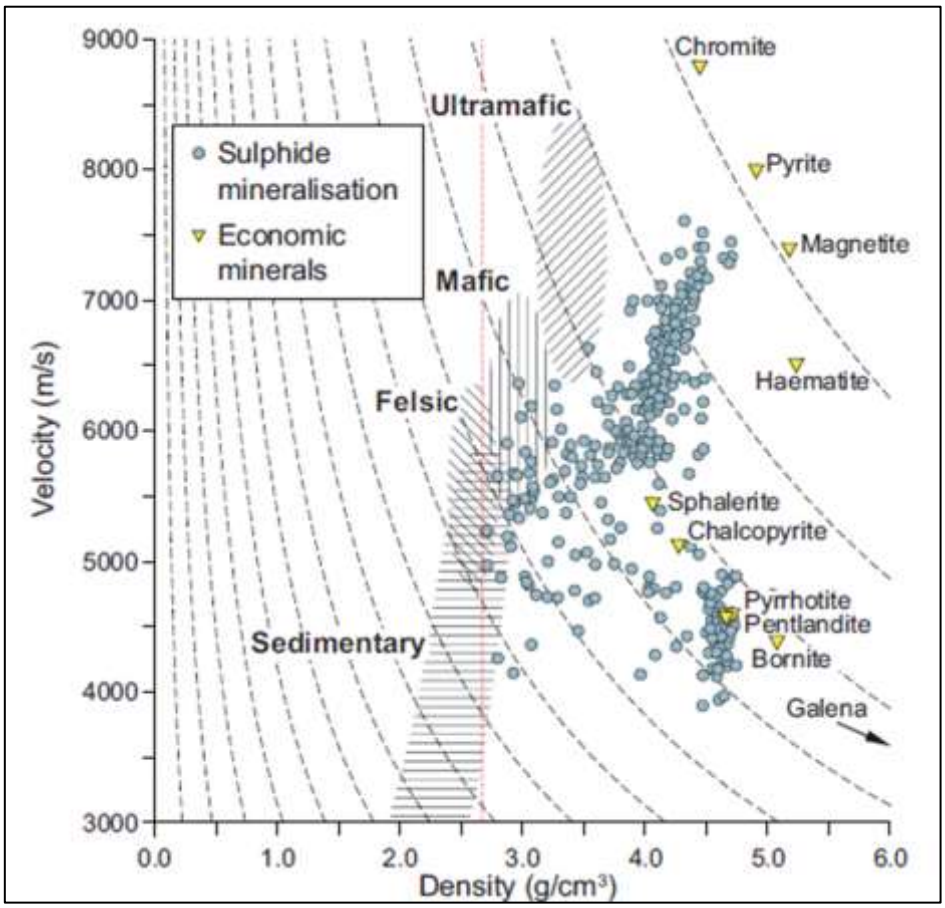

Figure 4.2: Velocity versus density plot for economic minerals, sedimentary rocks, felsic rocks, mafic rocks and ultramafic rocks. Sulphide mineralisation is also indicated (modified after Dentith and Mudge, 2014).

5. Methodology

A summary of the steps that are undertaken in this study is provided in Figure 5.1.

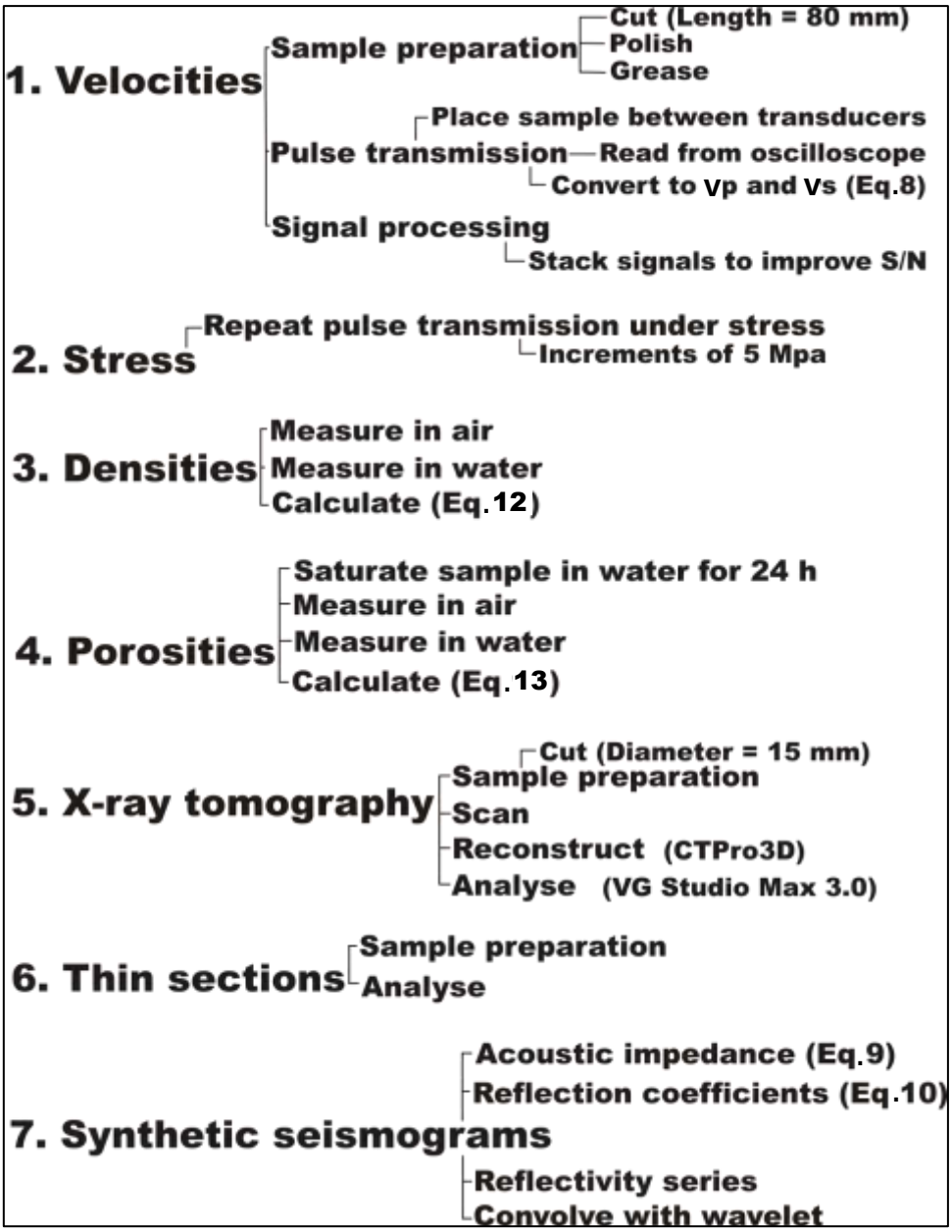

Figure 5.1: Flowchart summarizing all main steps taken during the course of the study.

5.1. Sampling

Forty nine drill-core samples were taken from borehole KWV near Willowvale (see Figures 2.1 and 2.2). Samples were taken from the lower Beaufort Group, the Ecca Group and the upper Dwyka Group, to a depth of ~2 400 m. In order to fully represent the entire drill-core, samples were taken from every lithological unit within each stratigraphic unit. The samples consist mostly of sandstones and shales, with abundant carbonaceous shales. Dolerite intrusions were also present throughout the stratigraphy. Table 5.1 presents a summary of the stratigraphy and lithology of each sample.

Each sample was named with the prefix W (Willowvale), followed by the number representing the order in which the samples were taken. The first sample would thus be called W1, and is the sample closest to the surface. A summary of the lithology and characteristic features of each sample is provided in Figures 6.1 to 6.49. The descriptions of the samples are based on observations from this study, as well as data from KARIN (CIMERA, n.d.).

Table 5.1: Summary of the stratigraphy and lithology of borehole KWV, with the location of samples indicated. Sample depths and thicknesses can be found in Figures 6.1 to 6.49 (CIMERA, n.d.).

Stratigraphy				Sample name	Lithology
Group	Sub-Group	Formation	Member		
Beaufort	Adelaide			W1	Sandstone
				W2	Mudstone
Ecca		Waterford		W3	Breccia
				W4	Sandstone interbedded shale
		Fort Brown		W5	Shale
				W6	Sandstone
				W7	Dolerite
				W8	Sandstone
				W9	Carbonaceous shale
		Ripon	Trumpeters	W10	Dark sandstone
				W11	Shale
				W12	Dolerite
				W13	Dark sandstone
			Wonder Fontein	W14	Shale
				W15	Massive shale
				W16	Dolerite
				W17	Massive black shale
			Pluto's Vale	W18	Massive sandstone
				W19	Massive carbonaceous shale
				W20	Carbonaceous shale
				W21	Sandstone
				W22	Dolerite
				W23	Sandstone with soft sediment deformation
				W24	Carbonaceous shale
				W25	Massive shale
				W26	Dolerite
				W27	Dolerite
				W28	Carbonaceous shale
				W29	Massive sandstone
				W30	Rhythmite
				W31	Dolerite
				W32	Dolerite
				W33	Dolerite
				W34	Dolerite
				W35	Sandstone
				W36	Sandstone
		Dolerite		W37	Dolerite
				W38	Dolerite
		Whitehill		W39	Carbonaceous shale
				W40	Carbonaceous shale breccia
				W41	Carbonaceous shale
				W42	Carbonaceous shale
		Prince Albert		W43	Shale
				W44	Shale
				W45	Massive shale
				W46	Rhythmite
				W47	Rhythmite
Dwyka				W48	Tillite
				W49	Tillite

5.2. Seismic velocity measurements

5.2.1. Sample preparation

The steps that were taken to prepare the samples for measurements are illustrated in Figure 5.2. The diameter of the samples range from 45 mm to 82 mm, and the samples were cut to lengths of 80 mm. Due to fractures and weaknesses within some of the samples, the lengths of these samples had to be shortened to account for fragmentation. Both ends of the samples were cut parallel to one another (Figure 5.2a). A lapping machine, shown in Figure 5.2b, was used to lap the edges of the samples to be perfectly smooth (Figure 5.2c), and silicon-carbide powder was used as a grinding paste. The ends of the samples were greased thinly, to ensure good contact between the sample and the transducers (Figure 5.2c).

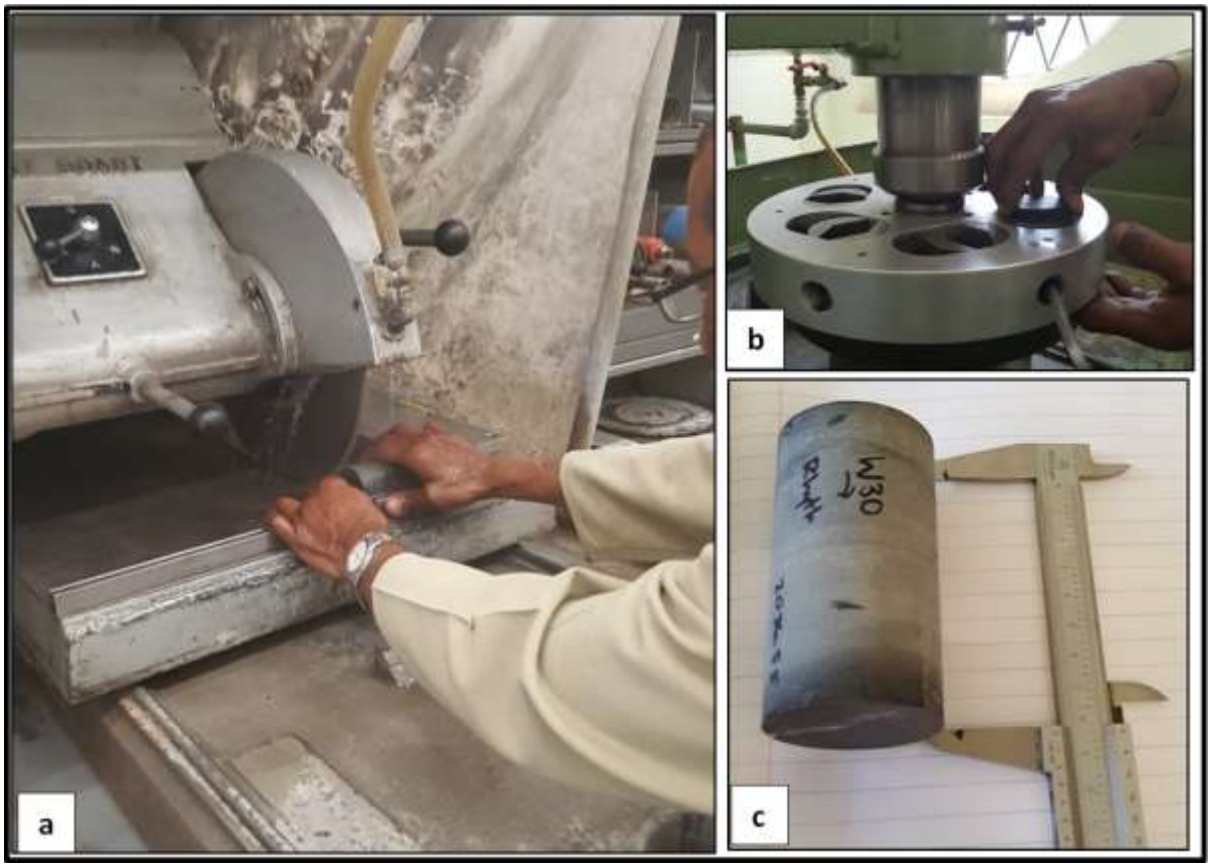

Figure 5.2: The main steps taken to prepare samples for the pulse transmission technique. a) Samples were cut to a length of ~80 mm. b) The edges of the samples were lapped so that they would be smooth and parallel to one another. c) The final result of the sample preparations (sample W30).

5.2.2. P- and S-wave velocity measurements

The P- and S-wave velocities were calculated for each sample using an ultrasonic pulse transmission technique (Birch, 1960). The experimental setup that was used to complete seismic velocity measurements on the samples are shown in Figure 5.3. A sample was placed between a transmitting and a receiving transducer, operating at 0.5 MHz (Figure 5.3a, b). The transducers were connected to a pulse generator and a Tektronix TDS2012C oscilloscope (Figure 5.3c). The pulse generator sent a pulse through the length of the sample via the transmitter. Once the pulse reaches the receiver, it is converted to an electrical signal and amplified. The resulting waveform is displayed on the oscilloscope (Figure 5.3c). Unconfined uniaxial compressive tests were also carried out on full-core samples. An AMSLER compression testing machine was used to measure the response of P- and S-wave velocities with increased uniaxial stress (Figure 5.3c, d, e). The load was applied on the samples by adjusting the length of the chamber (Figure 5.3c) and the stress readings are displayed on the measuring gauge (Figure 5.3d), which is controlled by the wheel shown in Figure 5.3e.

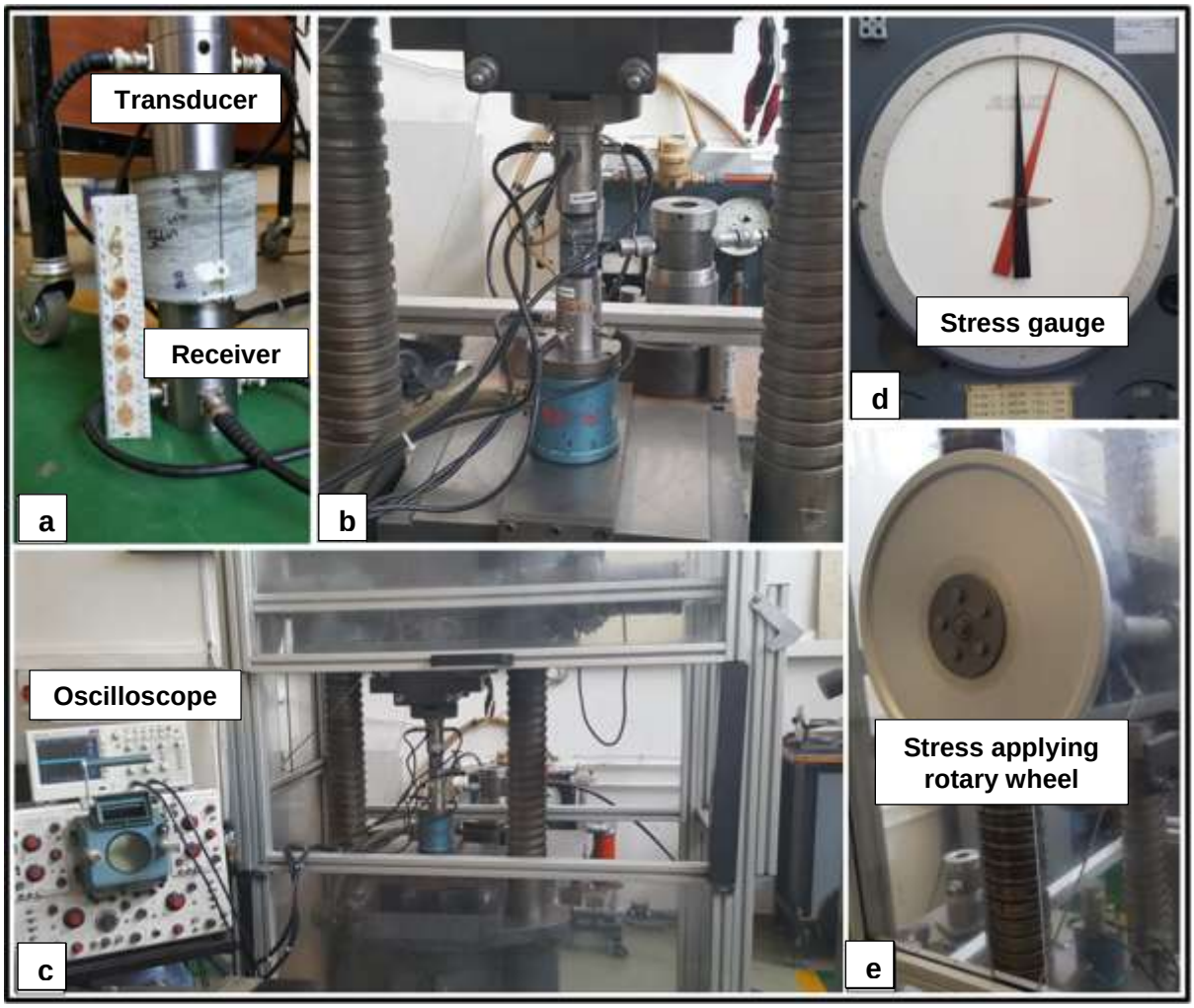

Figure 5.3: The main steps and components of the pulse transmission technique. a) The sample placed between the receiver and the transmitter. This is the setup for measuring the seismic velocities of the sample under

atmospheric stress b) The setup in a) is placed in a uniaxial stress applying system c) The applied stress is indicated on this wheel by the red needle, in units of MPa d) The setup as shown in b), connected to the pulse generator and oscilloscope e) The pressure applying rotary wheel.

From this waveform the first arrival times for the P-wave and S-wave through the sample was obtained. Thirty P-wave and S-wave travel time measurements for each sample were taken. The typical waveform that shows the positions in which the P-wave and S-wave are taken is indicated in Figure 5.4. The first arrival of the waveform (point 1) represents the P-wave velocity. The larger amplitude S-wave arrives when the waveform starts to change, i.e. the amplitude becomes larger. Point 2 indicates the leading edge of the S-wave and point 3 the first peak of the S-wave. For the purposes of this experiment, point 1 and 2 were used as the arrival times for the P- and S-wave, respectively.

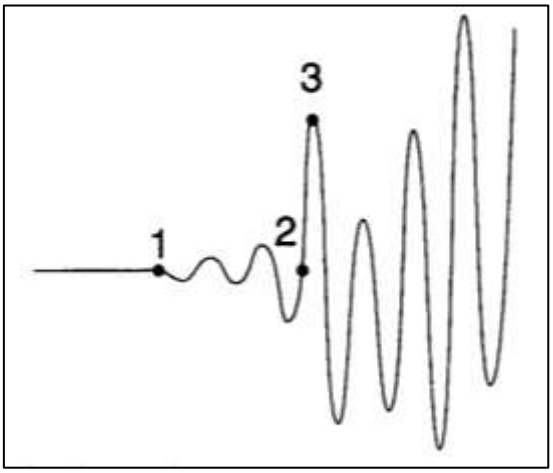

Figure 5.4: A schematic image of the output wave on the oscilloscope, indicating the position of the P-wave (1), the first S-wave arrival (2) and the peak of the S-wave. The horizontal axis is time and the vertical axis is the amplitude of the waveform (Qixian and Bungey, 1996).

Figure 5.4 shows an example of an output signal that was obtained from the oscilloscope. The locations where the P- and S-wave arrival times were picked are indicated. The arrival times, together with the length of the sample were used to calculate the seismic velocities using Equation 8. An error interval (Δt) around the picking location is also indicated in Figure 5.5. The interval was chosen so that there is a 95 % (two standard deviations) certainty that the true wave arrival is included in the interval. A quarter of the interval was used to calculate the experimental error for the seismic velocities.

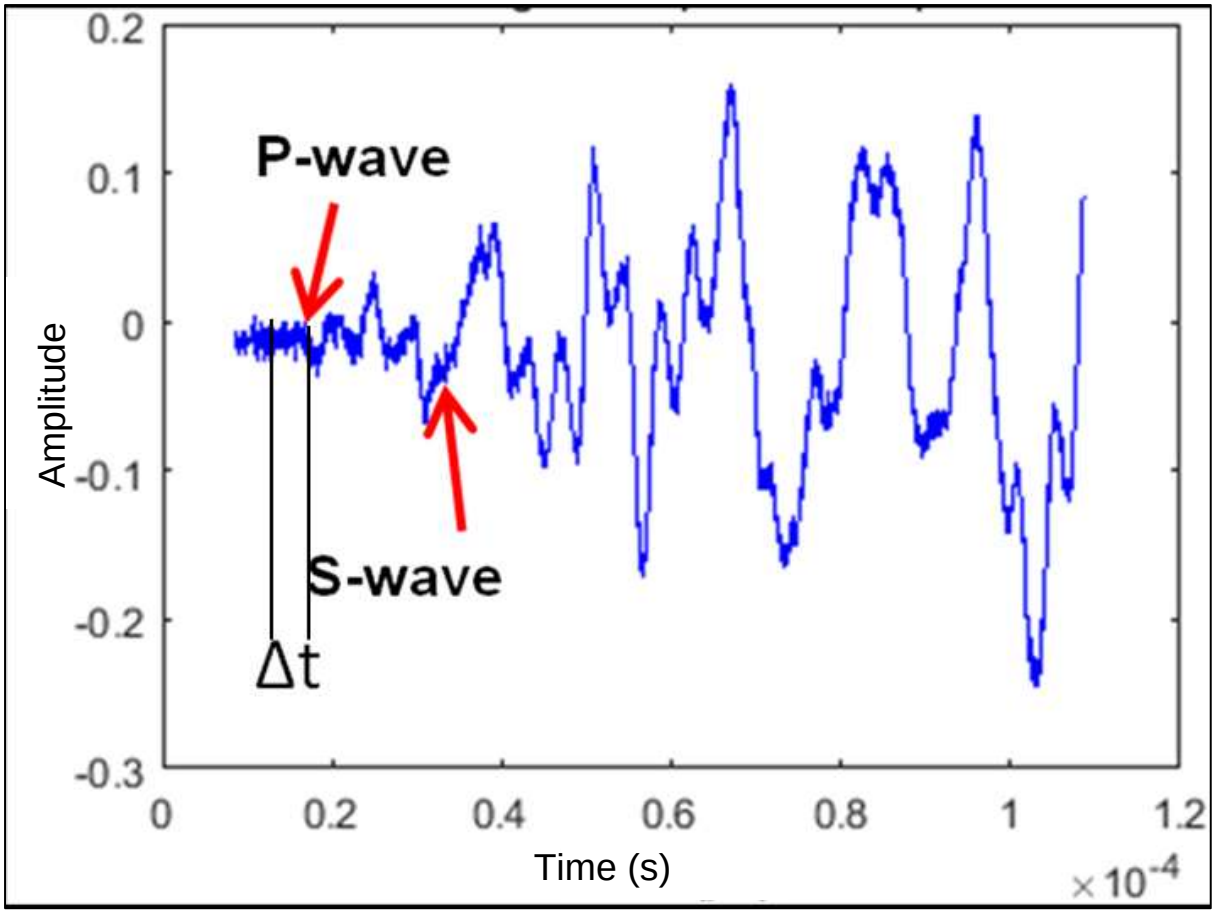

Figure 5.5: A single waveform output from the oscilloscope for a sandstone sample (sample W1). The locations of the first P- and S-wave arrivals are indicated on the waveform.

5.2.3. Signal processing

In order to improve the signal-to-noise ratio (S/N) of the signals from the oscilloscope and improve the picking locations of the P- and S-wave arrival times, some basic signal processing was done. For each sample, the seismic velocity measurement using the pulse transmission technique was repeated 30 times. Thirty different traces or waveforms for each sample were stacked using a data stacking program coded in MATLAB by Michael Westgate. The code allows the user to input traces or waveforms for a specific sample, and the program stacks (i.e., averages or adds) along the amplitudes of the signals, leaving the phase unaffected. The purpose of this step was to minimise random noise, and to obtain cleaner signals with less ambiguity in the picking of first wave arrival times.

5.2.4. Measuring seismic velocities under uniaxial stress

The P- and S-wave velocities of the borehole KWV samples were measured under uniaxial stress in order to mimic their in situ conditions. Although placing the samples under confined stress would be better than uniaxial stress, the sizes and geometries of the samples were not suitable for the confined stress chamber. For example, the samples were too big to fit into a chamber. The uniaxial stress applied on the samples was calculated using F/A where F is the applied load and A is the cross-sectional area of the specimen.

Placing the samples under uniaxial stress allowed us to investigate the presence of pores or non-visible cracks in the samples. Samples with known/visible small cracks or imperfections were not placed under stress, to ensure that these samples did not break.

Initial velocities at 0 MPa are re-measured per sample to remove velocity variations due to slight changes in the experimental setup. A sample was placed between the two transducers, which were placed between two pressurization pistons inside an AMSLER pressurization system (see Figure 5.3b and Figure 5.3c). A rotary wheel was turned until the pistons were in contact with the transducers. The wheel was further turned in stress increments of 5 MPa, up to a maximum of 80 MPa (see Figure 5.3d, e) which is the maximum stress expected at a depth of 2.5 km. Although a higher level of applied stress (200 MPa) (Malehmir et al., 2013; Punturo et al.; 2005) would be required to close all micro-fractures, this amount of stress is unexpected at our sample depth of 3 km.

After each incremental increase in uniaxial stress, the first arrival position of the P- and S-wave was noted on the oscilloscope. These values were used to calculate Vp and Vs at each stress interval using Equation 8.

5.3. Bulk density measurements

The weight of the samples in air and in water was used to determine the bulk densities of all the samples. Figure 5.6 shows the setup of the instrumentation for the experiments. A KERN and Sohn GmbH digital scale (model PCB-BA-e-1315) with a precision of 0.01 g was used to weigh the samples in air and under water (Figure 5.6a). The relative density for each sample was determined using Archimedes' principle (Jarman, 2012). This principle is defined by the following equation:

$$R_D = \frac{\text{Weight of sample in air}}{\text{Buoyancy force}} \qquad (12)$$

where R_D is the relative density of the sample and the buoyancy force is the difference of the weight of the sample in air and the weight of the sample in water (Figure 5.6b). The bulk density was determined by multiplying the relative density with the density of pure water, which is 1 g/cm^3 at 4 ºC (Jarman, 2012).

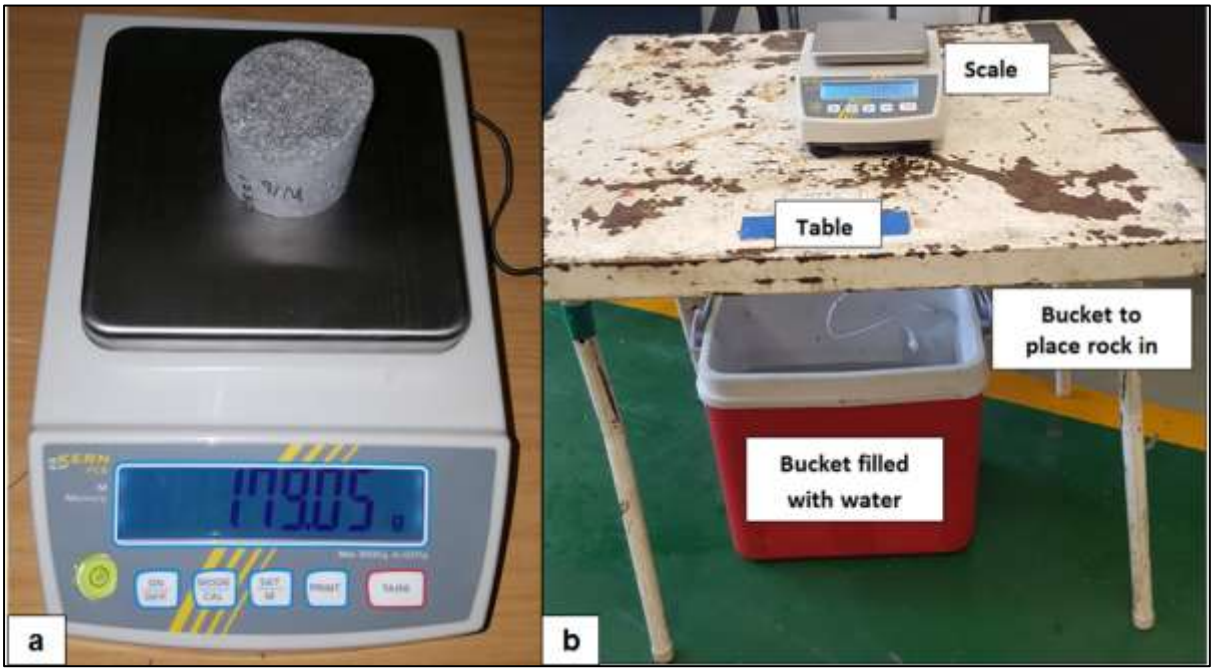

Figure 5.6: Method of obtaining the densities and porosities of the samples. a) Scale used to measure weight, and ultimately density, of samples. b) Laboratory Archimedes setup.

5.4. Porosity measurements

The method for determining the porosities of the samples is similar to the method for measuring densities. The samples were soaked in water for 24 hours until their pore spaces were saturated. The samples were then weighed in water to obtain their wet bulk densities, in addition to grain densities in air. Grain density was calculated using Equation 12. Porosity was then calculated as follows:

$$\text{Effective porosity (\%)} = 100\ (1- (\frac{Db}{Dg})) \qquad (13)$$

where Db is bulk density of the sample and Dg is the grain density of the sample (Manger, 1963). This method is effective for reservoir rocks that have a dominantly connected porosity.

5.5. Fracture analysis

The presence and orientations of micro-fractures in a rock influence the propagation of seismic waves through the rock (Wyllie et al., 1958; Punturo et al., 2005). X-ray tomography was used to investigate the presence and orientation of micro-fractures in the KWV samples.

Micro X-ray computed tomography is a non-destructive analytical technique that produces a 3D tomographic image of a sample. The technique is based on the principle that x-rays are attenuated in varying amounts by different densities (Schindler et al., 2016). Pore spaces and micro-fractures filled with air should have significantly lower densities and should thus be attenuated to a lesser extent than the surrounding rock. Figure 5.7 demonstrates the setup of x-ray scans, where the sample is placed between the ionizing radiation source and the detector, fitted entirely within the cone of x-rays.

An ionizing radiation source produces x-rays, which travel in a cone towards a detector. A rock sample is placed between the x-ray source and the detector, such that x-rays pass through the sample to the detector. Different densities in the sample should result in different degrees of attenuation of x-rays in the sample. This causes different x-rays to be transmitted through the sample that are detected and rasterized as pixels with different intensities (grey values) (Hoffman and De Beer, 2012). The pixels are plotted on a histogram of grey pixel value versus count. The grey values are picked to maximise the contrast of a two-dimensional grey scale image. The sample manipulator rotates the sample 360°, while bombarding the sample with x-rays. This results in numerous two-dimensional grey scale images, all taken at slightly different angles. A tomographic three-dimensional image of the sample is obtained once all the individual two-dimensional images are reconstructed into a single three-dimensional model.

The resolution obtained for the final image depends on the amount of energy used to radiate the sample, as well as the density of the sample. The higher the original energy, the higher the amount of transmitted energy through the sample. A minimum of 15% of the original energy is required to be transmitted through the sample, in order to obtain a useable image (Hoffman and De Beer, 2012). The denser the sample, the more energy is needed to achieve the required 15% transmitted energy. A higher original energy, on the other hand, makes it harder to focus the beam to smaller spot sizes. The smaller the spot size, the better the resolution.

Since the x-rays travel in a cone shape toward the detector, a smaller sample would be able to fit closer to the radiation source than a bigger sample. Thus a smaller sample permits

smaller spot sizes, and hence a higher resolution. The balance between the amount of energy (kV) and the spot size (μA) is thus of critical importance to obtain a desired resolution (μm). The parameters used for each of the Karoo samples are provided in Table 5.2.

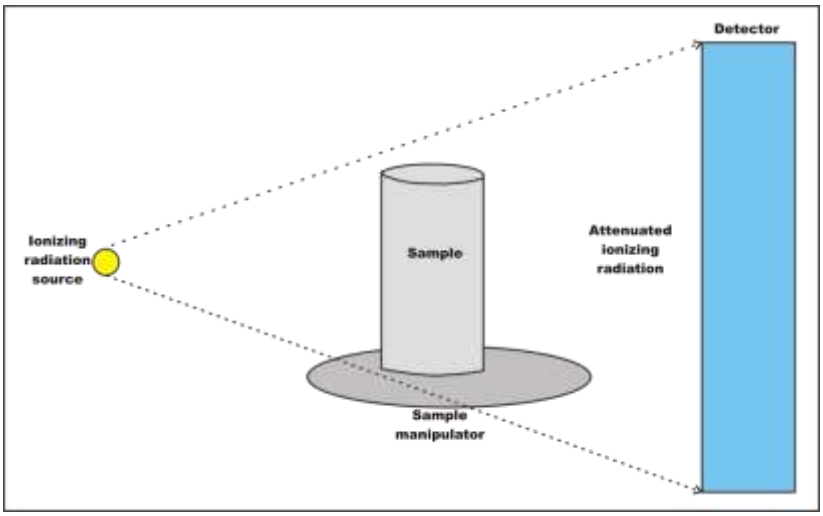

Figure 5.7: The setup of micro x-ray scans. The sample is placed within the cone of x-rays, between the radiation source and the detector (Adapted from Hoffman and De Beer, 2012).

5.5.1. Sample preparation

Since micro X-ray tomography is a time consuming and expensive process, only some samples were chosen to be scanned. Table 5.2 provides a list of all the samples that were analysed using micro x-ray tomography. Samples were chosen based on results from previous analyses, i.e. seismic velocity, bulk density and uniaxial stress measurements. All samples that showed increases in seismic velocity with applied uniaxial stresses were chosen. Samples with constant velocities under applied uniaxial stresses and anomalous densities were also chosen.

Since smaller samples are better resolved, the analysed samples were cut to diameters of 15 mm.

5.5.2. Micro x-ray tomography

The samples were scanned, reconstructed and analysed at the Micro-Focus X-ray Tomography Facility (MIXRAD) at the Nuclear Energy Corporation of South Africa (NECSA). The samples were scanned using a Nikon XTH 225 ST micro-focus x-ray tomography system (Figure 5.8). The parameters for the resolution, energy and beam current used to scan each image, are summarised in Table 5.2.

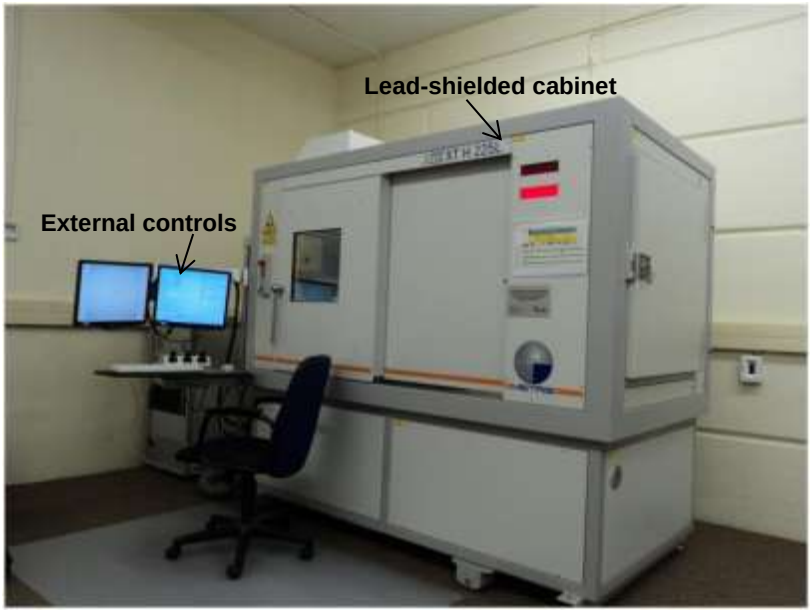

Figure 5.8: Micro x-ray machine at NECSA, South Africa (Hoffman and De Beer, 2012)

Table 5.2: The resolution and energy used to scan each sample during x-ray tomography.

Sample name	Resolution (µm)	X-ray (kV)	X-ray (µA)	Comments
W2	49.08	185	110	A big and small piece of the sample was scanned in order to compare the resolution obtained.
W2	28.4	100	100	
W8	33.23	100	100	
W9	22.56	100	100	
W16	33.23	100	100	Sample was rescanned at a higher resolution since no pores or fractures could be identified.
W16	13.18	100	100	
W17	14.05	100	100	
W18	33.23	100	100	
W19	33.23	100	100	
W21	33.23	100	100	
W24	22.2	100	100	
W26	33.23	100	100	Sample was rescanned at a higher resolution since no pores or fractures could be identified.
W26	13.18	100	100	
W28	20.9	100	100	
W30	46.7	185	110	A big and small piece of the sample was scanned in order to compare the resolution obtained.
W30	33.23	100	100	
W31	33.23	100	100	Sample was rescanned at a higher resolution since no pores or fractures could be identified.
W31	13.18	100	100	
W33	33.14	185	110	Sample was rescanned at a higher resolution since no pores or fractures could be identified. Big and small pieces of the sample were scanned.
W33	33.23	100	100	
W33	13.18	100	100	
W34	50.48	185	110	Sample was rescanned at a higher resolution since no pores or fractures could be identified. Big and small pieces of the sample were scanned.
W34	33.23	100	100	
W34	13.18	100	100	
W36	26.97	100	100	
W39	20.09	100	100	
W40	33.84	185	110	A big and small piece of the sample was scanned in order to compare the resolution obtained.
W40	29.04	100	100	
W42	50.48	185	110	A big and small piece of the sample was scanned in order to compare the resolution obtained.
W42	22.56	100	100	
W43	33.23	100	100	
W46	22.56	100	100	
W47	17.99	100	100	

Note: Small samples refer to samples with a diameter of 15 mm, while big samples refer to samples with a diameter larger than 40 mm.

Some of the denser samples (dolerite) were scanned twice, with a lower energy and beam current (spot size) to improve the resolution. Once the procedure was complete for each sample, the images were reconstructed to a final three-dimensional image using the CTPro3D

software. The three-dimensional image was then imported into the VG Studio Max 3.0 software, where minerals, pore spaces and micro-fractures were identified.

5.6. Petrography

Petrography was studied on selective samples. Thirteen samples were picked to investigate their mineralogy based on the results from the micro x-ray tomography. If different density minerals were present in the x-ray tomography images, the sample would be investigated petrographically to determine the mineral assemblage. The samples were cut to ~0.03 mm thick slices and mounted on a microscope slide. These slides were investigated using an Olympus BX41 microscope. Identification of minerals was done following the procedure by Nesse, 2004. Any observed alignment or foliation of the minerals was analysed. The foliation of minerals was analysed in terms of their shape preferred orientation (SPO). The results were cross-referenced with any anomalous seismic velocity or bulk density values.

5.7. Seismic anisotropy

Seismic anisotropic studies were also conducted on a few samples. Six samples were chosen (samples W19, W21, W33, W40, W42 and W46) based on different lithologies and micro-fracture orientations that were observed from the micro x-ray tomography. The seismic velocity through the samples were measured using the pulse transmission technique, following the same procedure as presented in Chapter 5.2.2. Possible sources of noise during the anisotropy measurements are the same as for the seismic velocity measurements. Due to the small sizes of the samples, interference between the two transducers may play a larger role in this procedure than in the previous measurements. A smaller set of transducers (17.6 mm) was used for these measurements. It was ensured that the surface area of the samples was larger than the surface area of the transducers.

The seismic velocities were measured in a direction parallel to the long axis of the sample (Y-direction) (Figure 5.9a), and perpendicular to the long axis of the sample (X-direction) (Figure 5.9b). The bulk anisotropy of each rock sample was calculated using Equation 11.

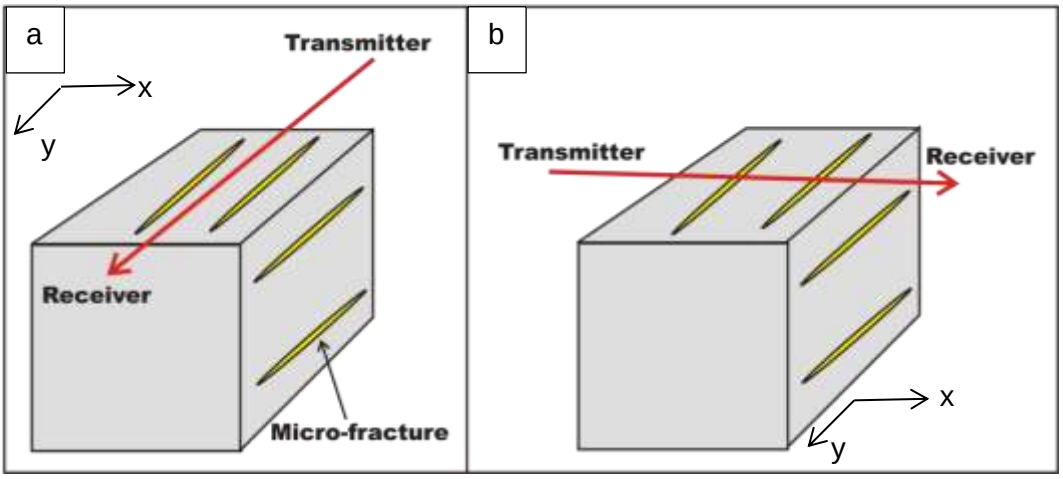

Figure 5.9: Schematic representation of the a) y-direction and b) x-direction of the samples that were used to measure seismic velocity anisotropy. Micro-fractures in the sample are represented by yellow lines running parallel to the long axis of the sample.

5.8. Construction of synthetic seismograms

Synthetic seismograms are constructed from seismic velocity measurements, as well as bulk density measurements. Figure 5.10 illustrates the steps that were taken in the construction of synthetic seismograms from the seismic velocities and bulk densities of the samples. The acoustic impedance of each sample was calculated using Equation 9 and plotted against depth. The reflection coefficients (Rc) was then calculated from the acoustic impedances (Equation 10) and plotted against depth. The depths were converted to two-way travel time (TWT), resulting in a plot of the reflectivity series. Finally, the reflectivity series was convolved with a source wavelet in order to obtain the synthetic seismogram. The source wavelet that yielded the best results visually was the Ricker wavelet, at 60 Hz frequency.

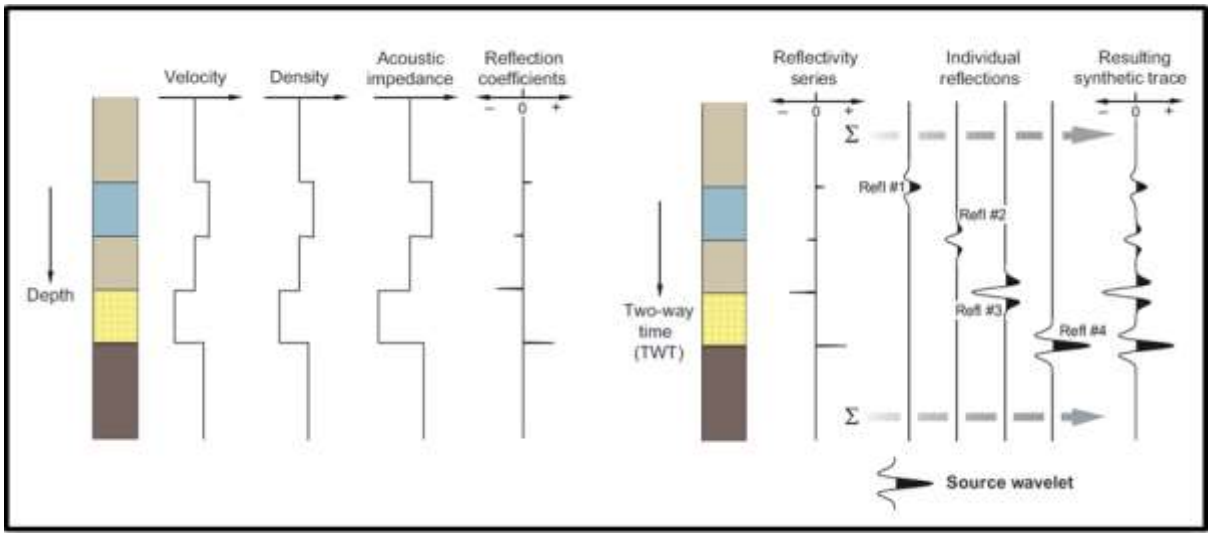

Figure 5.10: Steps taken in the construction of a synthetic seismogram (Dentith and Mudge 2014).

The TWT that was used to produce the reflectivity series was obtained by using an equation produced by Scheiber-Enslin et al. (2014). This equation can be used to convert measured

depth to TWT, and is provided in Figure 5.11. The equation was obtained by fitting a second order polynomial to a plot of measured depth against TWT of the Whitehill Formation throughout the Main Karoo Basin.

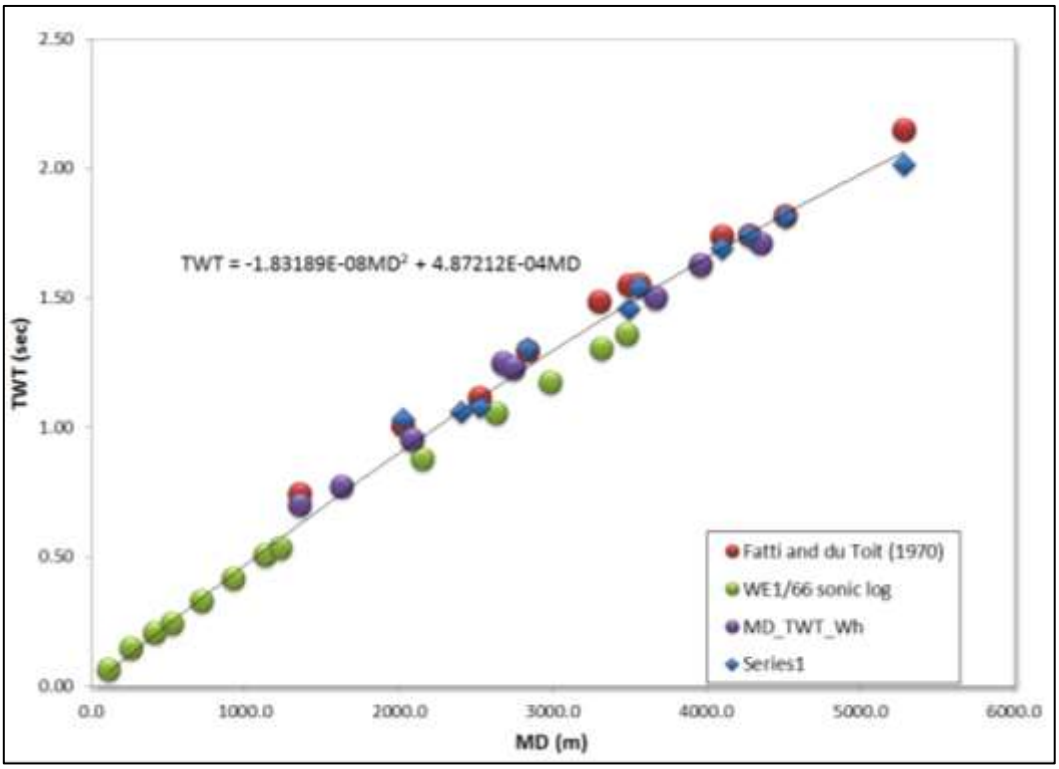

Figure 5.11: TWT plotted against measured depth (MD) of SOEKOR seismic data (Scheiber-Enslin et al., 2014). The measured depth (MD) and the TWT of the Whitehill Formation are plotted (MD_TWT_Wh). Interval velocities (Fatti and du Toit, 1970) and a sonic velocity log from well WE1/66 (Fatti, 1987) are also plotted.

The reflection seismogram for borehole KWV that were constructed in this study did not consider any attenuation of seismic waves through the subsurface, and it should assume a seismic isotropic nature for all the subsurface rocks.

5.9. Error propagation

Error propagation was used to calculate the errors of all average values and the errors of other values that were obtained from mathematical manipulations of our results. The following equation was used.

The error Δf of a two-variable function f(a,b) is computed using partial derivatives and quadratures

$$\Delta f = \sqrt{\frac{\partial f}{\partial a}^2 \Delta a^2 + \frac{\partial f}{\partial b}^2 \Delta b^2} \quad . \qquad (14)$$

Where f is a function and Δf is the error/uncertainty of the function. Δa and Δb are uncertainties associated with the quantities a and b. These uncertainties are either measurement precisions or one standard deviations of a group of measurements.

6. Results

All the results obtained in this study are presented in this chapter. The samples that were collected are listed with an accompanying image and basic descriptions. The images and final results that were obtained from the seismic velocity, bulk density and porosity, fracture analysis and mineralogical analyses are also provided. The results from the different analysis are compared and discussed.

6.1. Sampling

A total of 49 samples were collected from the KWV drill-core. The collected samples combined measures 7.79 m, which is 0.33 % of the total drill-core by length. Samples were taken from each major lithological unit of every stratigraphic unit in an effort to represent all lithologies intersected by the borehole. Figures 6.1 to 6.49 provide a summary of the name, depth, length, lithology and stratigraphy of each sample. Images of the hand specimens of the samples are also provided. Increasing sample number corresponds with increasing depth.

W1	Depth (m)	Stratigraphy	Lithology
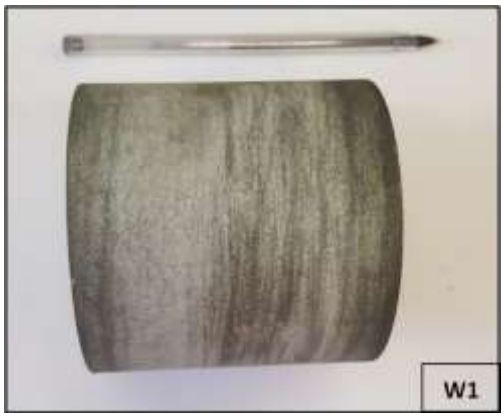	8.00-8.11	Adelaide Subgroup Koonap Formation	Sandstone

Figure 6.1: Sample W1, image and descriptions. This sample is a weakly weathered greyish white sandstone. It has green ripple mark textures with flaser bedding.

W2	Depth (m)	Stratigraphy	Lithology
	186.00-186.80	Adelaide Subgroup Koonap Formation	Mudstone

Figure 6.2: Sample W2, image and descriptions. The sample is a grey mudstone.

W3	Depth (m)	Stratigraphy	Lithology
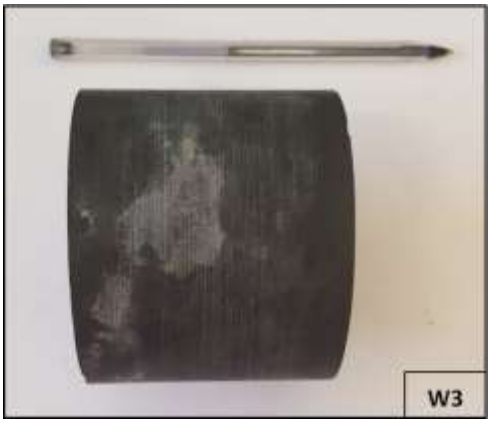	189.39-189.48	Ecca Group Waterford Formation	Breccia

Figure 6.3: Sample W3, image and descriptions. This sample is a grey-green mudstone with dark grey to black rounded shale particles from 2 mm to 10 mm. The size of the particles increases towards base.

W4	Depth (m)	Stratigraphy	Lithology
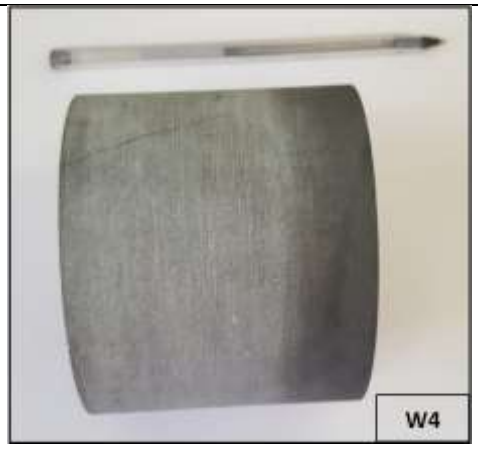	255.76-255.85	Ecca Group Waterford Formation	Sandstone with interbedded shale

Figure 6.4: Sample W4, image and descriptions. The sample is a grey sandstone with darker grey interbedded shale. Shale bedding is well defined by dark and light banding of 1 mm to 3 mm thick. The sandstone has strong ripple mark textures with flaser bedding. The bedding dips 60°.

W5	Depth (m)	Stratigraphy	Lithology
	324.51-324.65	Ecca Group Fort Brown Formation	Shale

Figure 6.5: Sample W5, image and descriptions. This sample is a grey to dark grey shale with well-defined bedding, which is indicated by dark and light interbeds 2 mm to 5 mm thick. The bedding dips 60°.

W6	Depth (m)	Stratigraphy	Lithology
	328.51-328.67	Ecca Group Fort Brown Formation	Sandstone

Figure 6.6: Sample W6, image and descriptions. The sample is a grey sandstone with well-defined bedding indicated by darker grey layers 2 mm to 6 mm thick.

W7	Depth (m)	Stratigraphy	Lithology
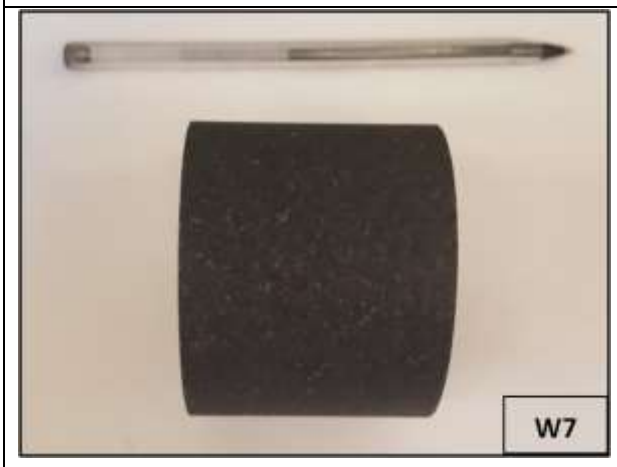	416.00-416.12	Intrusive	Dolerite

Figure 6.7: Sample W7, image and descriptions. The sample is a medium-grained dolerite.

W8	Depth (m)	Stratigraphy	Lithology
	783.26-783.37	Ecca Group Waterford Formation	Sandstone

Figure 6.8: Sample W8, image and descriptions. The sample is a light grey, fine grained sandstone. It is upward-grading, with lenticular lamination.

W9	Depth (m)	Stratigraphy	Lithology
	886.56-886.75	Ecca Group Waterford Formation	Carbonaceous shale

Figure 6.9: Sample W9, image and descriptions. The sample is a dark grey to black, very fine grained shale. It has well-defined bedding, which appears as 2 mm to 10 mm thick, dark grey to black and lighter grey interbeds of laminated shale.

W10	Depth (m)	Stratigraphy	Lithology
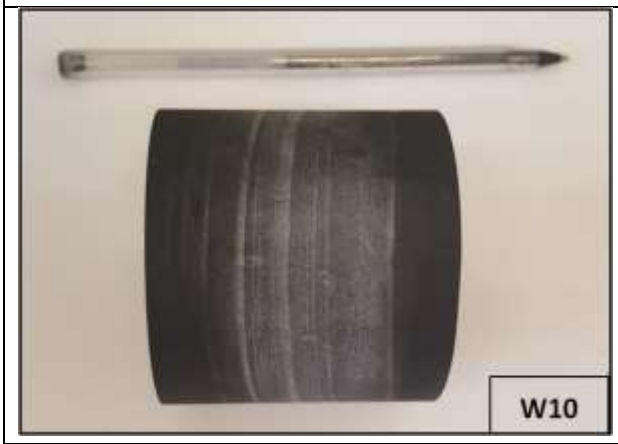	919.60-919.73	Ecca Group Ripon Formation Trumpeters Member	Sandstone

Figure 6.10: Sample W10, image and descriptions. The sample is a dark grey, fine grained sandstone with bedding dipping 5° to 7°.

W11	Depth (m)	Stratigraphy	Lithology
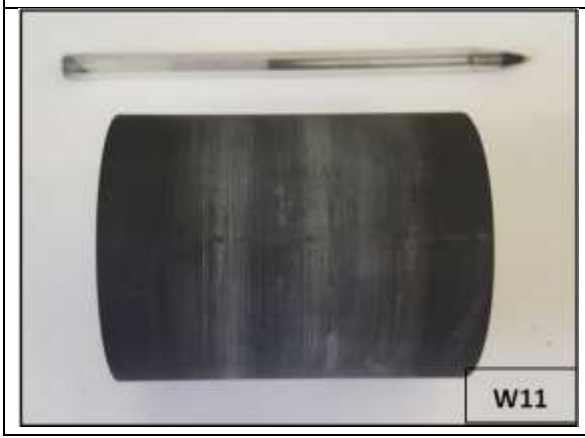	950.74-950.87	Ecca Group Ripon Formation Trumpeters Member	Shale

Figure 6.11: Sample W11, image and descriptions. The sample is a dark grey to black shale, laminated with well-defined bedding defined by dark and light grey interbeds.

W12	Depth (m)	Stratigraphy	Lithology
	961.33-961.52	Intrusive	Dolerite

Figure 6.12: Sample W12, image and descriptions. The sample is a light green dolerite with a phaneritic texture. The lower and upper contacts are very fine-grained crystalline.

W13	Depth (m)	Stratigraphy	Lithology
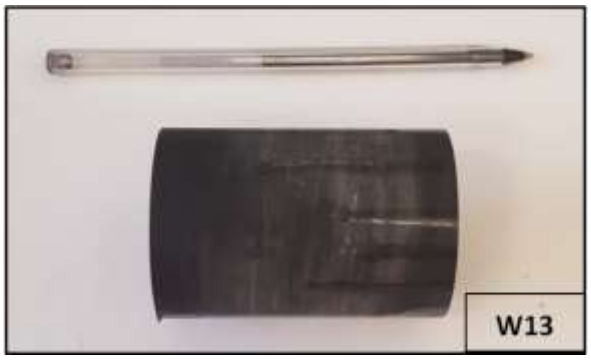	1043.73-1043.88	Ecca Group Ripon Formation Trumpeters Member	Sandstone

Figure 6.13: Sample W13, image and descriptions. The sample is a light grey, very fine-grained sandstone. It is laminated, with interbeds of shale.

W14	Depth (m)	Stratigraphy	Lithology
	1096.09-1096.23	Ecca Group Ripon Formation Wonderfontein Member	Shale

Figure 6.14: Sample W14, image and descriptions. The sample is a dark grey shale with grey silty interbeds that are 2 mm to 5 mm thick.

W15	Depth (m)	Stratigraphy	Lithology
	1190.09-1190.21	Ecca Group Ripon Formation Wonderfontein Member	Shale

Figure 6.15: Sample W15, image and descriptions. The sample is a grey, massive shale.

W16	Depth (m)	Stratigraphy	Lithology
	1230.96-1231.11	Intrusive	Dolerite

Figure 6.16: Sample W16, image and descriptions. The sample is a greenish grey, coarse-grained dolerite.

W17	Depth (m)	Stratigraphy	Lithology
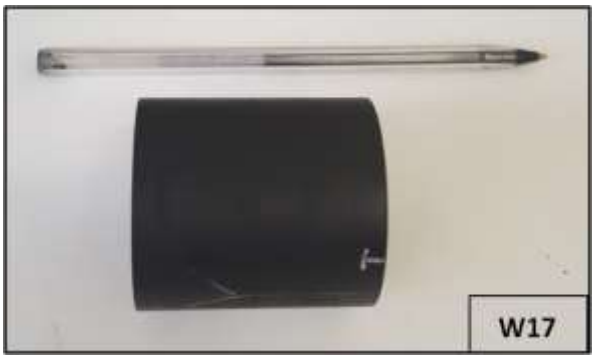	1325.37-1325.50	Ecca Group Ripon Formation Wonderfontein Member	Shale

Figure 6.17: Sample W17, image and descriptions. The sample is a massive black shale with poorly-defined bedding. It has occasional grey, very fine grained sandstone interbeds, of 5 mm thickness.

W18	Depth (m)	Stratigraphy	Lithology
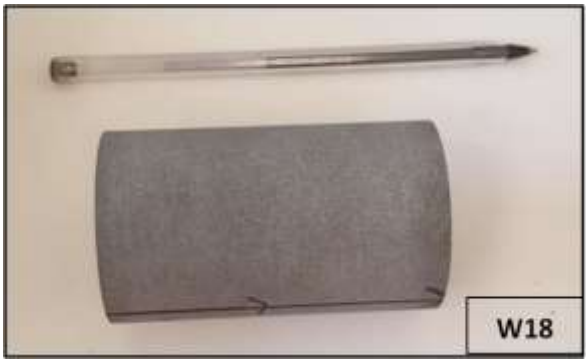	1396.22-1396.37	Ecca Group Ripon Formation Pluto's Vale Member	Sandstone

Figure 6.18: Sample W18, image and descriptions. The sample is a massive, light grey medium grained sandstone. It has very weak bedding definitions in places.

W19	Depth (m)	Stratigraphy	Lithology
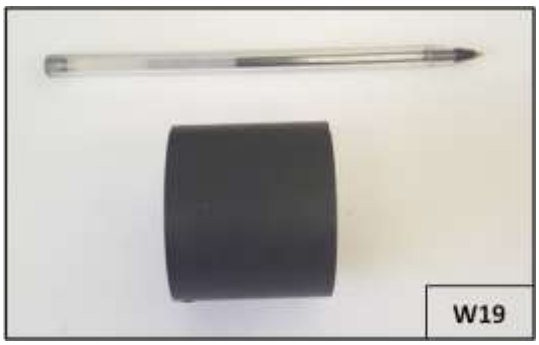	1427.51-1427.63	Ecca Group Ripon Formation Pluto's Vale Member	Carbonaceous shale

Figure 6.19: Sample W19, image and descriptions. The sample is a black carbonaceous shale with occasional light grey, medium grained sandstone interbeds.

W20	Depth (m)	Stratigraphy	Lithology
	1467.63-1467.74	Ecca Group Ripon Formation Pluto's Vale Member	Carbonaceous shale

Figure 6.20: Sample W20, image and descriptions. The sample is a black carbonaceous shale with weak bedding that is defined by occasional dark grey beds, of 1 mm to 2 mm thickness.

W21	Depth (m)	Stratigraphy	Lithology
	1472.51-1473.08	Ecca Group Ripon Formation Pluto's Vale Member	Sandstone

Figure 6.21: Sample W21, image and descriptions. The sample is a light grey, very fine grained sandstone. It has well-defined bedding indicated by brownish grey, very fine grained interbeds.

W22	Depth (m)	Stratigraphy	Lithology
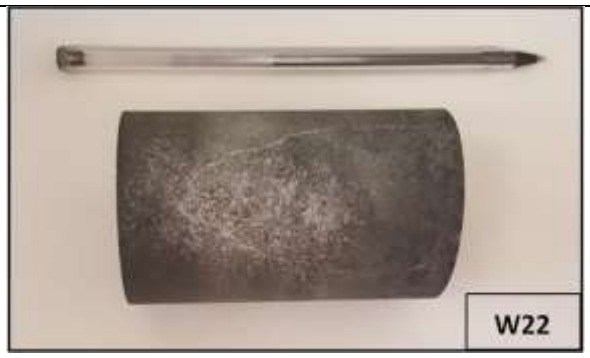	1478.39-1478.60	Intrusive	Dolerite

Figure 6.22: Sample W22, image and descriptions. The sample is a grey green, medium-grained dolerite.

W23	Depth (m)	Stratigraphy	Lithology
	1605.36-1605.57	Ecca Group Ripon Formation Pluto's Vale Member	Sandstone with soft sediment deformation.

Figure 6.23: Sample W23, image and descriptions. The sample is a grey, medium grained sandstone with well-defined bedding. It has upward-grading sequences and ripple marking in places.

W24	Depth (m)	Stratigraphy	Lithology
	1644.40-1644.68	Ecca Group Ripon Formation Pluto's Vale Member	Carbonaceous shale

Figure 6.24: Sample W24, image and descriptions. The sample is a black carbonaceous shale with sandstone interbeds that are 2 mm to 10 mm thick.

W25	Depth (m)	Stratigraphy	Lithology
	1677.14-1677.26	Ecca Group Ripon Formation Pluto's Vale Member	Shale

Figure 6.25: Sample W25, image and descriptions. The sample is a light grey, massive shale with lighter grey speckling throughout. It has dark grey, rusty and well-bedded layers.

W26	Depth (m)	Stratigraphy	Lithology
	1687.07-1687.21	Intrusive	Dolerite

Figure 6.26: Sample W26, image and descriptions. The sample is a grey green, medium- to coarse-grained dolerite.

W27	Depth (m)	Stratigraphy	Lithology
	1737.34-1737.55	Intrusive	Dolerite

Figure 6.27: Sample W27, image and descriptions. The sample is a grey green, fine- to medium-grained dolerite. It has a sharp horizontal basal contact.

W28	Depth (m)	Stratigraphy	Lithology
	1910.39-1910.55	Ecca Group Ripon Formation Pluto's Vale Member	Carbonaceous shale

Figure 6.28: Sample W28, image and descriptions. The sample is a black, massive carbonaceous shale with occasional thin, grey and fine-grained sandstone interbeds.

W29	Depth (m)	Stratigraphy	Lithology
	1960.22-1960.34	Ecca Group Ripon Formation Pluto's Vale Member	Sandstone

Figure 6.29: Sample W29, image and descriptions. The sample is a light grey to grey, fine-grained massive sandstone.

W30	Depth (m)	Stratigraphy	Lithology
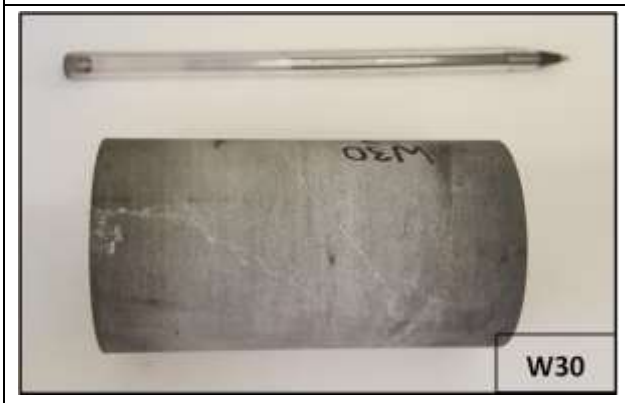	2036.55-2036.76	Ecca Group Ripon Formation Pluto's Vale Member	Rhythmite

Figure 6.30: Sample W30, image and descriptions. The sample is a grey, fine grained sandstone with rhythmic upward-grading cycles from light grey, fine grained sandstone to dark grey, very fine grained sandstone. It has strongly bleached zones throughout.

W31	Depth (m)	Stratigraphy	Lithology
	2050.40-2050.59	Intrusive	Dolerite

Figure 6.31: Sample W31, image and descriptions. The sample is a grey green, very coarse-grained dolerite with traces of magnetite.

W32	Depth (m)	Stratigraphy	Lithology
	2068.40-2068.55	Intrusive	Dolerite

Figure 6.32: Sample W32, image and descriptions. The sample is a grey green, fine- to medium-grained dolerite. It has patches of very coarse-grained dolerite with traces of magnetite.

W33	Depth (m)	Stratigraphy	Lithology
	2173.22-2173.39	Intrusive	Dolerite

Figure 6.33: Sample W33, image and descriptions. The sample is a grey green, fine-grained dolerite.

W34	Depth (m)	Stratigraphy	Lithology
	2183.44-2183.60	Intrusive	Dolerite

Figure 6.34: Sample W34, image and descriptions. The sample is a grey green to dark green, fine- to medium-grained dolerite. It has occasional near vertical calcite and quartz veins with hornblende at contacts.

W35	Depth (m)	Stratigraphy	Lithology
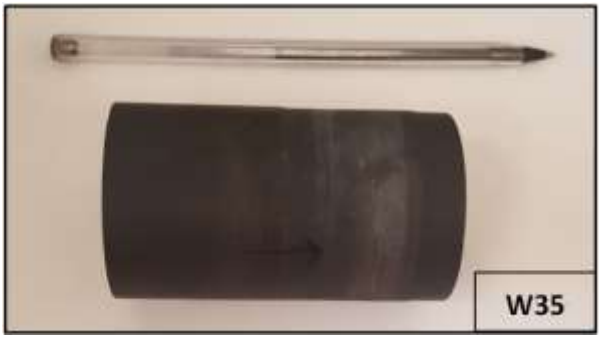	2191.89-2192.00	Ecca Group Ripon Formation Pluto's Vale Member	Sandstone rhythmite

Figure 6.35: Sample W35, image and descriptions. The sample is a fine- to medium-grained sandstone with dark grey to black, very fine to silty sandstone interbeds. Its bedding thickness varies from 5 mm to 30 mm. It has occasional faint rusty sections.

W36	Depth (m)	Stratigraphy	Lithology
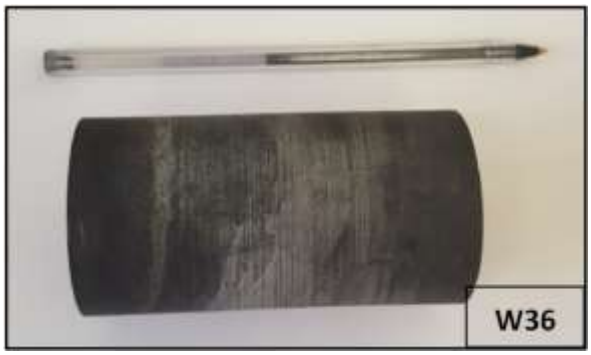	2272.07-2272.21	Ecca Group Ripon Formation Pluto's Vale Member	Sandstone

Figure 6.36: Sample W36, image and descriptions. The sample is a light grey to grey, very fine-grained sandstone with well-defined bedding. It has quartz veins with pyrrhotite.

W37	Depth (m)	Stratigraphy	Lithology
	2276.93-2277.05	Intrusive	Dolerite

Figure 6.37: Sample W37, image and descriptions. The sample is a grey green, very fine-grained dolerite with traces of magnetite. Its upper and lower contacts are irregular, but horizontal.

W38	Depth (m)	Stratigraphy	Lithology
	2293.74-2293.98	Intrusive	Dolerite

Figure 6.38: Sample W38, image and descriptions. The sample is a grey green, very fine-grained dolerite with traces of magnetite. Its upper and lower contacts are irregular, but horizontal. A fine-grained epidote alteration zone is present.

W39	Depth (m)	Stratigraphy	Lithology
	2299.31-2299.43	Ecca Group Whitehill Formation	Carbonaceous shale

Figure 6.39: Sample W39, image and descriptions. The sample is a black, near massive carbonaceous shale. Its bedding is defined by thin, light grey, very fine-grained sandstone beds. It has disseminated pyrrhotite throughout and on its bedding planes.

W40	Depth (m)	Stratigraphy	Lithology
	2301.71-2301.84	Ecca Group Whitehill Formation	Carbonaceous shale breccia

Figure 6.40: Sample W40, image and descriptions. The sample is a black, near massive carbonaceous shale. It has a brecciated appearance with soft sediment deformation. It is highly pyritic, with very fine quartz veins.

W41	Depth (m)	Stratigraphy	Lithology
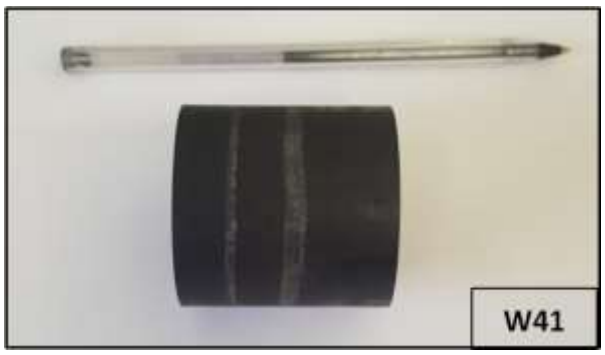	2305.12-2305.23	Ecca Group Whitehill Formation	Carbonaceous shale

Figure 6.41: Sample W41, image and descriptions. The sample is a black, well-bedded carbonaceous shale. Its bedding is defined by numerous disseminated pyrite bands on bedding plane. It has occasional grey to dark grey shale beds.

W42	Depth (m)	Stratigraphy	Lithology
	2308.20-2308.30	Ecca Group Whitehill Formation	Carbonaceous shale

Figure 6.42: Sample W42, image and descriptions. The sample is a black, well-bedded carbonaceous shale. Its bedding defined is by numerous disseminated pyrite bands on bedding plane. It has occasional grey to dark grey shale beds.

W43	Depth (m)	Stratigraphy	Lithology
	2313.61-2313.74	Ecca Group Prince Albert Formation	Shale

Figure 6.43: Sample W43, image and descriptions. The sample is a dark grey with black shale. Its bedding is indicated in places by thin, lighter grey shale or sandstone beds.

W44	Depth (m)	Stratigraphy	Lithology
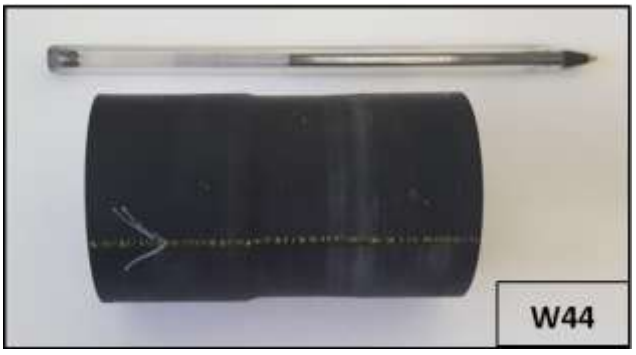	2322.81-2322.95	Ecca Group Prince Albert Formation	Shale

Figure 6.44: Sample W44, image and descriptions. The sample is a dark grey with black shale. Its bedding is indicated in places by thin, lighter grey shale or sandstone beds.

W45	Depth (m)	Stratigraphy	Lithology
	2330.38-2330.53	Ecca Group Prince Albert Formation	Carbonaceous shale

Figure 6.45: Sample W45, image and descriptions. The sample is a massive, dark grey to black shale. It has no visible bedding.

W46	Depth (m)	Stratigraphy	Lithology
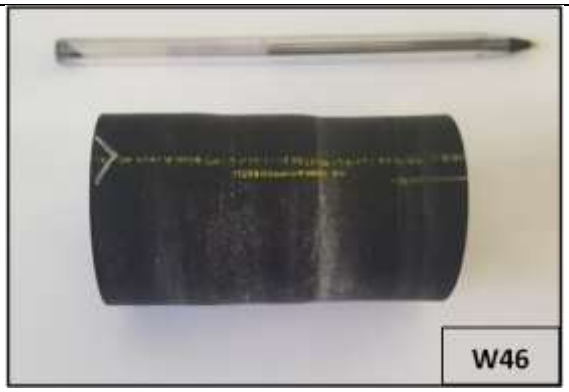	2334.51-2334.62	Ecca Group Prince Albert Formation	Rhythmite

Figure 6.46: Sample W46, image and descriptions. The sample is a grey, fine grained sandstone interbedded with dark grey to black shales.

W47	Depth (m)	Stratigraphy	Lithology
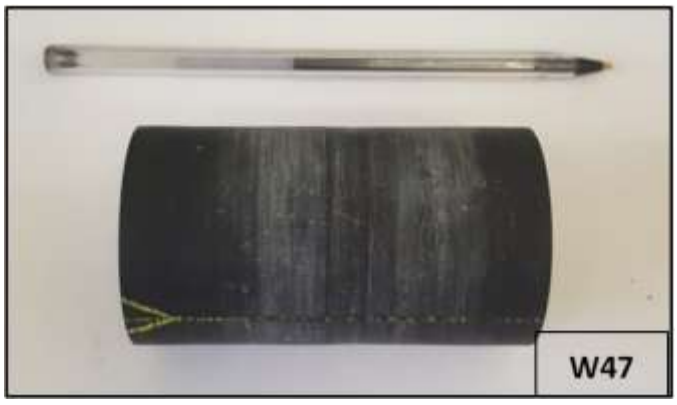	2338.44-2338.58	Ecca Group Prince Albert Formation	Rhythmite

Figure 6.47: Sample W47, image and descriptions. The sample is a grey, fine grained sandstone interbedded with dark grey to black shales.

W48	Depth (m)	Stratigraphy	Lithology
	2339.42-2339.58	Dwyka Group	Tillite

Figure 6.48: Sample W48, image and descriptions. The sample is a grey, coarse grained matrix with rounded and occasional sub-angular sandstone and quartz fragments that are up to 70 mm in diameter.

W49	Depth (m)	Stratigraphy	Lithology
	2347.73-2347.87	Dwyka Group	Tillite

Figure 6.49: Sample W49, image and descriptions. The sample is a grey, coarse grained matrix with rounded and occasional sub-angular sandstone and quartz fragments that are up to 70 mm in diameter.

6.2. Seismic velocities

The experimentally determined P- and S-wave velocities (Vp and Vs) are reported in this section. The oscilloscope images are also provided to indicate where the arrivals of the seismic waves were picked for each sample. Some basic signal processing results are also provided, in order to compare the original wave arrival pickings with those from stacked signals. The seismic velocity results of some of the samples under uniaxial stresses are also provided to suggest probable seismic velocities at the in situ environment.

6.2.1. P- and S-waves

The seismic velocities that were obtained from the pulse transmission technique are presented in this section. Tables 6.1 and 6.2 summarise the lithology, stratigraphy and P- and S-wave velocities for each sample. A seismic wave that travels through one sample as captured by the oscilloscope is illustrated in Figure 6.50. The arrival time positions of the P- and S-waves are also indicated on these Figures. . For some signals, the arrival positions of Vs are not clear

due to the complexity of the waveforms. The P-wave velocities are the focus of our discussions, as S-wave velocities are generally less well-constrained.

Table A1 in Appendix A provides all the data that was collected for each sample to calculate the seismic velocities from.

Twelve sandstone samples were collected. The average P-wave velocity of all the sandstone samples is 4391 (±496) m/s, and the average S-wave velocity of the samples is 2345 (±441) m/s (Table 6.1 and Table 6.2). However, samples W10 and W13, both dark sandstone samples from the Trumpeters Member, have very low seismic velocities. Their P-wave velocities are below 2000 m/s and S-wave velocities are below 1000 m/s. This is significantly lower than the results by Bräuer et al. (2007) (Vp is 4400 – 5440 m/s and Vs is 2600 m/s). Based on the uncertainties of our first arrival times and the anomalously low seismic velocities for these two samples, their seismic velocities are not included in the average seismic velocities for sandstone samples from the KWV borehole. The average P- and S-wave wave velocities of the remaining ten sandstone samples are 4904 (±536) m/s and 2623 (±471) m/s, respectively. These values correlate to the average P- and S-wave velocities calculated from the geophysical log, which are 4061 m/s and 2605 m/s, respectively.

Eighteen shale samples were collected. Nine were carbonaceous shales. The average P-wave velocity for all the shale samples is 3473 (±672) m/s and the average S-wave velocity is 1914 (±365) m/s (Table 6.1 and Table 6.2). This is lower than the velocities from Bräuer et al. (2007). Quite a few samples have seismic velocities that deviate significantly (Vp < 2000 m/s and Vs < 1100 m/s). Samples W14 (shale), W17 (massive black shale) and W19 (carbonaceous shale) exhibited very noisy signals that caused ambiguous identifications of the first wave time arrivals. When these samples are excluded from the average, the remaining samples' average for Vp and Vs are 3859 (±708) m/s and 2116 (±349) m/s, respectively. There is no significant difference or correlation between the seismic velocities for the shale and the carbonaceous shale samples. The average experimental P-wave velocity for the shale samples correlate well with the average P-wave velocity for the shale samples obtained from the geophysical log, which is 3970 m/s. The average S-wave velocity for the shale sample (Vs = 2547 m/s) from the geophysical log is slightly higher than the average experimental S-wave velocities (Vs = 2116 m/s), but is within the measurement uncertainty.

For twelve dolerite samples, the average Vp is 5105 (±423) m/s, while the average Vs is 2718 (±378) m/s (Table 6.1 and Table 6.2). These values are higher than the average velocities of the sandstone (Vp = 4909 m/s and Vs = 2623 m/s) and shale samples (Vp =3859 m/s and Vs = 2116 m/s). These observations are in agreement with studies by Fatti (1987) who reported

high seismic velocities for dolerites (Vp = 6200 m/s). However, it is also noted that results for dolerite samples show low average Vp and Vs values that are lower than those obtained from the geophysical log (Vp = 4213 m/s and Vs= 2706 m/s) for the same rock types. It is suspected that either the geophysical log results may be incorrect or our measurements for these rocks may have been compromised by analytical difficulties, which are discussed in the following chapter. Furthermore, the output signals for all the dolerite samples are much cleaner than that of sandstone and shale samples, which provided high precision picking of the seismic wave arrival times.

The seismic velocities of three rhythmite samples were measured. The average P-wave velocity of these samples is 3503 (± 247) m/s while the average S-wave velocity of the samples is 1959 (± 532) m/s (Table 6.1 and Table 6.2). The seismic wave arrival times from sample W46 are unclear due to the high noise level in its signal. This led to a very high uncertainty in the location of the first wave arrivals and correspondingly large errors for the rhythmite samples. If this value (W46) is removed from the average seismic velocity calculations, then the remaining two rhythmite samples from borehole KWV (samples W30 and W47) yield an average P-wave velocity of 4586 (± 377) m/s and an average S-wave velocity of 2432 (± 388) m/s. These values correlate well to the average rhythmite seismic velocities that were obtained from the geophysical log (Vp = 4178 m/s and the Vs = 2754 m/s).

Two tillite samples have an average P-wave velocity of 5135 (± 136) m/s and an average S-wave velocity of 2896 (± 261) m/s (Table 6.1 and Table 6.2). The average P-wave velocity of these samples is higher than that of the average P-wave velocity (Vp = 4174 m/s) of the tillite samples from the geophysical log. The average S-wave velocity (Vs = 2802 m/s) for the tillite samples as obtained from the geophysical log is comparable to our experimentally determined average S-wave velocity (Vs = 2896 m/s).

Table 6.1: The lithology, stratigraphy and P- wave velocity for each sample from the KWV borehole.

Sample name	Lithology	P-wave velocity (m/s)	Standard deviation based on 5 measurements	Experimental error
W1	Sandstone	5089	0	809
W2	Mudstone	961	17	223
W3	Breccia	2426	3	936
W4	Sandstone interbedded shale	5133	0	946
W5	Shale	3319	1	734
W6	Sandstone	5304	0	877
W7	Dolerite	5603	1	614
W8	Sandstone	4477	3	249
W9	Carbonaceous shale	2135	2	311
W10	Dark sandstone	1898	5	155
W11	Shale	2663	6	1108
W12	Dolerite	5752	1	412
W13	Dark sandstone	1748	3	218
W14	Shale	1679	3	494
W15	Massive shale	4430	1	248
W16	Dolerite	5050	0	316
W17	Massive black shale	1422	7	193
W18	Massive sandstone	4511	0	13
W19	Massive carbonaceous shale	1541	5	579
W20	Carbonaceous shale	2340	1	780
W21	Sandstone	5462	0	186
W22	Dolerite	5729	1	507
W23	Sandstone	3107	1	321
W24	Carbonaceous shale	2000	3	25
W25	Massive shale	5182	0	168
W26	Dolerite	4115	0	212
W27		5863	0	239
W28	Carbonaceous shale	3806	2	624
W29	Massive sandstone	5602	0	392
W30	Rhythmite	4872	0	135
W31	Dolerite	3574	0	160
W32		4321	0	247
W33		6033	0	227
W34		4431	0	122
W35	Sandstone	4956	0	311
W36		5400	0	328
W37	Dolerite	5076	1	879
W38		5712	0	462
W39	Carbonaceous shale	5799	1	1818
W40		4485	0	385
W41		5131	0	561
W42		4712	0	277
W43	Shale	4757	0	706
W44		2070	7	342
W45	Massive shale	5051	0	319
W46	Rhythmite	1338	3	335
W47		4299	2	230
W48	Tillite	4945	0	76
W49		5325	0	177

Table 6.2: The lithology, stratigraphy and S- wave velocity for each sample from the KWV borehole.

Sample name	Lithology	S-wave velocity (m/s)	Standard deviation based on 5 measurements	Experimental error
W1	Sandstone	2621	1	429
W2	Mudstone	696	3	234
W3	Breccia	1197	2	734
W4	Sandstone interbedded shale	2440	0	428
W5	Shale	1714	2	587
W6	Sandstone	2993	1	558
W7	Dolerite	2684	1	352
W8	Sandstone	2535	6	200
W9	Carbonaceous shale	1530	0	417
W10	Dark sandstone	950	9	39
W11	Shale	1501	2	586
W12	Dolerite	3065	0	585
W13	Dark sandstone	958	1	328
W14	Shale	1006	7	709
W15	Massive shale	2338	2	345
W16	Dolerite	2748	0	467
W17	Massive black shale	913	3	80
W18	Massive sandstone	2383	2	88
W19	Massive carbonaceous shale	795	7	231
W20	Carbonaceous shale	1188	2	231
W21	Sandstone	2867	2	102
W22	Dolerite	2927	0	265
W23	Sandstone	1736	3	401
W24	Carbonaceous shale	1169	8	170
W25	Massive shale	2795	1	245
W26	Dolerite	2587	2	209
W27		2927	2	297
W28	Carbonaceous shale	1905	3	313
W29	Massive sandstone	2845	2	1012
W30	Rhythmite	2869	0	117
W31	Dolerite	2184	1	96
W32		2426	3	194
W33		3160	1	624
W34		2516	1	316
W35	Sandstone	2892	1	265
W36		2924	1	480
W37	Dolerite	2607	0	463
W38		2780	1	274
W39	Carbonaceous shale	3190	3	211
W40		2171	2	226
W41		2941	4	239
W42		2696	1	453
W43	Shale	2577	2	415
W44		1214	6	141
W45	Massive shale	2805	1	246
W46	Rhythmite	1011	1	880
W47		1998	3	248
W48	Tillite	2874	1	257
W49		2918	0	265

6.2.2. Signal processing

The wave signals that were obtained from the pulse transmission technique have varying degrees of noise. In some cases, the noise affects our ability to determine the first arrivals of the P- and S-waves. Figure 6.50 shows our attempt to increase the signal-to-noise ratio by stacking multiple waveforms to better determine the first wave arrivals. In order to determine whether the stacking of the signals altered our seismic velocities, the P-wave arrivals are investigated. In cases where it is evident that the location of the P-wave arrival times shifted significantly, both the P- and S-wave velocities were recalculated.

In all cases, stacking significantly improved the signal-to-noise ratio of the data. However, the first arrivals of the P-wave remained similar for most samples, implying that our seismic velocities did not change in many cases. This can be seen where the blue (original pick for first arrival of P-wave) and red (refined pick for first arrival of P-wave after stacking) arrows point to the same positions on the time axes of the graphs (Figure 6.50). However, stacking provides high confidence of the initial picks.

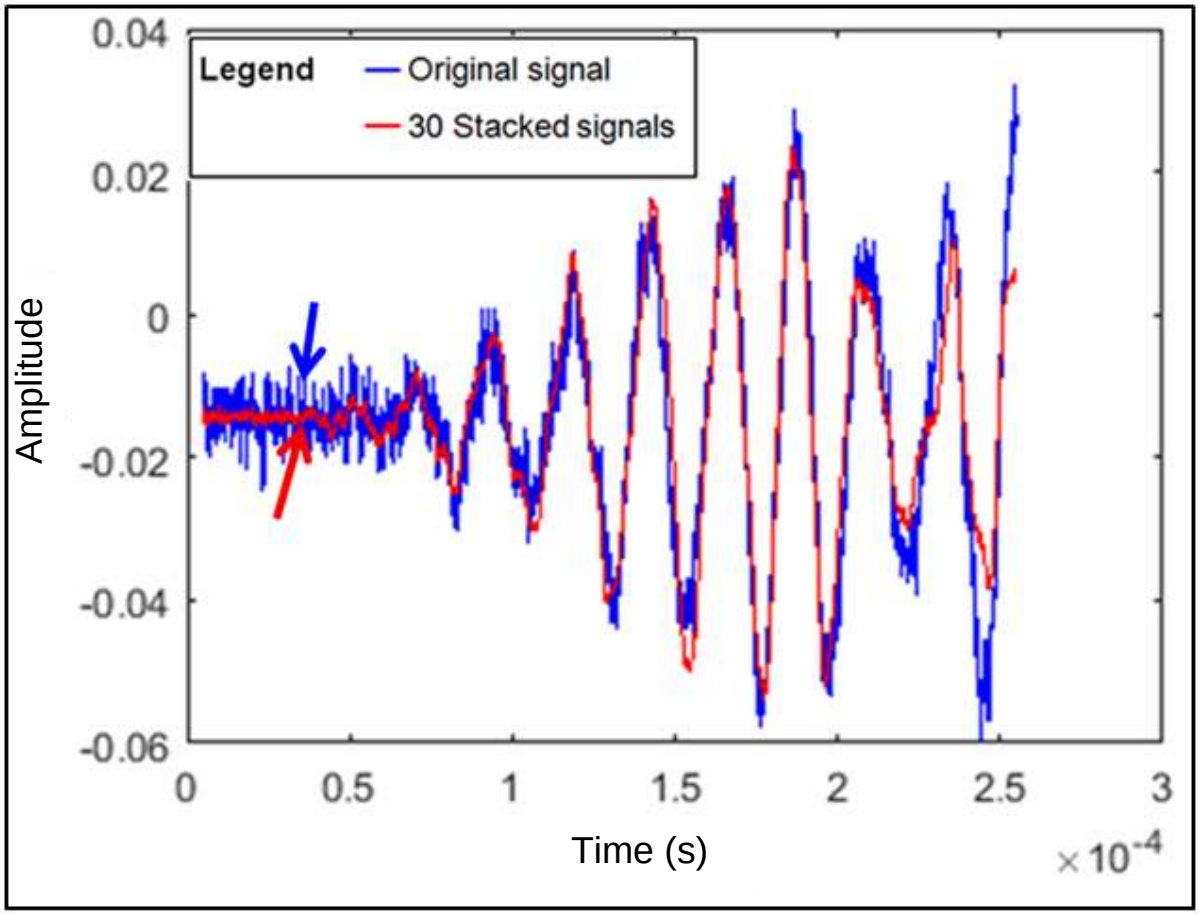

Figure 6.50: The result of stacking multiple waveforms for a single mudstone sample versus a single waveform output of a sample (W2). Multiple waveform outputs from the oscilloscope for a mudstone sample (W2) were stacked to produce the red, smooth signal.

Samples W9 and W39 (carbonaceous shales) were the only two samples that showed significant changes in seismic velocities after the stacking of the data. The original signal for W9 was very noisy and the first wave arrival was identified to be the large dip in the waveform, which yielded Vp and Vs values at 1962 m/s and 1039 m/s, respectively. After stacking it was evident that the noise in the original signal was masking several smaller peaks and dips earlier in the signal. Taking this into account, the Vp and Vs for W9 became 2134 m/s and 1749 m/s, respectively (Figure 6.51).

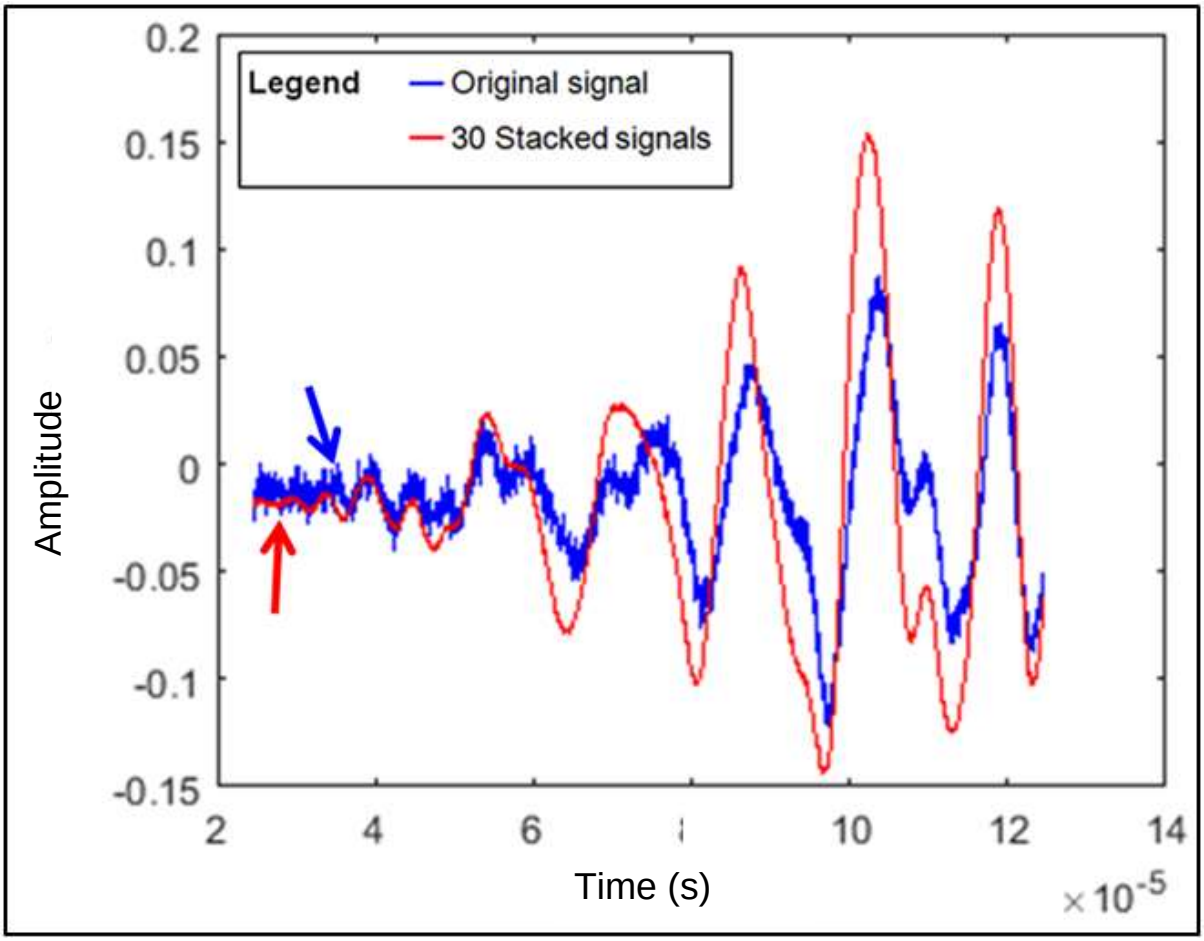

Figure 6.51: The result of stacking multiple waveforms for a single carbonaceous shale sample versus a single waveform output of a sample (W9). Multiple waveform outputs from the oscilloscope for a carbonaceous shale sample (W9) were stacked to produce the red, smooth signal.

Sample W39 showed trends similar to W9. The true first P- and S-wave arrivals were masked by noise in the signal. After stacking several signals for this sample, the Vp changed from 5613 m/s to 5799 m/s and Vs changed from 2418 m/s to 2500 m/s (Figure 6.52).

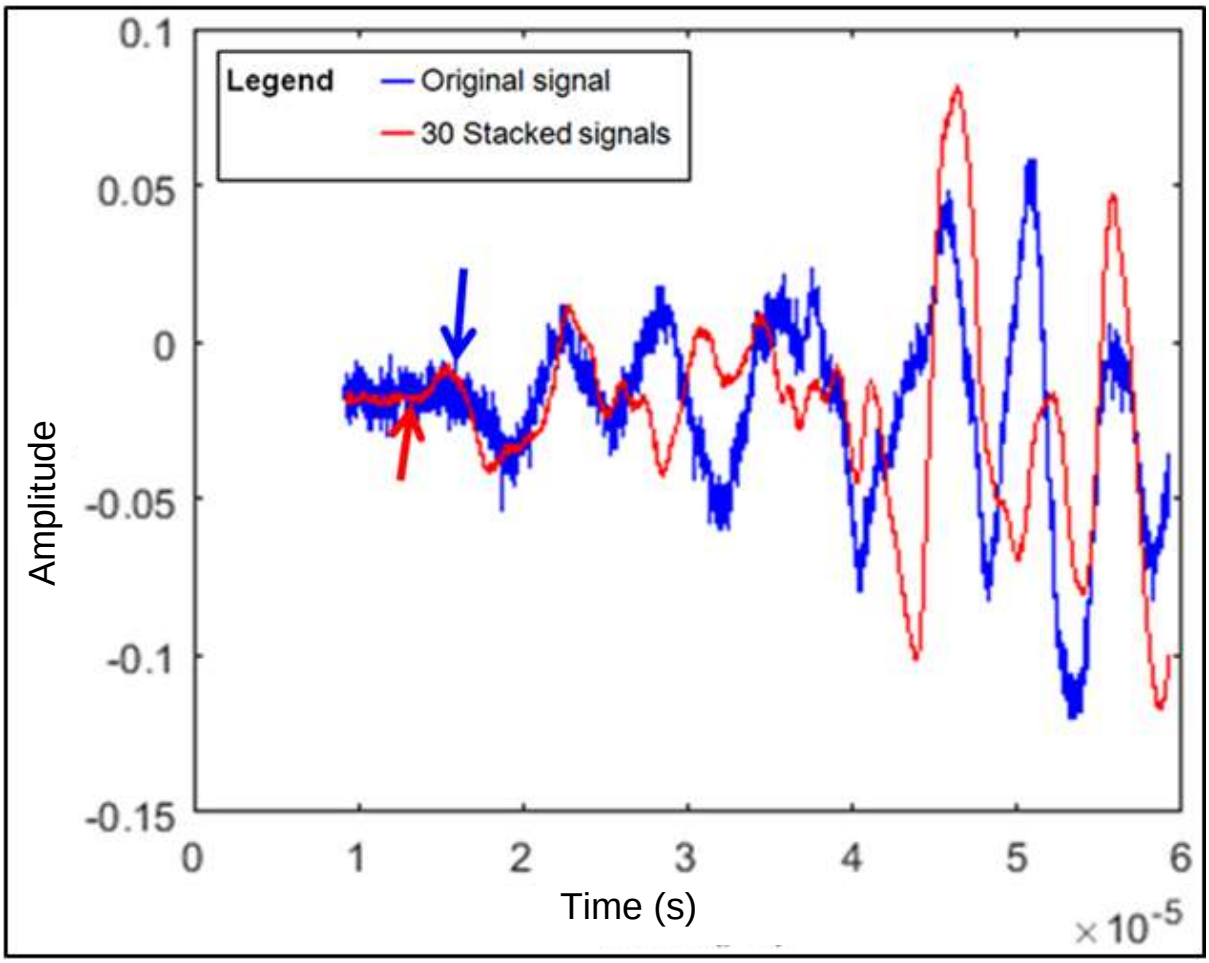

Figure 6.52: The result of stacking multiple waveforms for a single carbonaceous shale sample versus a single waveform output of a sample (W19). Multiple waveform outputs from the oscilloscope for a carbonaceous shale sample (W19) were stacked to produce the red, smooth signal.

6.2.3. Uniaxial stress

The uniaxial stress results of the samples are presented in this section (Figure 6.53 to Figure 6.58). The P-wave velocities were measured while the uniaxial stress on the samples was incrementally increased. Plots of seismic velocities versus uniaxial stresses for each sample are horizontally segmented into stress phases in increments of 10 MPa to allow for simple and accurate comparisons between samples.

The P-wave velocities of most samples (except W49) increased with increasing uniaxial stress (Table 6.3). The increases in seismic velocities of our samples did not occur at the same rate, but there is a common asymptotic trend of stress saturation that is rock type-dependent. The asymptotic behaviour may indicate complete closure of all pores and oriented fractures in the samples.

Table 6.3: A summary of the effect of uniaxial stress on the P-wave velocity of each sample. The initial P-wave velocity (at 0 MPa), saturation P-wave velocity (at 80 MPa) and total increase in P-wave velocity is indicated. Initial velocities at 0 MPa are re-measured for each sample and are similar to values presented in Table 6.1.

Sample	Lithology	Initial velocity (Vp) (~0.1 Mpa)	Saturation velocity (Vp) (m/s)	Total increase in seismic velocity (Vp) (m/s)	Relative increase in Vp (%)
W5	Shale	3876 +/- 172	5149 +/- 70	1273 +/- 186	33 +/- 5
W7	Dolerite	5575 +/- 231	5785 +/- 129	210 +/- 265	4 +/- 5
W8	Sandstone	4776 +/- 27	4953 +/- 30	177 +/- 40	4 +/- 1
W9	Carbonaceous shale	1912 +/- 95	4760 +/- 122	2848 +/- 155	149 +/- 11
W10	Sandstone	2180 +/- 502	4754 +/- 154	2574 +/- 525	118 +/- 36
W11	Shale	3235 +/- 52	4878 +/- 59	1643 +/- 78	51 +/- 3
W13	Sandstone	1565 +/- 69	4681 +/- 124	3116 +/- 142	199 +/- 13
W16	Dolerite	5040 +/- 62	5316 +/- 73	276 +/- 96	5 +/- 2
W17	Shale	2124 +/- 34	4272 +/- 137	2148 +/- 142	101 +/- 7
W18	Sandstone	4364 +/- 46	4937 +/- 29	573 +/- 55	14 +/- 1
W19	Carbonaceous shale	1088 +/- 114	4184 +/- 84	3096 +/- 142	285 +/- 33
W21	Sandstone	5519 +/- 37	5545 +/- 30	26 +/- 48	0 +/- 1
W25	Shale	5104 +/- 13	5216 +/- 67	112 +/- 69	2 +/- 1
W26	Dolerite	4000 +/- 40	4898 +/- 106	898 +/- 114	23 +/- 3
W31	Dolerite	3483 +/- 137	5179 +/- 67	1696 +/- 152	49 +/- 5
W33	Dolerite	6234 +/- 87	6250 +/- 96	16 +/- 130	0 +/- 2
W34	Dolerite	4431 +/- 48	4447 +/- -84	16 +/- 97	0 +/- 2
W37	Dolerite	5090 +/- 70	5199 +/- 36	109 +/- 79	2 +/- 2
W41	Carbonaceous shale	5241 +/- 185	5288 +/- 94	47 +/- 207	1 +/- 4
W42	Carbonaceous shale	4742 +/- 32	4751 +/- 28	9 +/- 43	0 +/- 1
W43	Shale	4551 +/- 204	4965 +/- 15	414 +/- 205	9 +/- 5
W44	Shale	2372 +/- 14	4585 +/- 53	2213 +/- 55	93 +/- 2
W45	Shale	5042 +/- 63	5063 +/- 63	21 +/- 89	0 +/- 2
W46	Rhythmite	1757 +/- 77	4704 +/- 110	2947 +/- 134	168 +/- 11
W47	Rhythmite	4069 +/- 163	4761 +/- 56	692 +/- 172	17 +/- 4
W48	Tillite	4998 +/- 61	5126 +/- 65	128 +/- 89	3 +/- 2
W49	Tillite	5383 +/- 73	5389 +/- 71	6 +/- 102	0 +/- 2

The P-wave velocities of the sandstone samples increased with uniaxial stress (Figure 6.53). The samples reached their saturation velocities in various phases of compression. The seismic velocities of samples W10 and W13 increased drastically (Table 6.3), and sample W10 reached maximum velocity in the first phase (0 – 10 MPa) of compression. However, their seismic velocities under atmospheric stress (~0.1 MPa) were unreliable. Therefore, it is possible that the initial seismic velocities (~0.1 MPa) are incorrect for these samples, similar to some of the carbonaceous shale samples (W9 and W19). Samples W8 and W18 reached

their saturation velocities at 45 MPa and 55 MPa, respectively, which is at higher stress regime than other sandstone samples. This may suggest that they might be more porous or fractured than other sandstone samples (Figure 6.53).

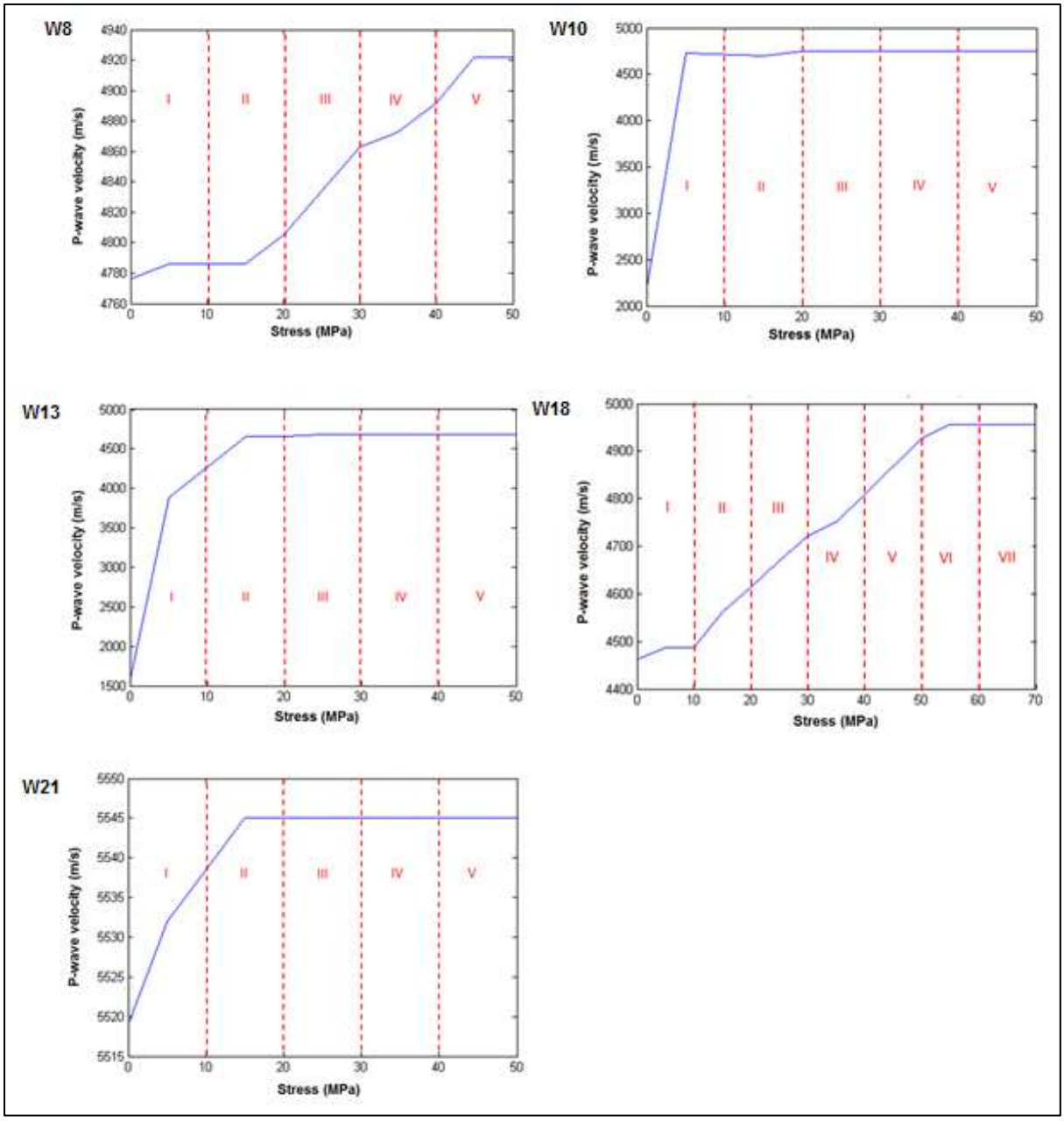

Figure 6.53: The effect of uniaxial stress on the P-wave velocity of sandstone samples from borehole KWV. The stress (x-axis) is divided into a number of phases.

The seismic velocities of all the shale samples increased under uniaxial stress (Figure 6.54). All the shale samples, except for sample W25, exhibit seismic velocity stabilisation within the first compression phase (0 - 10 MPa). Sample W25 showed a different trend with no velocity changes at up to 5 MPa and plateaued from 15 MPa to 25 MPa. It then increased again sharply between 25 MPa and 40 MPa, after which it finally stabilised. The P-wave velocities of the shale samples increased variably (Figure 6.54). While the velocity of sample W45 only

increased by 21 m/s, the velocity of sample W17 increased by 2148 m/s (Table 6.3). Since it was deduced (see Chapter 6.2.1.) that two of the shale samples (W17 and W44) are characterised by erroneously low P-wave velocities under atmospheric stress (~0.1 MPa), the high increase in seismic velocity of sample W17 is unrealistic. There is thus no consistent correlation between the increases of seismic velocity under uniaxial stresses for the shale samples. The shale samples may all have different porosities or fracture orientations.

The results for the carbonaceous shale samples show a similar velocity-stress relationship to the shale samples (Figure 6.55). Although the P-wave velocities of all the samples increased under uniaxial stress, the rates and the total increases per sample differ. Samples W9 and W19 exhibit more drastic increases in seismic velocities under uniaxial stresses. However these samples also exhibit anomalously low seismic velocities (Vp for W9 = 2135 m/s and Vp for W19 = 1541 m/s) under atmospheric stress (~0.1 MPa). With minimal uniaxial stress applied to these samples, their seismic velocities increase to values that are in agreement with previous studies of shale samples from the Karoo Basin (Bräuer et al., 2007). One probable reason for good measurements is that at atmospheric stress there was a poor contact between the samples and the transducers, and the application of stress improved the contacts. Another possibility is that the application of stress on the samples closed fractures that might have been introduced by drilling/removal of the core or during the sampling process. Samples W41 and W42 have more realistic initial P-wave velocities. While the seismic velocity of sample W42 stabilised within the first phase of compression, the velocity of sample W41 plateaued in the first phase, increased again in the third phase (20 – 30 MPa) and only stabilised at 25 MPa. This indicates that not all pores and fractures were closed at 5 MPa, but a majority did at 25 MPa.

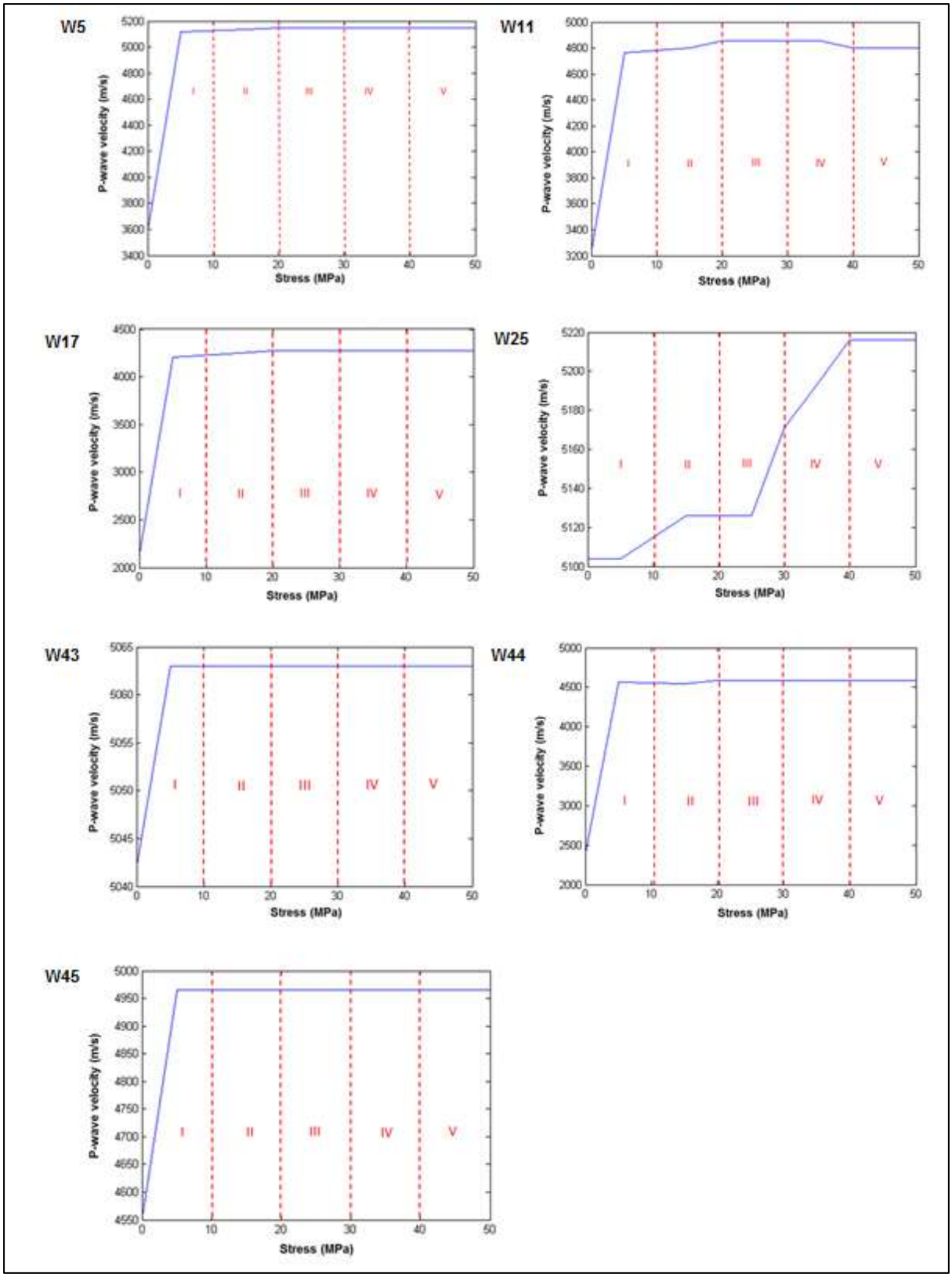

Figure 6.54: The effect of uniaxial stress on the P-wave velocity of shale samples from borehole KWV. The stress (x-axis) is divided into a number of phases.

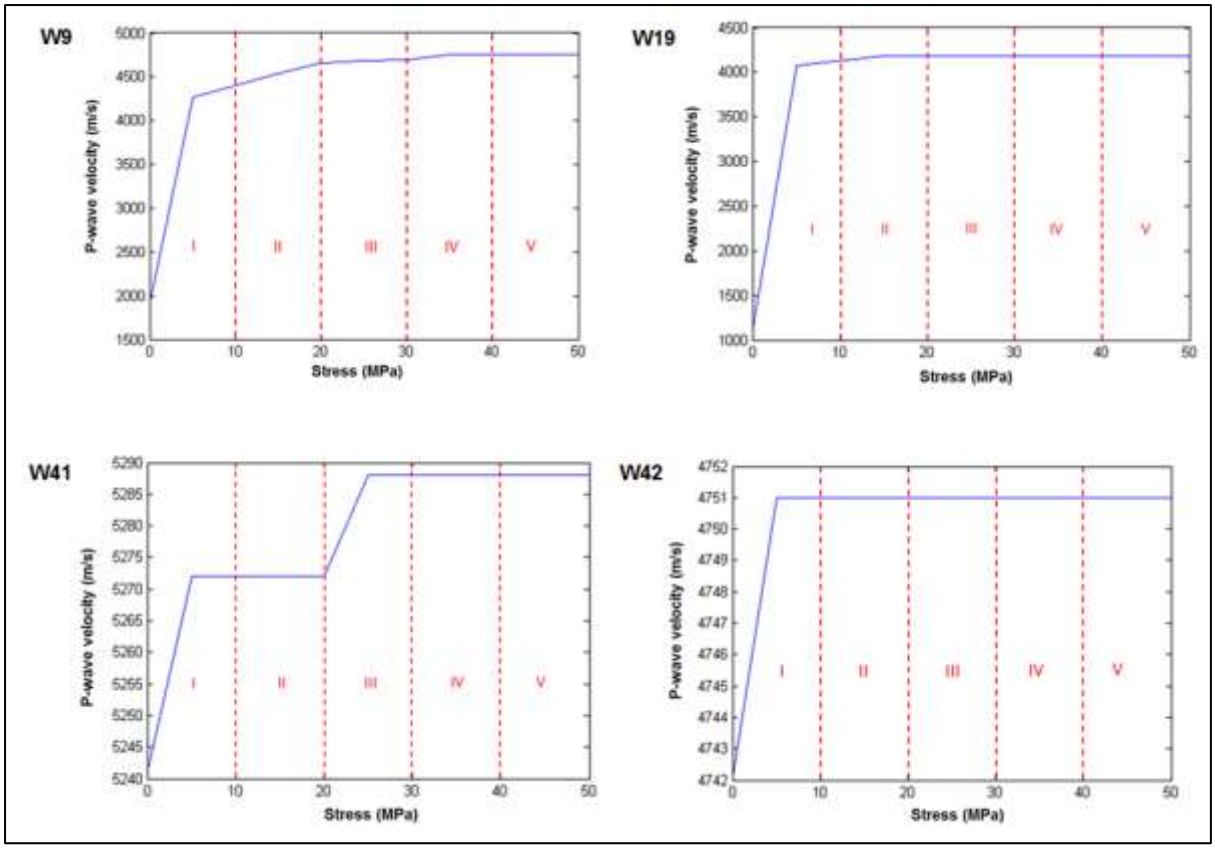

Figure 6.55: The effect of uniaxial stress on the P-wave velocity of carbonaceous shale samples from borehole KWV. The stress (x-axis) is divided into a number of phases.

The P-wave velocities of the dolerite samples tend to increase under uniaxial stress (Figure 6.56). The velocity-stress dependence behaviour varies considerably, depending on the sample physical condition. The velocities of samples W26 and W31 only stabilised in the seventh phase of compression (65 MPa and 70 MPa, respectively). These samples also showed significant changes in seismic velocities with an increase of 908 m/s for sample W26 and 1718 m/s for sample W31 (Table 6.3). Both of these samples along with samples W33, W34 and W37 are from the Pluto's Vale Member of the Ecca Group. The dolerite samples from this member are all grey-green, but only samples W26 and W31 are coarse crystalline, while the others are fine- to medium crystalline. These two samples are expected to be either more porous, or harder than the other dolerite samples. If this holds true, it may possibly be attributed to the grain size of the samples. Although these samples do not show visible fracturing, it is possible that the samples contain macro- and micro-fractures that are beyond optical resolution.

The remaining dolerite samples except for sample W16 all stabilised in either the first or second phase of compression (0 – 20 MPa). Sample W16 stabilised in the fifth phase of compression (40 – 50 MPa). This sample is from the Fort Brown Formation and is medium crystalline. The late-stage stabilisation of this sample may indicate its higher porosity than the

other samples or that the sample was initially less compressible. No consistent relationship was observed between the dolerite samples.

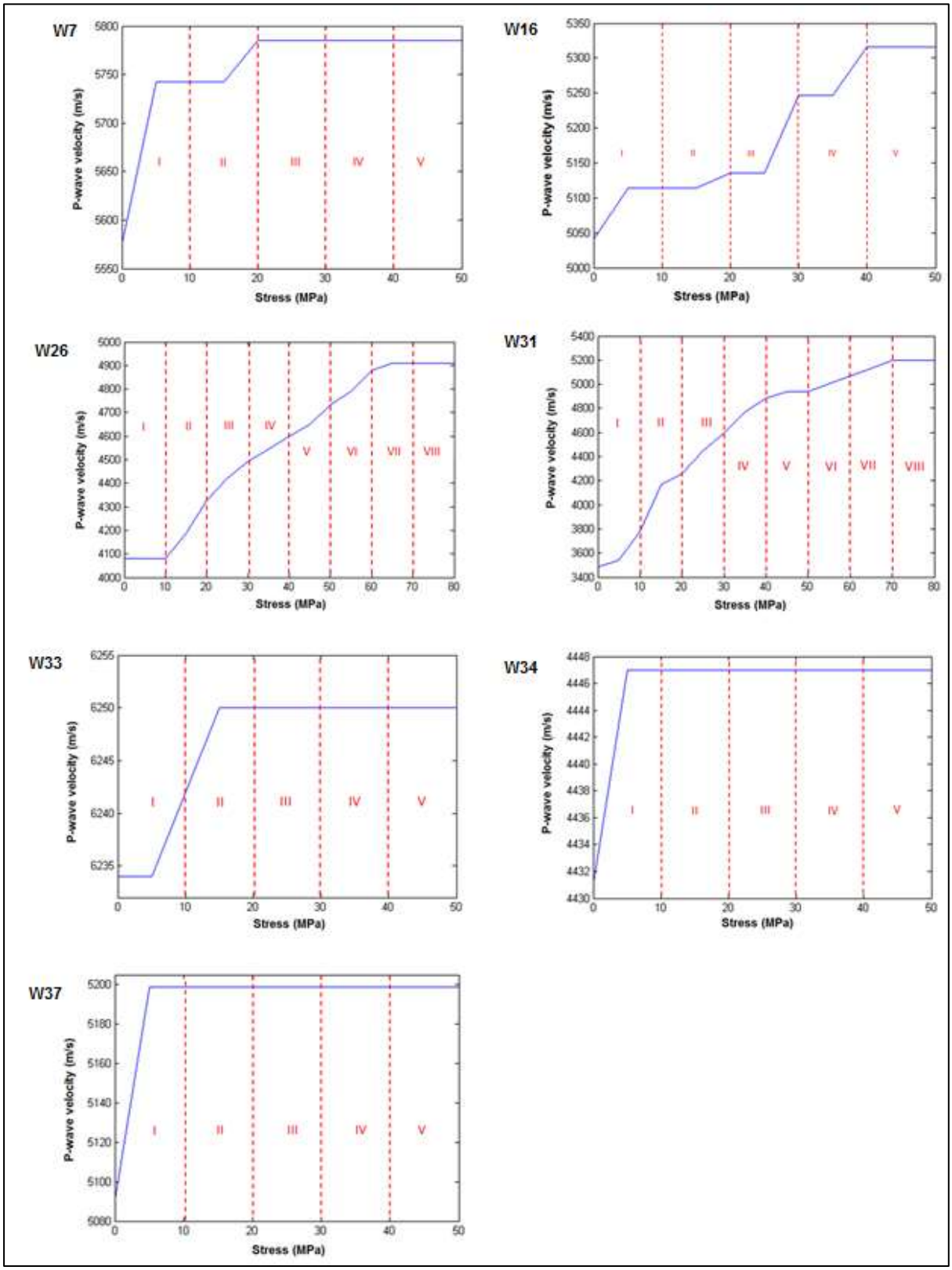

Figure 6.56: The effect of uniaxial stress on the P-wave velocity of dolerite samples from borehole KWV. The stress (x-axis) is divided into a number of phases.

The rhythmite samples also show a P-wave velocity increase under uniaxial stress (Figure 6.57). Sample W46 shows a significantly larger (2947 m/s) increase in seismic velocity than sample W47 (692 m/s) (Table 6.3). Sample W47 had an abnormally low seismic velocity (1757 m/s) under atmospheric stress (~0.1 MPa), which may explain the large increase in seismic velocity under uniaxial stress. Sample W46 stabilised in the first phase of compression and sample W47 in the second phase of compression. The seismic velocities of the samples showed no further increase at higher stresses. Since both samples consist of similar fine-grained sandstones with interbeds of dark shales, the different behaviours of the samples under stress cannot be attributed to lithological variations within the samples. Instead, the differences observed may be explained by pore spaces and/or or micro-fractures in each sample that effectively close under different amounts of stress.

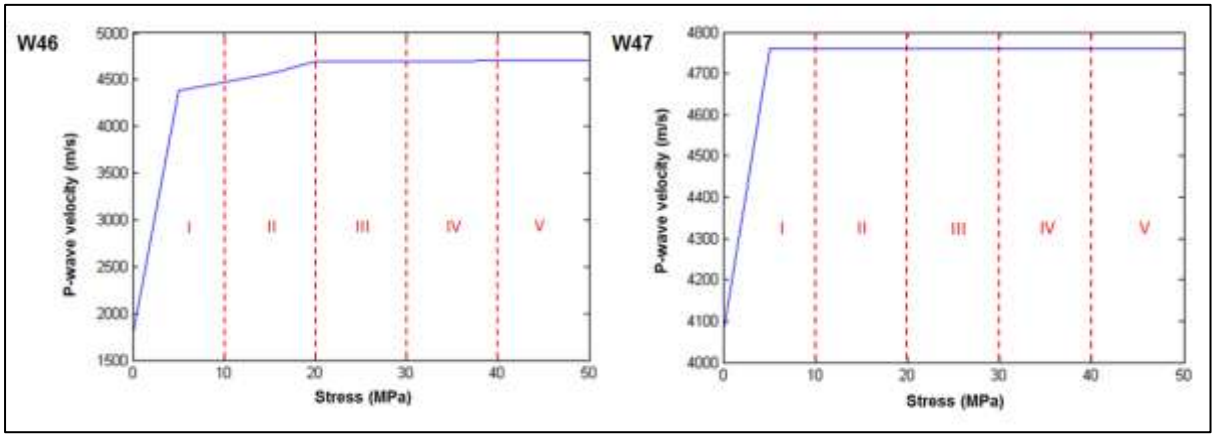

Figure 6.57: The effect of uniaxial stress on the P-wave velocity of rhythmite samples from borehole KWV. The stress (x-axis) is divided into a number of phases.

The tillite samples showed little to no increase in P-wave velocities with the application of uniaxial stress (Figure 6.58). The seismic velocity of sample W48 increases by 128 m/s (Table 6.3) and stabilises in the first phase of compression (0 – 10 MPa). Sample W49 had a constant P-wave velocity (Vp = 5389 m/s) throughout the stress application. This may indicate that the sample had no pore spaces and/or micro-fractures that attenuated wave propagation.

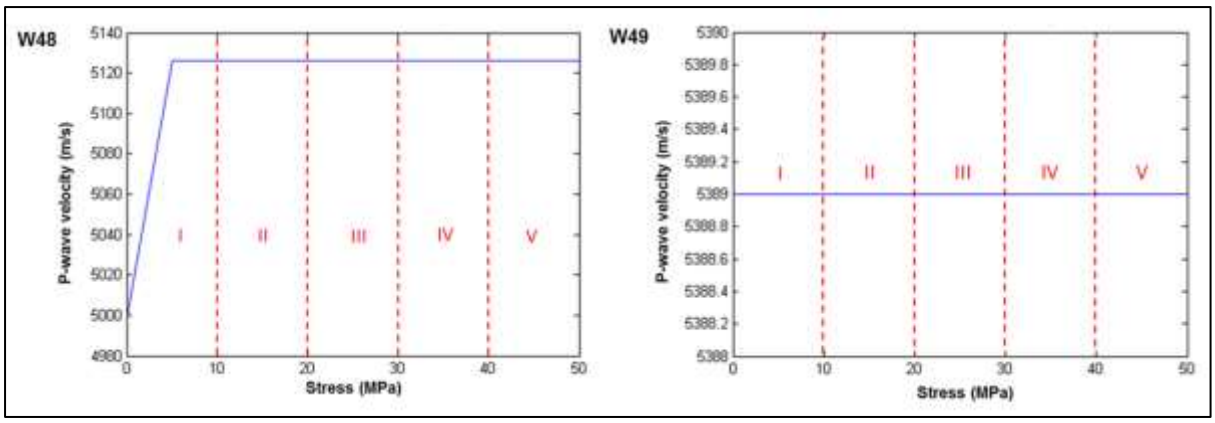

Figure 6.58: The effect of uniaxial stress on the P-wave velocity of tillite samples from borehole KWV. The stress (x-axis) is divided into a number of phases.

Figure 6.59 indicates the amount that the P-wave velocities increased for each sample that was placed under uniaxial stress. It also indicates their saturation P-wave velocities. A few of the samples were subjected to high experimental errors (large uncertainties in the time of wave arrivals) leading to the presence of a few 'false highs' on the plot. Figure 6.60 also indicates the amount of increase in seismic velocity under uniaxial stress, but only for the samples that exhibited realistic initial seismic velocities.

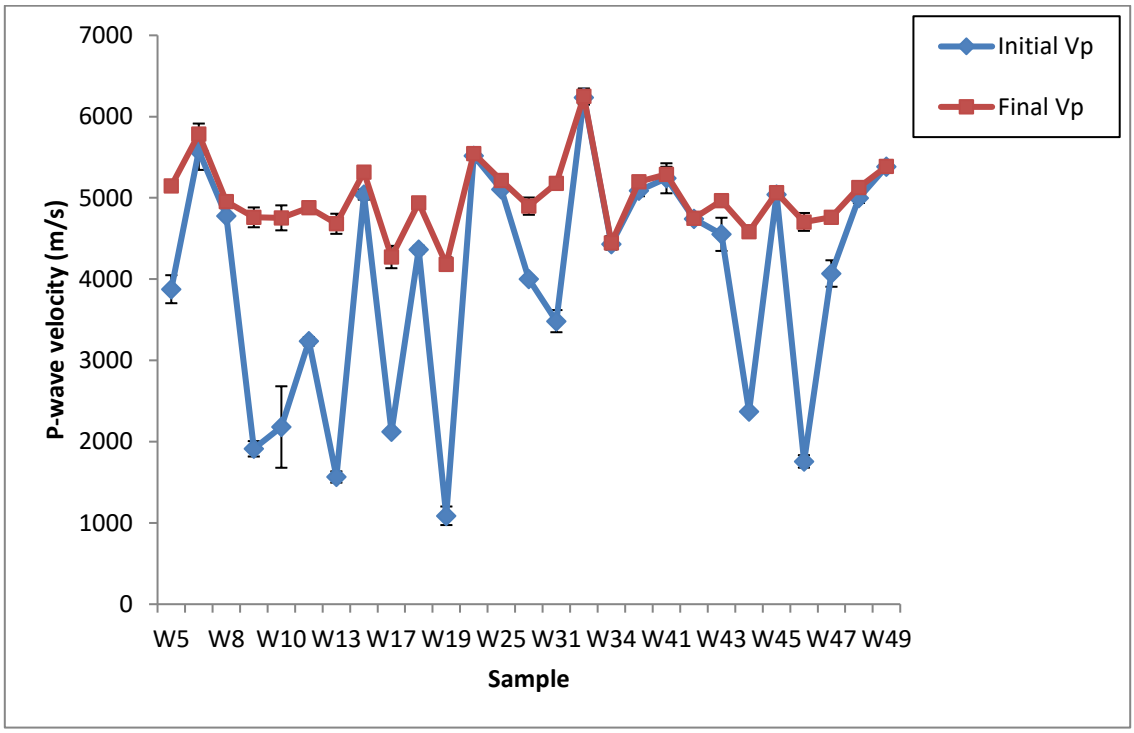

Figure 6.59: The total increase in P-wave velocities with uniaxial stress for all samples from borehole KWV. The initial (~ 0.1 MPa) and final (~ 80 MPa) P-wave velocities are plotted.

No correlation exists between the total seismic velocity increases of the samples with depth (Figure 6.60). There is also no correlation between the total seismic velocity increases and the lithologies of the samples.

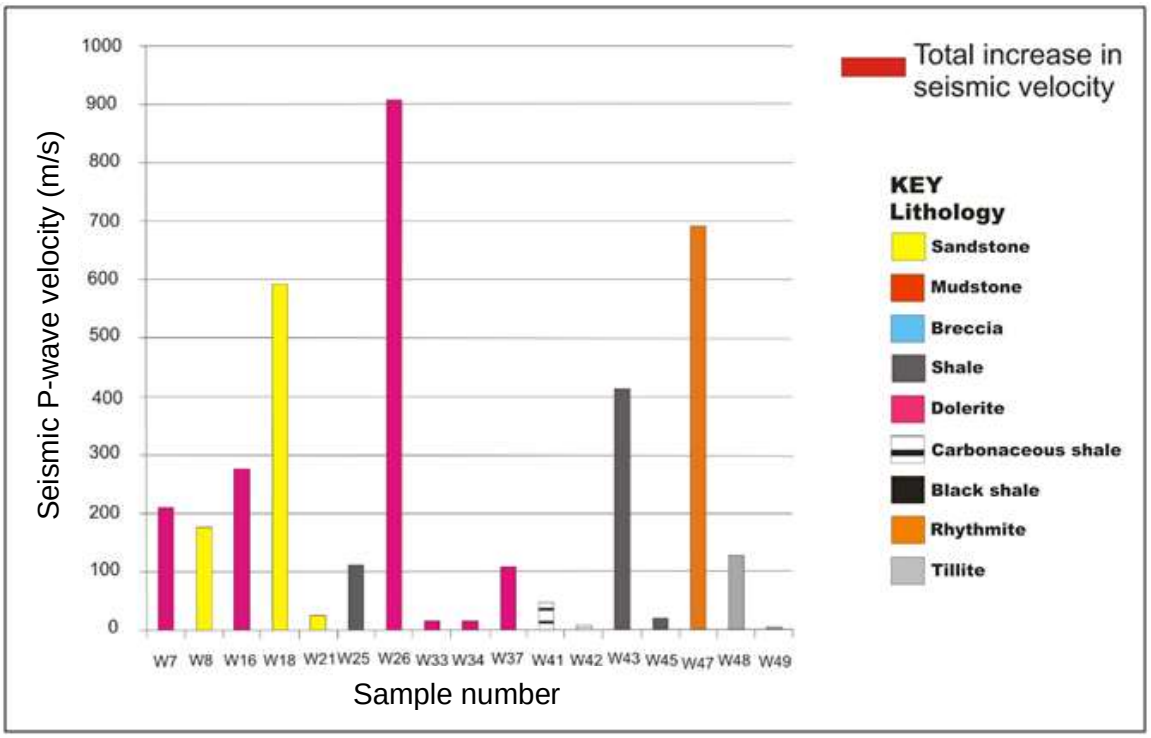

Figure 6.60: The total increase in P-wave velocities with uniaxial stress for samples from borehole KWV. The samples with initial velocities below 2000 m/s are excluded in this plot, as these values are deduced to be unrealistic.

6.3. Bulk density

The bulk densities for all samples from the KWV borehole are presented in this section (Table 6.4). The bulk densities were obtained by using the method described in Chapter 5.3. The relationship between the bulk densities and the P-wave velocities for all samples is presented in Figure 6.61. Only one mudstone sample (W2) was collected. The bulk density for this sample (sample W2) is 2.53 g/cm^3. This value corresponds well with the density of 2.59 g/cm^3 obtained from the geophysical log.

The bulk densities of the twelve sandstone samples range from 2.60 g/cm^3 to 2.73 g/cm^3 (Table 6.4). The average density for these samples is 2.68 (± 0.01) g/cm^3. Baiyegunhi et al. (2014) found that the bulk densities of sandstone samples from the Main Karoo Basin in the Eastern Cape Province range from 2.67 g/cm^3 to 2.77 g/cm^3. Based on the geophysical log, the average density for the sandstone samples is 2.72 g/cm^3. The bulk densities for our sandstones correspond well with the values from the geophysical log and with previous studies.

A total of eighteen shale samples were analysed. These samples include shale, carbonaceous shale, massive shale and shale breccia. The bulk densities range from 2.64 g/cm^3 to 2.81 g/cm^3 (Table 6.4), with an average of 2.74 (± 0.00) g/cm^3. This correlates well with the results (2.53 g/cm^3 to 2.76 g/cm^3) from Baiyegunhi et al. (2014). The average bulk density of the shale

samples is slightly higher than that of the sandstone samples. This may be due to the presence of pyrite in some of the shale samples. The average bulk density of the shale samples corresponds well with that obtained from the geophysical log (2.72 g/cm^3) and those of previous studies (Baiyegunhi et al., 2014).

Twelve dolerite samples were analysed. As expected, the dolerite samples have higher bulk densities than the shale and sandstone samples. The dolerite densities range from 2.59 g/cm^3 to 3.14 g/cm^3 (Table 6.4), with an average of 2.95 (± 0.00) g/cm^3. The average bulk density value is slightly higher than that obtained from the geophysical log, which is 2.86 g/cm^3.

The bulk densities of the three rhythmite samples range from 2.70 g/cm^3 to 2.79 g/cm^3. The average bulk density of the rhythmite samples is 2.76 (± 0.00) g/cm^3.

The bulk densities of the two tillite samples from the Dwyka Group are very similar, with an average of 2.75 (± 0.00) g/cm^3 (Table 6.4). This correlates well with the average density of tillite samples from borehole KWV that was obtained from the geophysical log, which is 2.73 g/cm^3.

Table 6.4: Bulk density results for the Karoo samples from the KWV borehole.

Sample name	Lithology	Stratigraphy	Bulk density (g/cm3)
W1	Sandstone	Adelaide Subgroup	2.60 +/- 0.00
W2	Mudstone		2.53 +/- 0.01
W3	Breccia	Waterford Member	2.75 +/- 0.00
W4	Sandstone interbedded shale		2.65 +/- 0.02
W5	Shale	Fort Brown Formation	2.71 +/- 0.00
W6	Sandstone		2.70 +/- 0.00
W7	Dolerite		2.94 +/- 0.00
W8	Sandstone		2.62 +/- 0.01
W9	Carbonaceous shale		2.64 +/- 0.02
W10	Dark sandstone	Trumpeters Member	2.70 +/- 0.00
W11	Shale		2.72 +/- 0.00
W12	Dolerite		2.96 +/- 0.00
W13	Dark sandstone		2.71 +/- 0.01
W14	Shale	Wonderfontein Member	2.69 +/- 0.00
W15	Massive shale		2.73 +/- 0.01
W16	Dolerite		2.95 +/- 0.01
W17	Massive black shale		2.72 +/- 0.00
W18	Massive sandstone	Pluto's Vale Member	2.67 +/- 0.00
W19	Massive carbonaceous shale		2.75 +/- 0.01
W20	Carbonaceous shale		2.76 +/- 0.01
W21	Sandstone		2.71 +/- 0.00
W22	Dolerite		2.96 +/- 0.00
W23	Sandstone		2.68 +/- 0.00
W24	Carbonaceous shale		2.81 +/- 0.00
W25	Massive shale		2.74 +/- 0.01
W26	Dolerite		2.96 +/- 0.00
W27			3.14 +/- 0.00
W28	Carbonaceous shale		2.77 +/- 0.00
W29	Massive sandstone		2.68 +/- 0.01
W30	Rhythmite		2.70 +/- 0.00
W31	Dolerite		2.98 +/- 0.00
W32			2.99 +/- 0.00
W33			2.96 +/- 0.00
W34			2.59 +/- 0.00
W35	Sandstone		2.68 +/- 0.01
W36			2.73 +/- 0.00
W37	Dolerite		2.94 +/- 0.01
W38			2.98 +/- 0.01
W39	Carbonaceous shale	Whitehill Formation	2.73 +/- 0.00
W40			2.67 +/- 0.03
W41			2.71 +/- 0.00
W42			2.77 +/- 0.01
W43	Shale	Prince Albert Formation	2.84 +/- 0.01
W44			2.79 +/- 0.00
W45	Massive shale		2.80 +/- 0.00
W46	Rhythmite		2.79 +/- 0.01
W47			2.79 +/- 0.00
W48	Tillite	Dwyka Group	2.75 +/- 0.00
W49			2.74 +/- 0.00

The relationship between the bulk density and the P-wave velocity is indicated in Figure 6.61. The S-wave velocities were not considered, due to uncertainties in the picking of the first arrival times. The mudstone sample (W2) has the lowest bulk density and P-wave velocity of

all the samples, and this plots in the bottom left corner of the graph. The sandstone and shale samples both plot over a large vertical range and a limited horizontal range. They also overlap extensively. The dolerite samples plot to the right side of the graph, with the highest bulk densities and P-wave velocities. The cause of the data spread is the range in seismic velocities for each lithological group. These wide ranges in velocities may be attributed to physical defects of the samples and/or invisible mineralogical heterogeneities. Additionally, first arrival times may have been picked inconsistently. The range in bulk densities for each lithological group is considerably more constrained, with only a few outliers. It is evident that the correlation between Vp and density is essentially non-existent based on our data (Figure 6.61). Hence density alone is not a good predictor of Vp, per lithology. The presence of physical imperfections and mineralogical heterogeneities such as micro-fractures in the samples may be a stronger control on Vp.

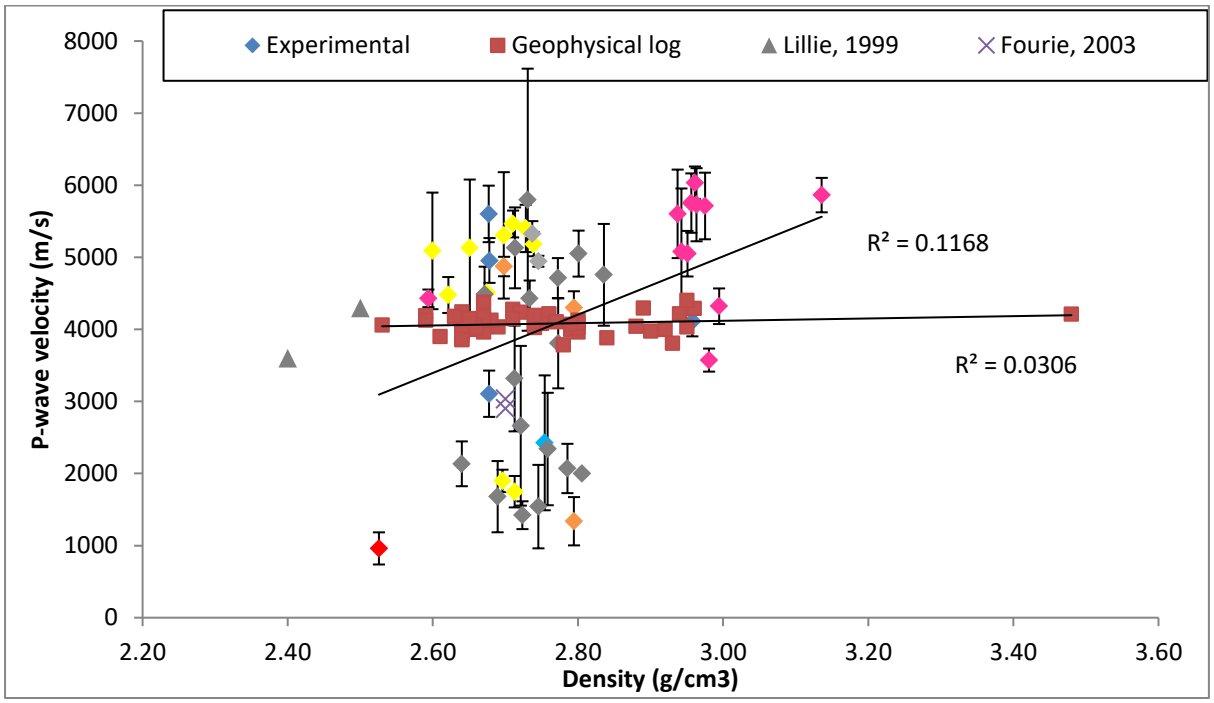

Figure 6.61: The relationship between the bulk density and the P-wave velocity for all the samples collected from borehole KWV. The pink colours are dolerite, yellow is sandstone, blue is breccia, red is mudstone, orange is rhythmite, dark grey is shale and light grey is tillite.

6.4. Porosity

This section presents the effective porosity (henceforth referred to as porosity) results for all the KWV samples (Table 6.5). It also provides a discussion of the relationship between the porosities and bulk densities of the samples.

The mudstone sample has a very low porosity of 0.45 +/- 0.00 %.

The porosity values for the twelve sandstone samples range from 0.17 % to 2.73 %, with the average porosity for the samples being 1.12 (± 0.02) %.

The shale samples have a slightly larger range of porosities. The eighteen samples range from 0.32 % to 3.85 %, with the average porosity for the shale samples being 1.66 (± 0.02) %.

The porosity values for the twelve dolerite samples range from 0.06 % to 3.07 %. The average porosity for the dolerite samples is 1.65 (± 0.02) %. The porosities of the rhythmite samples from borehole KWV range from 2.22 % to 3.47 %. The average porosity is 3.04 (± 0.02) %. This is the highest average porosity of all investigated lithologies. The tillite samples have an average porosity of 2.39 (± 0.00) %.

The dolerites appear to be slightly more porous than the sandstone and shale. However, the opposite is expected based on the higher bulk densities of the dolerite samples. One reason for this discrepancy could be due to more invisible dense minerals in some samples. Additionally, the error of the average dolerite porosity is slightly higher than the error values of the other lithologies. There is essentially no correlation between the densities and porosities of the samples based on our data (Figure 6.62). As seen in Figure 6.61, the bulk densities are more precise than the porosities.

Table 6.5: Porosity results for Karoo samples from the KWV borehole.

Sample name	Lithology	Stratigraphy	Porosity (%)
W1	Sandstone	Adelaide Subgroup	0.42 +/-0.03
W2	Mudstone		0.45 +/-0.00
W3	Breccia	Waterford Member	0.09 +/-0.00
W4	Sandstone interbedded shale		0.17 +/-0.00
W5	Shale	Fort Brown Formation	0.38 +/-0.00
W6	Sandstone		0.29 +/-0.00
W7	Dolerite		0.35 +/-0.01
W8	Sandstone		1.32 +/-0.03
W9	Carbonaceous shale		2.59 +/-0.00
W10	Dark sandstone	Trumpeters Member	0.61 +/-0.00
W11	Shale		0.32 +/-0.00
W12	Dolerite		0.06 +/-0.00
W13	Dark sandstone		1.57 +/-0.01
W14	Shale	Wonderfontein Member	2.33 +/-0.01
W15	Massive shale		1.17 +/-0.03
W16	Dolerite		2.87 +/-0.05
W17	Massive black shale		3.79 +/-0.01
W18	Massive sandstone	Pluto's Vale Member	2.11 +/-0.02
W19	Massive carbonaceous shale		2.12 +/-0.00
W20	Carbonaceous shale		0.50 +/-0.02
W21	Sandstone		0.53 +/-0.00
W22	Dolerite		1.85 +/-0.00
W23	Sandstone		1.27 +/-0.03
W24	Carbonaceous shale		3.85 +/-0.02
W25	Massive shale		0.34 +/-0.02
W26	Dolerite		3.07 +/-0.00
W27			0.39 +/-0.04
W28	Carbonaceous shale		0.53 +/-0.00
W29	Massive sandstone		1.56 +/-0.01
W30	Rhythmite		2.22 +/-0.02
W31	Dolerite		1.89 +/-0.00
W32			1.61 +/-0.01
W33			1.61 +/-0.01
W34			1.43 +/-0.00
W35	Sandstone		0.91 +/-0.02
W36			2.73 +/-0.00
W37	Dolerite		2.30 +/-0.00
W38			2.40 +/-0.03
W39	Carbonaceous shale	Whitehill Formation	2.93 +/-0.02
W40			1.30 +/-0.02
W41			0.86 +/-0.03
W42			0.40 +/-0.02
W43	Shale	Prince Albert Formation	1.96 +/-0.00
W44			3.02 +/-0.00
W45	Massive shale		1.43 +/-0.03
W46	Rhythmite		3.47 +/-0.03
W47			3.42 +/-0.00
W48	Tillite	Dwyka Group	2.55 +/-0.00
W49			2.23 +/- 0.00

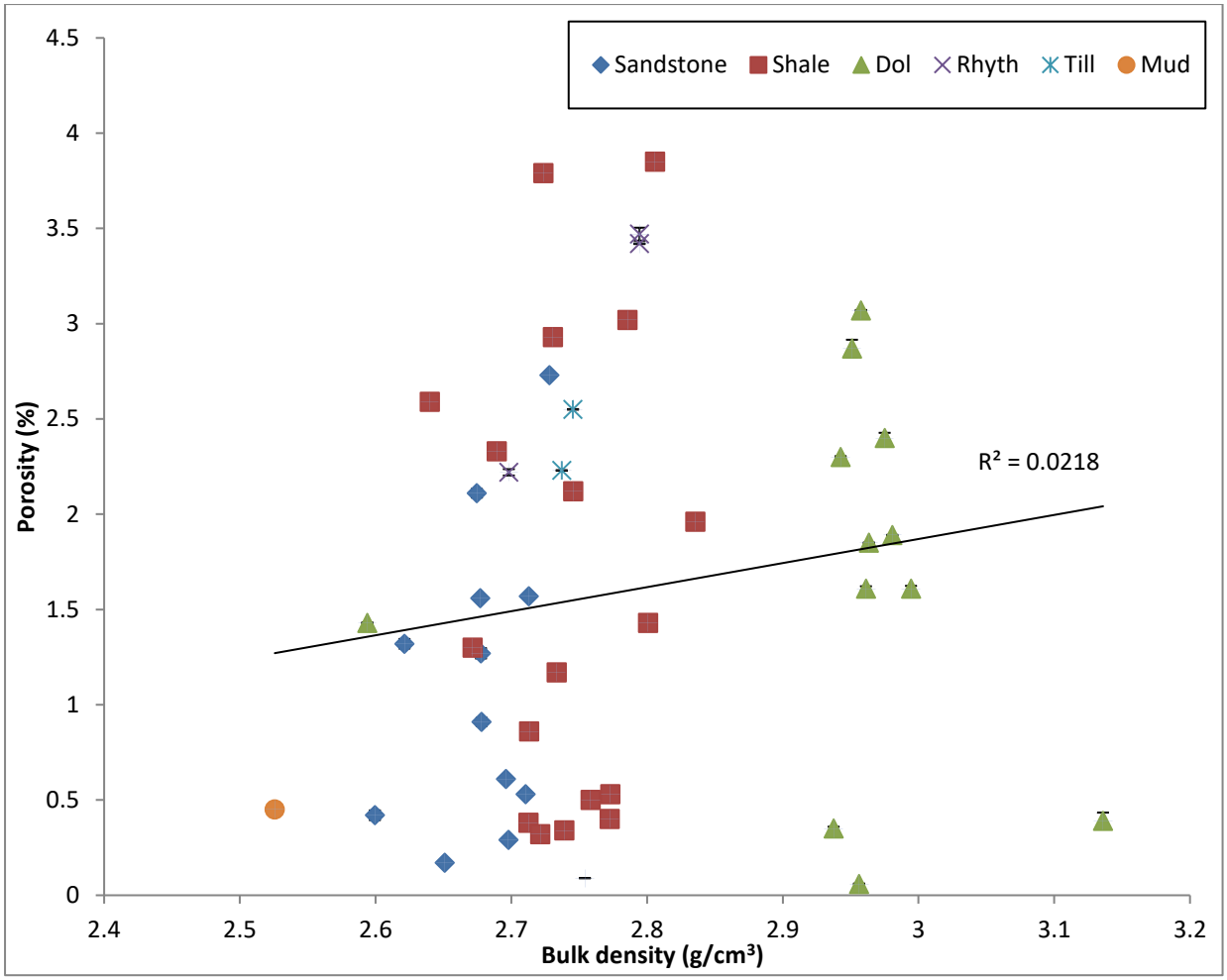

Figure 6.62: The correlation between the density of the samples and the porosity of the samples.

6.5. Fracture analysis

The results obtained from the micro-fracture analysis of the samples are presented in this section. Pseudo three-dimensional (3D) images of the samples and slices through the front and side of the samples are provided. The purpose of these analyses is to investigate the presence and orientations of non-visible fractures in the samples, as well as to investigate the presence of dense minerals in the samples.

6.5.1. Micro x-ray tomography

This method is discussed in Chapter 5.5.2. Figures 6.63 to 6.84 show the results that were obtained from the micro x-ray tomography technique. The images on the left are 3D images of the sample, where low to high density regions per sample are luminance-mapped from white to black. The images on the right represent slices through the samples, after fracture analysis. Any micro-cracks in the samples are indicated in these slices. It is important to note that the samples that were scanned with x-rays are only small portions of the original samples and are possibly incomplete representations of the lithologies. These results should only be

used to explain anomalous seismic velocities and/or bulk densities, and anisotropic seismic velocities.

The 3D image of sample W2 (Figure 6.63) indicates density variations orientated diagonally across the sample. This mudstone sample has micro-fractures most of which are parallel to the long axis of the sample. The long axis of the sample is also the principal seismic wave propagation direction during our measurements. This sample has anomalously low seismic velocities (Vp = 961 m/s and Vs = 696 m/s) (Table 6.1 and Table 6.2) and a typical bulk density of 2.53 g/cm^3. The micro-fractures in the sample do not appear to affect its bulk density or porosity. Since the seismic velocities of this sample have large uncertainties, the effect of the micro-fractures on the seismic velocity of the sample cannot be determined.

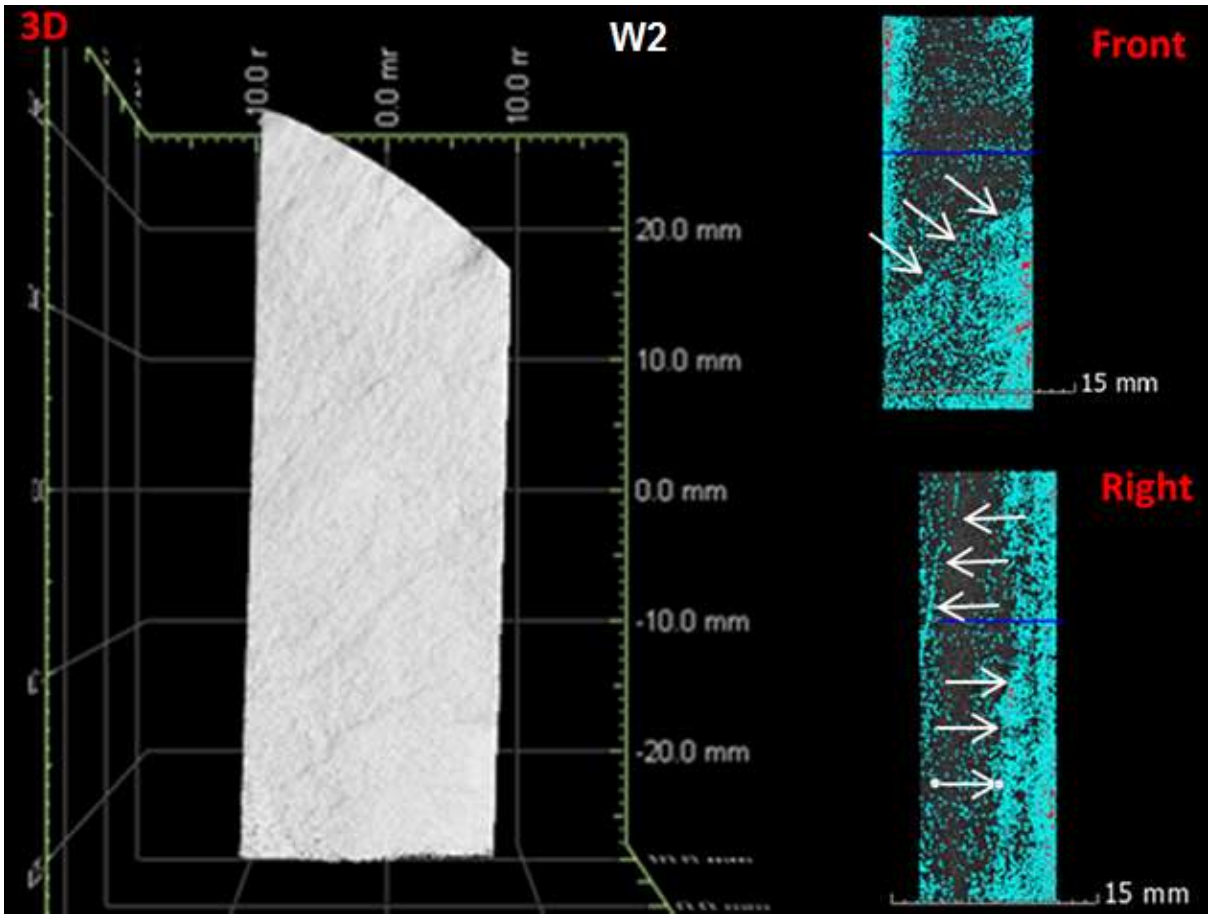

Figure 6.63: The x-ray tomography results for the mudstone sample (Sample W2). A 3D image of the sample, as well as slices through the front and right of the sample is depicted in the image. In the 3D image, lighter and darker shades of grey represent relatively more and less dense sections of the sample. In the slices, bright colours represent low local density spots that are typical of pore spaces and fractures.

The fine-grained, well-bedded nature of the sandstone samples is evident from the x-ray tomography results (Figures 6.64 to 6.67). Only sample W18 has weak to no bedding. Sample W21 has possible micro-fractures running along a bedding plane, perpendicular to the long axis of the sample. The seismic velocity for sample W21 (Vp = 5462 m/s, Vs = 2867 m/s) is higher than the average seismic velocity of our sandstone samples (Vp = 4904 m/s, Vs = 2623

m/s) (Table 6.1and Table 6.2). The bulk density of sample W21 (2.71 g/cm^3) is unlikely to be affected by the presence of micro-fractures, since it is similar to the average bulk density of sandstone samples (2.68 g/cm^3) from borehole KWV) (Table 6.4). Alternatively, all samples from borehole KWV may have fractures, but the fractures are not visible and the samples were not analysed.

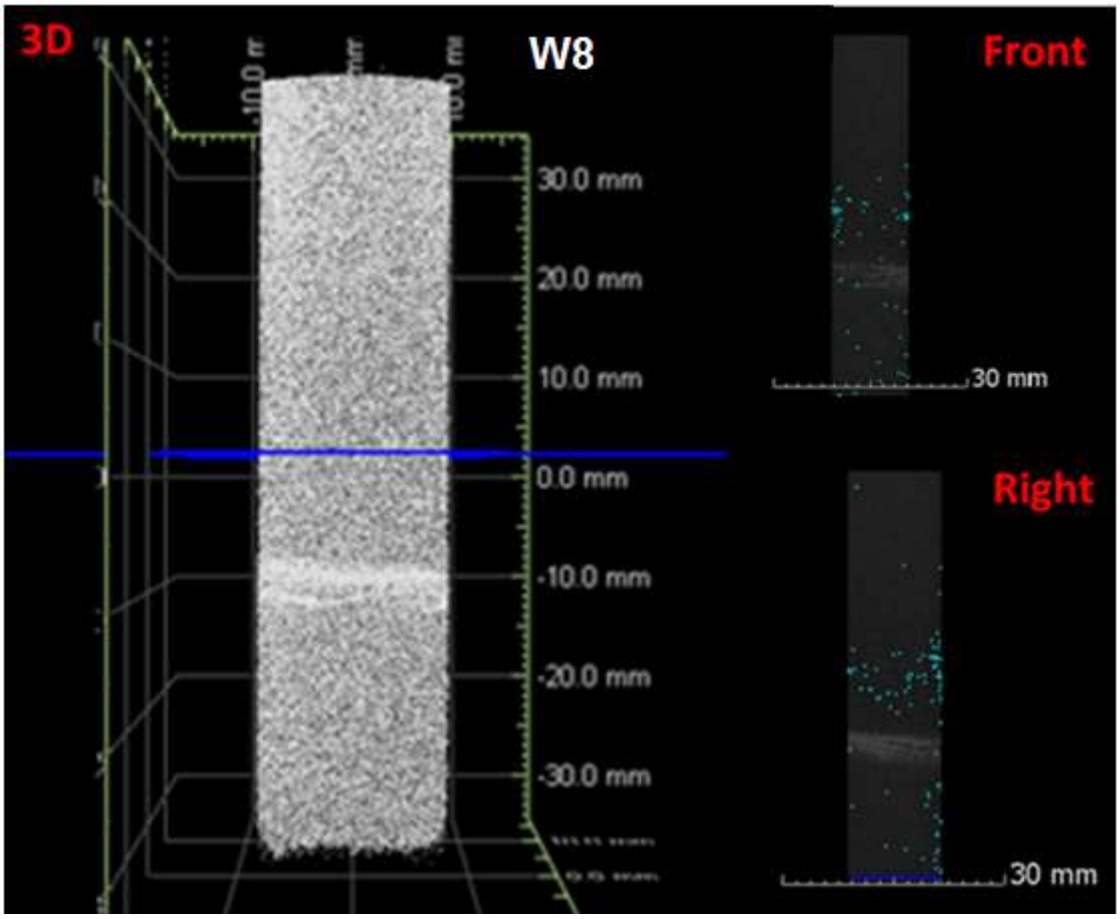

Figure 6.64: The x-ray tomography results for a sandstone sample (sample W8). The dark blue planes are location references for the slices.

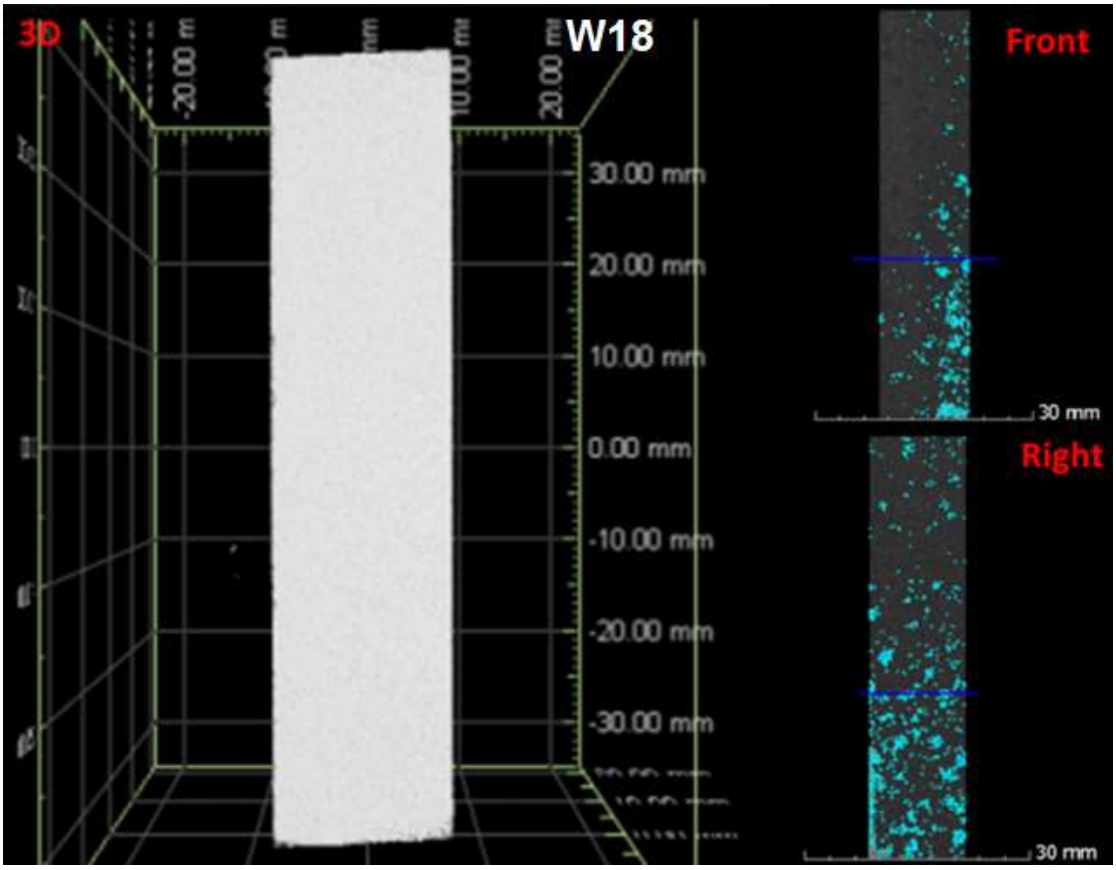

Figure 6.65: The x-ray tomography results for a sandstone sample (sample W18).

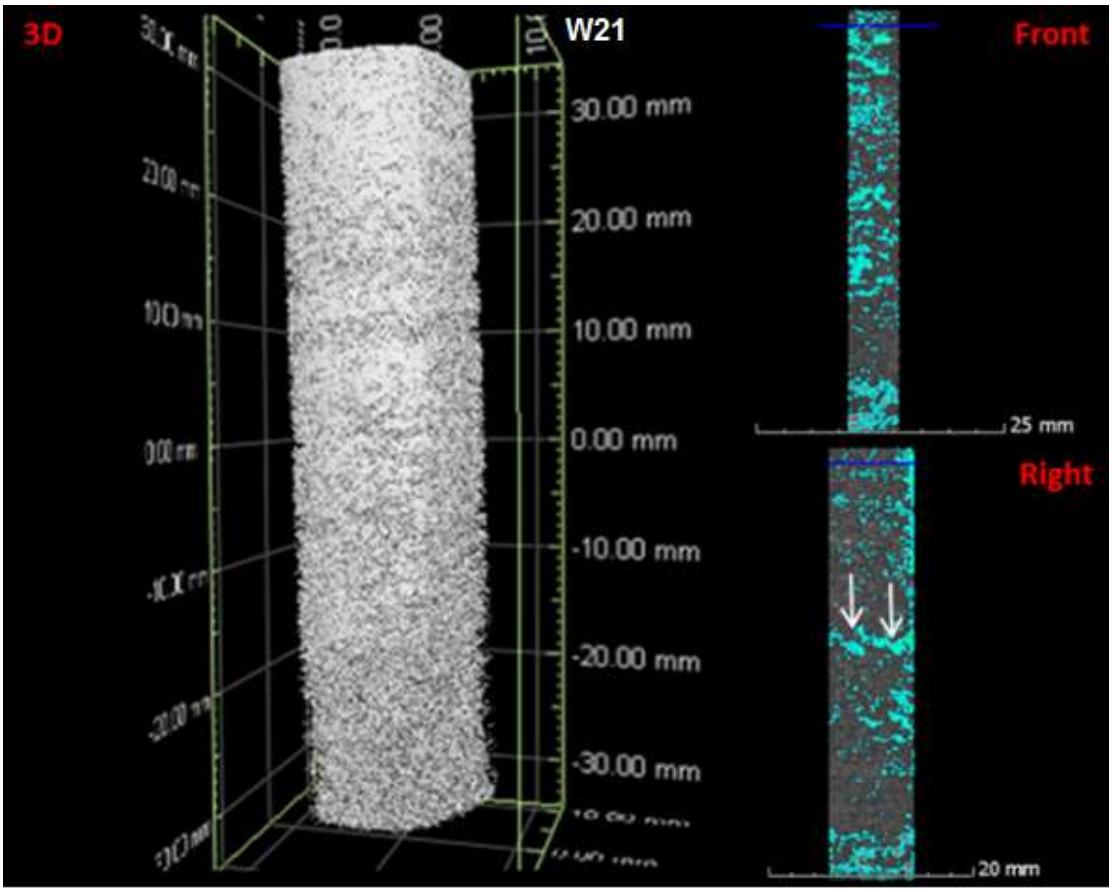

Figure 6.66: The x-ray tomography results for a sandstone sample (sample W21).

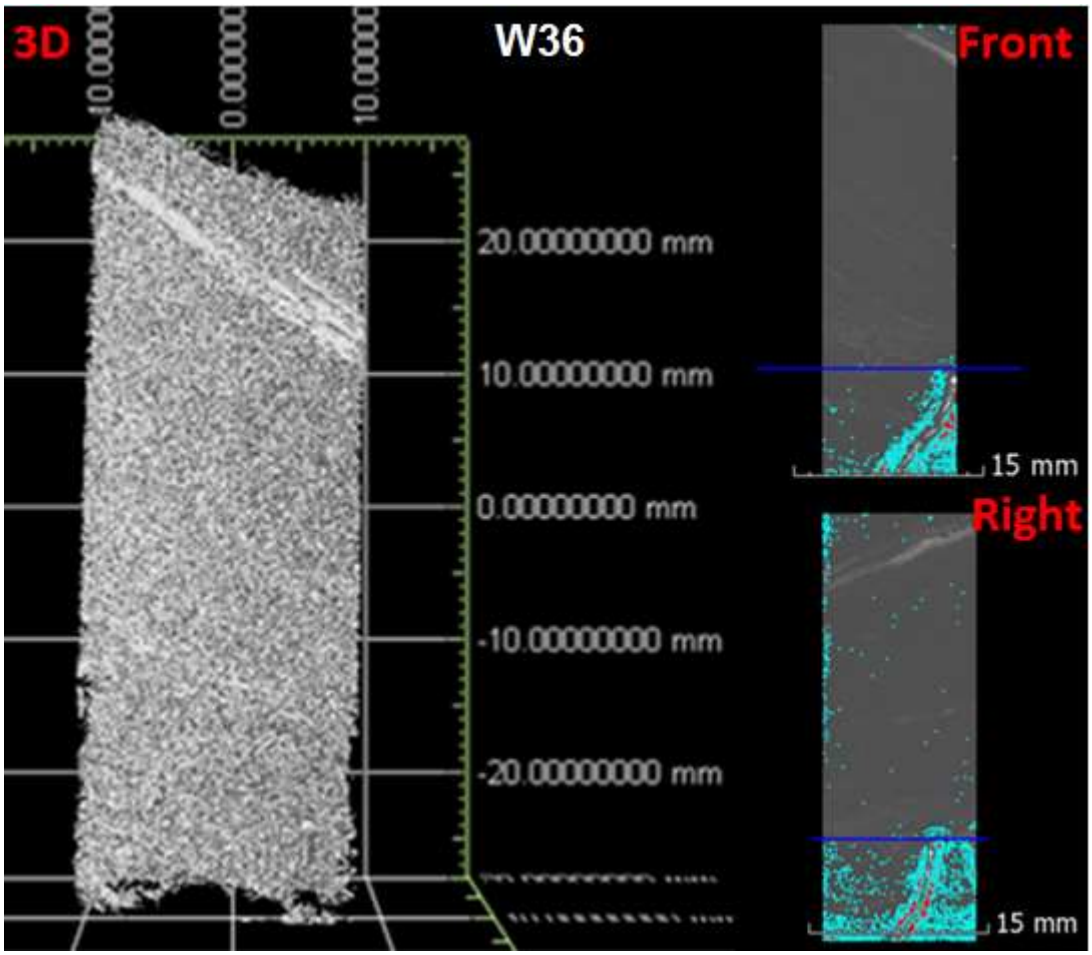

Figure 6.67: The x-ray tomography results for a sandstone sample (sample W36).

The x-ray tomography results for the dolerite samples did not yield useful information (Figure 6.68 to Figure 6.72). The samples were too dense to examine their porosities, hence micro-fractures were not identified in the samples. These samples are thus assumed to be internally homogeneous. A dense mineral vein can be seen running through sample W33. Based on our hand desription of this sample, the vein is most likely pyrite (Chapter 6.1.). The seismic velocity of sample W33 (Vp = 6033 m/s, Vs = 3160 m/s) is the highest of our dolerite samples (Table 6.1and Table 6.2). The presence of the pyrite vein may contribute to the high seismic velocity. The bulk density of this sample (2.96 g/cm^3) is not significantly different than that of the other dolerite samples (the average bulk density of all dolerite samples from borehole KWV is 2.95 g/cm^3) (Table 6.4) .

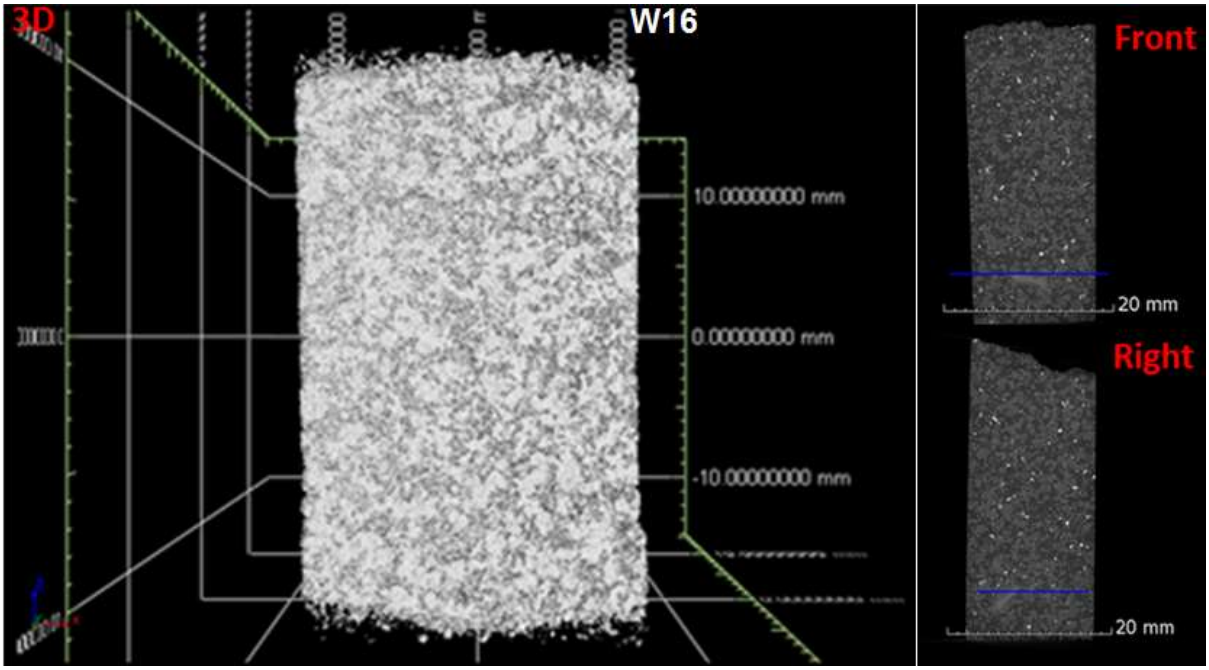

Figure 6.68: The x-ray tomography results for a dolerite sample (sample W16).

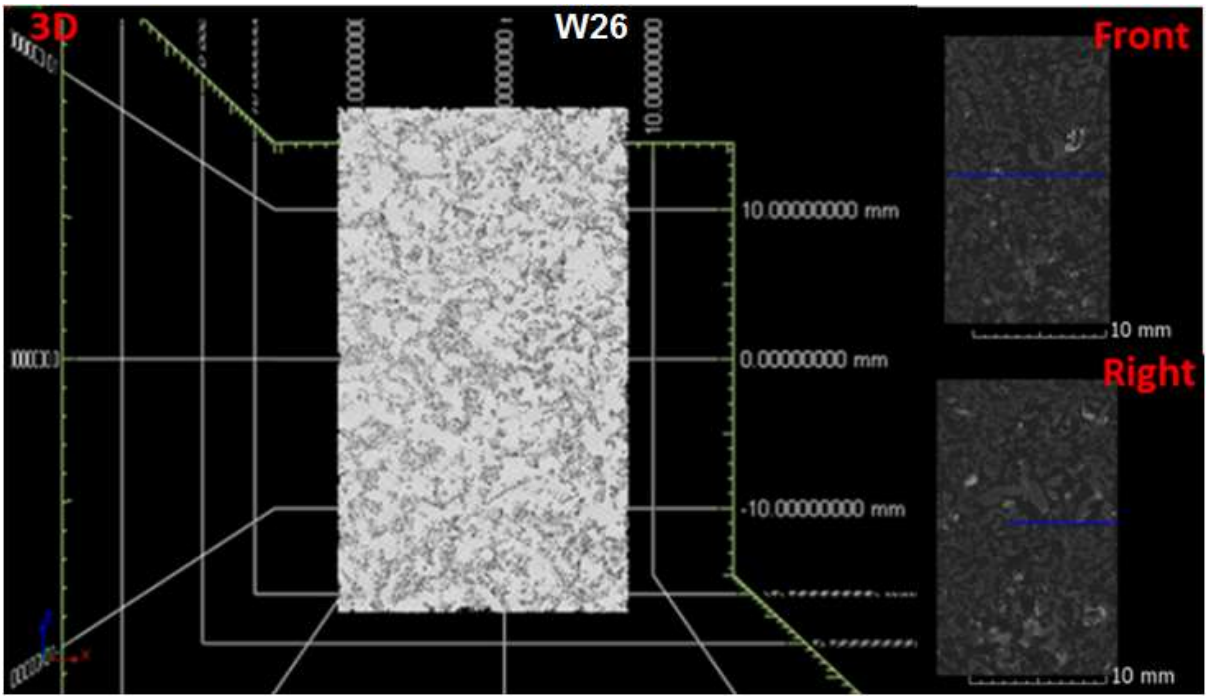

Figure 6.69: The x-ray tomography results for a dolerite sample (sample W26).

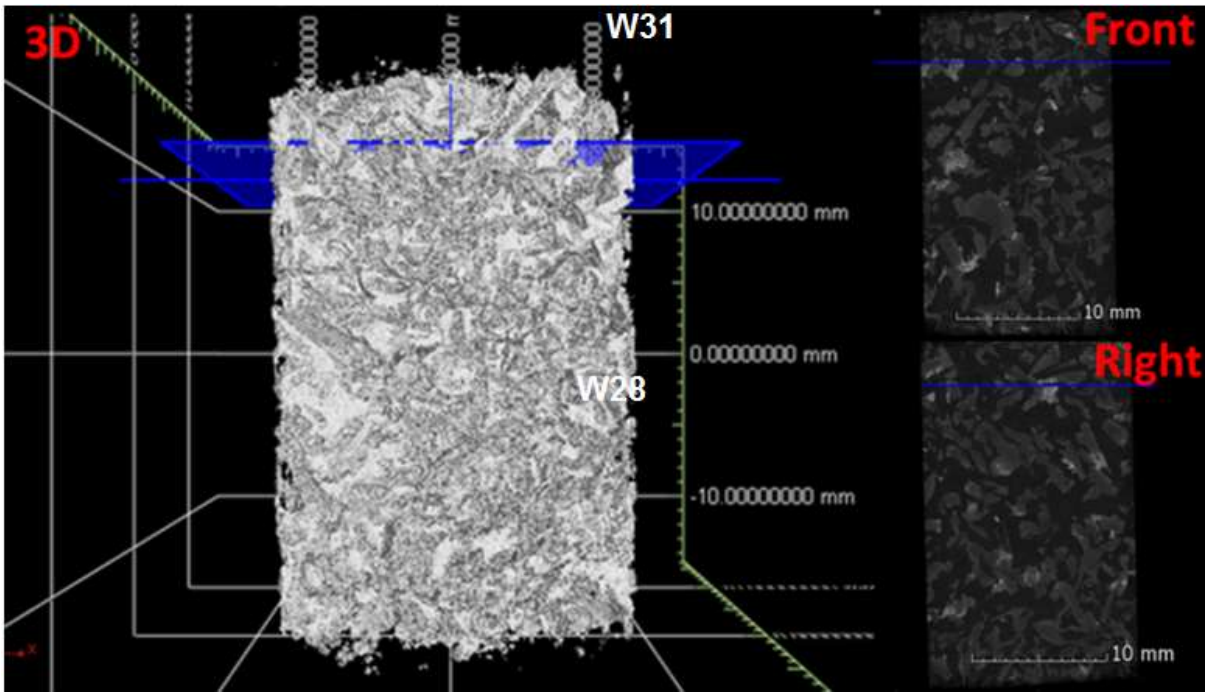

Figure 6.70: The x-ray tomography results for a dolerite sample (sample W31).

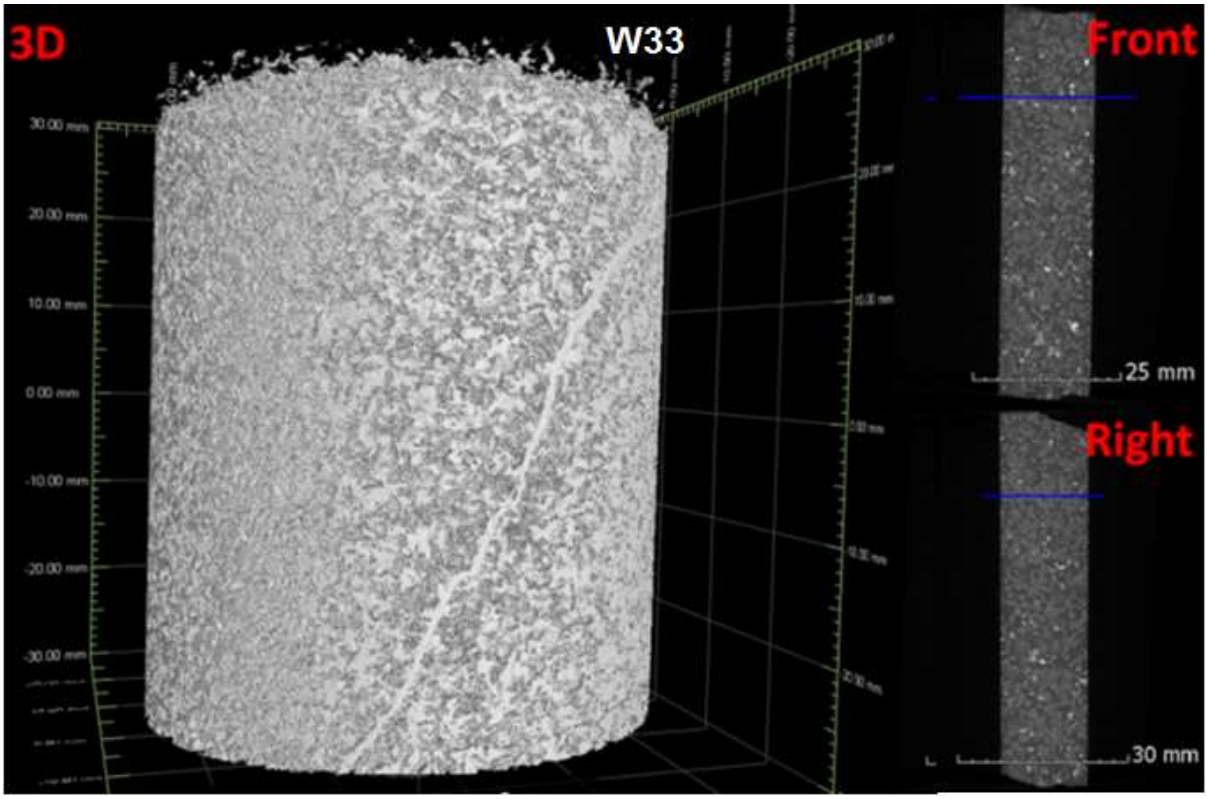

Figure 6.71: The x-ray tomography results for a dolerite sample (sample W33).

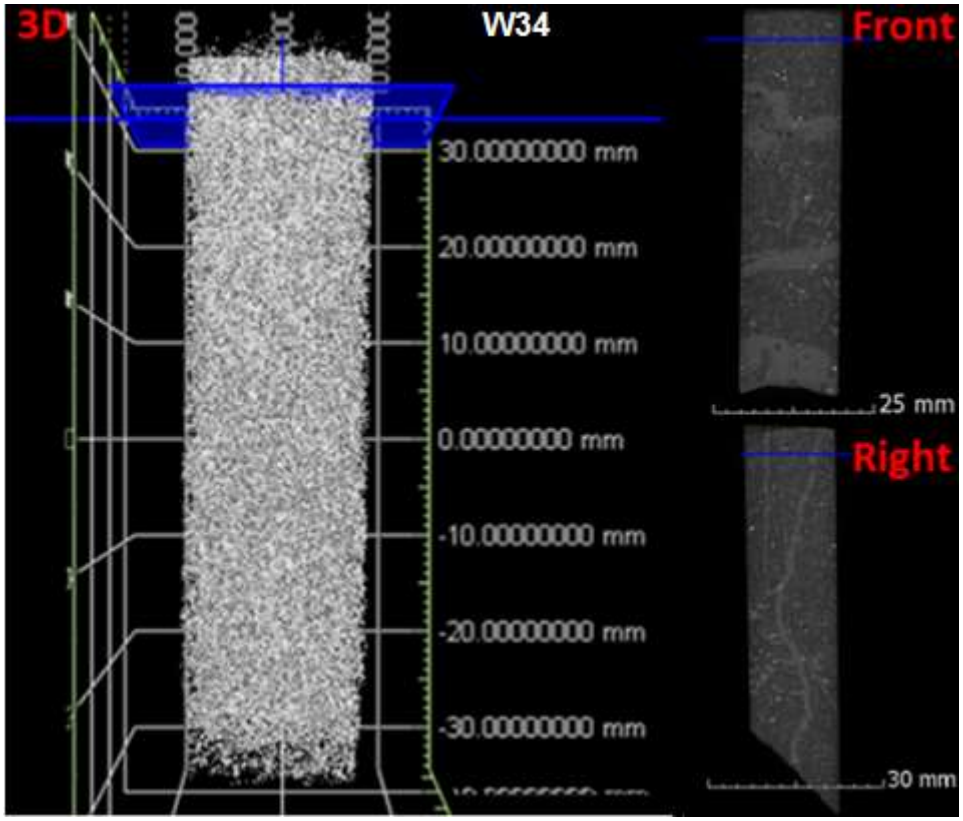

Figure 6.72: The x-ray tomography results for a dolerite sample (sample W34).

One of the two shale samples that were analysed with x-ray tomography had micro-fractures lines (Figure 6.73 and Figure 6.74). Sample W17 had micro-fracture lines oriented perpendicular to the long axis of the sample. The seismic velocity of this sample was anomalously low and probably incorrect, hence the effect of the micro-fractures on the seismic velocity of the sample cannot be determined. The presence of micro-fractures does not seem to significantly affect the bulk density of the sample (2.72 g/cm^3), since it is similar to the average bulk density of shale samples from borehole KWV (2.74 g/cm^3) (Table 6.4).

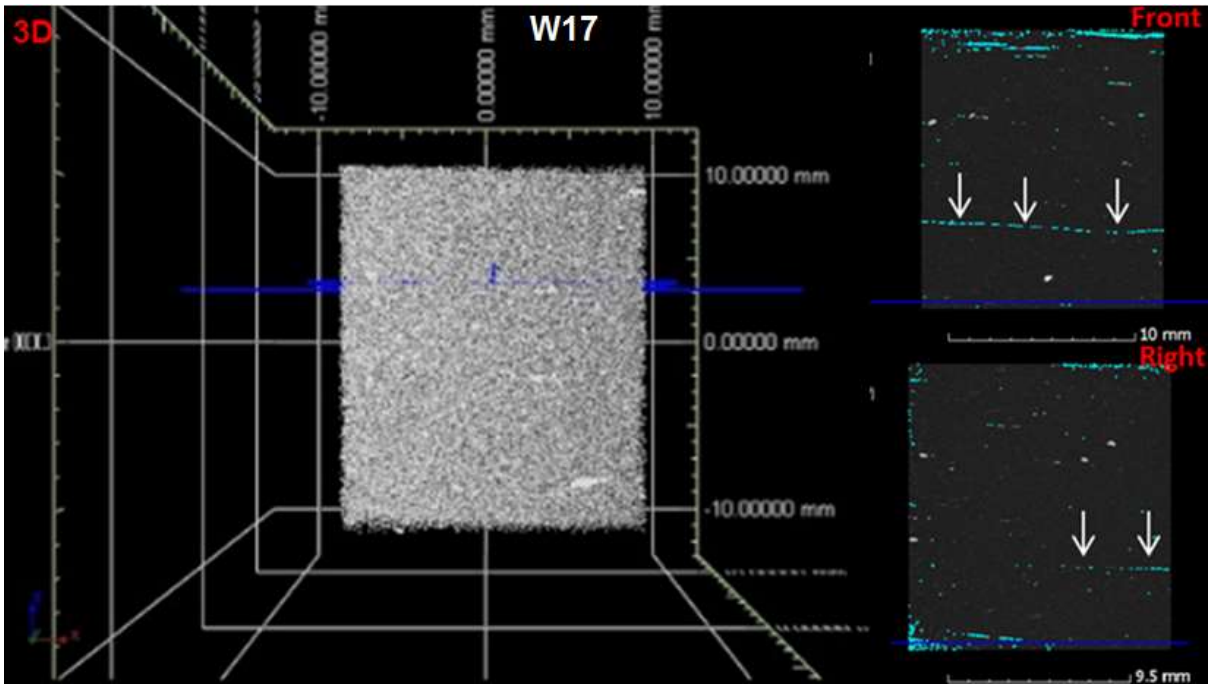

Figure 6.73: The x-ray tomography results for a shale sample (W17).

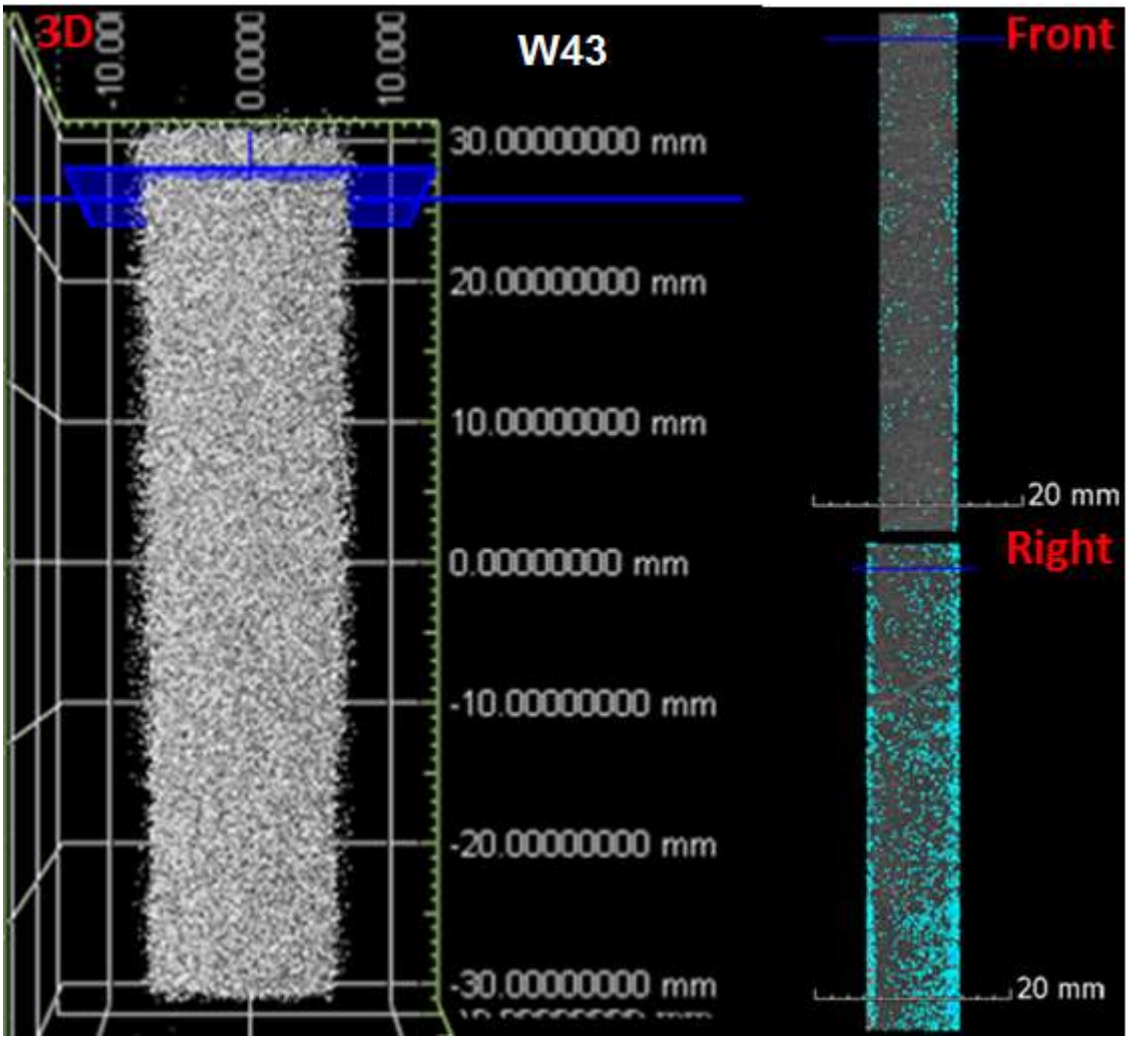

Figure 6.74: The x-ray tomography results for a shale sample (W43).

The x-ray tomography results for the carbonaceous shale samples are shown in Figures 6.75 to 6.81. Samples W9 and W28 do not feature obvious micro-fractures. W28 does, however, have small-scale fractures present at the edges of the sample, perpendicular to the long axis of the sample. The seismic velocity of sample W28 (Vp = 3806 m/s, Vs = 1905 m/s) is comparable to the average seismic velocity of shale samples in borehole KWV (Vp = 3859 m/s, Vs = 2116 m/s) (Table 6.1and Table 6.2), and the bulk density (2.77 g/cm^3) is similar to the average bulk density of shale samples (2.74 g/cm^3) from borehole KWV (Table 6.4). Thus, the presence of micro-fractures in sample W28 does not appear to affect the seismic velocity or the bulk density of the sample.

The effect of the long axis-parallel micro-fracture lines on the seismic velocity of sample W19 cannot be confidently determined due to high uncertainty associated with the measurements of the velocities. It seems that the bulk density (2.75 g/cm^3) of sample W19 is not affected by the presence of the micro-fractures, since it closely resembles the average bulk density (2.74 g/cm^3) of shale samples from borehole KWV.

Both samples W24 and W42 have micro-fractures present, perpendicular to the long axes of the samples. Although samples W24 and W42 have seismic velocities that considerably differ from each other (Vp = 2000 m/s and Vs = 1169 m/s for sample W24; Vp = 4712 m/s and Vs = 2696 m/s for sample W42) as well as from the average seismic velocity for shales from borehole KWV (Vp = 3859 m/s and Vs = 2116 m/s) (Table 6.1and Table 6.2), the seismic velocities of the samples is probably affected more by the presence of dense minerals in sample W42 than by micro-fractures. The presence of dense minerals, possibly pyrite, can be seen in the 3D image of sample W42, disseminated as well as concentrated in a vein. The bulk densities of the samples W24 (2.81 g/cm^3) and W42 (2.77 g/cm^3), do not seem to be significantly affected by the presence of the micro-fractures, since both are close to the average bulk density of shale samples from borehole KWV (Table 6.4).

Samples W39 and W40 are also characterised by micro-fractures lines cutting diagonally through the long axes of the samples. As with the other carbonaceous shale samples, these micro-fractures do not seem to affect the seismic velocities and bulk densities of the samples. The 3D images of both samples indicate the presence of dense mineral inclusions, possibly pyrite, which could increase their seismic velocities to higher than the average seismic velocity of shale samples from borehole KWV.

There is no correlation observed between micro-fractures, seismic velocities and bulk densities of the shale samples. There also seems to be no correlation between the orientation of micro-fractures and seismic velocities in the shale samples.

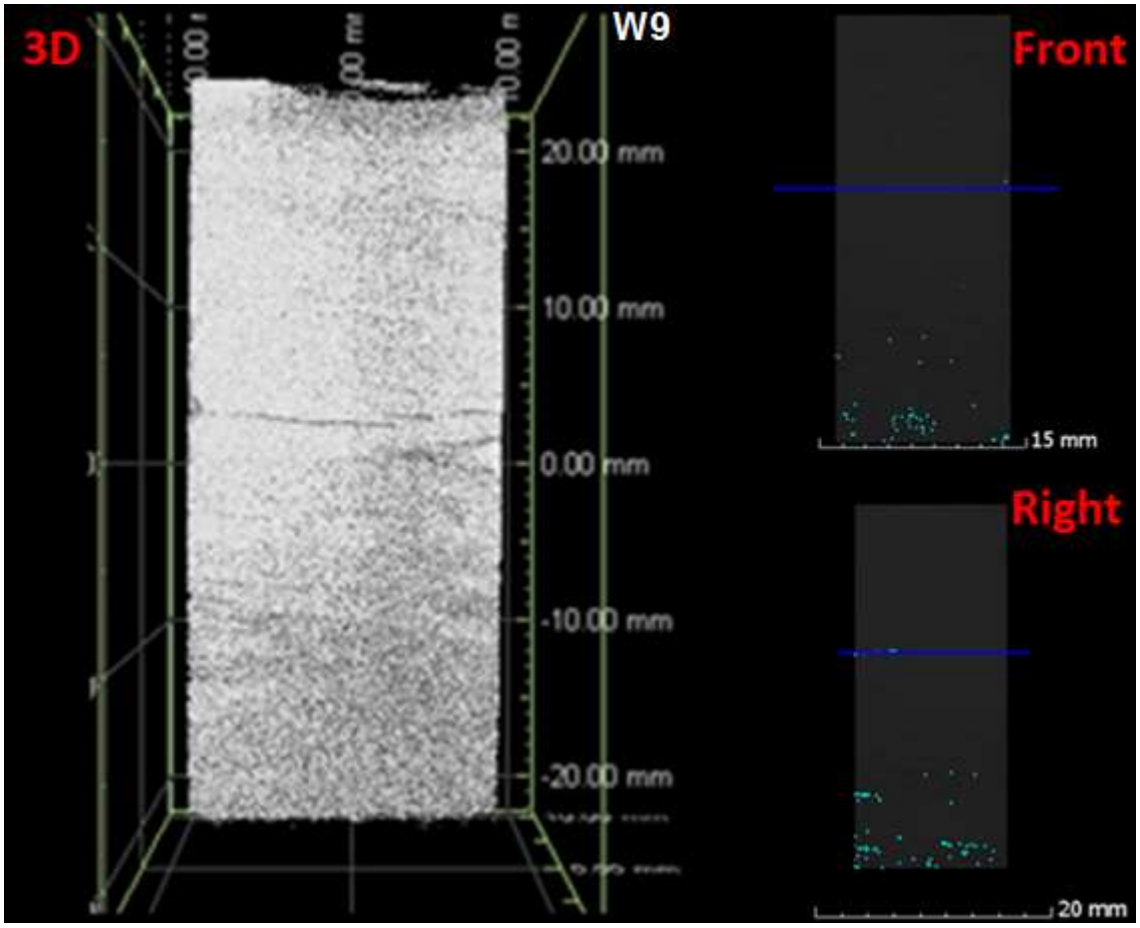

Figure 6.75: The x-ray tomography results for a carbonaceous shale sample (W9).

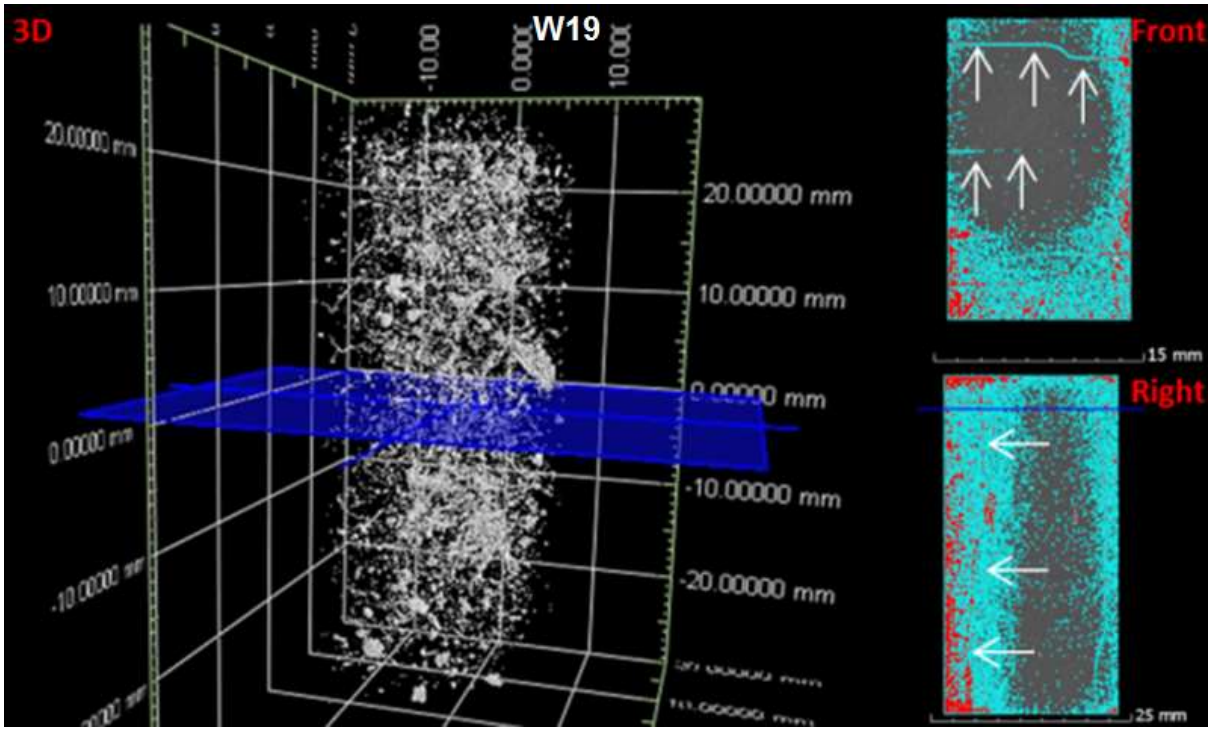

Figure 6.76: The x-ray tomography results for a carbonaceous shale sample (W19).

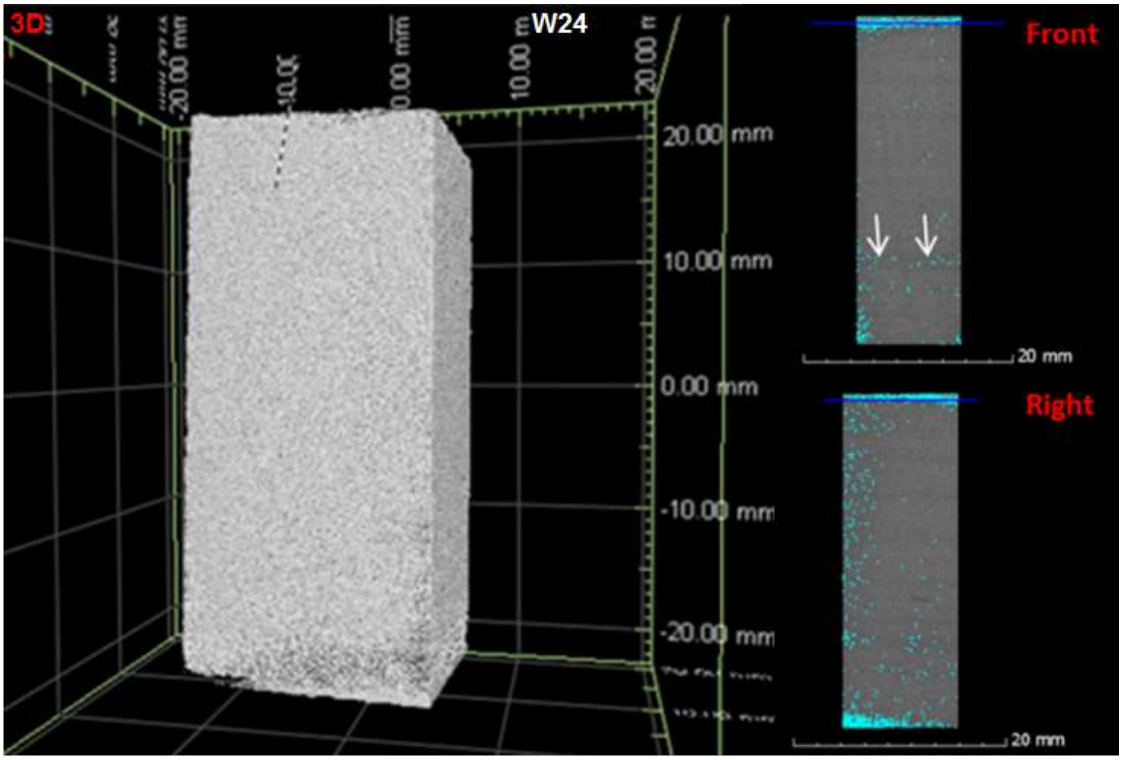

Figure 6.77: The x-ray tomography results for a carbonaceous shale sample (W24).

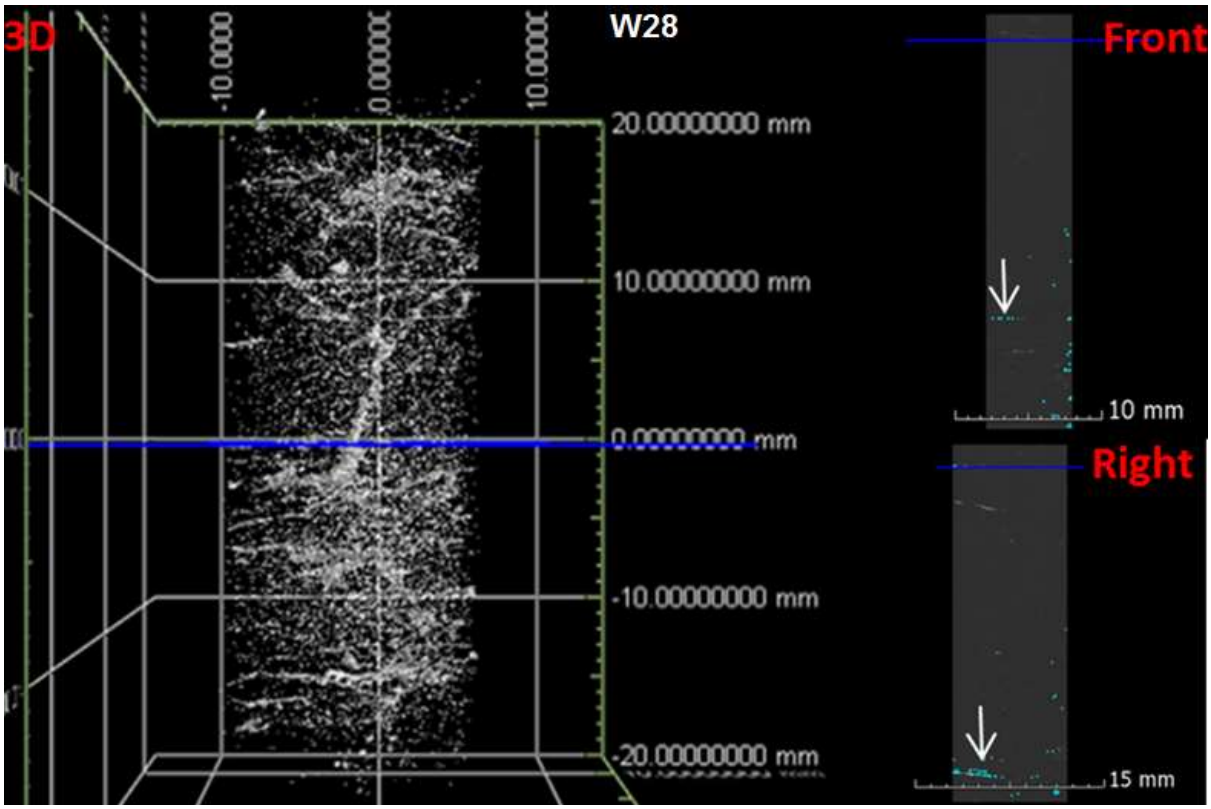

Figure 6.78: The x-ray tomography results for a carbonaceous shale sample (W28).

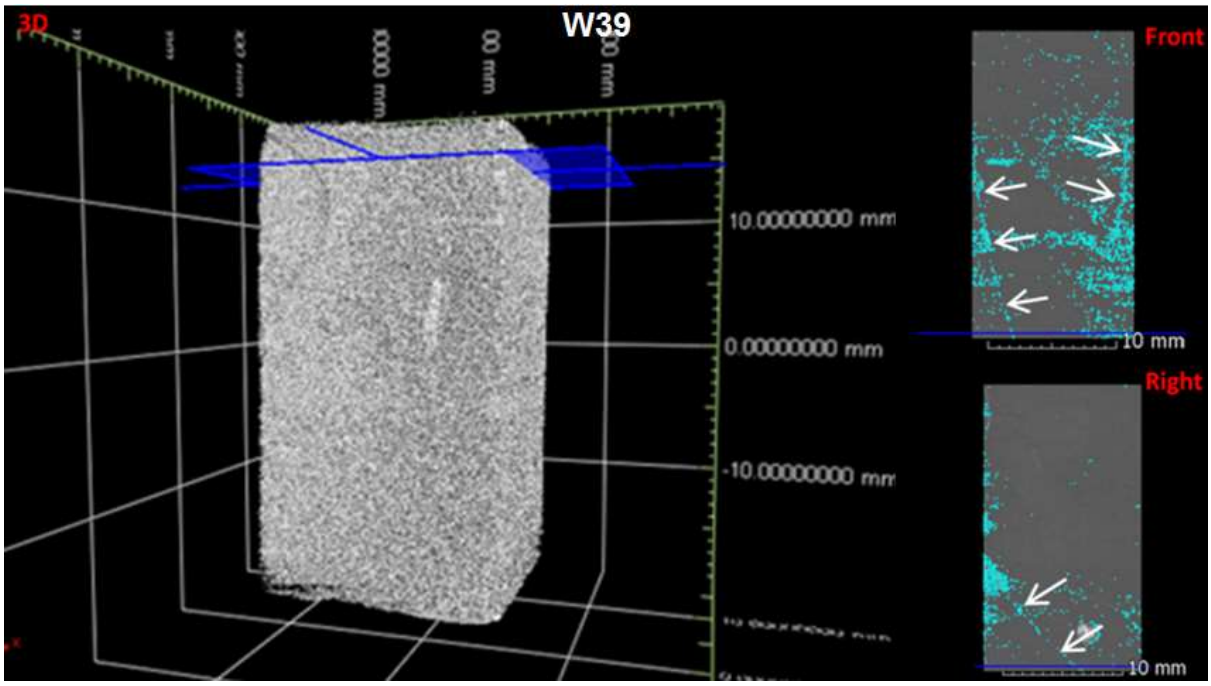

Figure 6.79: The x-ray tomography results for a carbonaceous shale sample (W39).

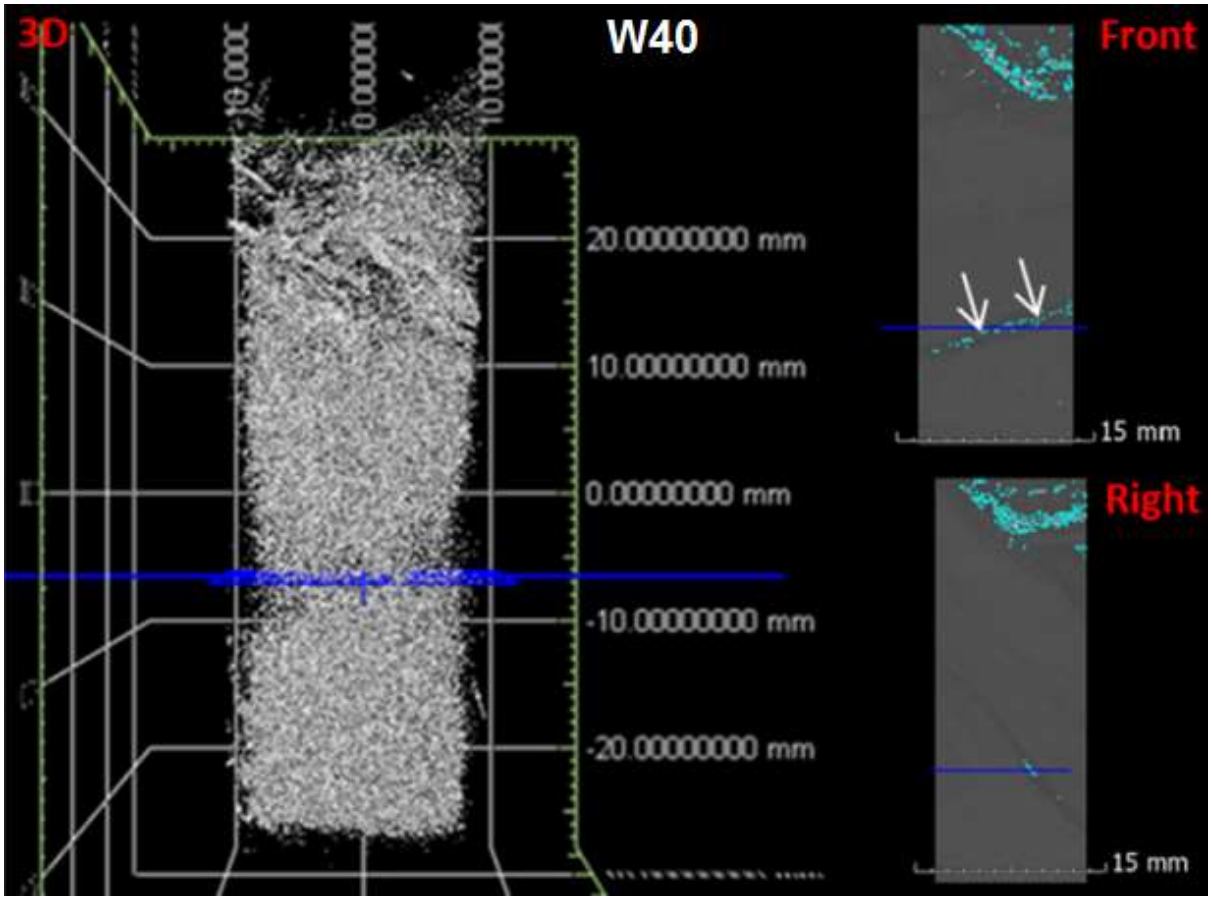

Figure 6.80: The x-ray tomography results for a carbonaceous shale sample (W40).

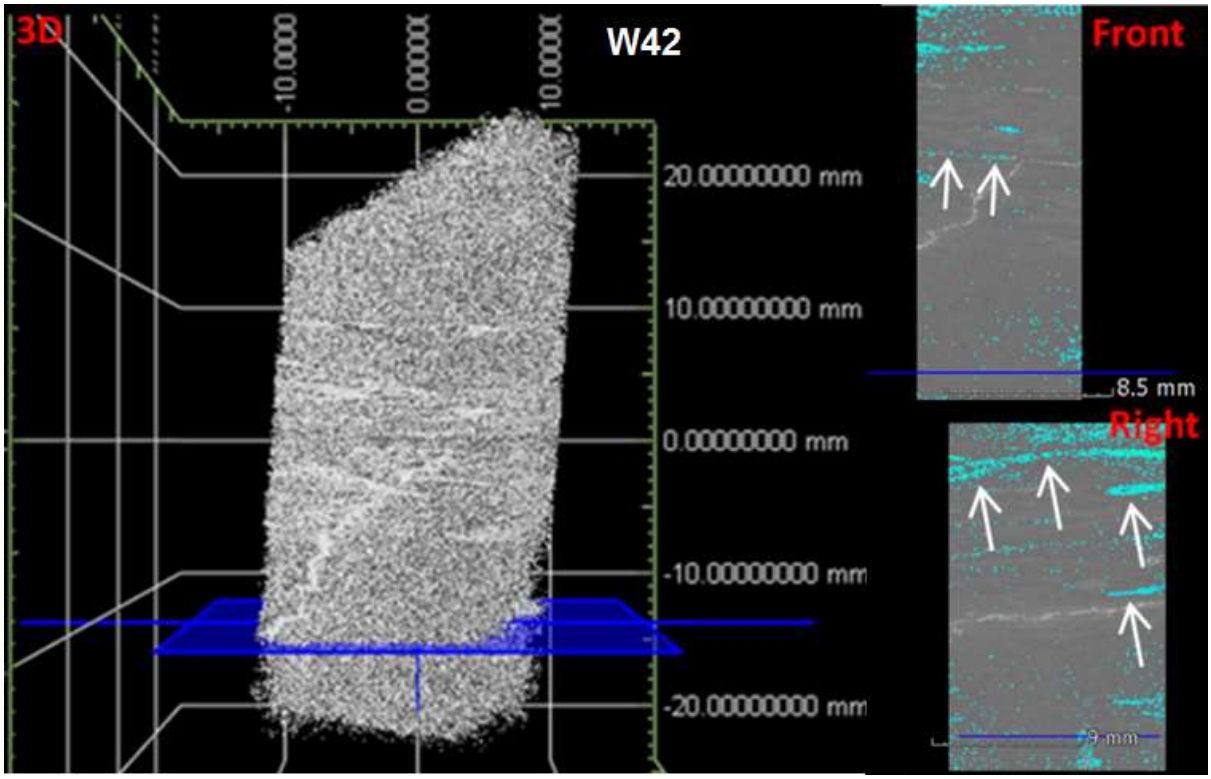

Figure 6.81: The x-ray tomography results for a carbonaceous shale sample (W42).

The x-ray tomography results for the rhythmite samples show that all three analysed samples exhibit micro-fractures (Figure 6.82, Figure 6.83 and Figure 6.84). In all three cases the micro-fractures lines were perpendicular to the long axes of the samples. The bulk densities of the rhythmite samples do not seem te have been affected by the presence of micro-fractures, since all three values are similar (Table 6.4).

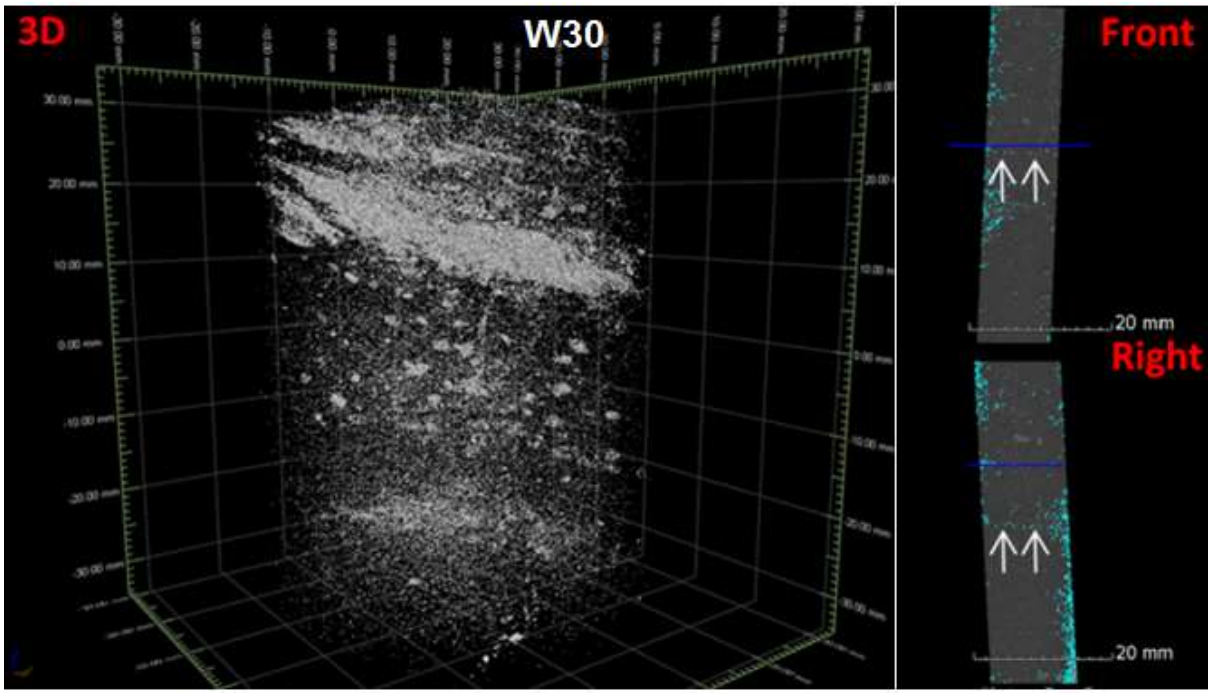

Figure 6.82: The x-ray tomography results for a rhythmite sample (W30).

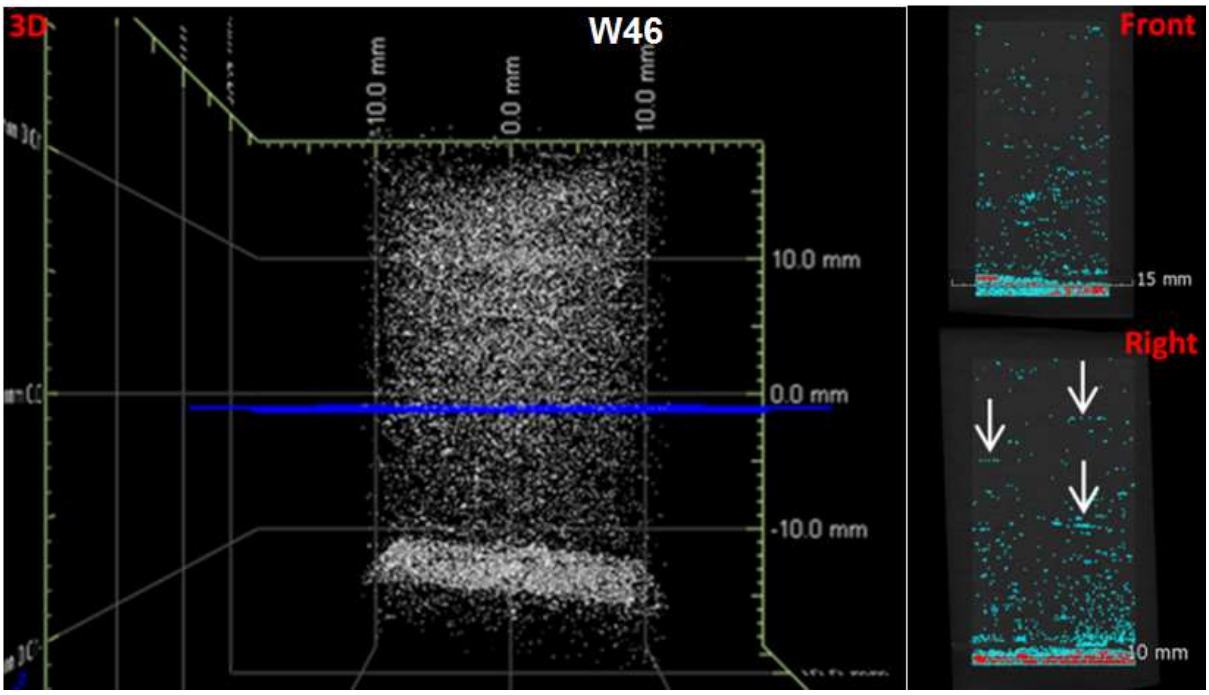

Figure 6.83: The x-ray tomography results for a rhythmite sample (46).

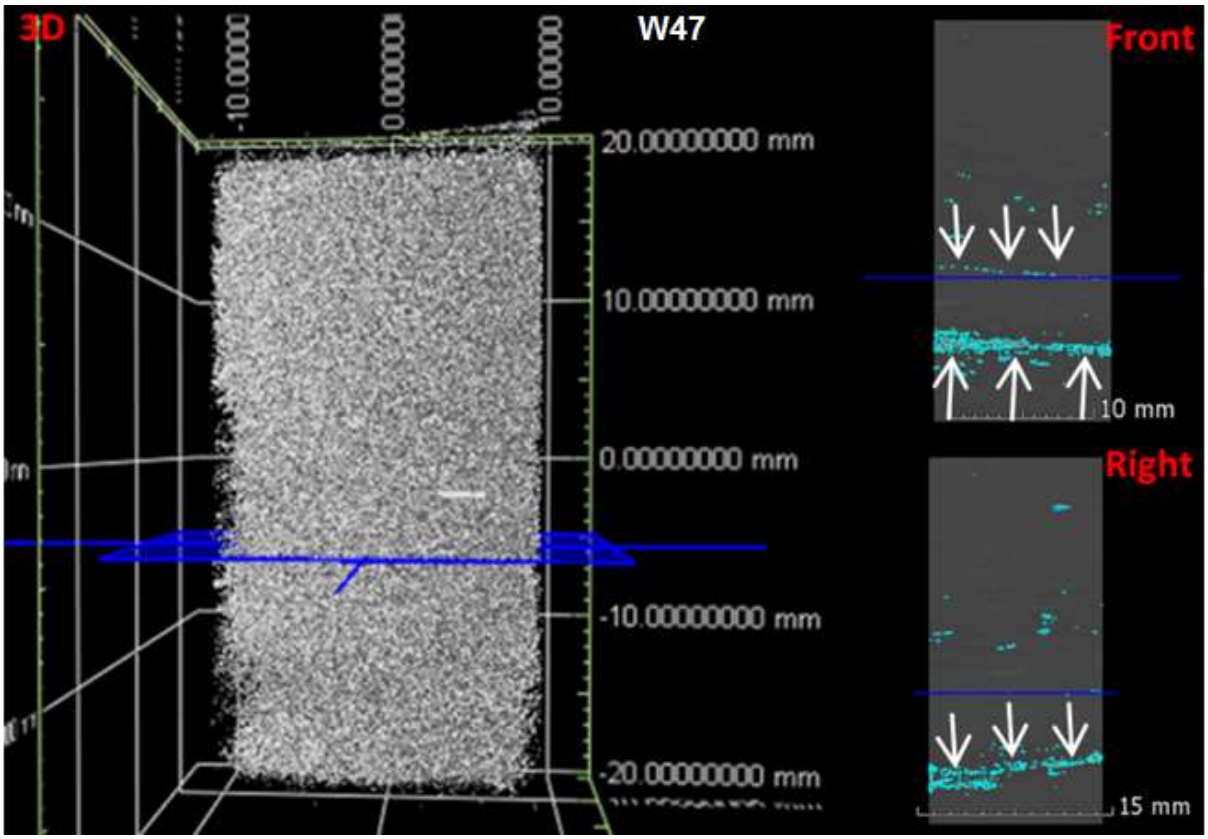

Figure 6.84: The x-ray tomography results for a rhythmite sample (47).

6.6. Petrography

The results of the petrographic analyses of the samples are provided in this section. Images from the microscopic analyses of the samples are presented.

The mudstone sample (sample W2) (Figure 6.85) consists of a clay matrix with few grains in between. These grains are quartz with interstitial micas. The micas are biotite, muscovite and chlorite. Trace amounts of pyrite are present. No foliations or mineral orientations were observed. Minerals appear to be distributed homogeneously.

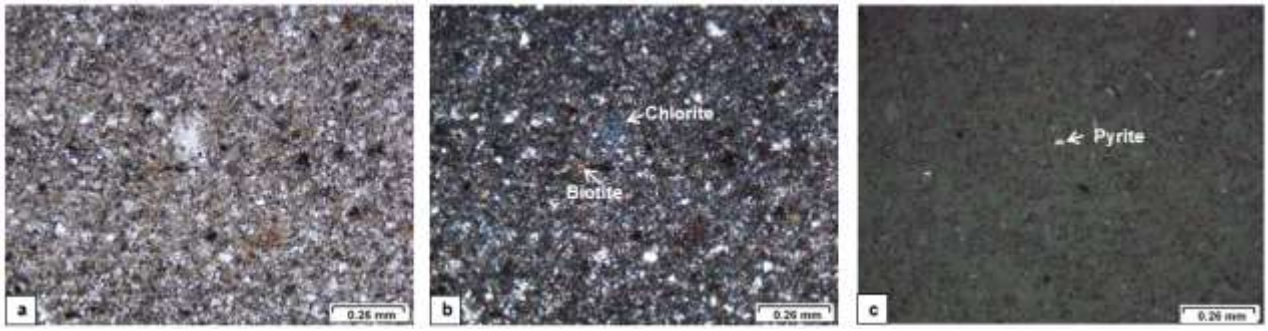

Figure 6.85: Thin section results for the mudstone sample (sample W2). a) is the microscopic image under plane polarized light (PPL), b) is the same image under cross polarized light (XPL) and c) is the sample under reflected light.

The sandstone sample (sample W8) (Figure 6.86) consists mainly of quartz grains of various shapes and sizes. Plagioclase, muscovite, biotite and chlorite are all present. The minerals in this sample are clearly shape oriented, with the foliation plane perpendicular to the long axis of the sample.

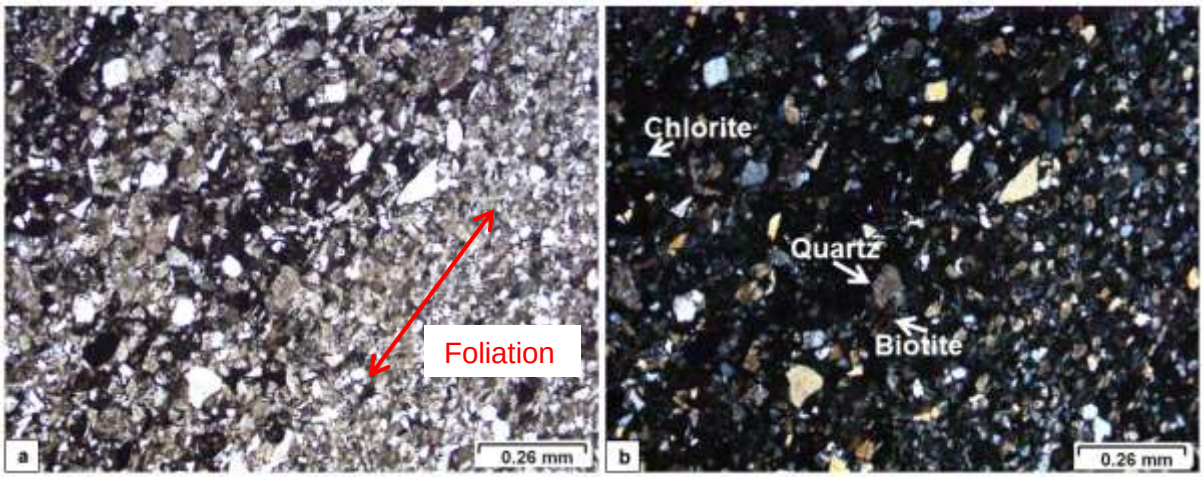

Figure 6.86: Thin section results for the sandstone sample (sample W8).

The shale sample (sample W17) (Figure 6.87) is very fine-grained and no minerals were identified from a petrographic analysis. Most of the sample is a very fine clay-dominated

matrix. An air-filled fracture was observed running through the sample. The fracture is in the same plane as the mineral foliation, which runs perpendicular to the long axis of the sample.

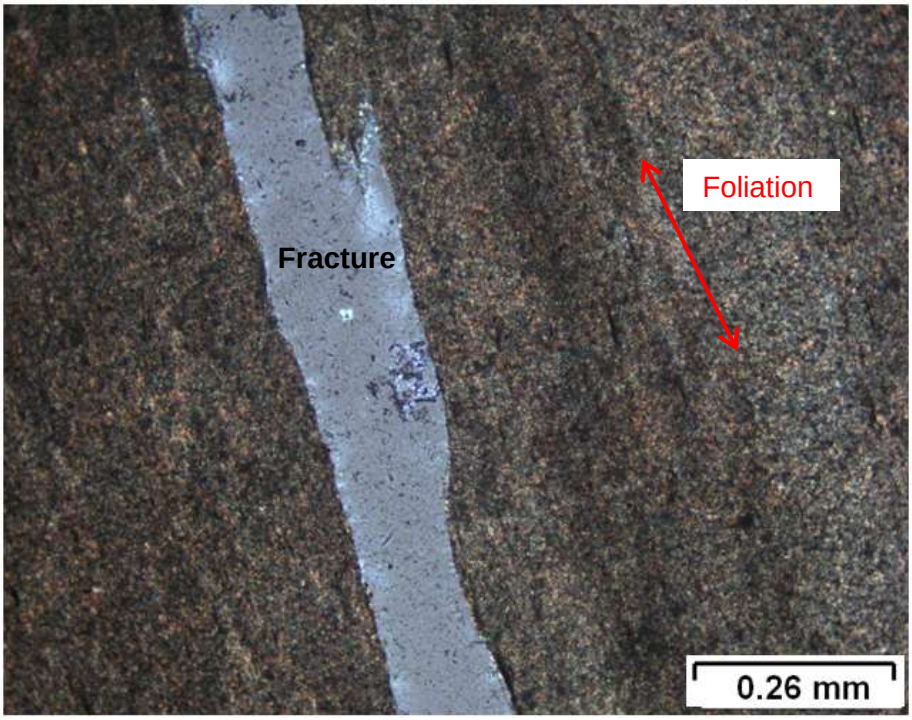

Figure 6.87: Thin section results for the shale sample (sample W17) under cross polarized light (XPL).

The shale sample (sample W18) (Figure 6.88) consists of very fine and densely packed mineral grains. These minerals are quartz, plagioclase, biotite, muscovite and chlorite. The grains appear to be homogeneously distributed and oriented.

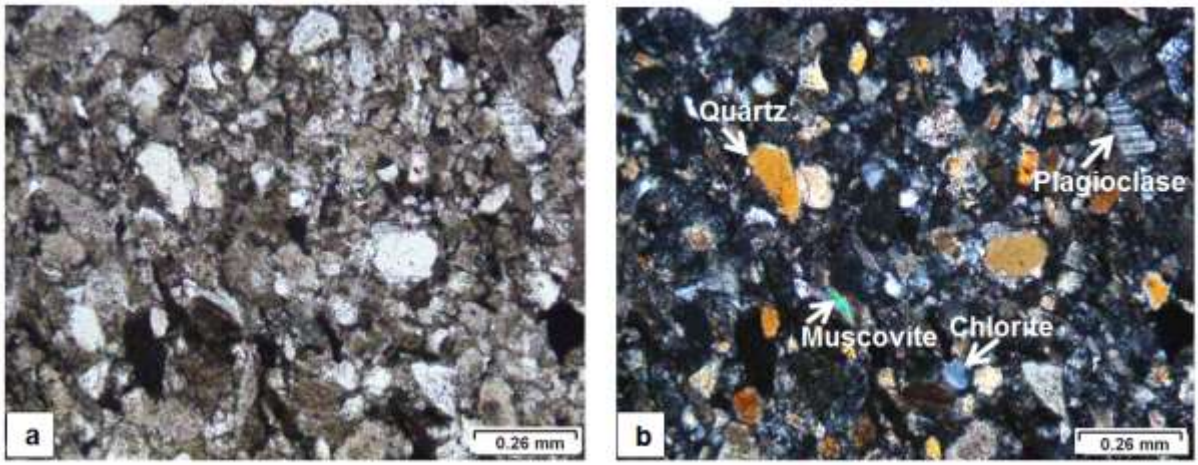

Figure 6.88: Thin section results for the sandstone sample (sample W18).

The sandstone sample (sample W21) (Figure 6.89) consists of a feldspar-dominated matrix. The turbidity texture of the matrix and the sericite concentrated in veins suggest that this sandstone is a feldspathic wacke. The elongation directions of quartz, chlorite and muscovite grains are aligned perpendicular to the long axis of the sample.

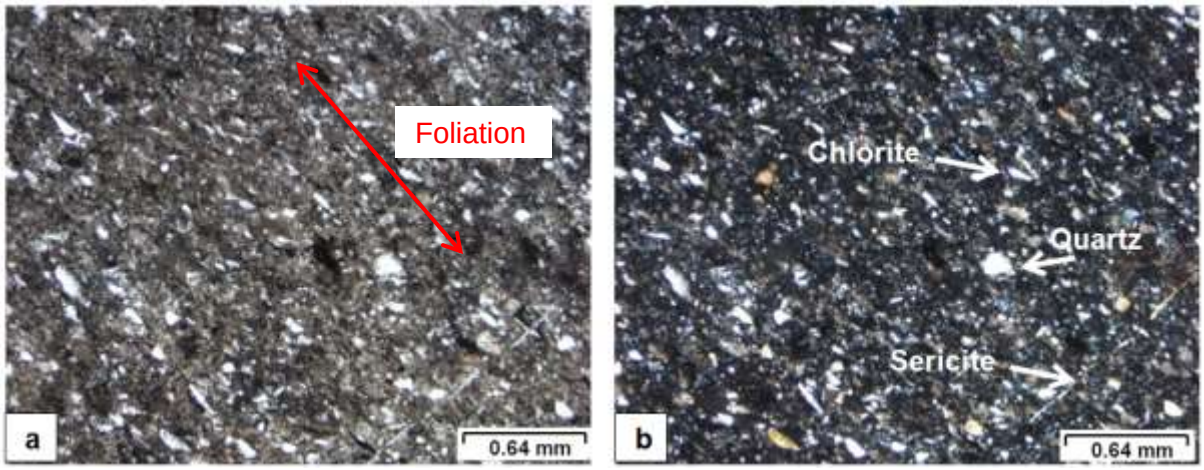

Figure 6.89: Thin section results for the sandstone sample (sample W21).

The carbonaceous shale sample (sample W24) (Figure 6.90) consists of a clay matrix that is too fine to identify individual minerals. Fractures are running parallel to the foliation plane in this sample. The foliation plane is perpendicular to the long axis of the sample.

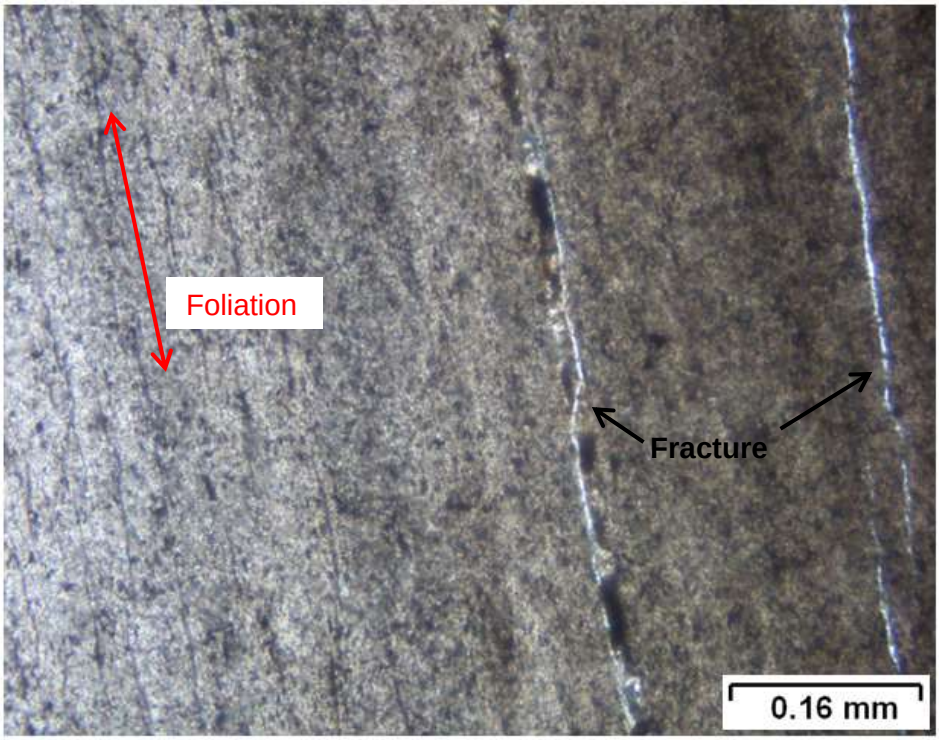

Figure 6.90: Thin section results for the carbonaceous shale sample (sample W24) under cross polarized light (XPL).

The shale sample (sample W25) (Figure 6.91) consists of a turbuditic matrix of sericite, indicating that it is feldspar-dominated. It is characterised by some quartz and chlorite grains. The dark spots in the thin section are clay. The minerals in the sample appear to be homogeneously distributed and oriented.

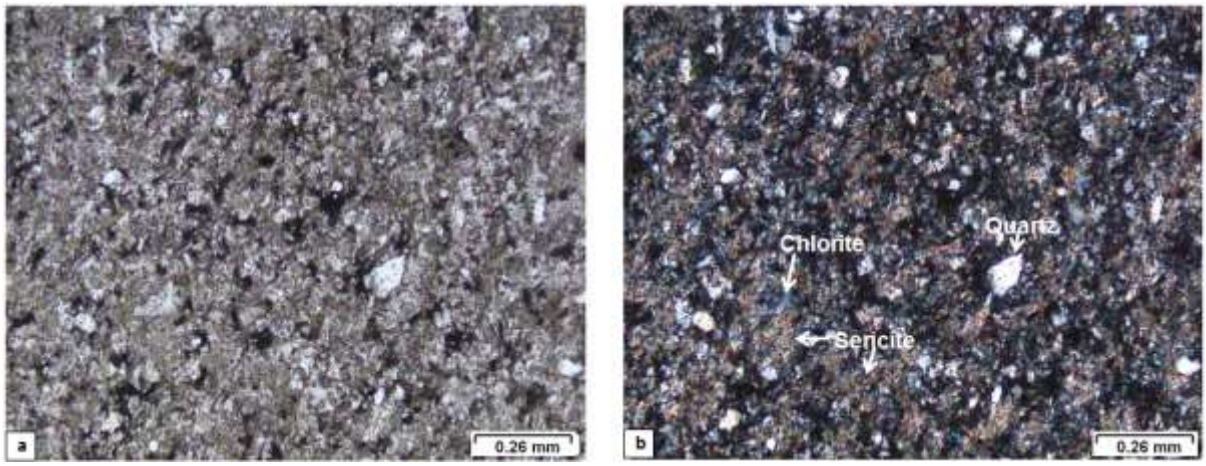

Figure 6.91: Thin section results for the shale sample (sample W25).

The rhythmite sample (sample W30) (Figure 6.92) consists of fine grained minerals in a turbudite matrix. Some of the visible minerals are recrystallized quartz, chlorite and fibrous muscovite. The minerals seem to be homogeneously oriented. The brown spots in the thin section are feldspars that have been altered to clay.

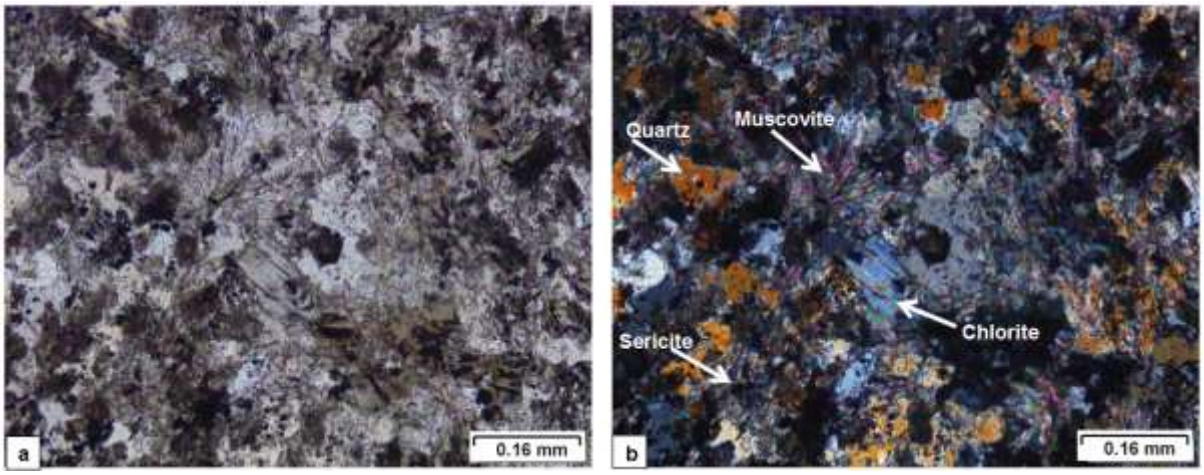

Figure 6.92: Thin section results for the rhythmite sample (sample W30).

The dolerite sample (sample W33) (Figure 6.93) is characterized by an ophitic texture, and consists of plagioclase and clino-pyroxene. The clino-pyroxene has been altered to clay. A carbonate vein is observed in the sample. The minerals in the sample appear homogeneously distributed and oriented.

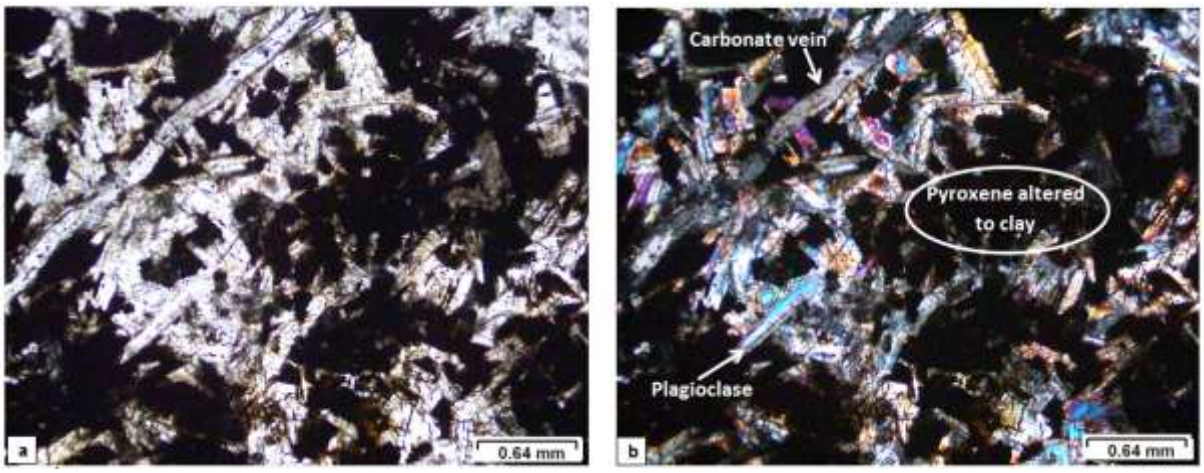

Figure 6.93: Thin section results for the dolerite sample (sample W33).

Quartz and pyrite are the only minerals that were identified in the thin section of the sandstone sample W36 (Figure 6.94). Other than quartz veins, no foliation or mineral alignments could be observed.

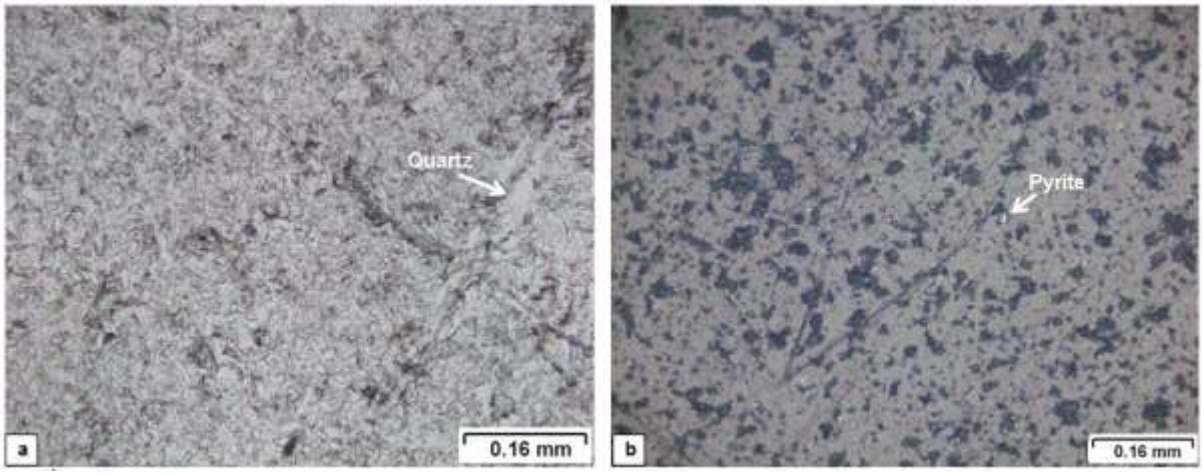

Figure 6.94: Thin section results for the sandstone sample (sample W36).

The carbonaceous shale sample (sample W40) (Figure 6.95) is very fine grained. Bright spots are visible, which are probably quartz or lithic fragments. A network of fine veins is present. The veins consist of calcite encased by sericite. The sample appears to have a foliation plane that is sub-perpendicular to the long axis of the sample.

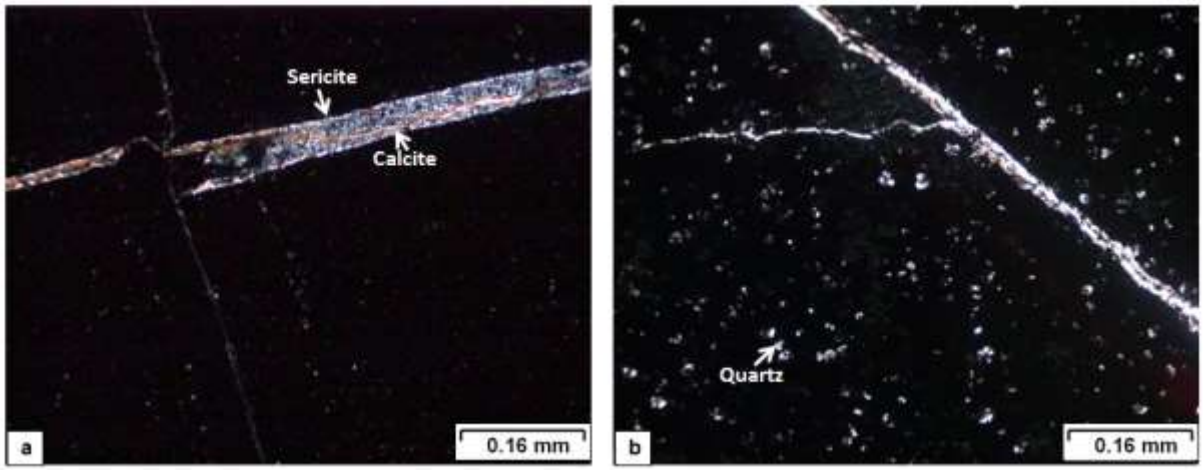

Figure 6.95: Thin section results for the carbonaceous shale sample (sample W40).

The carbonaceous shale sample (sample W41) (Figure 6.96) consists of a very fine clay matrix. No minerals were identified in thin section, however, a pyrite vein is observed. The pyrite is secondary to the mud matrix. Some degree of bedding/foliation is visible, perpendicular to the long axis of the sample.



Figure 6.96: Thin section results for the carbonaceous shale sample (sample W41).

The carbonaceous shale sample (sample W42) (Figure 6.97) is characterized by a well-defined bedding, with the foliation plane perpendicular to the long axis of the sample. Pyrite zig-zags through the sample, sometimes perpendicular to the foliation. Elongated muscovite grains are observed parallel to the foliation.



Figure 6.97: Thin section results for the carbonaceous shale sample (sample W42).

6.7. Seismic anisotropy

The seismic anisotropy results are provided in this section. The P- and S-waves velocities of six samples were measured in two orthogonal directions.

Table 6.6 shows that the S-wave velocities of the samples have significantly larger anisotropy than their P-wave velocities. This observation is unreliable due to ambiguities in the pickings of the S-wave arrivals. Thus the seismic anisotropy of the samples were analysed by considering mainly the P-wave velocities.

The shale sample (sample W19) displays two very different P-wave velocities in two orthogonal planes (Table 6.6). For example, the Vp of the shale sample in the Y-direction (along the long axis) is anomalously lower (1056 m/s) compared to the Vp along the X-direction (5730 m/s). This could be due to fractures in the sample or inaccurate picking of the arrival times (See Chapter 6.2.1.). The seismic anisotropy for this shale sample can therefore not be interpreted with confidence.

The dolerite sample (sample W33) is essentially isotropic (0.8%) This is corroborated by the homogeneity of the sample by physical appearance and through thin section analyses.

The sandstone sample (sample W21) is more anisotropic (5.9%), with the higher P-wave velocity (5827 m/s) in the X-direction (perpendicular to the long axis)). The fast P-wave along the X-direction of the sandstone sample coincides with the micro-fracture lines and the foliation direction in the sample, i.e., the fracture lines and foliation direction are parallel to the direction of the fast P-wave velocity (Table 6.7). Thus, the cause of the higher P-wave velocity may be due to a combination of the oriented micro-fractures and the preferred mineral orientations in the sample.

Both carbonaceous shale samples (samples W40 and W42) show some degree of seismic velocity anisotropy. The fast P-wave for both samples is along the X-direction. However, sample W42 has a higher anisotropy value (11.4%) than sample W40, which has an anisotropy of 5.8%. Table 6.7 illustrates that the highest P-wave velocity, the micro-fractures and the mineral SPO direction of sample W42 are all co-planar. The direction of higher P-wave velocity of sample W40 does not lie in the same plane as the micro-fractures and mineral SPO directions. This may have reduced the seismic anisotropy of sample W42 compared to sample W40. Furthermore, the co-planar nature of observed features in sample W42 suggests that neither micro-fractures nor the mineral SPO orientation are contributing factors for the P-wave seismic anisotropies of the carbonaceous shale samples.

The rhythmite sample (sample W46) also demonstrated some seismic velocity anisotropy (7.5%). As with the other samples, the direction of the fast P-wave of the rhythmite sample is along the X-direction. This direction corresponds with the micro-fracture lines of the sample. Since no data on the mineral orientation of the sample are available, the seismic anisotropy of the sample may be attributed to the micro-fractures in the sample, and possibly the mineral SPOs.

Table 6.6: Seismic velocity results in two orthogonal directions, X and Y. The bulk anisotropy of the samples is also provided. The signals for sample W19 was too low to pick the arrival time of the S-wave.

Sample name	**P-wave (m/s)**			**S-wave (m/s)**		
	Y-direction	**X-direction**	**Anisotropy (%)**	**Y-direction**	**X-direction**	**Anisotropy (%)**
W19 Shale	1056 +/- 114	5730 +/- 60	138 +/- 11	-	-	-
W21 Sandstone	5491 +/- 304	5827 +/- 31	6 +/- 7	3344 +/- 44	2921 +/- 19	14 +/- 2
W33 Dolerite	6557 +/- 41	6500 +/- 86	1 +/- 2	4520 +/- 39	3403 +/- 52	28 +/- 2
W40 Carbonaceous shale	4907 +/- 36	5200 +/- 659	6 +-/ 16	3180 +/- 15	2644 +/- 170	18 +/- 8
W42 Carbonaceous shale	4984 +/- 24	5588 +/- 135	11 +/-3	3659 +/- 26	3261 +/- 50	12 +/- 2
W46 Rhythmite	2755 +/- 336	5957 +/- 102	8 +/- 14	1696 +/- 137	3431 +/- 73	68 +/- 9

Table 6.7: A comparison between the seismic anisotropy, micro-fracture orientation and mineral orientation of samples from borehole KWV.

Sample name	Lithology	Greatest velocity direction	Fracture lines	SPO
W19	Carbonaceous shale	↔	↕	No data
W21	Sandstone	↔	↔	↔
W33	Dolerite	None	None	None
W40	Carbonaceous shale	↔	↙↗	↙↗
W42	Carbonaceous shale	↔	↔	↔
W46	Rhythmite	↔	↔	No data
				x y

6.8. Synthetic seismogram

To determine if the rocks can be imaged using the reflection seismic method, the acoustic impedances Z (product of the seismic velocity and density) and the corresponding normal incidence reflection coefficients [Rc = (Z1 − Z2) / (Z1 +Z2)] were calculated (Yilmaz, 2001). The most important parameter that influences the strength of the seismic reflection is the contrast in acoustic impedance. Abrupt changes in this parameter in a stratigraphic context typically produce strong seismic reflections that allow the subsurface geology to be interpreted. The ability of the boundary to generate a strong reflection is described by Rc, which describes the amplitude of a reflected wave relative to an incident wave. For an interface to be detected by the reflection seismic method it should reflect at least 6% of incident energy (Salisbury et al., 2003).

This section reports the results obtained for the acoustic impedances and reflection coefficients for all the samples. The acoustic impedances and reflection coefficients were also used to generate the synthetic reflection seismograms, which can be used to establish the feasibility of a reflection seismic survey for hydrocarbon reservoirs in the Main Karoo Basin. Generation of the synthetic seismogram was performed in MATLAB software programme by Michael Westgate. In creating a synthetic seismogram, the program permits the interpreter to tie time data (the seismic data) to depth data (the borehole data) by integrating over the velocity profile. An impedance log and reflection coefficients are generated from the velocity

and density profiles. The reflection coefficients are convolved with a seismic wavelet to produce a synthetic seismic trace. A 60 Hz Ricker wavelet was used to create synthetic trace to mimic the acquisition of the real seismic survey. In the absence of check-shot survey data or vertical seismic profiles (VSP), synthetic seismogram provided a means to correlate seismic reflections with core lithologies. The data show intriguing results, with reflection coefficient values ranging from ~ 3 to ~ 69% between the different lithological interfaces (Table 6.8). Thus, the results show that the contrast in the seismic velocities and bulk density variations may have the potential to produce strong seismic reflections in KWV borehole lithologies.

Table 6.8: A summary of the seismic velocities, bulk densities, acoustic impedances and reflection coefficients of the samples from borehole KWV.

Sample	Stratigraphy	Lithology	Vp (m/s)	Density g/(cm3)	Acoustic impedance	Rc (%)
W1	Adelaide Subgroup	Sandstone	5089 +/- 809	2.60 +/- 0.00	13229 +/- 2103	69 +/- 23
W2		Mudstone	961 +/- 223	2.53 +/- 0.01	2427 +/- 563	47 +/- 42
W3	Waterford Formation	Breccia	2426 +/- 936	2.75 +/- 0.00	6681 +/- 2578	34 +/- 19
W4		Sandstone	5133 +/- 946	2.65 +/- 0.02	13606 +/- 2508	20 +/- 15
W5	Fort Brown Formation	Shale	3319 +/- 734	2.71 +/- 0.00	9002 +/- 1991	23 +/- 14
W6		Sandstone	5304 +/- 877	2.70 +/- 0.00	14310 +/- 2366	7 +/- 10
W7		Dolerite	5603 +/- 614	2.94 +/- 0.00	16459 +/- 1804	17 +/- 8
W8		Sandstone	4477 +/- 249	2.62 +/- 0.01	11734 +/- 653	40 +/- 6
W9		Carbonaceous shale	2135 +/- 311	2.64 +/- 0.02	5087 +/- 821	0 +/- 9
W10	Trumpeters Member	Sandstone	1898 +/- 155	2.70 +/- 0.00	5117 +/- 418	17 +/- 29
W11		Shale	2663 +/- 1108	2.72 +/- 0.00	7247 +/- 3015	40 +/- 10
W12		Dolerite	5752 +/- 412	2.96 +/- 0.00	17005 +/- 1218	56 +/- 9
W13		Sandstone	1748 +/- 218	2.71 +/- 0.01	4741 +/- 591	2 +/- 15
W14	Wonderfontein Member	Shale	1679 +/- 494	2.69 +/- 0.00	4516 +/- 1328	46 +/- 7
W15			4430 +/- 248	2.73 +/- 0.01	12108 +/- 678	10 +/- 4
W16		Dolerite	5050 +/- 316	2.95 +/- 0.01	14902 +/- 933	59 +/- 8
W17		Shale	1422 +/- 193	2.72 +/- 0.00	3874 +/- 526	51 +/- 2
W18	Pluto's Vale Member	Sandstone	4511 +/- 13	2.67 +/- 0.00	12066 +/- 35	48 +/- 5
W19		Carbonaceous shale	1541 +/- 579	2.75 +/- 0.01	4232 +/- 1590	21 +/- 27
W20			2340 +/- 780	2.76 +/- 0.01	6455 +/- 2152	39 +/- 7
W21		Sandstone	5462 +/- 186	2.71 +/- 0.00	14805 +/- 504	7 +/- 5
W22		Dolerite	5729 +/- 507	2.96 +/- 0.00	16979 +/- 1502	34 +/- 8
W23		Sandstone	3107 +/- 321	2.68 +/- 0.00	8321 +/- 860	19 +/- 7
W24		Carbonaceous shale	2000 +/- 25	2.81 +/- 0.00	5612 +/- 70	43 +/- 3
W25		Shale	5182 +/- 168	2.74 +/- 0.01	14194 +/- 460	8 +/- 3
W26		Dolerite	4115 +/- 212	2.96 +/- 0.00	12171 +/- 627	20 +/- 3
W27			5863 +/- 239	3.14 +/- 0.00	18387 +/- 749	27 +/- 5
W28		Carbonaceous shale	3806 +/- 624	2.77 +/- 0.00	10553 +/- 1730	17 +/- 7
W29		Sandstone	5602 +/- 392	2.68 +/- 0.01	14997 +/- 1049	7 +/- 4
W30		Rhythmite	4872 +/- 135	2.70 +/- 0.00	13146 +/- 364	10 +/- 2
W31		Dolerite	3574 +/- 160	2.98 +/- 0.00	10653 +/- 477	10 +/- 4
W32			4321 +/- 247	2.99 +/- 0.00	12938 +/- 740	16 +/- 3
W33			6033 +/- 227	2.96 +/- 0.00	17866 +/- 672	22 +/- 3
W34			4431 +/- 122	2.59 +/- 0.00	11493 +/- 316	7 +/- 4
W35		Sandstone	4956 +/- 311	2.68 +/- 0.01	13273 +/- 833	5 +/- 4
W36			5400 +/- 328	2.73 +/- 0.00	14732 +/- 895	1 +/- 9
W37		Dolerite	5076 +/- 879	2.94 +/- 0.01	14937 +/- 2587	6 +/- 9
W38			5712 +/- 462	2.98 +/- 0.01	16993 +/- 1374	15 +/- 15
W39	Whitehill Formation	Carbonaceous shale	5799 +/- 1818	2.73 +/- 0.00	12598 +/- 4964	3 +/- 21
W40			4485 +/- 385	2.67 +/- 0.03	11980 +/- 1028	7 +/- 7
W41			5131 +/- 561	2.71 +/- 0.00	13922 +/- 1522	3 +/- 6
W42			4712 +/- 277	2.77 +/- 0.01	13065 +/- 768	2 +/- 8
W43	Prince Albert Formation	Shale	4757 +/- 706	2.84 +/- 0.01	13488 +/- 2002	35 +/- 14
W44			2070 +/- 342	2.79 +/- 0.00	6446 +/- 953	37 +/- 7
W45			5051 +/- 319	2.80 +/- 0.00	14146 +/- 893	63 +/- 9
W46		Rhythmite	1338 +/- 335	2.79 +/- 0.01	3200 +/- 936	58 +/- 7
W47			4299 +/- 230	2.79 +/- 0.00	12012 +/- 643	6 +/- 3
W48	Dwyka	Tillite	4945 +/- 76	2.75 +/- 0.00	13575 +/- 209	4 +/- 2
W49			5325 +/- 177	2.74 +/- 0.00	14575 +/- 484	- +/- 7

Figure 6.98 illustrates the results from the construction of the synthetic seismogram using our mean velocities and densities. The acoustic impedance (Figure 6.98a) has various highs and lows, and when this is used to plot the reflection coefficient (Figure 6.98b) it becomes clear that there are various reflections (Figure 6.98c).

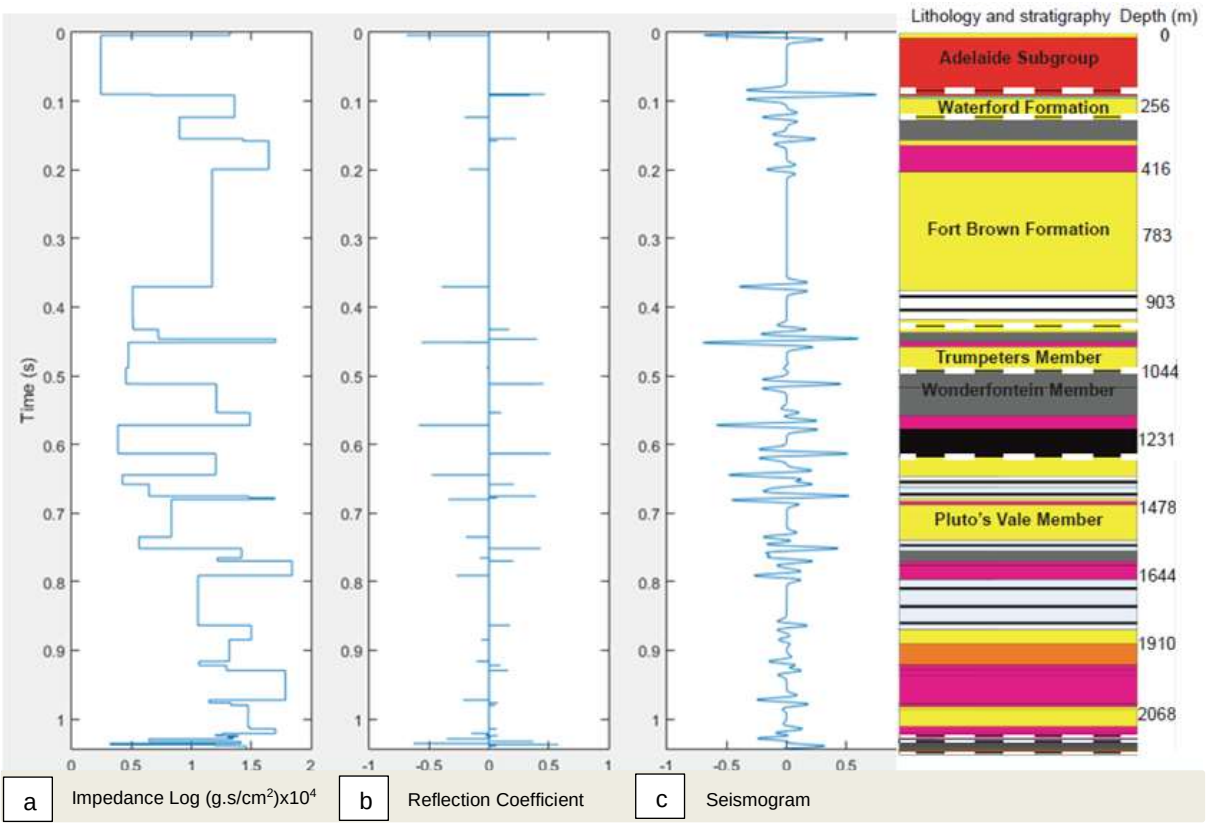

Figure 6.98: The construction of a synthetic seismogram, where a) is a plot of the acoustic impedance, b) is the resulting reflection coefficient and c) is the synthetic seismogram and the lithology and stratigraphy of borehole KWV**.**

Figure 6.99 compares the synthetic seismograms for maximum (Figure 6.99a) and minimum (Figure 6.99b) reflection coefficients of the data. The maximum and minimum reflection coefficients were obtained by respectively maximizing and minimizing the impedance contrasts between adjacent lithological units. Compared to Figure 6.98, most of the bigger reflections can still be observed. The reflection at the top of the Trumpeters Member (Figure 6.99a) becomes significantly smaller in the maximum reflection coefficient seismogram. However this peak is still easily detectable.

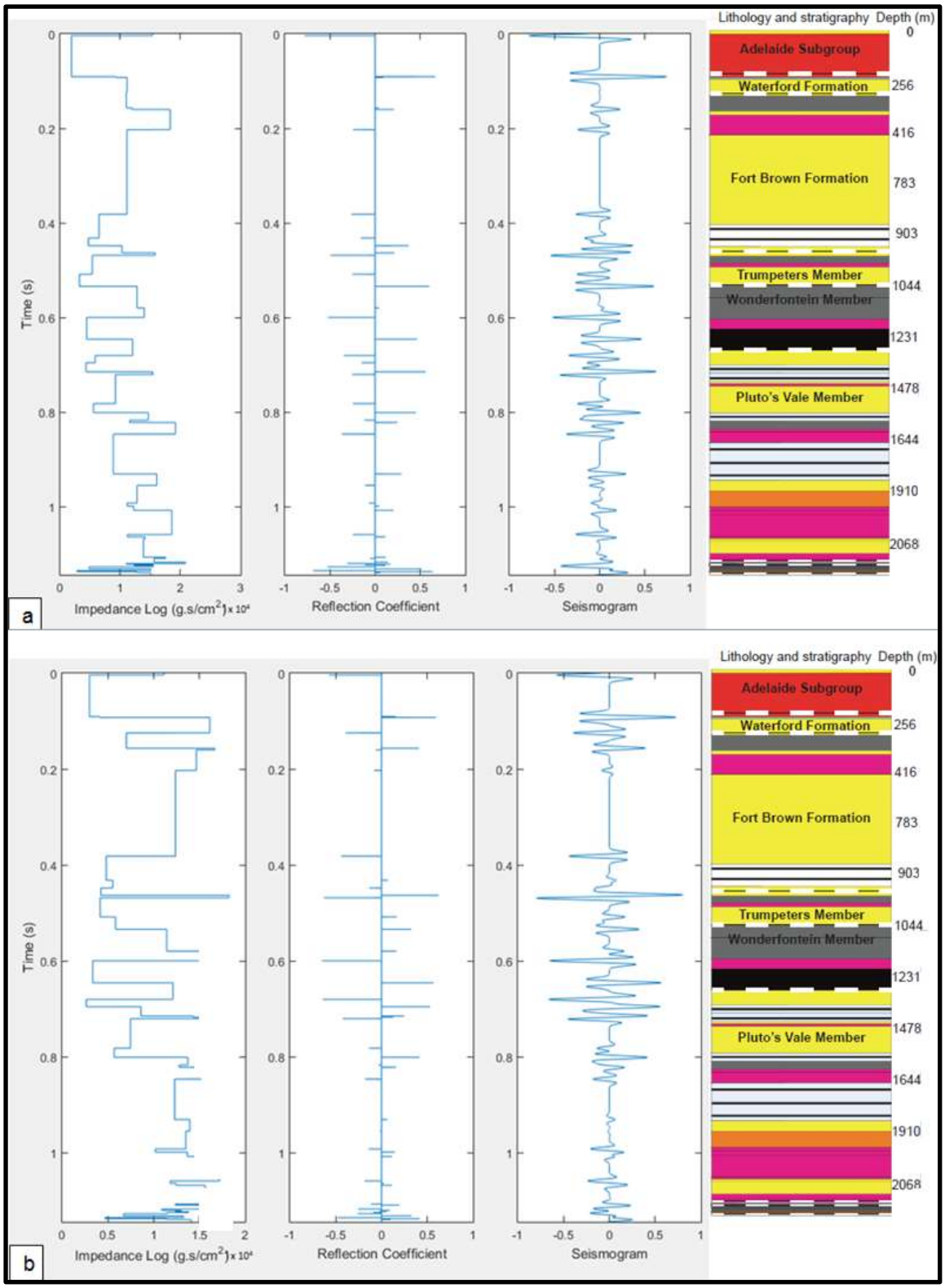

Figure 6.99: The synthetic seismograms for the (a) maximum and (b) minimum reflection coefficient.

Although velocity anisotropy was observed in some of the samples (Table 6.6), they do not appear to have any major effect on the synthetic seismogram (Figure 6.100). Hence we do not expect seismic velocity anisotropy to play a significant role in the feasibility of reflection seismics in our study area.

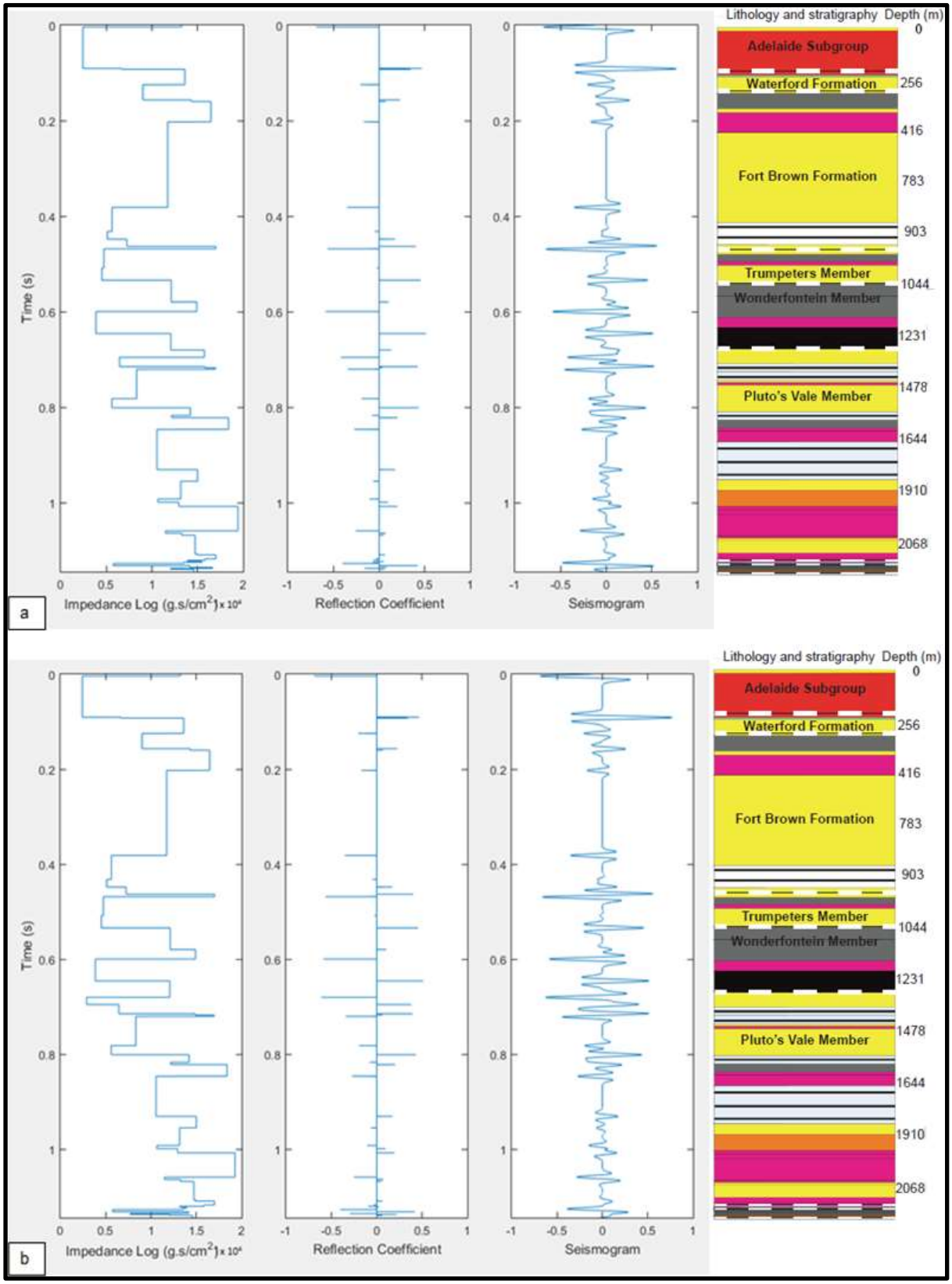

Figure 6.100: The synthetic seismograms for the a) highest and b) lowest anisotropy values.

7. Data integration and discussion

7.1. Sources of error

During the measurement of the seismic velocities of the samples, various sources of systematic and random error may have been introduced. Possible sources of noise may include (1) the equipment, (2) laboratory environment, (3) sample length measurements, (4) the operator picking wave arrivals and (5) by the sample itself.

The equipment could have timing errors. However, these errors could not be measured or controlled, and was considered to be negligible. The size of the samples, in relation to the transducers is a source of error. The diameter of the sample should be significantly larger than the diameter of the transducers. This is a necessary condition to ensure that the plane wave approximation is valid (Zhang et al., 2002). When the sample's surface area is only 14% of the transducer's surface area, the seismic velocity decreases by 1.4%. The measurement of most seismic velocities (under ambient stress, uniaxial stress and during anisotropic measurements) was conducted under conditions where the samples were significantly larger than the transducers. Some samples are smaller than the transducers in the case of the 45 mm diameter samples (samples W13 to W49). The diameters of the transducers are 54.8 mm. This means the samples' contact area is 67% of transducers' contact area. This implies that the size of the samples should not have affected the results.

Environmental noise could be a result of vibrations in the laboratory from other machines. This was minimised by switching off other machines in close proximity to our equipment. Since this noise level was not systematic, it was difficult to deduce its exact effect on any particular sample. However, in general, more signal noise on a given sample increased the uncertainties associated with the seismic velocities.

When measuring the sample lengths a Vernier calliper was used to minimise any error to 0.01 cm. The relative contributions of length measurement errors to the velocity results are negligible as they are several orders of magnitude smaller than the uncertainties of first-arrivals.

The largest source of error was introduced by the first wave arrivals. To incorporate uncertainties in the picking of first-arrivals, a 95% confidence time interval was estimated around each first-arrival location. This time interval was used to determine the first-arrival measurement precision. Each measurement was then repeated five times per sample and the standard deviation of the measurements was used to examine the reproducibility. The

time interval error was generally substantially larger than the standard deviation of the five measurements and was thus used as velocity measurement errors. As can be seen in our results, this error produced relatively large errors in the acoustic impedances and reflection coefficients.

Sample integrity and contacts are suspected issues for a few samples exhibiting anomalously low seismic velocities. Under uniaxial stress, these samples rapidly increased in seismic velocities. This can indicate that the edges of the sample were not perfectly parallel and sufficiently smooth. This can cause insufficient contacts between the samples and the transducers. Alternatively, the samples may have internal fractures that were rapidly closed under uniaxial stress. We expect these issues to decrease the affected velocity measurements. However, these issues were not visually apparent in the laboratory and their consequences are not easily quantified.

A possible source of systematic error may have been introduced by the application of uniaxial stress. Samples at depth experience bulk stress that is not axially-dependent. Hence our setup may have caused micro-fractures to enlarge in planes that are not normal to the direction of applied stress. A complete imitation of the in situ conditions was therefore not achieved. However, the effects of this error are difficult to quantify.

Another possible cause for systematic inaccurate measurements might be attributed to the fact that the change in length of the sample under uniaxial stress was not incorporated in the measurements. As uniaxial stress is applied to a sample, the length of that sample should decrease. Since the change in sample length is in the order of micro-meters, it was considered as negligible and the effect it may have had on the seismic velocities was omitted from this study. Omission of this effect implies that our saturation velocities for every sample were slightly under-estimated. However, compared to the large uncertainties in the first-arrival times, this effect is negligible.

The density and porosity measurements were repeated three times per sample and the standard deviation of these measurements was calculated and used as the error of the measurements. The standard deviations were larger than the instrument precision (0.01 g), and were thus used as the measurement errors. There was no method to measure the fractions of connected porosity in the samples, hence the porosity was systematically underestimated. However, none of our lithologies are known to have a large fraction of connected porosity, which is consistent with our thin section analyses.

7.2. Seismic velocities, bulk density, porosity

It is widely expected that average seismic velocities of sedimentary rocks should increase with density (Birch, 1960). Although this correlation is valid in very general terms, in this study there is no obvious density-velocity relationship, in part because Vp and Vs values for individual rock types can vary widely, independent of bulk rock density.

Figure 7.1 summarizes the average P-wave and S-wave seismic velocities measured in all the samples. Figure 7.2 illustrates the Vp and Vs for all the samples from borehole KWV. The P-wave velocity data obtained for all the samples are compared to the P-wave data from the geophysical log (Figure 7.3). Figure 7.4 summarises the results for the bulk density and porosity for all the samples, while Figure 7.5 indicates the relationship between the porosities and bulk densities of all the samples collected from borehole KWV.

Sandstone samples

The sandstone samples have average seismic velocities (Vp is 4904 ± 536 m/s and Vs is 2623 ± 471 m/s) (Figures 7.1 and 7.2) that are similar to those reported in the previous studies (Vp is 4400 – 5440 m/s and Vs is 2600 m/s) (Bräuer et al., 2007). The values are slightly higher than that recorded on the geophysical log (Vp is 4061 ± 103.40 m/s and Vs is 2605 ± 152.36 m/s) (Figure 7.3). Sample W36 consists of pyrite, which was observed in hand sample and confirmed by thin section (Figure 6.94). The presence of pyrite in this sample may be the cause for the high seismic velocity of the sample (Vp is 5400 m/s and Vs is 2924 m/s), compared to the average seismic velocity of all the sandstone samples from borehole KWV. The results suggest that if the pyrite has any effect on the physical properties of the sandstone sample, it is only on the seismic velocity of the sample, and not the bulk density.

Shale samples

The shale samples have average seismic velocities (Vp is 3859 ± 708 m/s and Vs is 2116 ± 349 m/s) (Figures 7.1 and 7.2) that are similar to those from the geophysical log (Vp = 3970 ± 97 m/s and Vs = 2547 ± 123 m/s) (Figure 7.3). Our experimental values are comparable to that in previous studies (Vp is 4400 – 5440 m/s and Vs is 2600 m/s) (Bräuer et al., 2007). The bulk densities of all the shale samples are close to the average bulk density (2.74 g/cm^3), including the pyrite-bearing samples. Six of the shale samples (samples W15, W39, W40, W41, W42 and W45) contain pyrite; this was observed on hand samples as well as on thin sections. The seismic velocities of the pyrite-bearing shale samples are significantly higher (Vp ranges from 4430 m/s to 5799 m/s) than the average seismic velocity of normal shale samples from borehole KWV (Figures 7.1 and 7.2).

Rhythmite samples

The rhythmite samples have average seismic velocities (Vp is 4586 ± 377 m/s and Vs is 2432 ± 388 m/s) (Figures 7.1 and 7.2) that are slightly higher than those from the geophysical log (Vp is 4178 ± 174 m/s and Vs is 2754 ± 176 m/s) (Figure 7.3). One of the rhythmite samples (sample W46) was excluded from the average, due to its anomalously low seismic velocities. The densities (average bulk density of 2.76 g/cm^3) and porosities (average porosity is 3.04%) of the rhythmite samples (Figures 6.61 and 7.5) are all mutually similar, thus the lithological differences between the samples (see Figures 6.30, 6.46 and 6.47) do not seem to significantly affect the physical properties.

Dolerite samples

The average seismic velocities of the dolerite samples (Vp is 5150 ± 423 m/s and Vs is 2718 ± 378 m/s) (Figures 7.1 and 7.2) are generally comparable to those from the geophysical log (Vp is 4213 ± 107 m/s and Vs is 2706 ± 179 m/s) (Figure 7.3). The experimental average P-wave velocity is relatively higher than geophysical log P-wave velocities. Furthermore, experimental values are lower than the values recorded in previous studies (Vp is > 6200 m/s) (Fatti, 1987). The dolerite samples have a relatively higher average bulk density (2.95 g/cm^3) than other samples (Figure 7.4). Samples W27 and W34 (2.59 g/cm^3) exhibit bulk densities (3.14 g/cm^3 and 2.59 g/cm^3) that plot further from the average value (Figure 7.4). Hand descriptions of these samples indicate that sample W27 do not contain any minerals that are unique. Sample W34 has calcite veins running through the sample. These veins could be the main cause for the low bulk density of the sample (Dentith and Mudge, 2014).

Tillite

The average P- and S-wave velocities of the tillite samples are 5135 ± 136 m/s and 2896 ± 261 m/s respectively (Figures 7.1 and 7.2). The average P-wave velocity is significantly higher than that from the geophysical log (4174 ± 30 m/s), while the average S-wave velocity seems to correlate well with that from the geophysical log (2802 ± 55 m/s) (Figure 7.3). The two tillite samples (samples W48 and W49) have the same lithologies and similar bulk densities (2.75 g/cm^3 and 2.74 g/cm^3, respectively) and porosities (2.55% and 2.23%, respectively) (Figures 7.4 and 7.5).

In general, the seismic velocity data from the geophysical log are more constrained than the data from our experimental study (Figures 7.1 to 7.3), varying between 3 500 and 4 500 m/s. The wide range of data from our study might be attributed to experimental errors, as discussed previously.

Summarily, it is evident that dolerite has the highest P-wave velocity, followed by tillite samples (Figures 7.1 and 7.2). However, tillite has a higher S-wave velocity than the dolerite samples. As discussed earlier, P-wave velocity results are more precise than the S-wave results due to the uncertainty in picking the first S-wave arrivals. The P-wave values for the different lithologies are significantly less constrained than the values for average bulk density (Figures 7.1 to 7.4). Dolerite has the highest bulk density while mudstone has the lowest bulk density. The average porosity values for the different lithological groups from borehole KWV are widely scattered (Figures 7.4 and 7.5). However, most values are small enough such that the porosities are not expected to have a major influence on the seismic velocities. It is worth noting that no attempt was made to saturate the samples during seismic velocity measurements because of the assumed low porosities of the samples.

From the porosity-bulk density relationship plot (Figure 7.5), there does not appear to be any significant relationships between the porosities and bulk densities. In particular, a linear fit results in a very low R^2 value. Although the range in porosities are quite wide, the porosities are still small enough to be considered as an insignificant factor affecting the seismic velocities, and hence also the reflection seismic exploration for hydrocarbon reservoirs in the Main Karoo Basin. By comparing the density-velocity relationship of the experimental data from this study to the geophysical log data (Figure 6.61), it can be observed that the trend lines through these data sets indicate that both data sets are positively correlated with very low R^2 values. Our experimental data further show a stronger positive linear correlation with the geophysical log data. However, data from the geophysical log is better constrained than our experimental data.

A few data points from previous studies (Lillie, 1999; Fourie, 2003) on rocks from the Main Karoo Basin are also plotted (Figure 6.61). These points are not enough to compare the density-velocity trend with that of the experimental and geophysical log data. Limited information is published on physical properties from the Main Karoo Basin, especially where the seismic velocities and bulk densities were both investigated in one study.

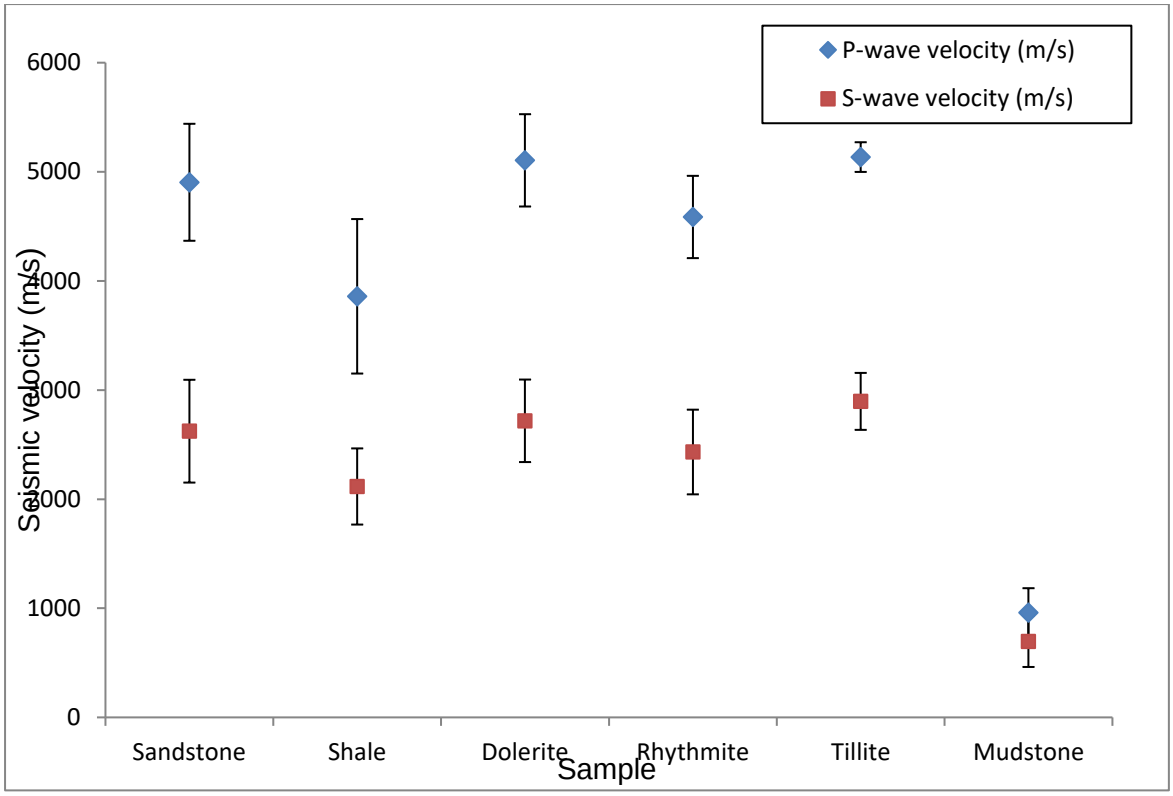

Figure 7.1: A summary of the average seismic velocities obtained in this study.

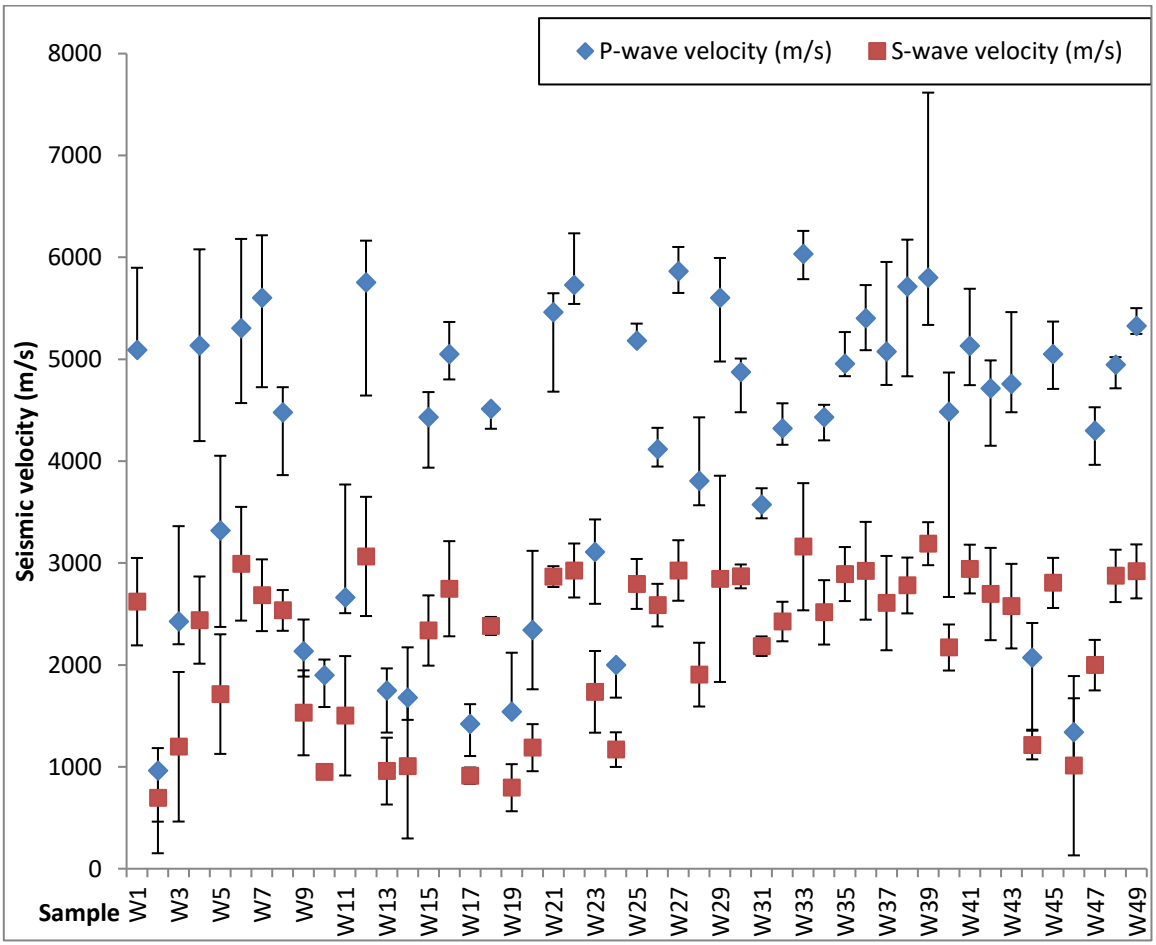

Figure 7.2: The P- and S-wave velocities of all the samples from borehole KWV.

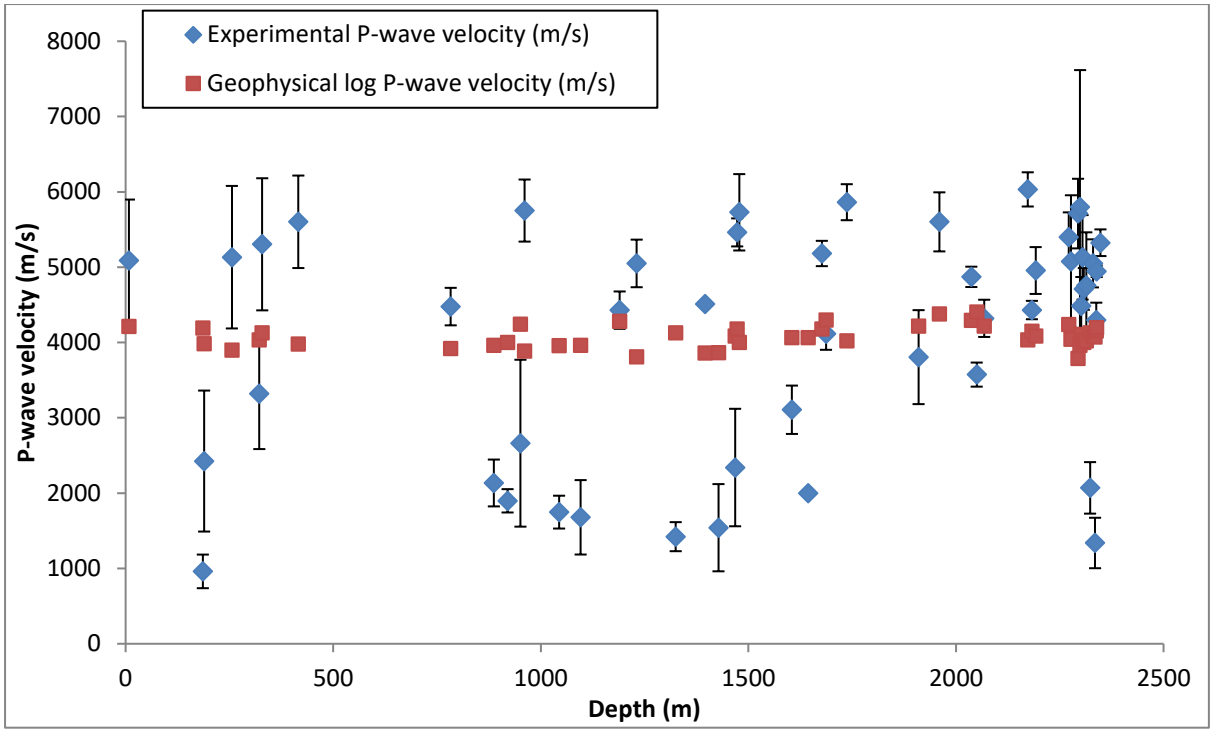

Figure 7.3: A comparison between the experimental P-wave velocity data at atmospheric stress and the P-wave velocity data from the geophysical log.

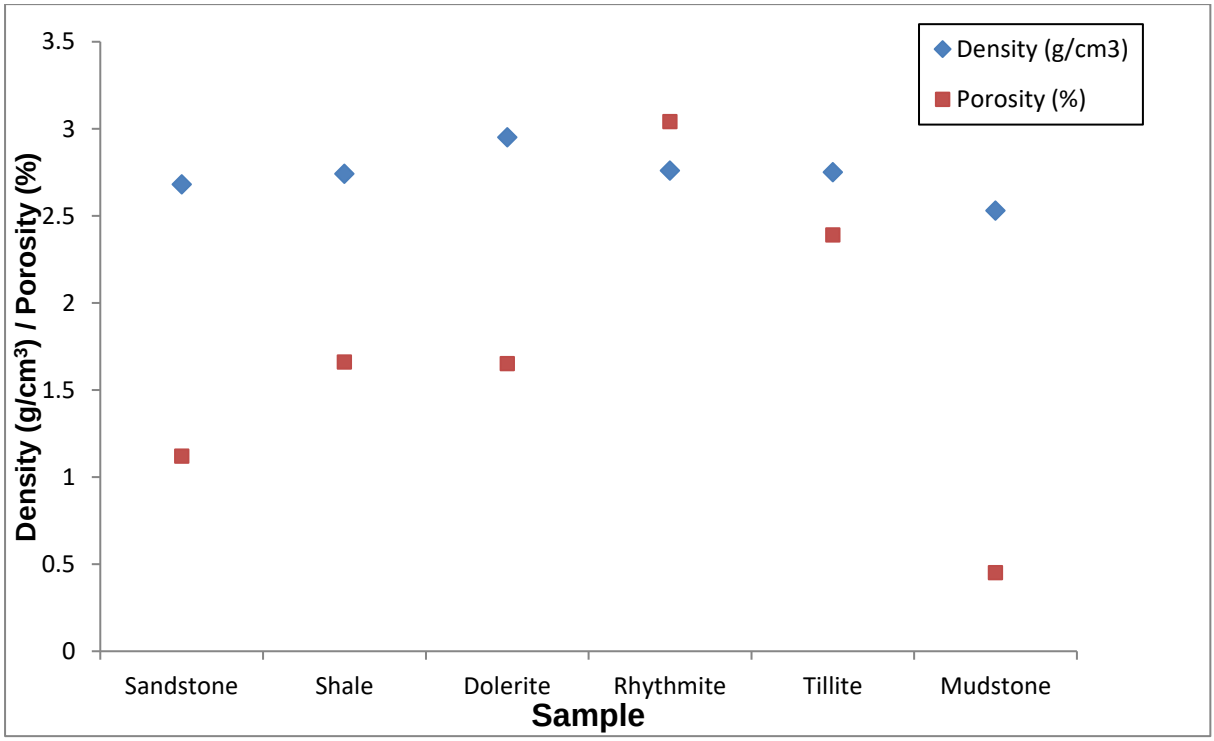

Figure 7.4: The summarised results of the average bulk density and porosity of all the samples from borehole KWV.

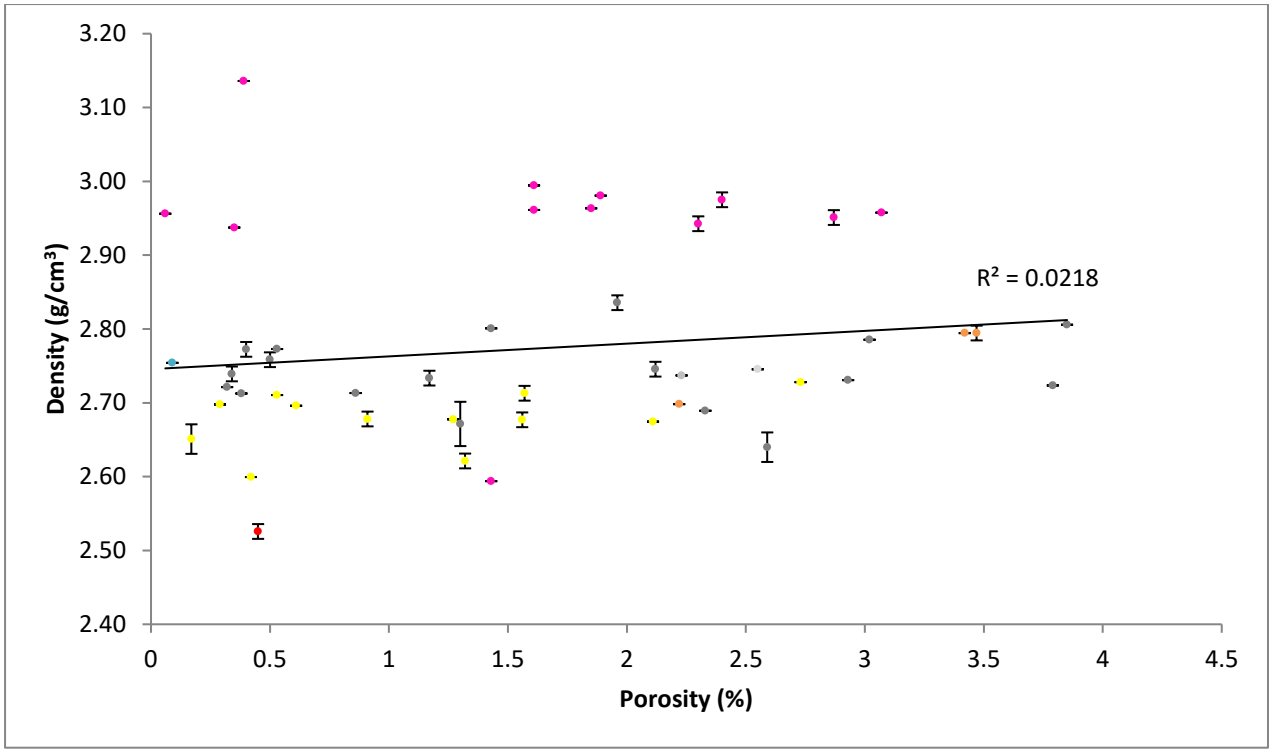

Figure 7.5: The relationship between the porosity and bulk density of all the samples collected from borehole KWV. The pink colours are dolerite, yellow is sandstone, blue is breccia, red is mudstone, orange is rhythmite, dark grey is shale and light grey is tillite.

7.3. Seismic velocities at elevated axial stress

The seismic wave velocity depend on the stress applied to the sample. In some cases, this stress effect is quite strong. The reason for this dependence is well known and is caused by the ubiquitous mechanical micro-defects (micro-fractures and grain contacts) that tend to close under the effect of increasing differential stress, thereby increasing the rigidity of the material. To test the dependence of seismic velocities to applied stress, we measured the seismic velocities (mainly P-wave) of KWV borehole samples at elevated stresses up to 85 MPa (corresponding to a lithostratigraphic depth of ~ 3km).

Sandstone samples

The P-wave velocity of all the sandstone samples increase as a function of uniaxial stress (see Figure 6.53). Samples W8 and W18 reached their saturation velocities later than the other sandstone samples (45 MPa and 55 MPa, respectively). Both of these samples are well-bedded, like the other sandstone samples, and have very small porosities (< 2.5%) (see Figures 7.4 and 7.5). The same description can be applied to samples W10 and W13. Yet these samples reached their saturation velocities sooner, while the increase in seismic velocities was much larger for these samples (e.g., sample W10 increased by 2574 m/s and sample W13 increased by 3116 m/s). No trends between the depths or porosities of the

samples and the increase in seismic velocity under uniaxial stress can be observed (Figures 7.6 and 7.7). The mechanisms for the total change in seismic velocities under uniaxial stress, or the stress needed to close up all pores of the samples, are not evident from the physical properties of the sandstone samples. For these samples, there is no correlation between the amounts of increase and the rates of increase of the seismic velocities under uniaxial stress.

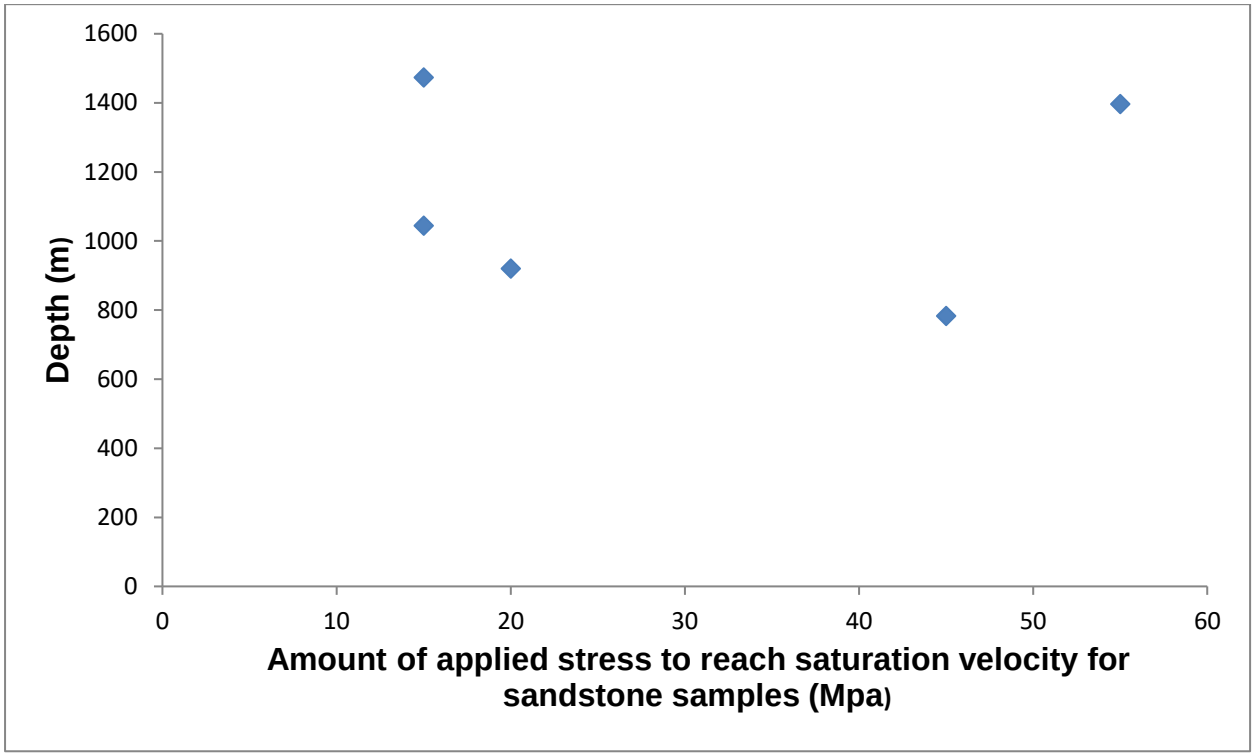

Figure 7.6: The relationship between the depth of sandstone samples from borehole KWV and the amount of stress required reach saturation velocity in the sandstone samples.

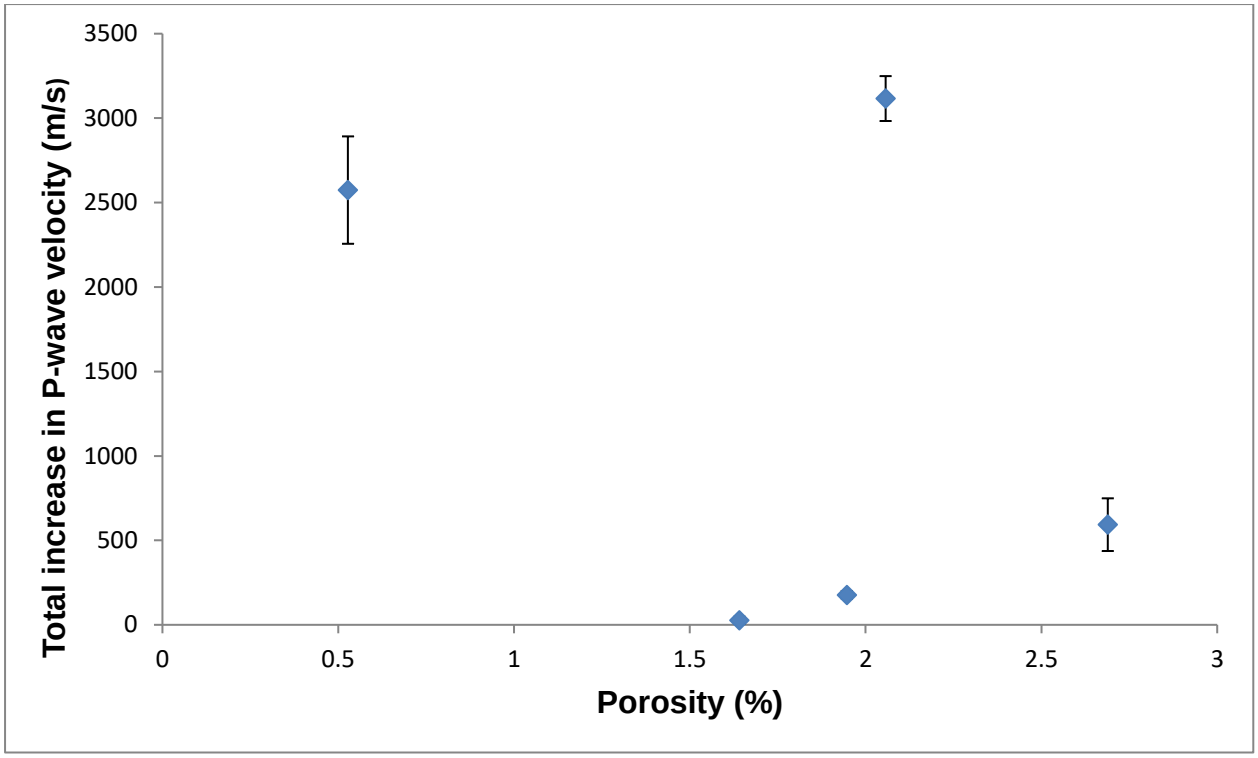

Figure 7.7: The relationship between the porosities of sandstone samples from borehole KWV and the total increase in P-wave velocities.

Shale samples

The P-wave velocity of all the shale samples increases as a function of uniaxial stress (see Figure 6.54 and 6.55). Similar to the sandstone samples, the rate of the seismic velocity increase under uniaxial stress seems to be sample-dependant. Samples W5, W25 and W43 reach their saturation velocities at 20 MPa, 40 MPa and 5 MPa, respectively. The seismic velocities of these samples increase by 1273 m/s, 112 m/s and 2314 m/s, respectively. The hand descriptions and thin section analyses of the samples yield no findings that may explain the differences between the behaviours of the shale samples under uniaxial stress. The total increase of P-wave velocity and the amount of stress to saturation do not correlate with the depths of the samples (Figure 7.8). The amount of increase in seismic velocity of the shale samples under uniaxial stress also does not correlate with the porosities of the samples (Figure 7.9). The mechanisms for the total change in seismic velocities under uniaxial stress, or the stress needed to close up all pores of the samples, are not evident from the physical properties of the shale samples.

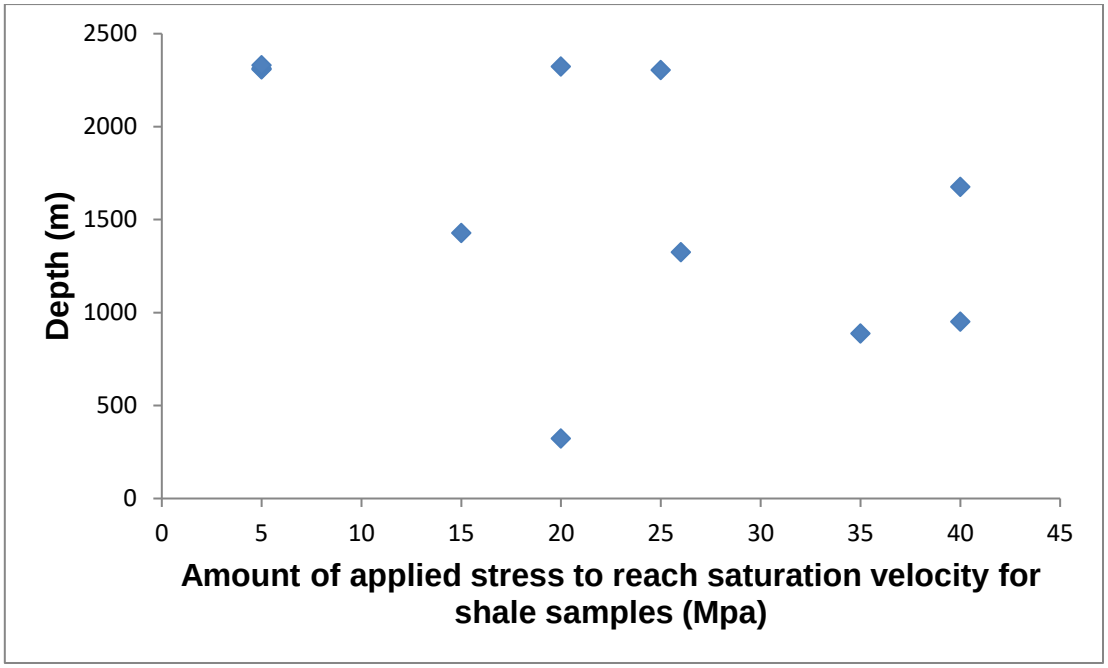

Figure 7.8: The relationship between the depth of shale samples from borehole KWV and the amount of stress required to each saturation velocity in the sandstone samples.

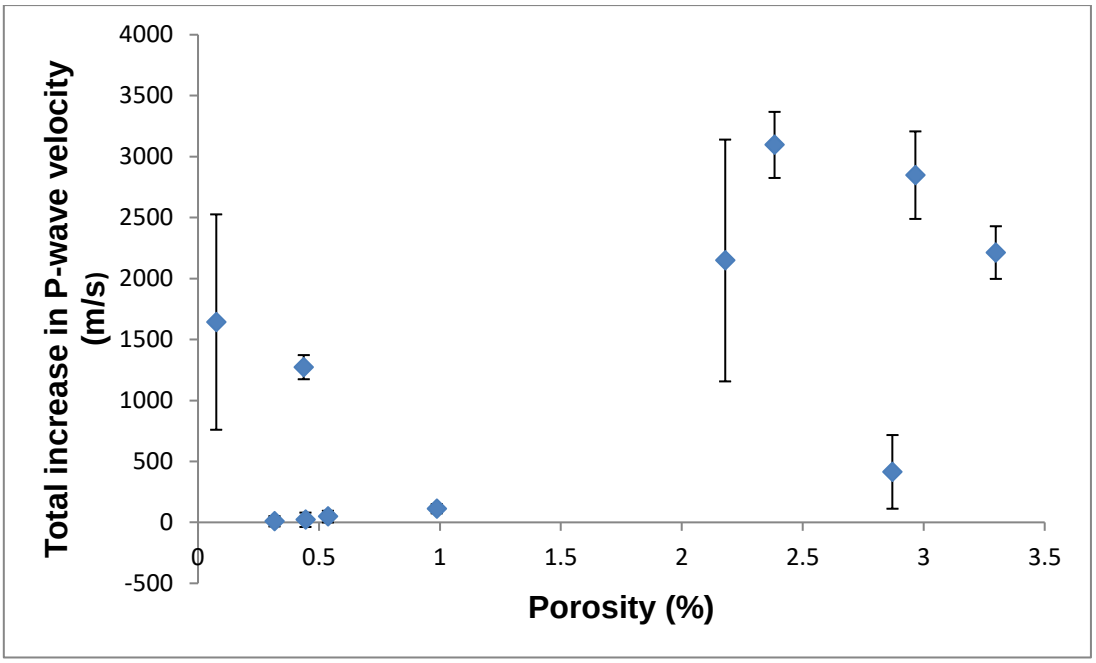

Figure 7.9: The relationship between the porosities of shale samples from borehole KWV and the total increase in P-wave velocities.

Dolerite samples

The amount of stress needed to reach saturation velocity in the dolerite samples varies widely between 5 MPa (samples W34 and W37) and 70 MPa (sample W31). No evidence was discovered in our sample analyses to explain this wide range of required uniaxial stress. The amount of stress is also not related to the depths of the samples, or their porosities (Figures 7.10 and 7.11).

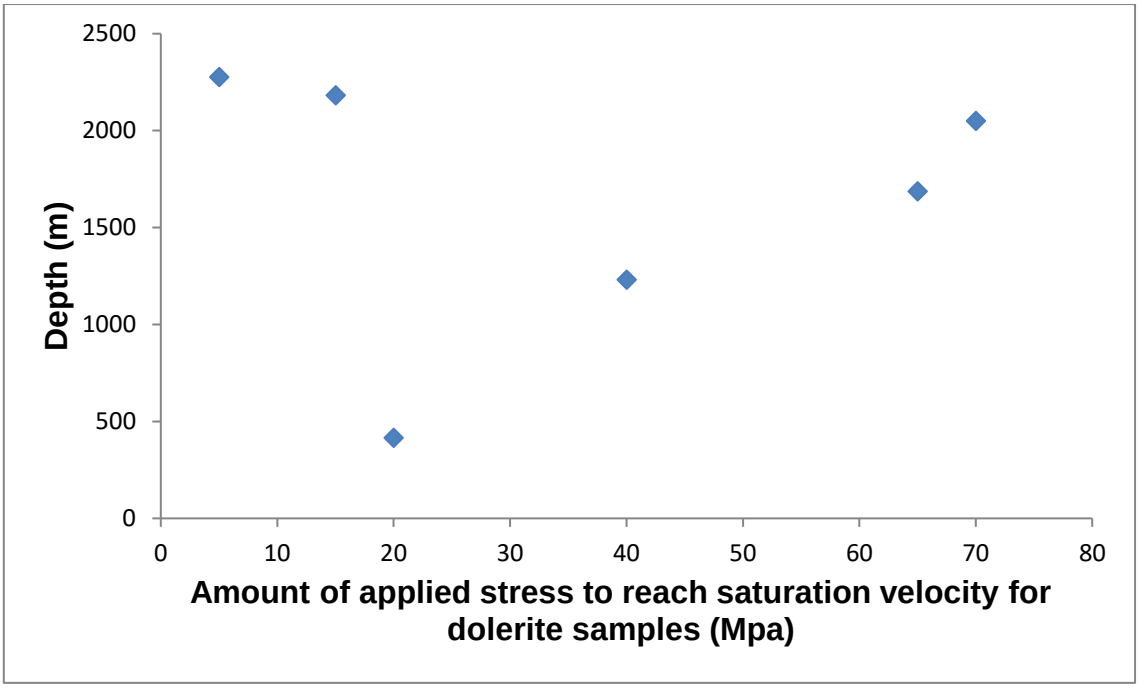

Figure 7.10: The relationship between the depth of dolerite samples from borehole KWV and the amount of stress required to reach saturation velocity in the sandstone samples.

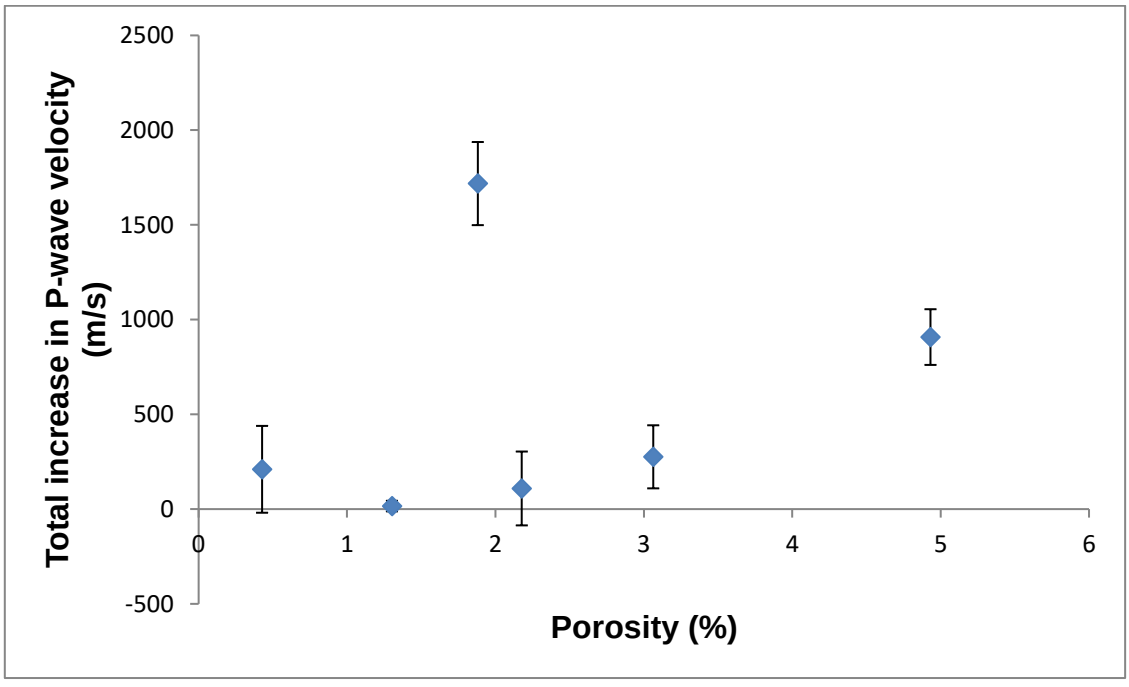

Figure 7.21: The relationship between the porosities of dolerite samples from borehole KWV and the total increase in P-wave velocities.

Rhythmite samples

One of the three rhythmite samples (W30) exhibit visible cracks that suggest a state of compromised physical integrity. Since this sample was not subjected to uniaxial stress and sample W46 has unrealistic seismic velocities under atmospheric stress (~0.1 MPa), the

correlation between the hand descriptions, applied uniaxial stress, bulk densities and porosities could not be established.

Experimental P-wave velocity-uniaxial stress relationship versus geophysical log P-wave velocity

In order to compare the Vp data from the geophysical log with more accurate, in situ velocity data of the rock samples, we plotted experimental Vp at uniaxial stress and geophysical log P-wave velocity against depth (Figure 7.12). This saturated velocity data (all pore spaces and oriented micro-fractures are probably closed) mimic the in situ stress, and thus seismic velocity, conditions of the rocks. Although the lower seismic velocities seem to have disappeared in Figure 7.12, the experimental data still do not match the data from the geophysical log. The experimental data are less constrained and characterized by higher P-wave velocities. These velocities are expected to be more accurate than the velocities from the geophysical log, since they were measured under conditions resembling the in situ conditions, where pore spaces and oriented micro-fractures are probably closed due to stresses caused by overlying rocks. It would have been preferable to measure the seismic velocities under confined stress instead of only uniaxial stress, but the sample geometries were not of such a nature to fit the confined stress apparatus that was available for the experiment. Generally, we observe that the stress-velocity relationship exhibits the renowned initial steep velocity increase with elevated uniaxial stress, typically illustrating the stress sensitivity of seismic wave velocities, due to progressive closure of micro-fractures. This suggests that micro-fractures may have a significant effect on the intrinsic seismic velocities, in addition to the lithological influences. These results demonstrate the importance of conducting laboratory physical property measurements of rocks ahead of designing and acquiring the reflection seismic data for hydrocarbon exploration.

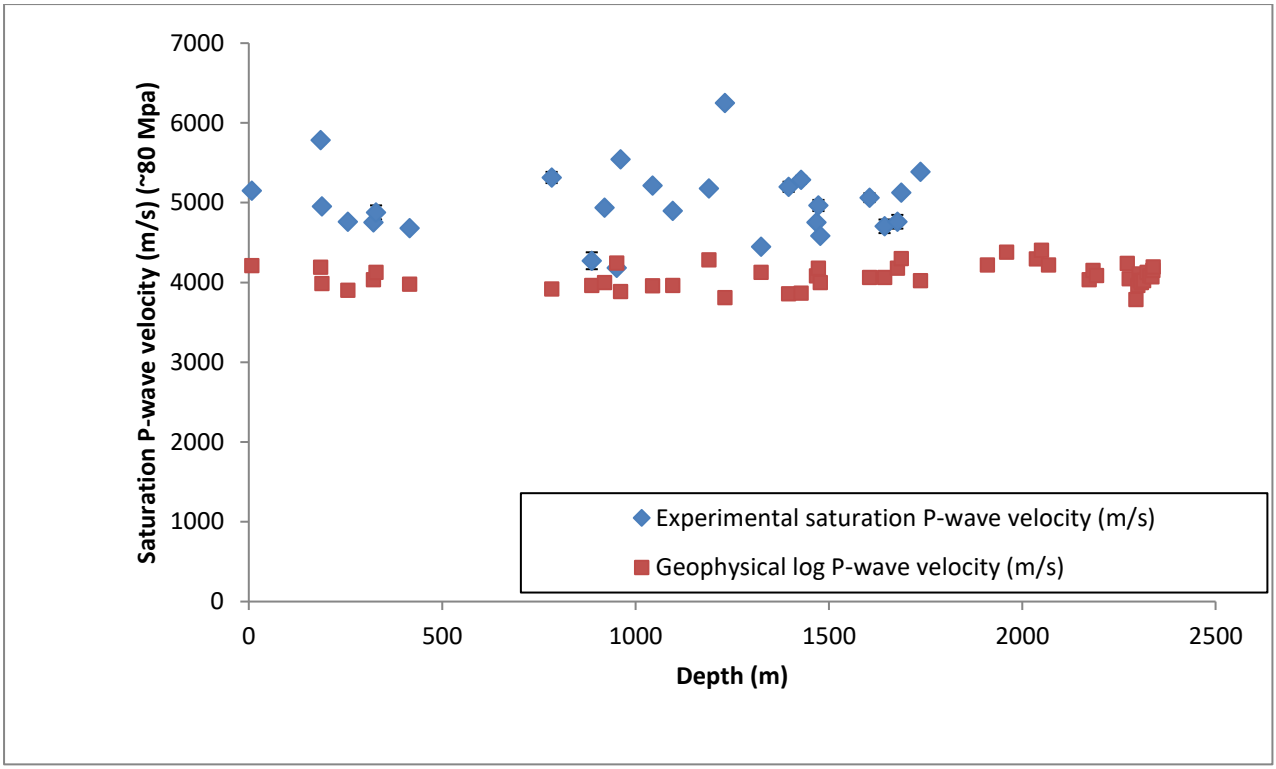

Figure 7.32: A comparison between the experimental seismic velocity data under elevated axial stress and the P-wave velocity data from the geophysical log.

7.4. Seismic anisotropy

Another important parameter for reflection seismic exploration is seismic anisotropy. The seismic anisotropy of the samples was only investigated in two directions since the minerals and micro-fractures were only orientated in one direction in the samples. Figure 7.13 summarises the seismic anisotropy results from our study. The degrees of anisotropy for each sample are compared.

The shale sample (sample W19) exhibit the largest amount of velocity anisotropy (137.8 %) (see Table 6.6). However, the Vp value for this sample in the y-direction (the long axis of the sample) is anomalously low (1056 m/s) for a shale, and is considered to be inaccurate. The velocity anisotropy for this sample can therefore not be compared to the velocity anisotropy of the other samples. The S-wave arrival of the shale sample was completely masked by noise and could therefore not be picked with high confidence.

The Vs anisotropies are larger for all the samples than the Vp anisotropies. The dolerite has the weakest velocity anisotropy (0.8 %) and is essentially isotropic (Table 6.6). This correlates well with the homogenous and non-foliated nature of the dolerite that was observed in thin section (see Figure 6.94). Of the remaining samples, the carbonaceous shale sample (sample W42) exhibit the highest degree of seismic P-wave anisotropy (11.4 %) (see Table 6.6).

The samples could not be placed under stress during the anisotropy measurements, because of the small contact areas of the transducers. Our equipment only allows us to place the larger transducers (54.8 mm) under uniaxial stress. These transducers would have been significantly larger than the samples themselves, and would not have yielded accurate results.

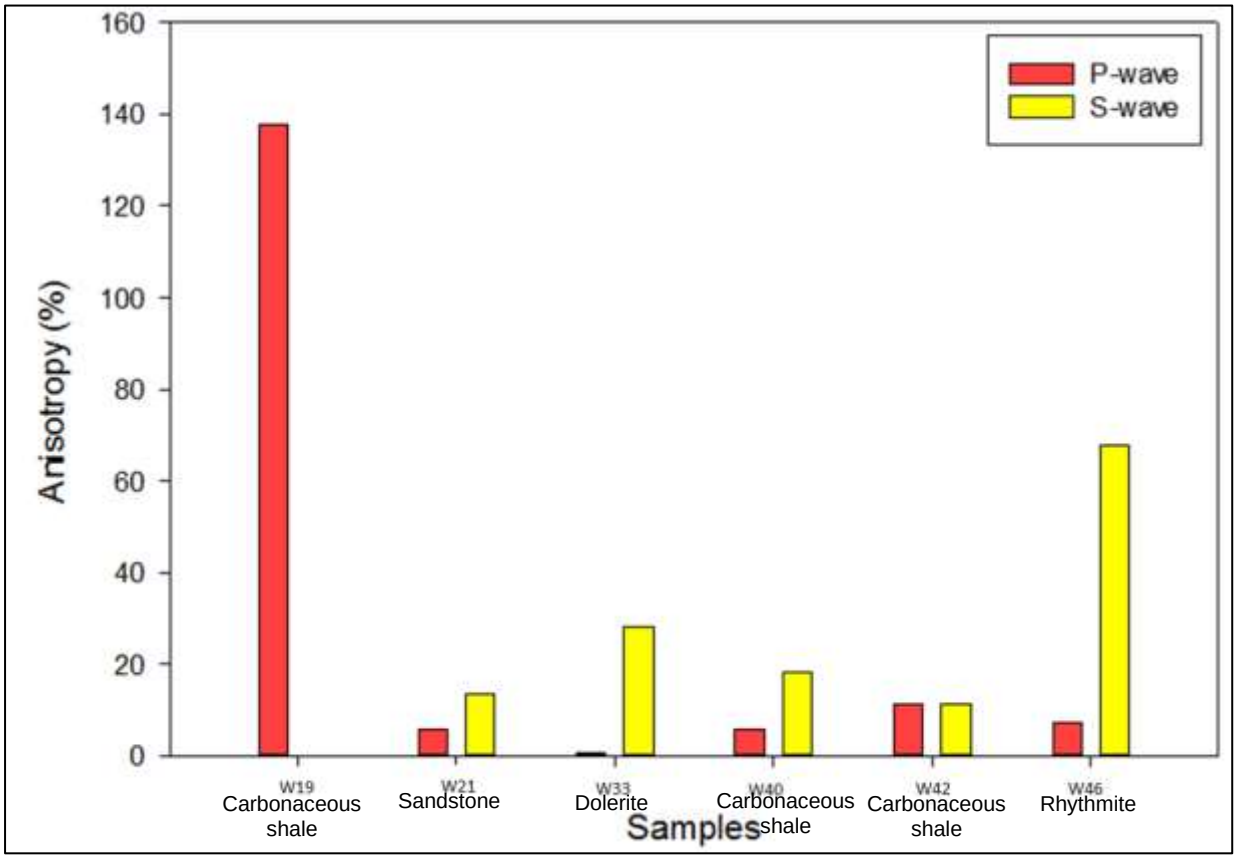

Figure 7.43: The P- and S-wave seismic anisotropies of samples based on seismic velocity measurements on samples in two orthogonal directions.

The results also allow us to establish the correlation between the seismic anisotropy, mineral orientation and micro-fracture orientation of some the samples from borehole KWV (see Table 6.7). The carbonaceous shale sample (sample W19) exhibit the greatest seismic velocity in the direction perpendicular to the long axis of the sample, and perpendicular to the orientation of micro-fractures in the sample. However, we have established that the seismic velocity results from this sample are inaccurate, and the sample's results are not discussed further here.

It is important to note that the cause of any of the micro-fractures that were observed in the x-ray tomography results are not known. The cracks could have been natural, or artificial through the extraction and sampling procedures. It could also have been introduced during the application of uniaxial stress.

The sandstone sample (sample W21) exhibits micro-fractures oriented perpendicular to the long axis of the sample (see Table 6.7). Minerals in the sample are oriented parallel to the micro-fractures, where the seismic velocity is largest. The dolerite sample is essentially homogeneous and isotropic. Seismic waves are thus not expected to be affected by micro-fractures or foliation in the dolerite.

The carbonaceous shale samples (samples W40 and W42) also have micro-fractures and mineral foliation oriented perpendicular to the long axis of the samples. Since thin section analysis did not yield useful data for the rhythmite sample (sample W46), the only relationship that could be established is between the seismic anisotropy and the micro-fracture orientations in the sample. The micro-fracture lines are oriented perpendicular to the wave propagation direction, and the seismic wave may be slow along this direction.

7.5. Implications for seismic reflectivity

Figure 6.98c indicates the reflections that might be expected during a reflection seismic survey. Multiple reflections can be observed in this seismogram. Most of the stratigraphic units have a reflection coefficient large enough to produce an observable reflection in a seismic survey. The contact between the Pluto's Vale Member and the Whitehill Formation has a Rc of 15%, which is large enough to be imaged by a reflection seismic survey. This implies that the top of the Whitehill Formation, which is the formation of interest in hydrocarbon exploration, may be imaged by the technique. Reflection seismic exploration for hydrocarbons, specifically targeting the Whitehill Formation of the lower Ecca Group, is thus feasible in the eastern part of the Main Karoo Basin, at least in terms of acoustic impedance contrast. However, the seismic imaging also depends on the size and the geometry of the target. The bottom of the Whitehill Formation (Rc ~ 2%), however, cannot be seismically imaged.

The reflections are not altered significantly by the anisotropy in the rocks (see Figure 6.100). All major reflections are still present and easily distinguished in the seismograms. It is worth noting that the synthetic seismogram does not incorporate attenuation or geometrical spreading of the source wave. It is also important to note that the seismic velocities were measured at low frequencies, which are not representative of the reflection seismic surveys. Measuring at high frequencies was not possible with our experimental set-up, particularly when compressing the samples at the same time. While we aim to carry out these measurements in the near future, the current measurements provide first-hand information about the potential acoustic impedance contrast that may exists between different rock units. The fact that even at low frequencies the significant velocity contrast is observed between

most lithological units suggests that the ultra-high frequency measurements may provide the same result.

The synthetic seismogram does not incorporate attenuation or geometrical spreading of the source wave.

8. Conclusions

The physical properties (seismic velocity, bulk density, porosity, micro-fractures) and mineralogy of rocks from borehole KWV in the eastern Main Karoo Basin have been investigated in this study. Possible correlations between the physical properties have been examined. The seismic velocities and bulk densities of the samples were also used to generate synthetic seismograms of the borehole, to determine whether the reflection seismic method would be successful in mapping the possible hydrocarbon deposit in the Main Karoo Basin.

Pyrite-bearing shale and sandstone samples exhibit higher seismic velocities than the average seismic velocity of shale and sandstone samples in the borehole. The bulk densities appear to be unaffected by the pyrite in the samples.

The seismic velocities of most samples from borehole KWV increase as a function of uniaxial stress. Therefore the samples seem to have pores and oriented micro-fractures that close up with the application of uniaxial stress. The saturation stress and the net change in seismic velocities do not correspond with the sample depths, porosities or lithologies.

The porosities of all the samples from borehole KWV are small enough (< 5%) to be considered as having an insignificant contribution to the seismic velocities of the samples. There was no relationship between the porosities and the bulk densities. There was also no relationship between the bulk densities and the seismic velocities of the samples. This implies that micro-fractures in the rocks may exert a stronger control on Vp than the bulk density.

The micro-fracture orientations and foliation directions of the samples that were analysed are roughly perpendicular to the wave propagation direction (long axis of the sample). The samples also display some degree of velocity anisotropy. The seismic velocity is generally the greatest in the same plane and direction as the micro-fractures and mineral SPO. The seismic wave would thus be expected to propagate slowly in this direction during reflection seismic exploration for hydrocarbon deposits. Based on the synthetic seismogram results of borehole KWV, the top of the Whitehill Formation is expected to be seismically imaged due to a significant reflection coefficient (Rc ~ 15%), while the bottom of the formation is unlikely to be mapped seismically due to a low reflection coefficient (Rc ~ 2%). The seismic wave velocities show notable anisotropy, especially in the shale samples, which points to the pyrite orientations dominant in the samples as the cause of this anisotropy. This implies that velocity anisotropy should be incorporated in future seismic survey designs, because these could generate seismic reflections from different directions.

This study improves our understanding of the seismic velocities of some major rock types and hydrocarbon deposits of South Africa, which is important for the interpretation of surface seismic data, as well as for the design of deep exploration programs. Comprehensive knowledge of physical properties, including bulk density, P- and S-wave velocities and anisotropy is essential for robust interpretation of seismic data in soft rock environments and will be hopefully routinely carried out in South Africa in the future.

Recommendations

To address any limitations of the analyses conducted and the results obtained in this study, we propose the following recommendations:

The seismic velocities should be measured in a quiet environment where no laboratory noise can interfere with the results.

The core samples could be analysed with x-ray tomography before the application of uniaxial stress, and then again afterward, to establish or eliminate this procedure as the cause of the micro-fractures.

The use of a confining pressure system may yield more accurate results.

The heating of samples could also yield useful results to quantify the effect of temperature on physical properties.

References

Aarnes, I., Svensen, H., Polteau, S. and Planke, S., 2011. Contact metamorphic devolatilization of shales in the Karoo Basin, South Africa, and the effects of multiple sill intrusions. *Chemical Geology*, 281 pp. 181-194.

Baiyegunhi, C., Oloniniyi, T.L. and Gwavava, O., 2014. The correlation of dry density and porosity of some rocks from the Karoo Supergroup: A case study of selected rock types between Grahamstown and Queenstown in the Eastern Cape Province, South Africa. *IOSR Journal of Engineering*, 04(12), pp. 30-40.

Birch, F., 1960. The velocity of compressional waves in rocks to 10 kilobars, part 1. *Journal of Geophysical Research*, 65(4), pp. 1083-1102.

Bräuer, B., Ryberg, T. and Lindeque, A.S., 2007. Shallow seismic velocity structure of the Karoo Basin, South Africa. *South African Journal of Geology*, 110, pp. 439-448.

Cadle, A.B., Cairncross, B., Christie, A.D.M. and Roberts, D.L., 1993. The Karoo Basin of South Africa: Type basin for the coal-bearing deposits of southern Africa. *International Journal of Coal Geology*, 23, pp. 117-157.

Catuneanu O, Hancox PJ, and Rubidge BS., 1998. Reciprocal flexural behaviour and contrasting stratigraphies: a new basin development model for the Karoo retro-arc foreland system, South Africa. *Basin Research,* 10, pp. 417-439.

Christensen, N.I., 1996. Poisson's ratio and crustal seismology. *Journal of Geophysical Research*, 101(B2), pp. 3139-3156.

CIMERA (n.d.) KARIN; Borehole KWV. CIMERA n.d. available from <http://www.CIMERA.co.za/index.php/karin-feedback>. Viewed 09/03/2016.

Cole, D.I., Robey, K., Chevallier, L. and Viljoen, J., 2011. Report on the geology of shales with a gas potential in the Main Karoo Basin of South Africa. *Council of Geoscience,* pp. 1-27.

Dentith, M. and Mudge, S.T., 2014. Geophysics for the Mineral Exploration Geoscientist. Cambridge University Press: New York, pp. 515.

De Wit, M.J., 2011. The great shale debate in the Karoo. *South African Journal of Science*, 107(7/8), pp. 1-9.

Domenico, S.N., 1977. Elastic properties of unconsolidated porous sand reservoirs. *Geophysics*, 42(7), pp. 1339-1368.

Fatti, J.L., 1987. Reflection seismic surveys in the Karoo Basin by Soekor. *SAGA yearbook*, pp. 22-30.

Fatti, L. and du Toit, J.J.L., 1970. A regional reflection-seismic line in the Karoo basin near Beaufort West. *Geological Society of South Africa - Transcations and Proceedings*, 73, pp. 17-28.

Fourie, F.D., 2003. Application of electroseismic techniques to geohydrological investigations in Karoo rocks. Doctor of Philosophy, University of the Free State.

Gadallah, M. R. and Fisher, R., 2009. Exploration Geophysics: An introduction. Springer-Verlag: Berlin, pp. 262.

Geel, C., DeWit, M., Booth, P., Schulz, H-M. and Horsfield, B., 2015. Palaeo-environment, diagenesis and characteristics of Permian black shales in the lower Karoo Supergroup flanking the Cape Fold Belt near Jansenville, Eastern Cape, South Africa: Implications for the shale gas potential of the Karoo Basin. *South African Journal of Geology*,118(3), pp. 249-274.

Geel, C., Schulz, H.M., Booth, P., DeWit, M. and Horsfield, B., 2013. Shale gas characteristics of permian black shales in South Africa: Results from recent drilling in the Ecca Group (Eastern Cape). *Energy Procedia,* 40, pp. 256-265.

Han, D., Nur, A. and Morgan, D., 1986. Effects of porosity and clay content on wave velocities in sandstones. *Geophysics*, 54(11), pp. 2093-2107.

Hoffman, J.W. and De Beer, F.C., 2012. Characteristics of the micro-focus x-ray tomography facility (MIXRAD) at NECSA in South Africa. *18th World Conference on Nondestructive Testing.* Durban, South Africa, 16-20 April 2012.

Ivankina, T.I., Zel, I.Y., Lokajicek, T., Kern, H., Lobanov, K.V. and Zharikov, A.V., 2017. Elastic anisotropy of layered rocks: Ultrasonic measurements of plagioclase-biotite-muscovite (sillimanite) gneiss versus texture-based theoretical predictions (effective media modelling). *Tectonophysics*, 712-713, pp. 82-94.

Jarman, D.J., 2012. Comparison of rock density determination methods used in South African platinum mines for resource planning purposes. Master of Science, University of Pretoria.

Ji, S., Shao, T., Michibayashi, K., Oya, S., Satsukawa, T., Wang, Q., Zhao, W. and Salisbury, M.H., 2015. Magnitude and symmetry of seismic anisotropy in mica- and amphibole-bearing metamorphic rocks and implications for tectonic interpretatation of seismic data from the southeast Tibetan Plateau. *Journal of Geophysical Research: Solid Earth*, 120, pp. 6404-6430.

Johnson, M.R., Van Vuuren, C.J., Hegenberger, W.F., Ket, R. and Shoko, U., 1996. Stratigraphy of the Karoo Supergroup in southern Africa: an overview. *Journal of African Earth Sciences*, 23(1), pp. 3-15.

Johnson, M.R., Anhaeusser, C.R. & Thomas, R.J., 2006. The Geology of South Africa. 1st Ed. Geological Society of South Africa: Johannesburg & Council for Geoscience: Pretoria, pp. 691

Kassab, M.A. and Weller, A., 2013. Porosity estimation from compressional wave velocity: A study based on Egyptian carbonate samples. *Journal of Earth Science and Engineerin*g, 3, pp. 314-321.

Lillie, R.J., 1999. Whole earth geophysics: an introductory textbook for geologists and geophysicists. Upper Saddle River, New Jersey, Prentice Hall.

Lin, J., Sturhahn, W., Zhao, J., Shen, G., Mao, H. and Hemley, R.J., 2005. Sound velocities of hot dense iron: Birch's law revisited. *Science*, 308, pp. 1892-1894.

Lindeque, A., de Wit, M.J., Ryberg, T., Weber, M. and Chevallier, L., 2011. Deep crustal profile across the southern Karoo Basin and Beattie Magnetic Anomaly, South Africa: an integrated interpretation with tectonic implications. *South African Journal of Geology*, 114(3-4), pp. 265-292.

Malehmir, A., Andersson, M., Urosevic, M. and Mikhaltsevitch, V., 2013. Experimental estimation of velocities and anisotropy of a series of Swedish crystalline rocks and ores. *Geophysical Prospecting,* 61, pp. 153-167.

Manger, G.E., 1963. Porosity and bulk density of sedimentary rocks. *Geological Survey Bulletin*, (1144-E), USGPO, pp. E1-E55.

Nesse, W.D., 2004. Introduction to optical mineralogy. Oxford University Press: New York, pp. 348.

Nkosi, N.Z., Manzi, M.S.D. and Drennen, G.R., 2016. Seismic velocities and their dependence on mineralogy and stress: Implication for the poor seismic reflectivity of the world's deepest gold orebody, Witwatersrand Basin (South Africa). *Studia Geophysica et Geodaetica*, pp. 48.

Park, R.G., 1997. Foundations of Structural Geology 3rd Ed. Routledge; Taylor and Francis Group: London and New York, pp. 202.

Prasanna Lakshmi, K.J., Senthil Kumar, P., Vijayakumar, K., Ravinder, S., Seshunarayana, T. and Sen, M.K., 2014. Petrophysical properties of the Deccan basalts exposed in the Western Ghats escarpment around Mahabaleshwar and Koyna, India. *Journal of Asian Earth Sciences*, 84, pp. 176-187.

Punturo, R., Kern, H., Cirrincione, R., Mazzoleni, P. and Pezzino, A., 2005. P- and S-wave velocities and densities in silicate and calcite rocks from the Peloritani Mountains, Sicily (Italy): The effect of pressure, temperature and the direction of wave propagation. *Tectonophysics*, 409, pp. 55-72.

Pysklywec, R.N. and Mitrovica, J.X., 1999. The Role of subduction-induced subsidence in the evolution of the Karoo Basin. *The Journal of Geology,* 107, pp. 155-164. *Tectonophysics*, 409, pp. 55-72.

Qixian, L. and Bungey, H., 1996. Using compression wave ultrasonic transducers to measure the velocity of surface waves and hence determine dynamic modulus of elasticity for concrete. *Construction of Building Materials*, 10(4), pp. 237-242.

Rybach, L. and Buntebarth, G., 1982. Relationships between the petrophysical properties density, seismic velocity, heat generation, and mineralogical constitution. *Earth and Planetary Science Letters*, 57, pp. 367-376.

SACS (South African Committee for Stratigraphy), 1980. Stratigraphy of South Africa. Part 1 (Compiled by Kent). Lithostratigraphy of the Republic of South Africa, South West African/Namibia, and the Republics of Bophuthatswana, Transkei and Venda. Handbook 8, Geological Survey, South Africa, 690 pp.

Salisbury, M. H., Harvey, G. W. and Mathews, L., 2003. The acoustic properties of ores and host rocks in hardrock terranes. In: Eaton D. W., Milkereit B., Salisbury M. H., (Eds.),

Hardrock Seismic Exploration. Geophysical Development Series, 10, Society of Exploration Geophysics, pp. 9-19.

Scheiber-Enslin, S.E., Webb, S.J. and Ebbing, J., 2014. Geophysically plumbing the Main Karoo Basin, South Africa. *South African Journal of Geology*, 117 (2), pp. 275-300.

Schindler, M., Batzle, M.L. and Prasad, M., 2016. Micro X-ray computed tomography imaging and ultrasonic velocity measurements in tetrahydrofuran-hydrate-bearing sediments. *Geophysical Prospecting*, pp. 1-12.

Smith, R.M.H., 1980. The lithology, sedimentology and taphonomy of flood-plain deposits of the lower Beaufort (Adelaide Subgroup) strata near Beaufort West. *Transactions of the Geological Society of South Africa*, 83, pp. 399-413.

Smith, R.M.H., 1990. A Review of Stratigraphy and Sedimentary Environments of the Karoo Basin of South Africa. *Journal of African Earth Sciences*, 10(1/2), pp. 117-137.

Smith, R.M.H. and Botha-Brink, J., 2011. Morphology and composition of bone-bearing coprolites from the late Permian Beaufort Group, Karoo Basin, South Africa. *Palaeogeography, Palaeoclimatology, Palaeoecology*, 312, pp. 40-53.

Tankard, A., Welsink, H., Aukes, P., Newton, R. and Stettler, E., 2009. Tectonic evolution of the Cape and Karoo Basins of South Africa. *Marine and Petroleum Geology,* 26(8), pp. 1379-1412.

Vermeulen, P.D., 2012. A South African perspective on shale gas hydraulic fracturing. *International Mine Water Association: Annual conference*, pp. 149-156.

Vogt, J., 2009. Elastic media and seismic waves. *Course 210392: Earth and Planetary Physics*. Jacobs University Bremen.

Warren, C.H., 2013. Shale gas in South Africa. *African Security Review,* 22(1), pp. 67-73.

Wilson A, Flint S, Payenberg T, Tohver E and Lanci L., 2014. Architectural styles and sedimentology of the fluvial lower Beaufort Group, Karoo Basin, South Africa. *Journal of Sedimentary Research*, 84, pp. 326-348.

Wyllie, M.R.J., Gregory, A.R. and Gardner, G.H.F., 1958. An experimental investigation of factors affecting elastic wave velocities in porous media. *Geophysics*, 23(3), pp. 459-493.

Yilmaz, Ö., 2001. Seismic data analysis-Processing, inversion, and interpretation of seismic data. *Society of Exploration Geophysicists*, Tulsa, Oklahoma, 2027.

Zhang, R., Jiang, B. and Cao, W., 2002. Influence of sample size on ultrasonic phase velocity measurements in piezoelectric ceramics. *Journal of Applied Physics*, 91(12), pp. 10194-10198.

A. Appendix A – Seismic velocities

Table A.1: Data acquired to determine seismic velocities. P1 to P5 are the P-wave first arrival times for measurements 1 to 5 for each sample.

Sample name	Length (m)	P1 (µs)	P2 (µs)	P3 (µs)	P4 (µs)	P5 (µs)	<P> (µs)
W1	0.0800	16	15	15	16	16	16
W2	0.0517	85	46	46	46	46	54
W3	0.0786	35	28	35	33	31	32
W4	0.0696	13	13	14	14	14	14
W5	0.0750	25	23	21	21	23	23
W6	0.0802	16	15	15	15	16	15
W7	0.0511	10	9	9	9	9	9
W8	0.0804	23	18	17	16	17	18
W9	0.0733	32	32	36	36	36	34
W10	0.0580	40	26	28	29	30	31
W11	0.0800	41	26	27	29	27	30
W12	0.0803	16	14	14	13	13	14
W13	0.0699	38	36	40	44	42	40
W14	0.0714	41	47	42	41	41	43
W15	0.0792	17	18	18	18	19	18
W16	0.0808	16	16	16	16	16	16
W17	0.0524	37	25	41	41	39	37
W18	0.0803	18	18	18	18	18	18
W19	0.0410	19	24	30	30	30	27
W20	0.0351	16	15	15	13	15	15
W21	0.0804	14	15	15	15	15	15
W22	0.0809	13	15	14	14	14	14
W23	0.0752	25	26	24	23	23	24
W24	0.0802	38	44	39	39	39	40
W25	0.0798	15	15	15	15	15	15
W26	0.0800	20	19	19	19	19	19
W27	0.0720	12	12	12	12	12	12
W28	0.0580	19	14	14	14	15	15
W29	0.0800	14	14	14	14	14	14
W30	0.0878	18	18	18	18	18	18
W31	0.0803	23	22	22	22	22	22
W32	0.0757	17	17	18	18	18	18
W33	0.0800	13	13	13	13	13	13
W34	0.0802	18	18	18	18	18	18
W35	0.0789	16	16	16	16	15	16
W36	0.0890	16	16	17	17	17	16
W37	0.0733	13	14	15	15	15	14
W38	0.0706	13	12	12	12	12	12
W39	0.0740	12	12	12	13	14	13
W40	0.0522	12	12	12	12	12	12
W41	0.0587	12	11	11	11	11	11
W42	0.0803	17	17	17	17	17	17
W43	0.0801	16	17	17	17	17	17
W44	0.0784	45	31	31	31	31	34
W45	0.0800	16	16	16	16	16	16
W46	0.0600	59	59	58	61	59	59
W47	0.0803	22	18	18	17	17	19
W48	0.0803	17	16	16	16	16	16
W49	0.0803	15	15	15	15	15	15

Table A.2: Data acquired to determine seismic velocities. S1 to S5 are the S-wave first arrival times for measurements 1 to 5 for each sample.

Sample name	Length (m)	S1 (μs)	S2 (μs)	S3 (μs)	S4 (μs)	S5 (μs)	<S> (μs)
W1	0.0800	31	30	30	32	30	31
W2	0.0517	-	78	73	73	73	74
W3	0.0786	67	-	66	10	64	52
W4	0.0696	29	28	28	29	29	29
W5	0.0750	44	46	46	41	41	44
W6	0.0802	25	27	27	27	27	27
W7	0.0511	20	18	19	20	19	19
W8	0.0804	42	29	29	29	29	32
W9	0.0733	48	48	48	18	48	42
W10	0.0580	69	46	59	66	65	61
W11	0.0800	79	55	55	51	51	58
W12	0.0803	27	26	26	26	26	26
W13	0.0699	74	73	71	74	73	73
W14	0.0714	74	81	69	65	65	71
W15	0.0792	33	36	31	35	35	34
W16	0.0808	29	29	29	29	29	29
W17	0.0524	56	52	59	61	60	57
W18	0.0803	31	35	35	35	-	34
W19	0.0410	40	52	55	55	56	52
W20	0.0351	32	46	32	42	42	39
W21	0.0804	31	27	27	27	27	28
W22	0.0809	28	28	28	28	28	28
W23	0.0752	48	43	43	42	42	43
W24	0.0802	79	61	67	67	-	69
W25	0.0798	28	-	28	29	29	29
W26	0.0800	33	30	29	31	32	31
W27	0.0720	26	24	21	26	26	25
W28	0.0580	37	29	28	29	29	30
W29	0.0800	31	27	27	27	27	28
W30	0.0878	30	31	31	31	31	31
W31	0.0803	49	47	47	42	42	46
W32	0.0757	34	29	34	29	31	31
W33	0.0800	24	26	25	26	26	25
W34	0.0802	30	32	33	32	32	32
W35	0.0789	29	26	29	28	25	27
W36	0.0890	32	30	30	30	30	30
W37	0.0733	29	28	28	28	28	28
W38	0.0706	27	25	25	25	25	25
W39	0.0740	30	29	29	30	29	30
W40	0.0522	26	21	22	25	25	24
W41	0.0587	25	25	25	25	25	25
W42	0.0803	28	30	30	30	30	30
W43	0.0801	33	29	31	31	31	31
W44	0.0784	81	63	60	59	59	65
W45	0.0800	29	29	29	29	27	29
W46	0.1230	60	69	71	70	79	70
W47	0.0803	46	39	39	39	39	40
W48	0.0803	25	29	28	29	29	28
W49	0.0803	28	27	27	28	28	28

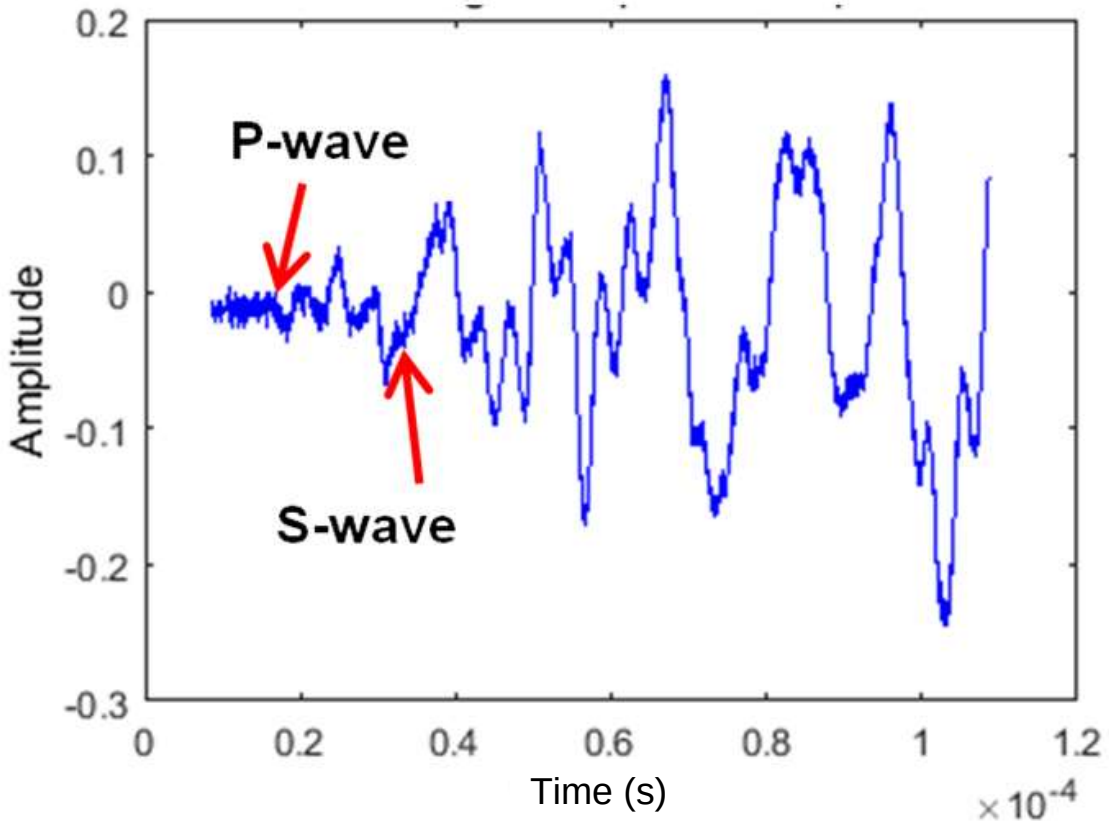

Figure A.1: The output waveform of sample W1.

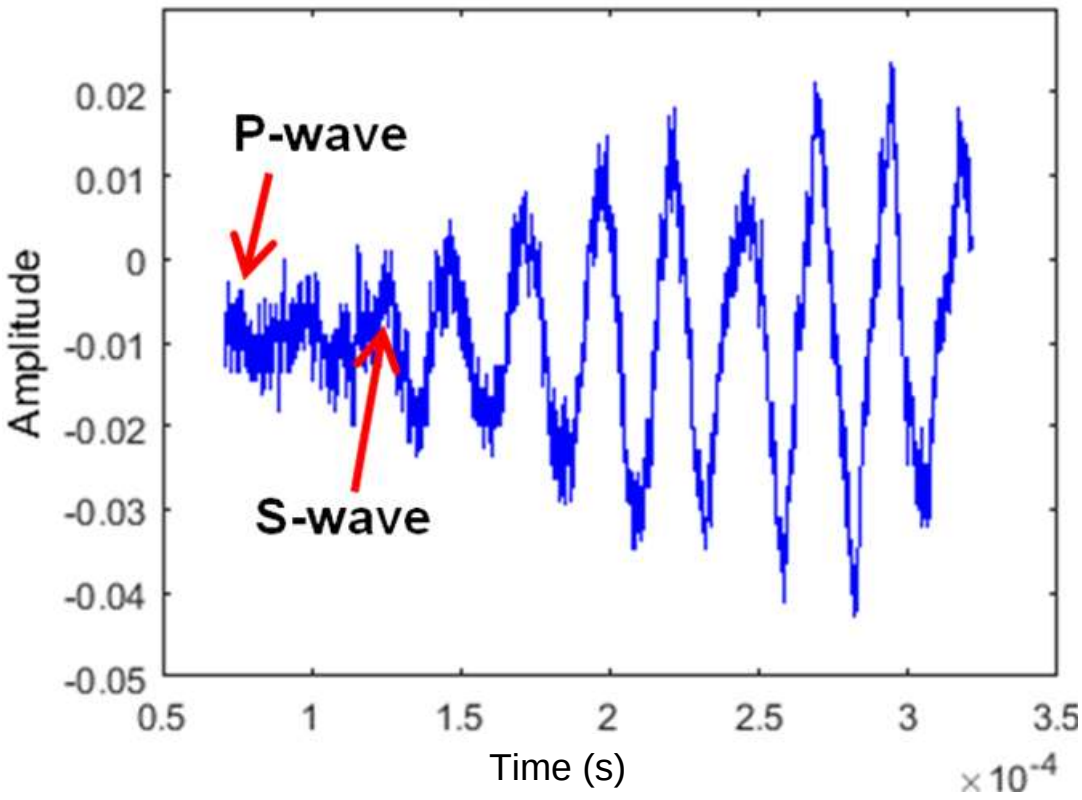

Figure A.2: The output waveform of sample W2

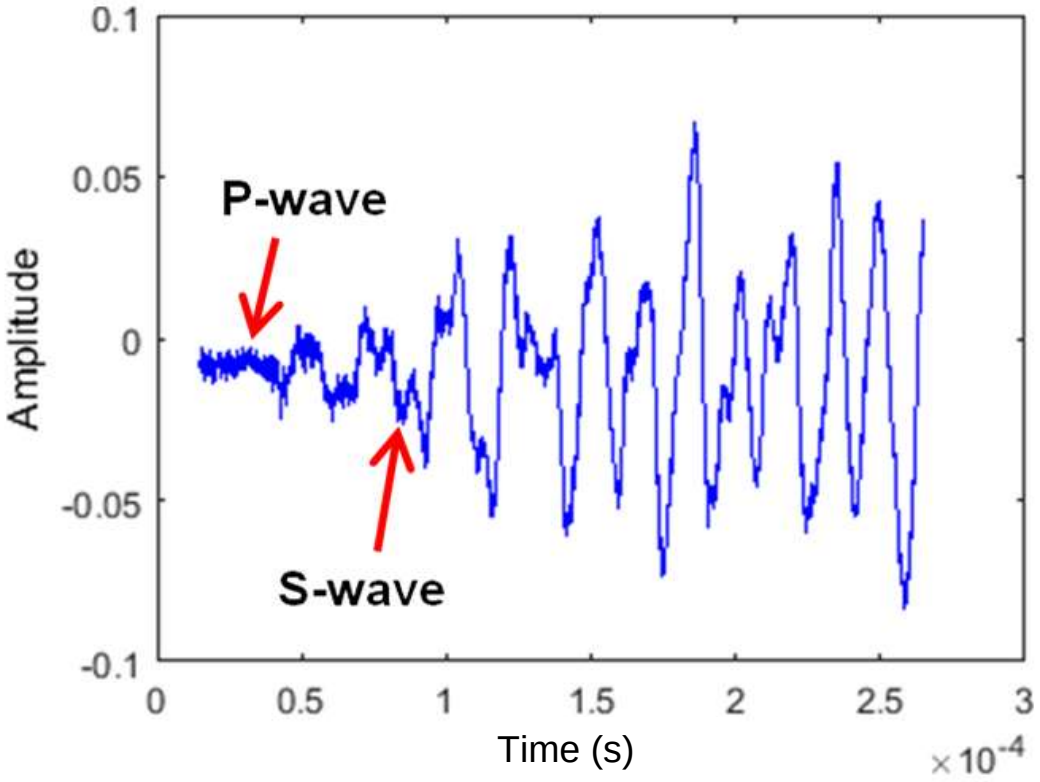

Figure A.3: The output waveform of sample W3

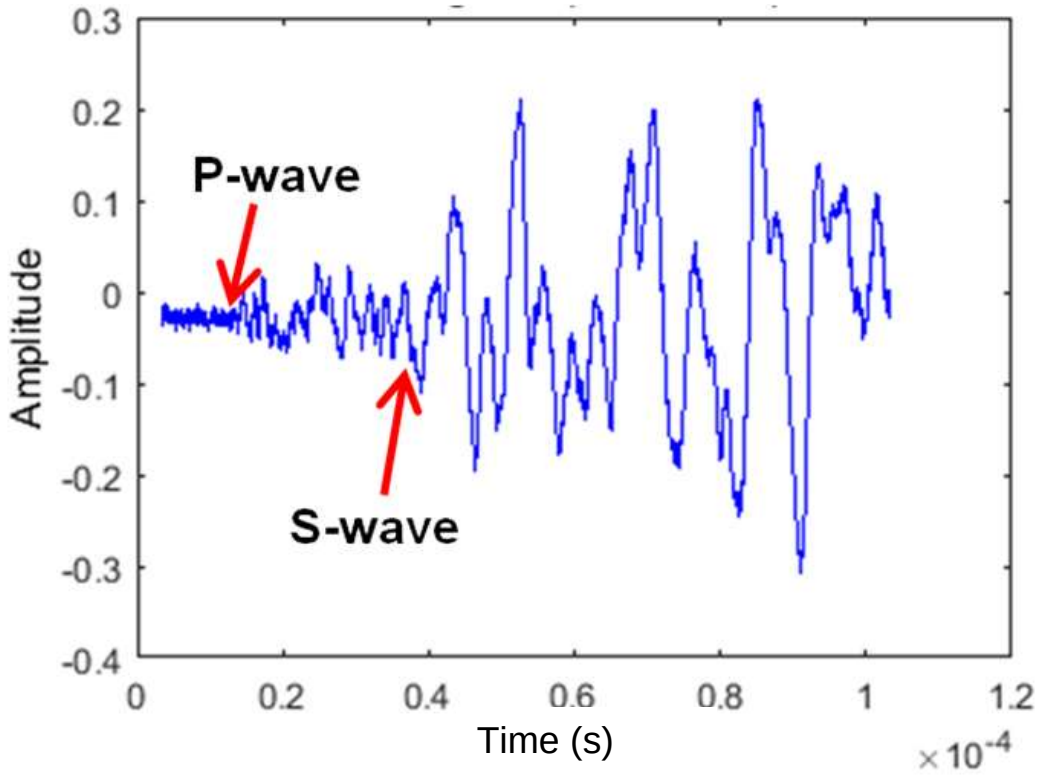

Figure A.4: The output waveform of sample W4

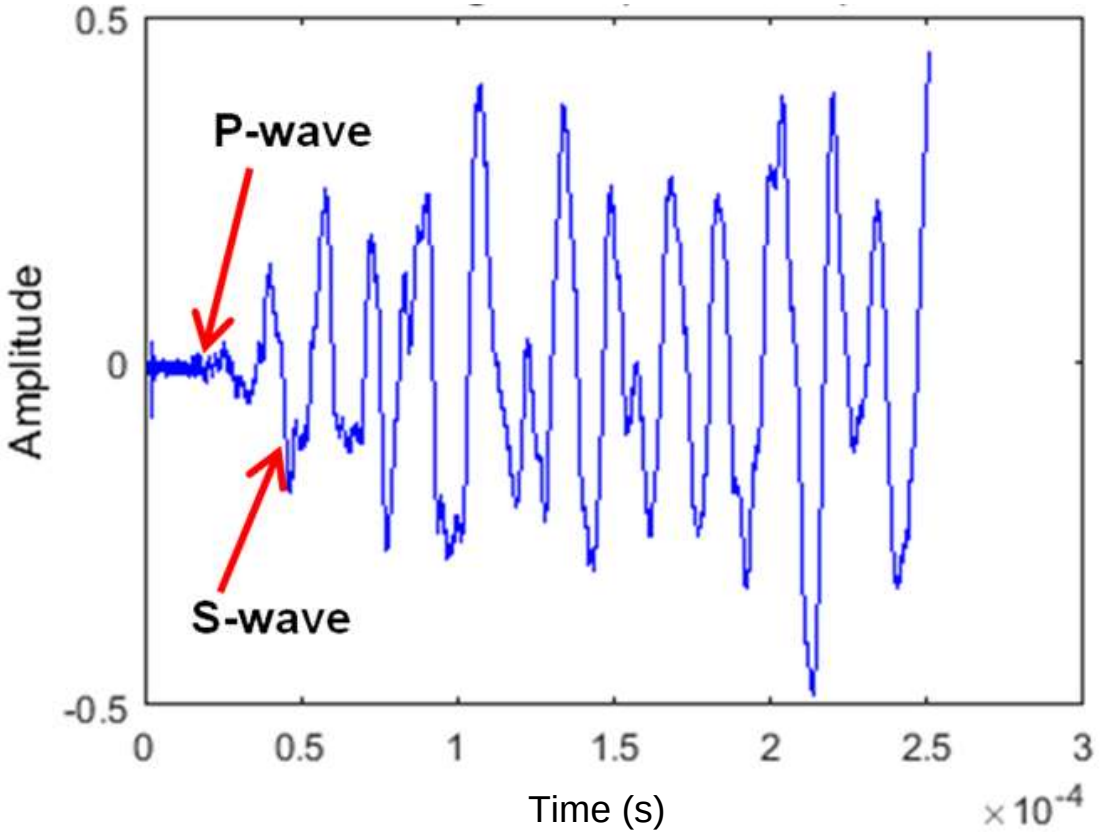

Figure A.5: The output waveform of sample W5

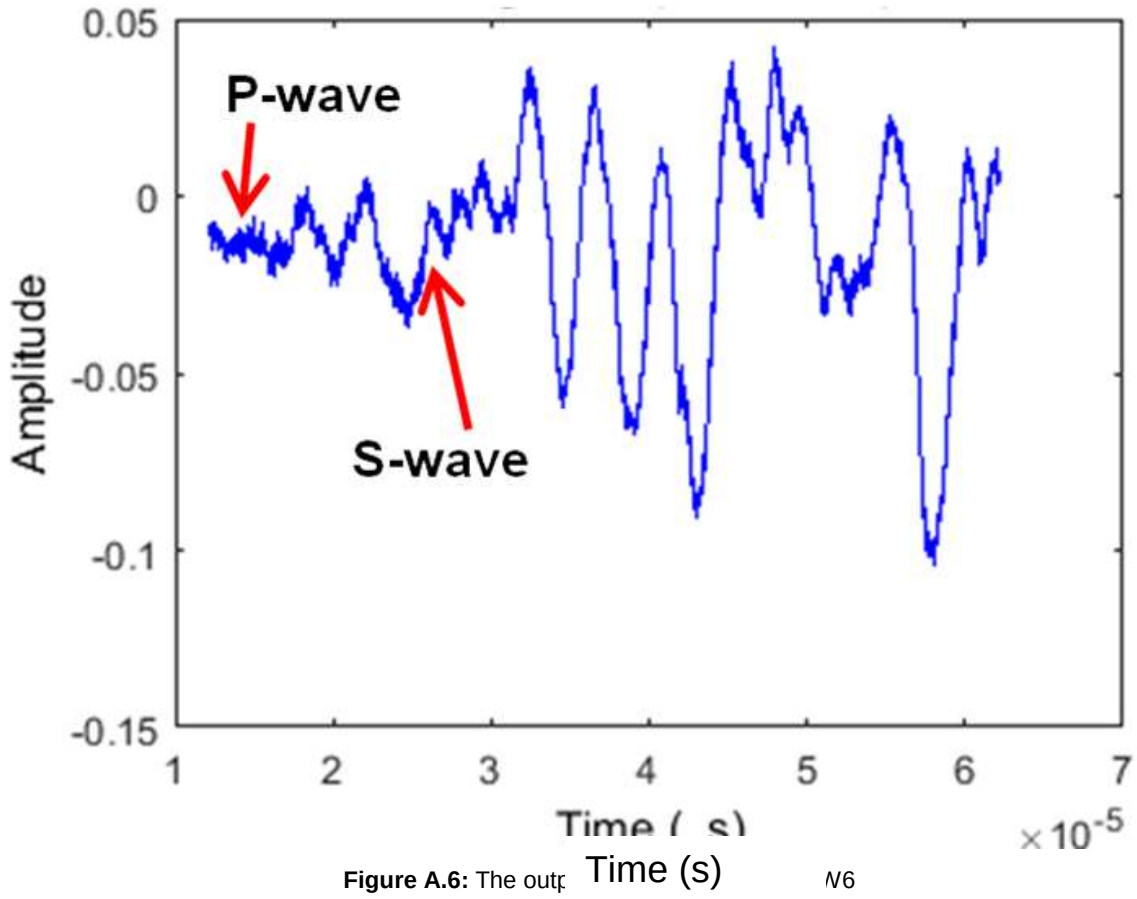

Figure A.6: The outp Time (s) W6

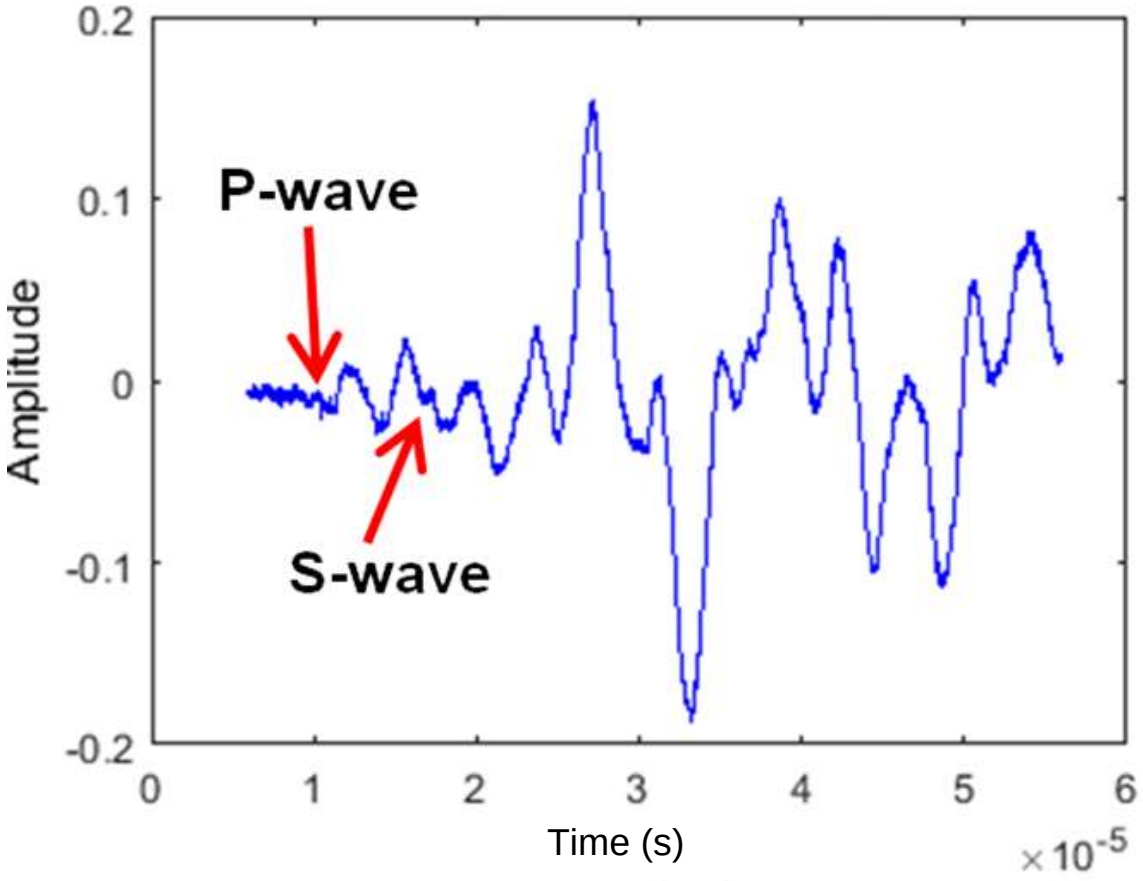

Figure A.7: The output waveform of sample W7

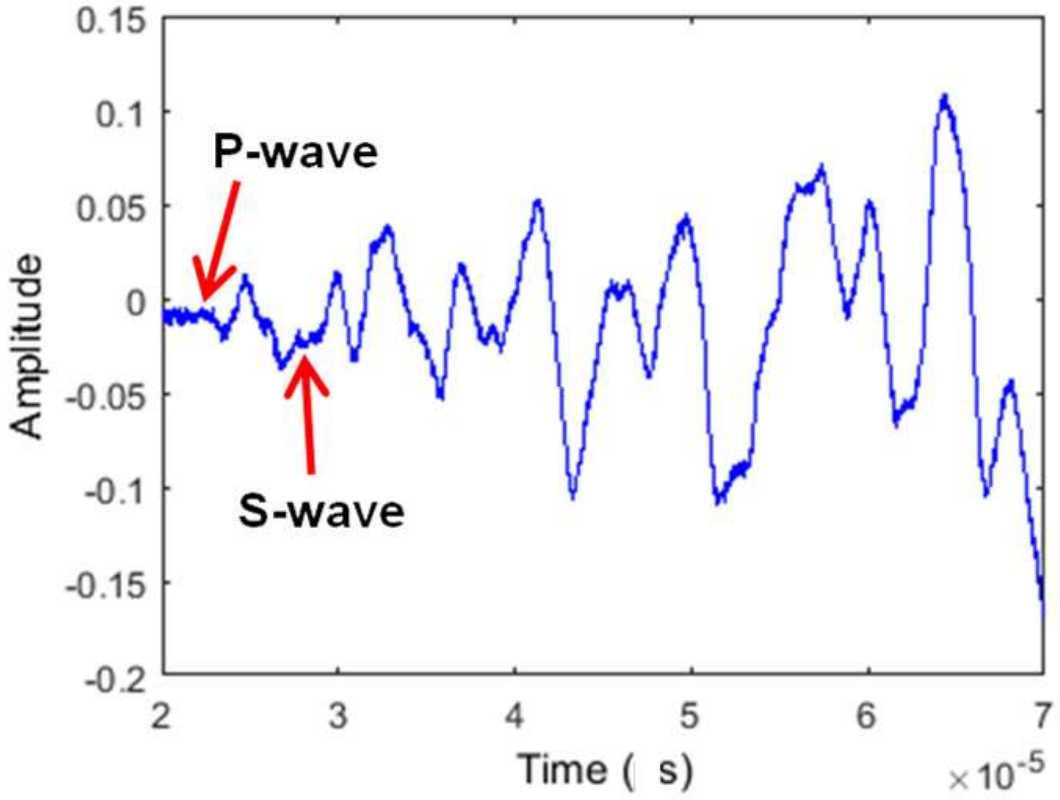

Figure A.8: The output waveform of sample W8

Time (s)

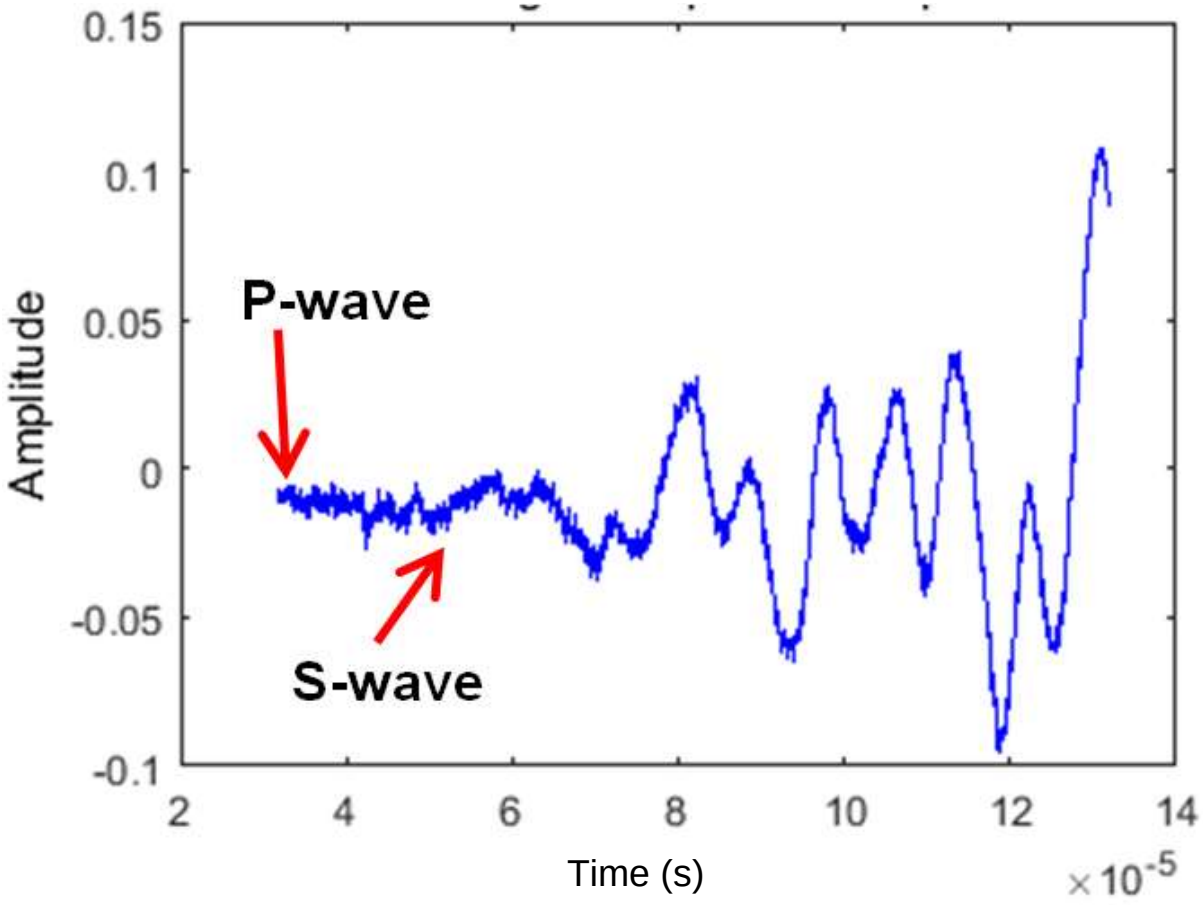

Figure A.9: The output waveform of sample W9

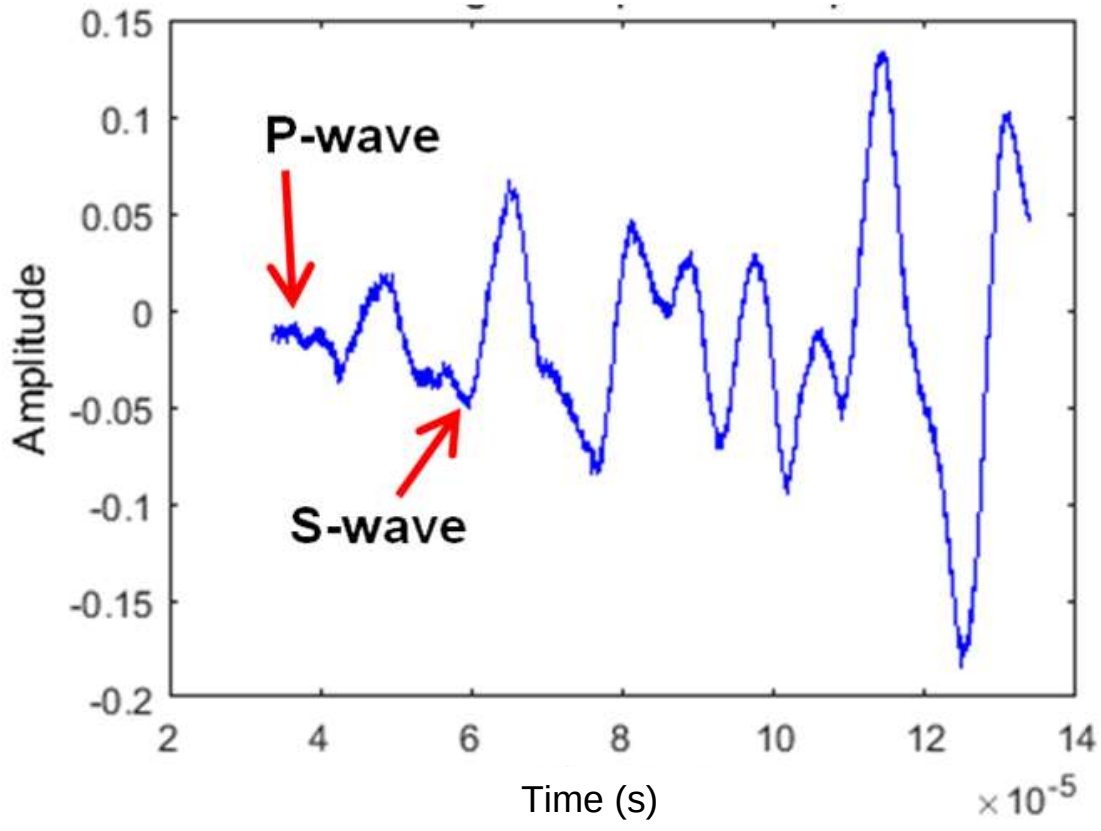

Figure A.10: The output waveform of sample W10

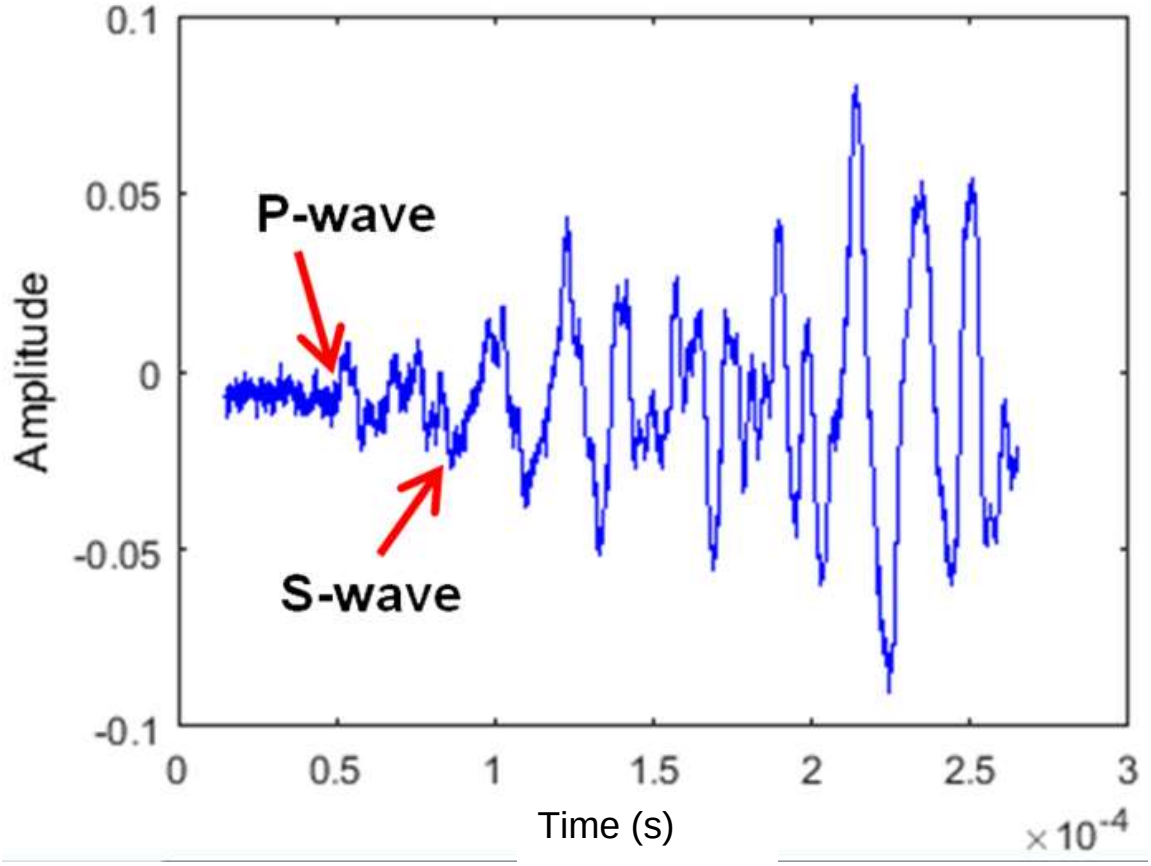

Figure A.11: The output waveform of sample W11

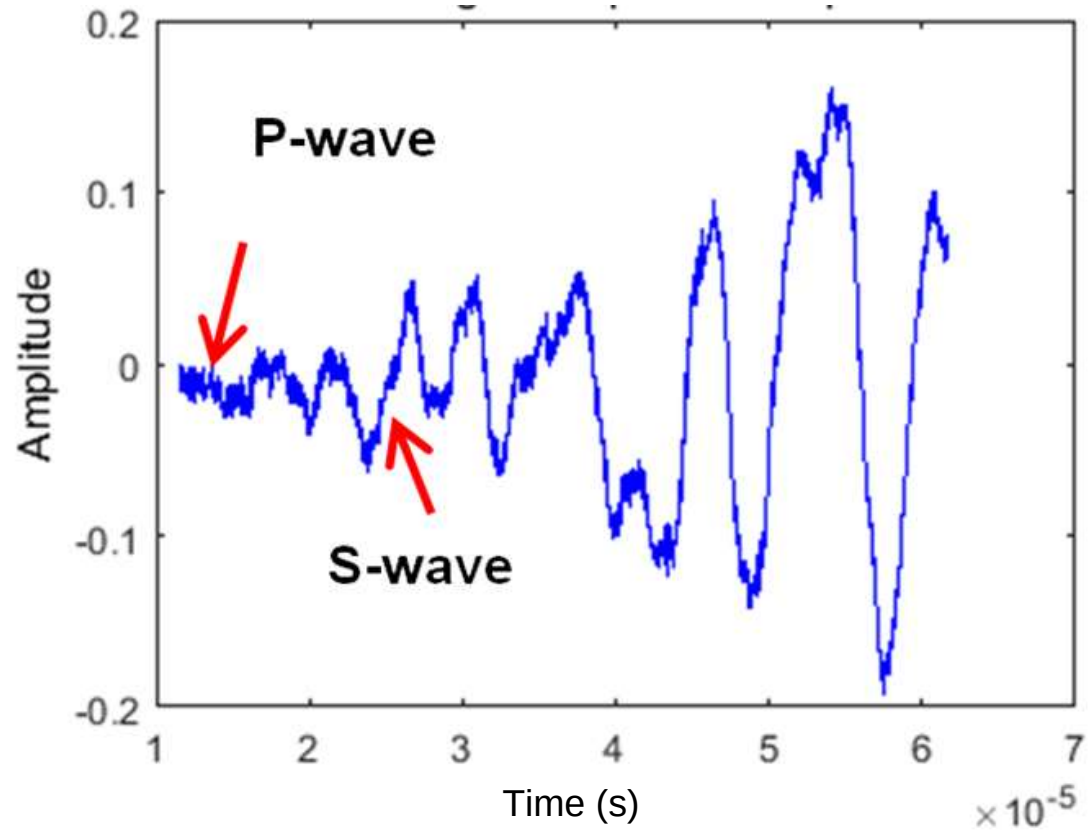

Figure A.12: The output waveform of sample W12

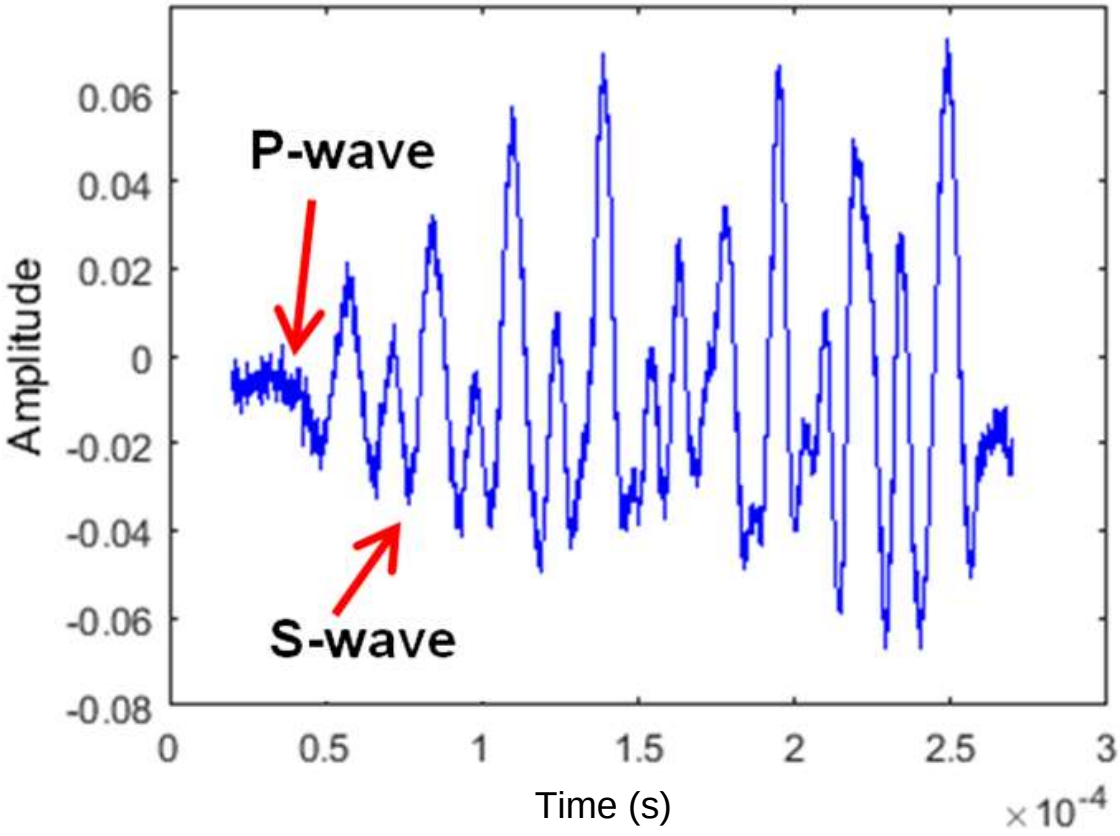

Figure A.13: The output waveform of sample W13

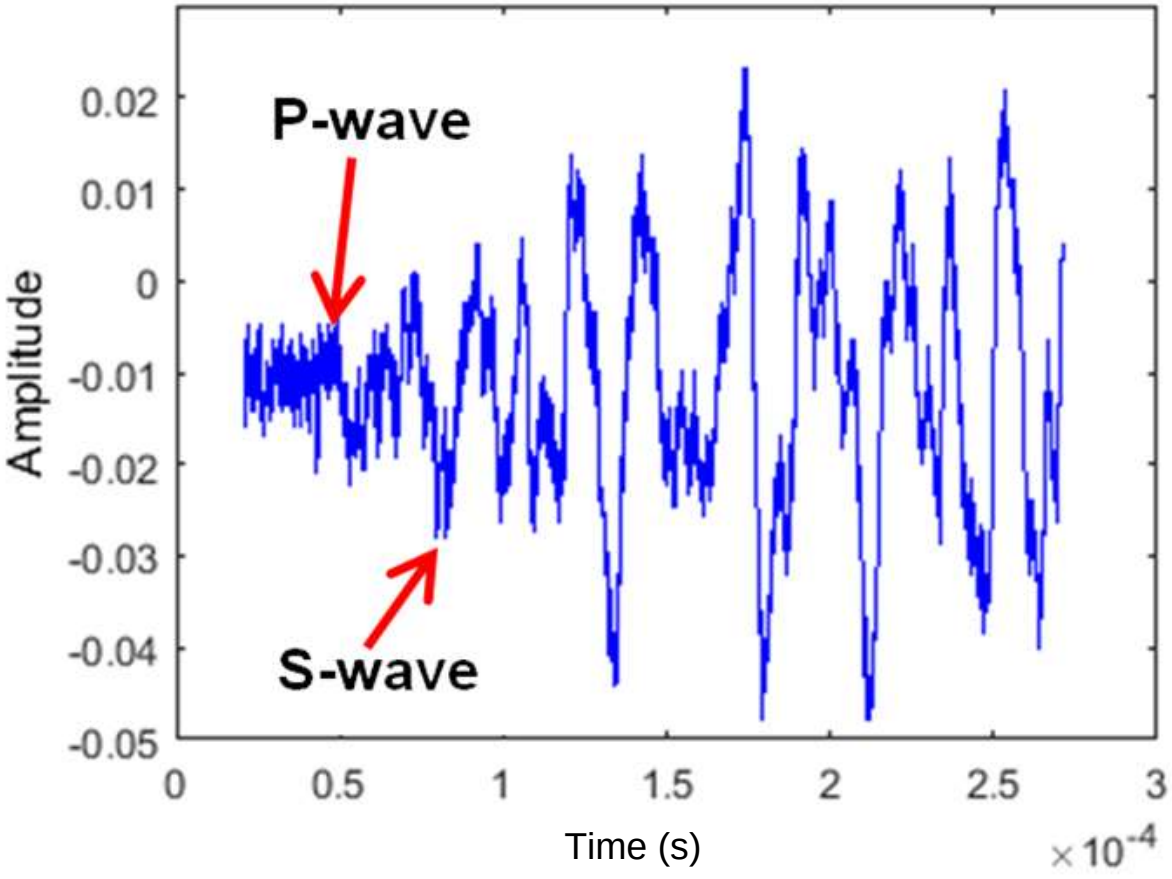

Figure A.14: The output waveform of sample W14

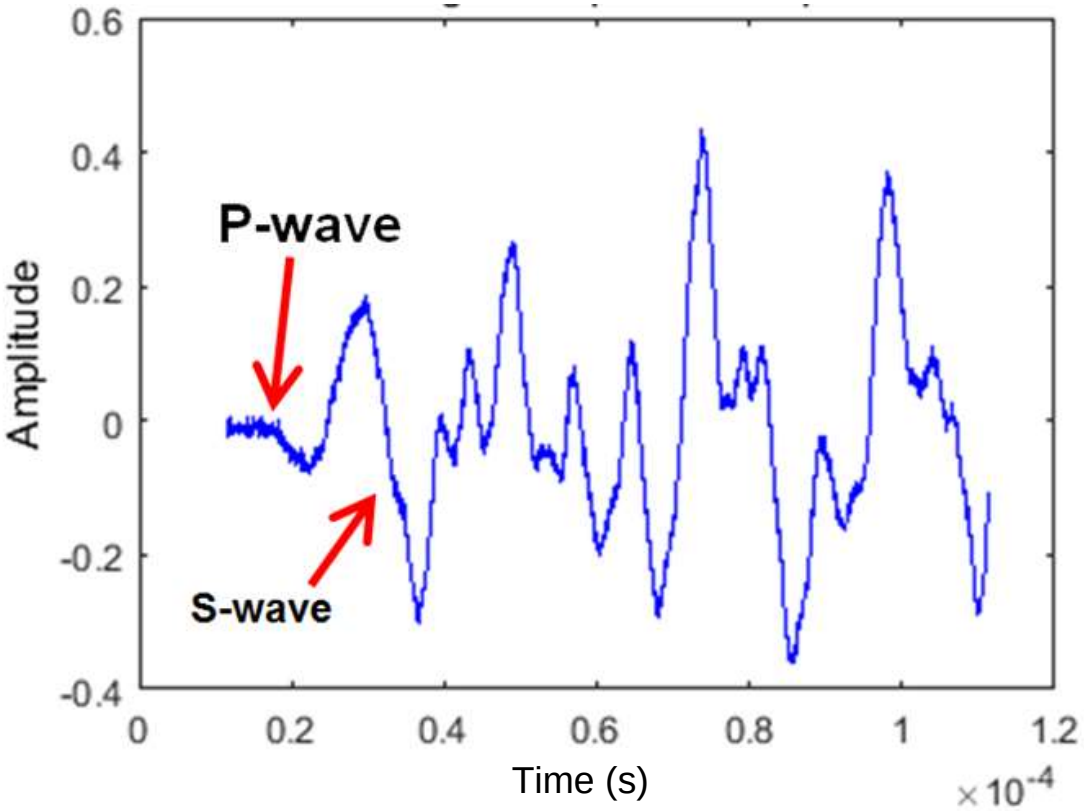

Figure A.15: The output waveform of sample W15

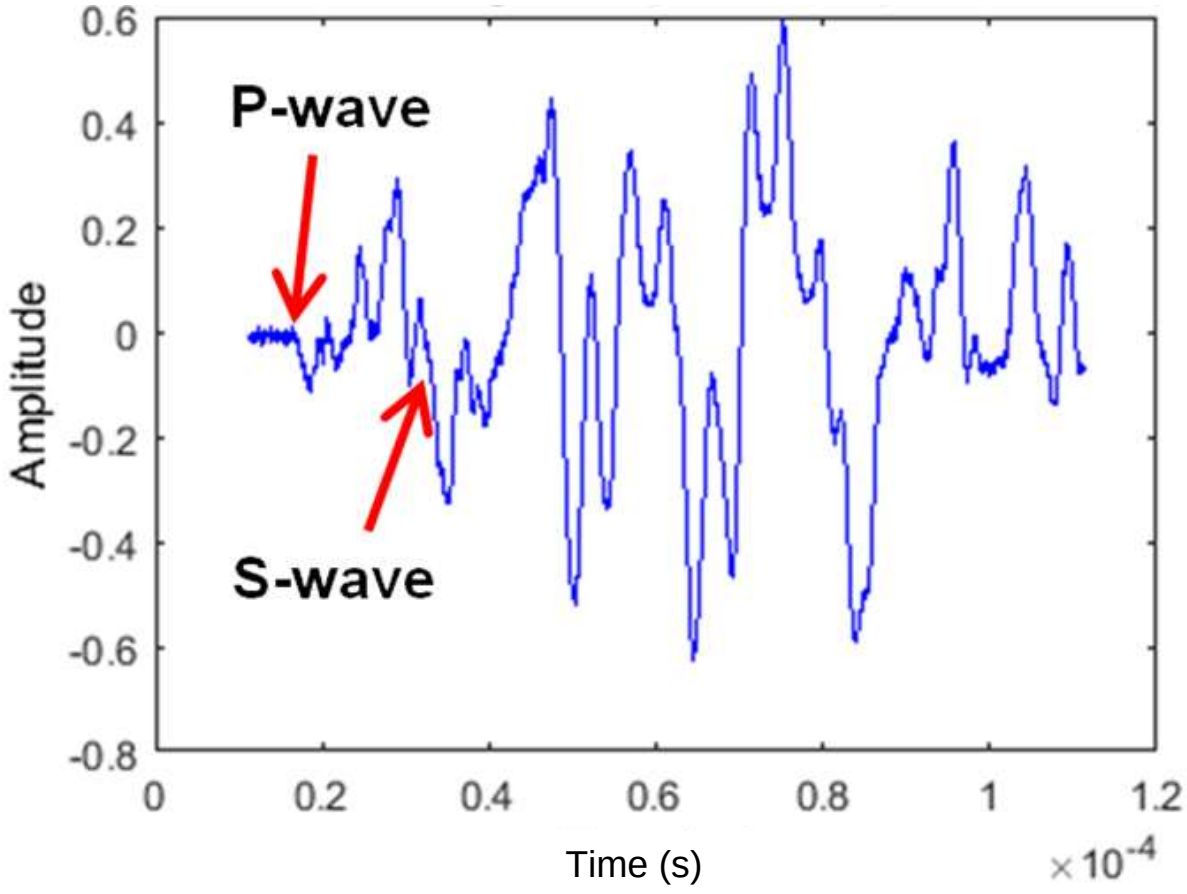

Figure A.16: The output waveform of sample W16

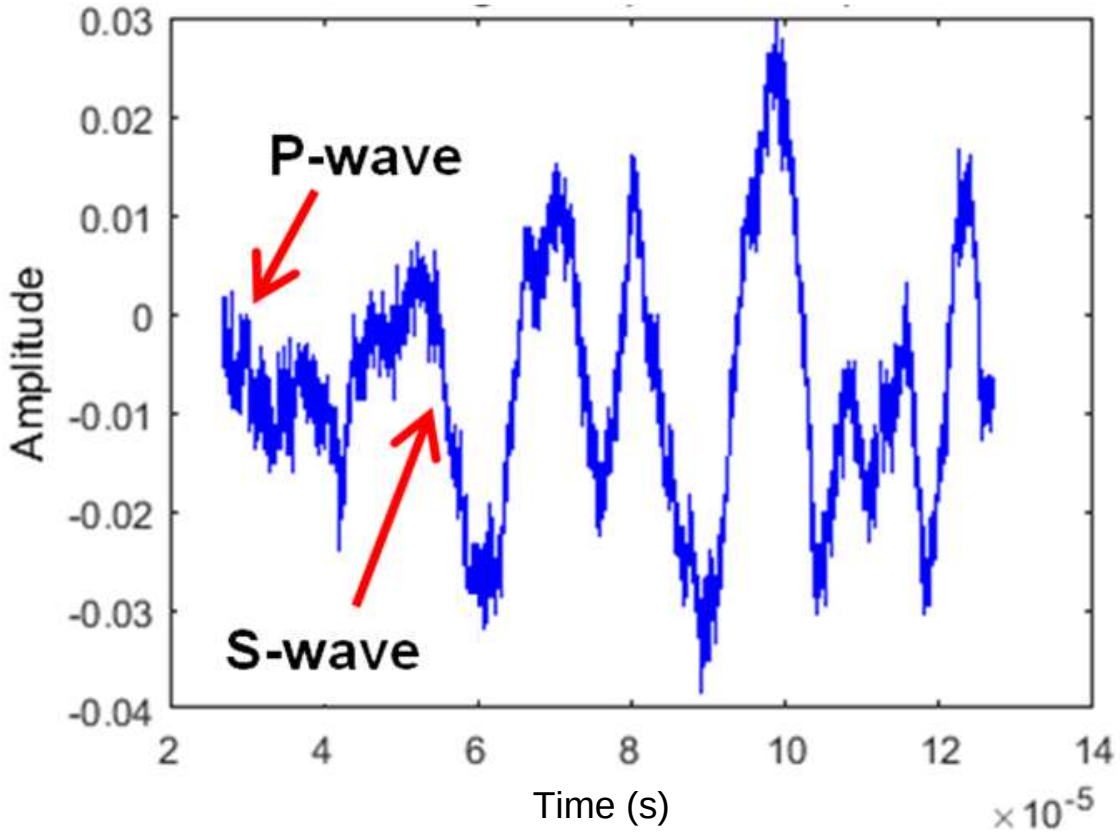

Figure A.17: The output waveform of sample W17

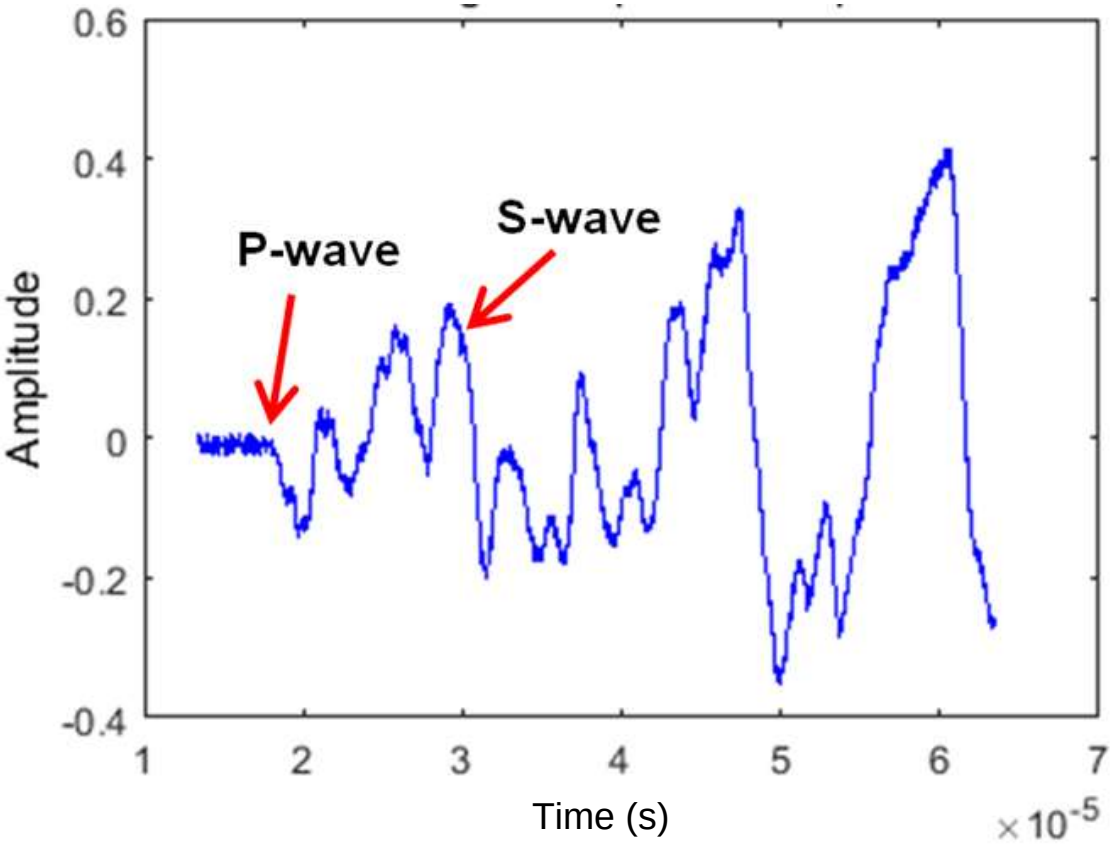

Figure A.18: The output waveform of sample W18

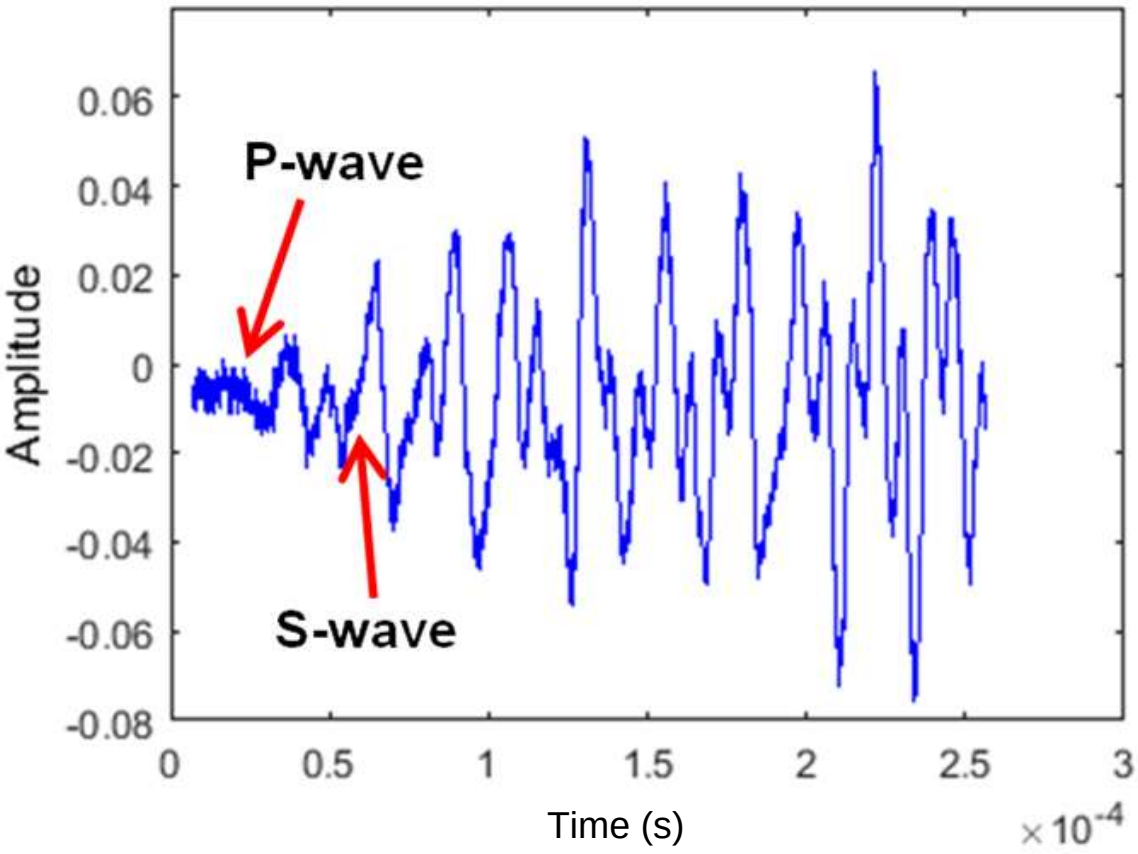

Figure A.19: The output waveform of sample W19

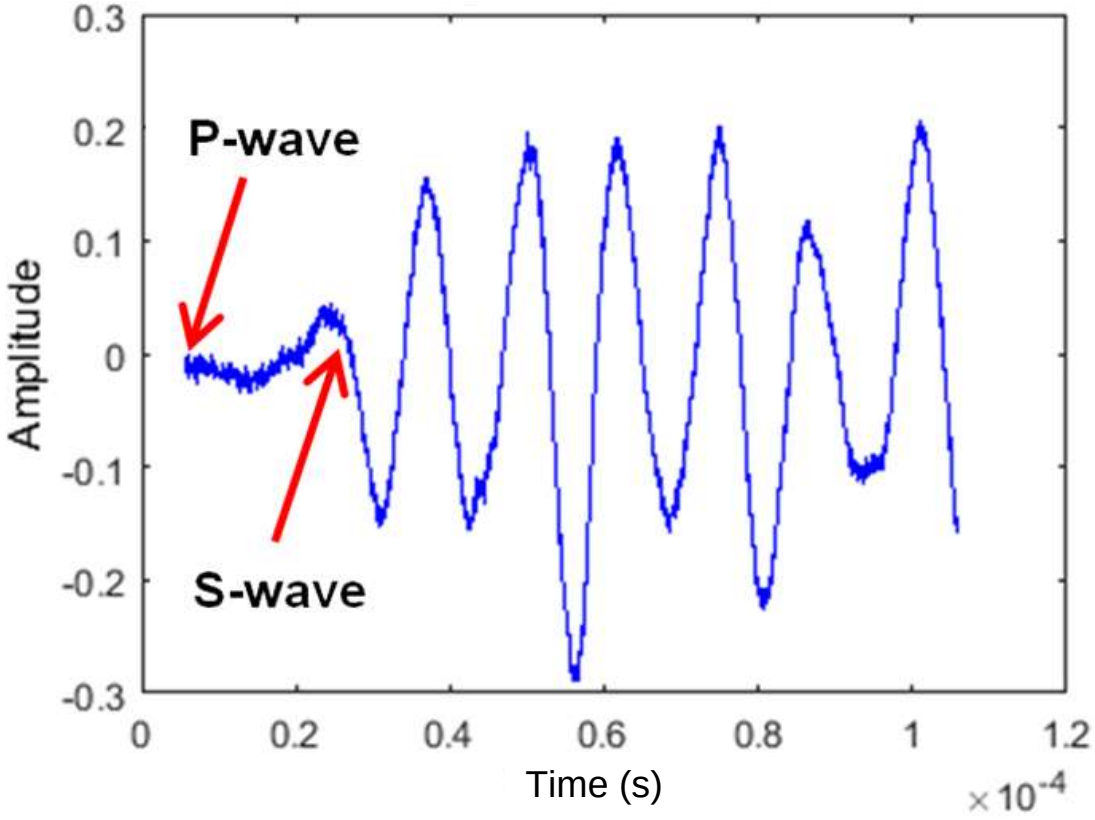

Figure A.20: The output waveform of sample W20

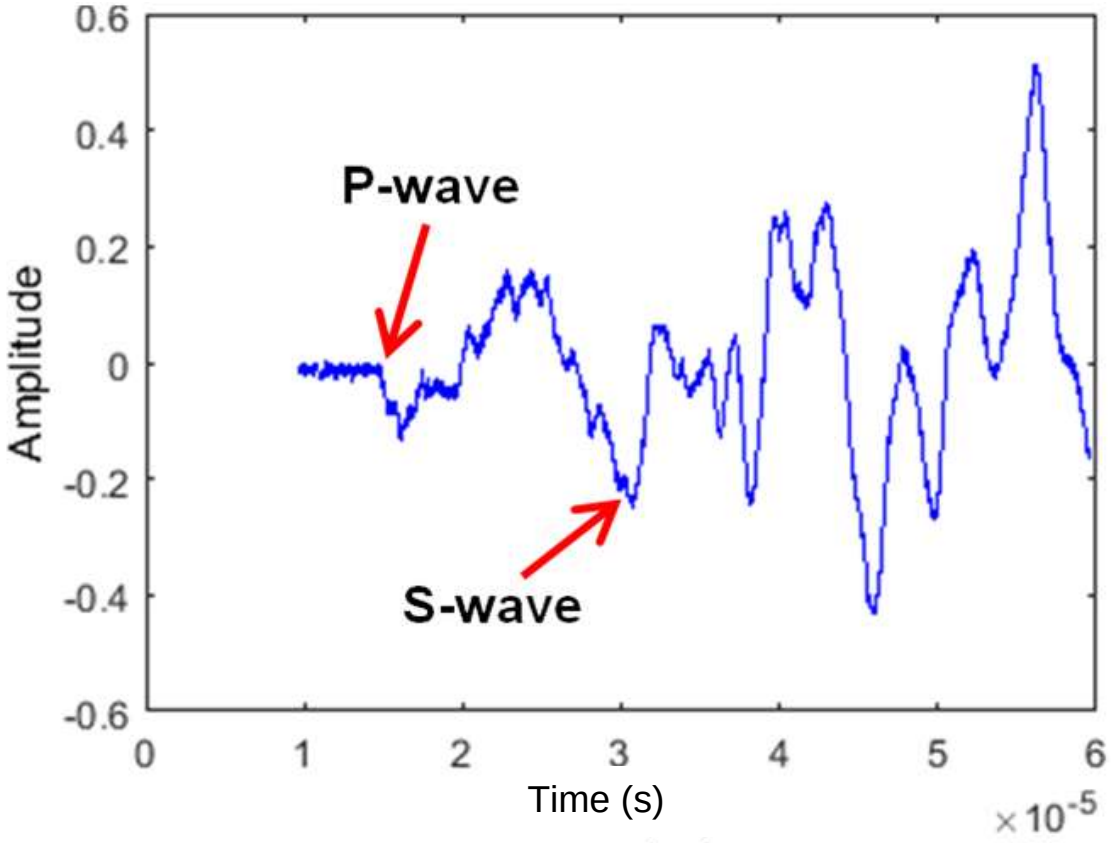

Figure A.21: The output waveform of sample W21

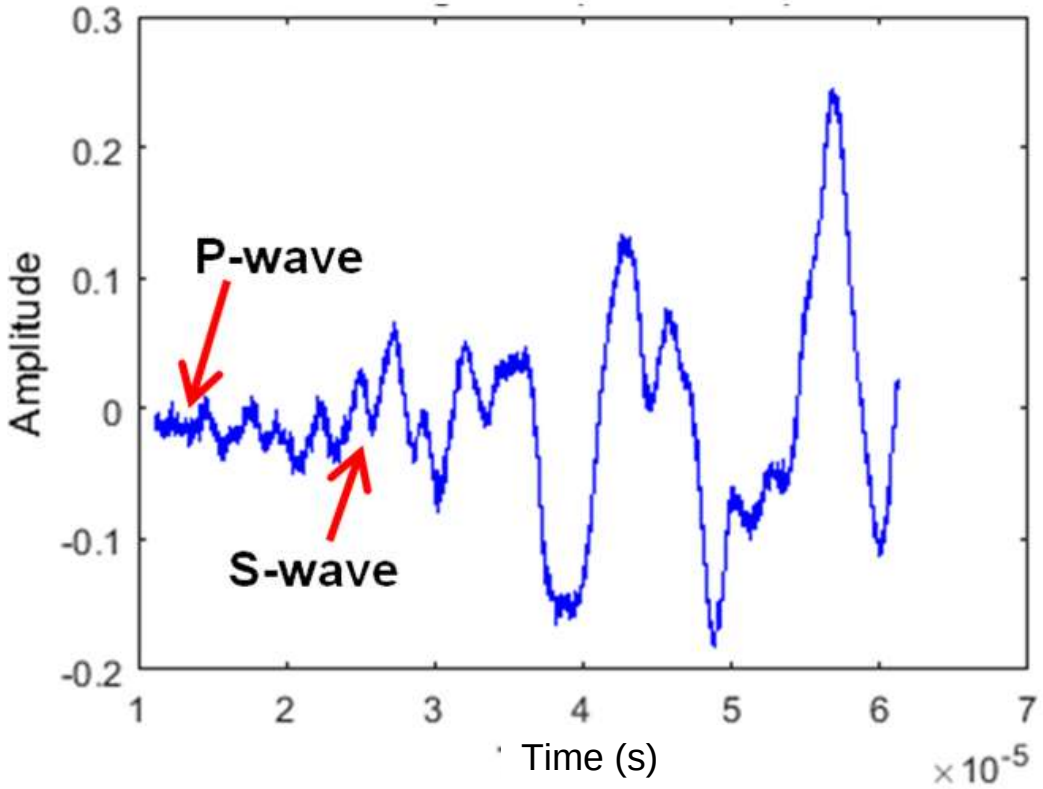

Figure A.22: The output waveform of sample W22

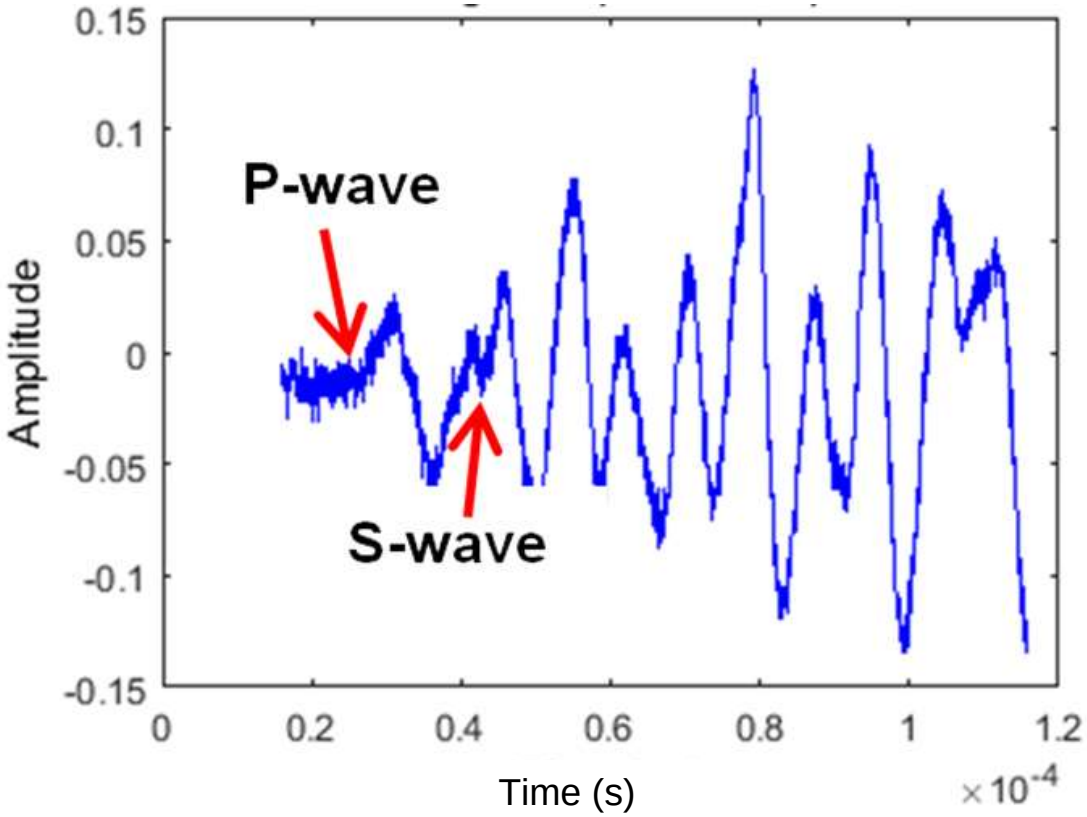

Figure A.23: The output waveform of sample W23

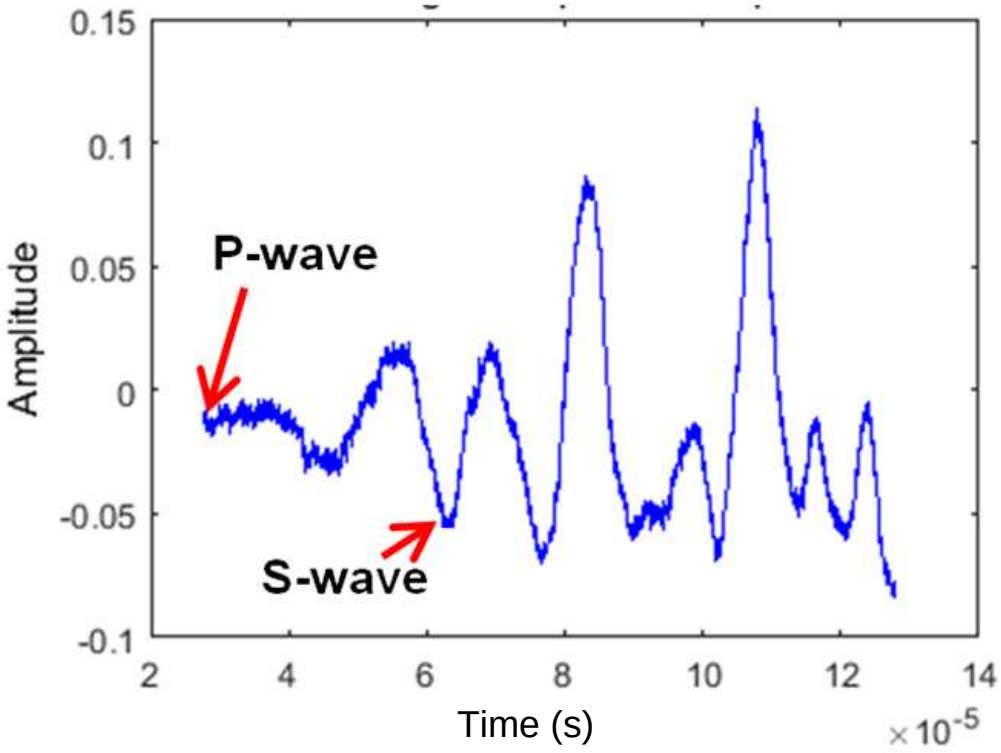

Figure A.24: The output waveform of sample W24

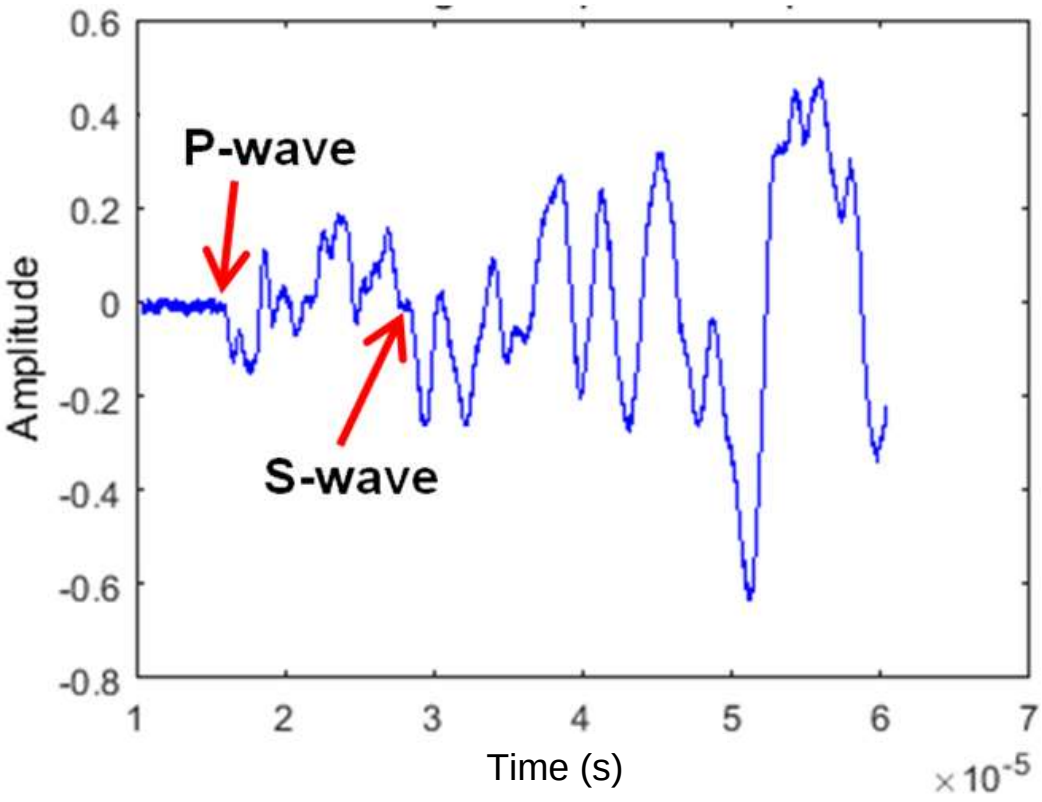

Figure A.25: The output waveform of sample W25

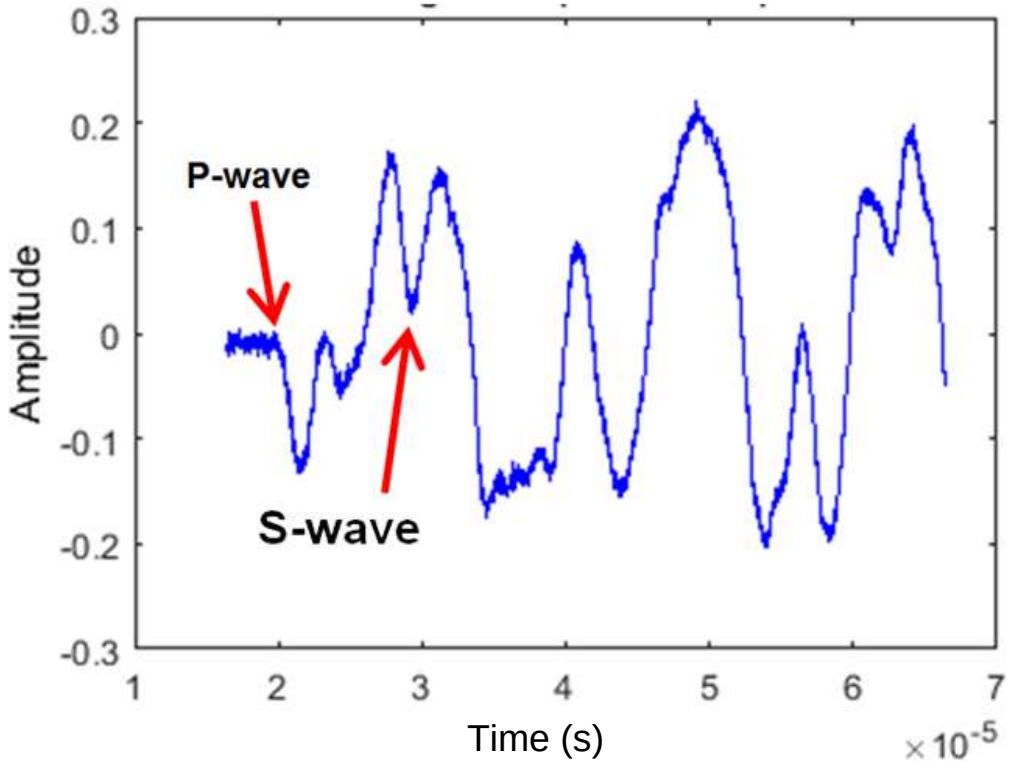

Figure A.26: The output waveform of sample W26

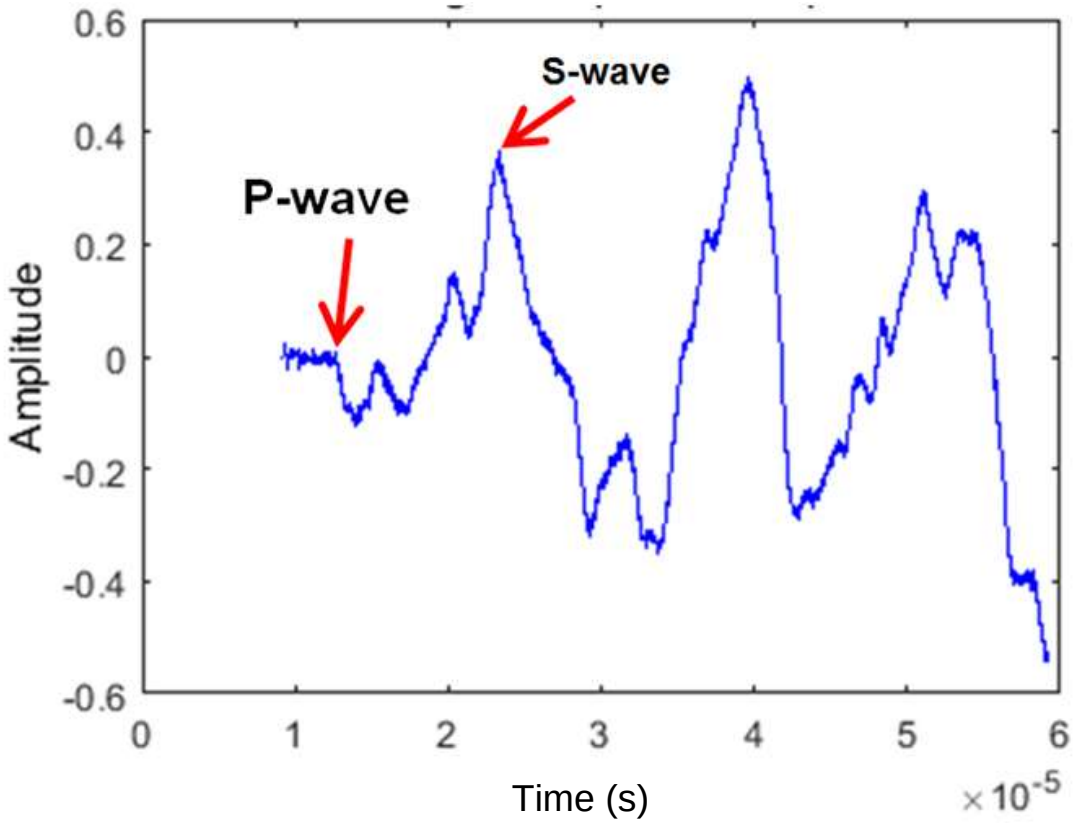

Figure A.27: The output waveform of sample W27

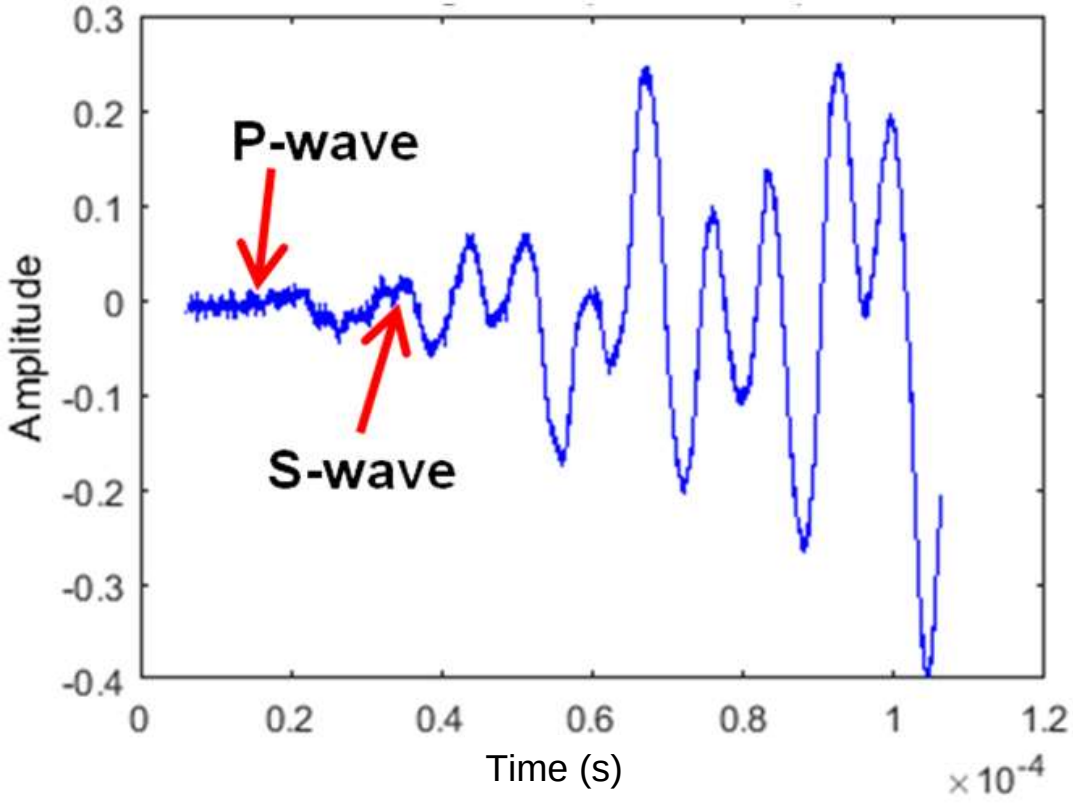

Figure A.28: The output waveform of sample W28

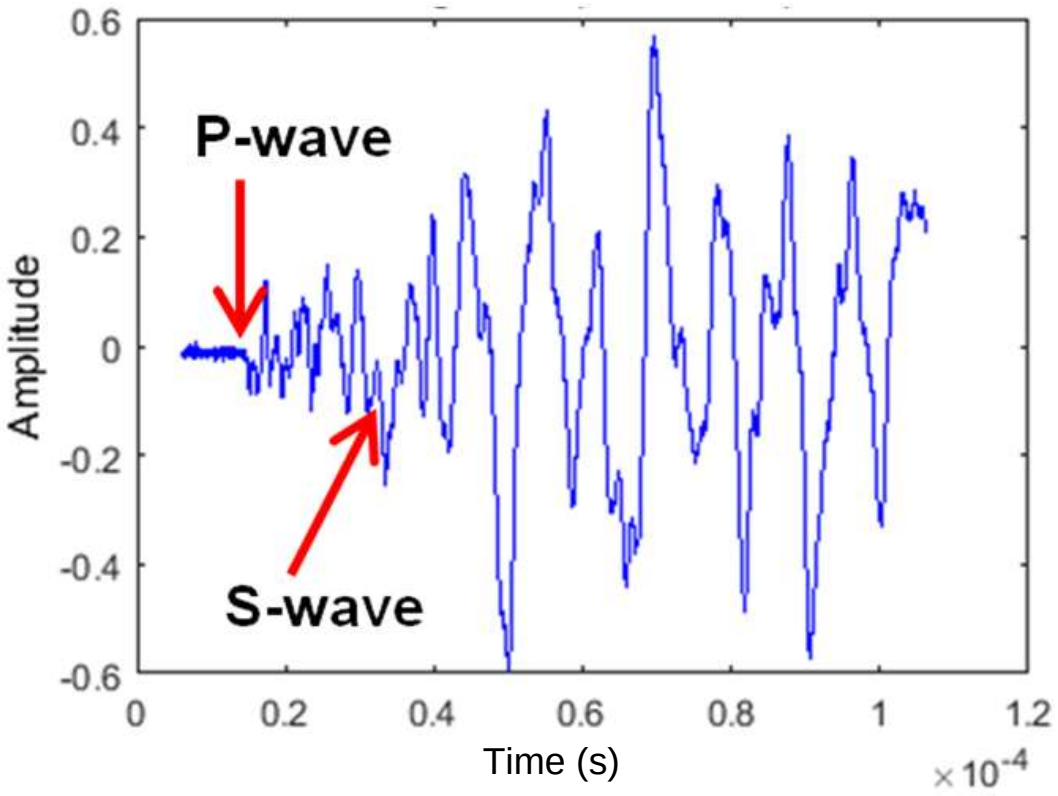

Figure A.29: The output waveform of sample W29

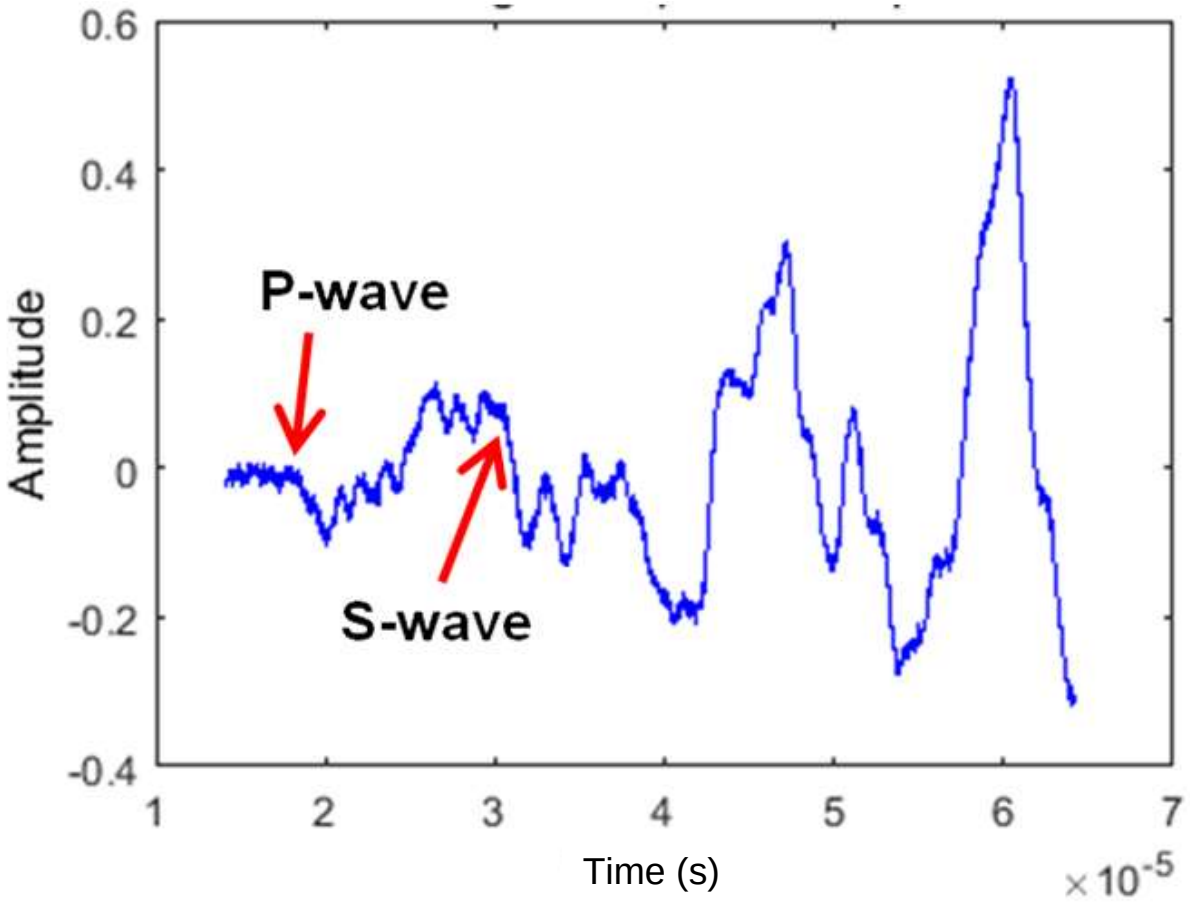

Figure A.30: The output waveform of sample W30

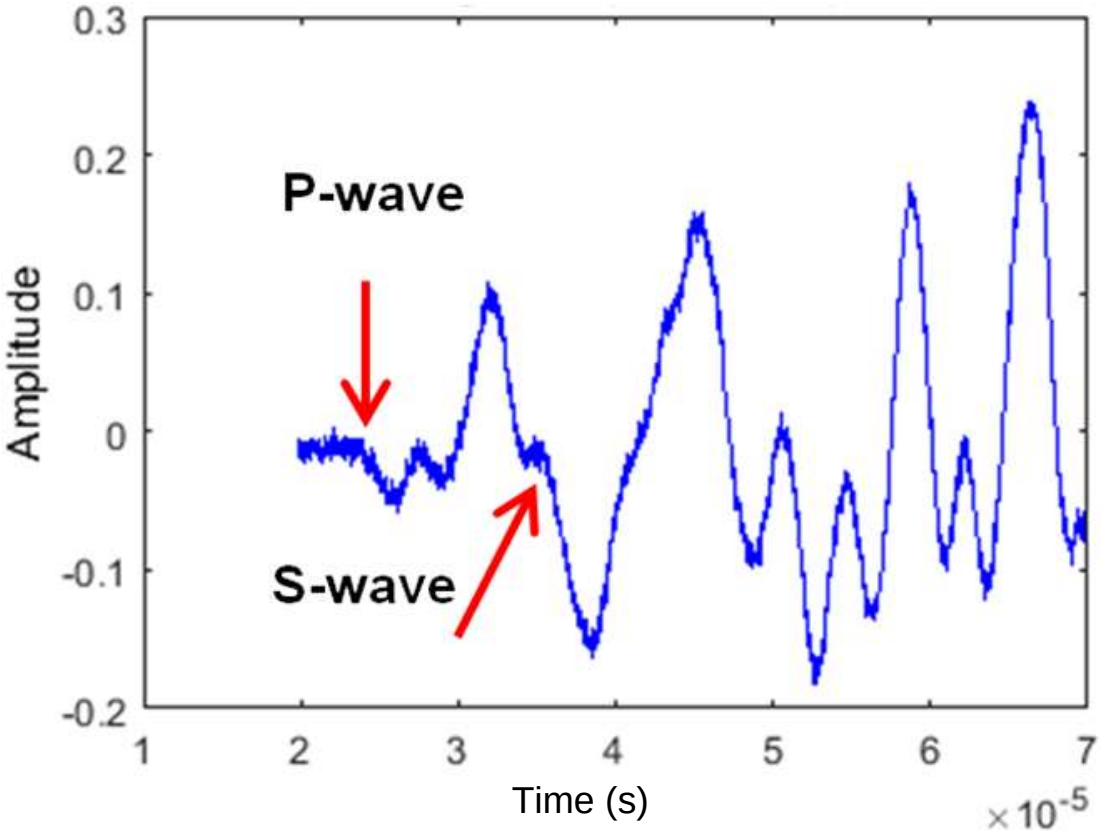

Figure A.31: The output waveform of sample W31

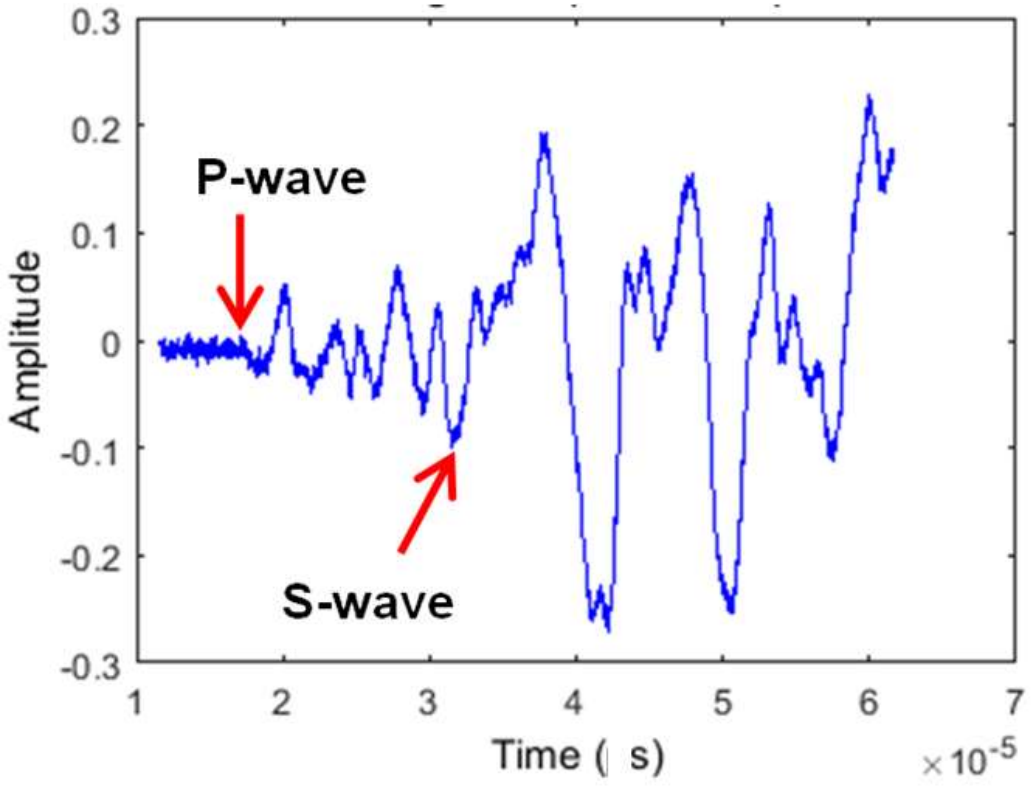

Figure A.32: The output waveform of sample W32

Time (s)

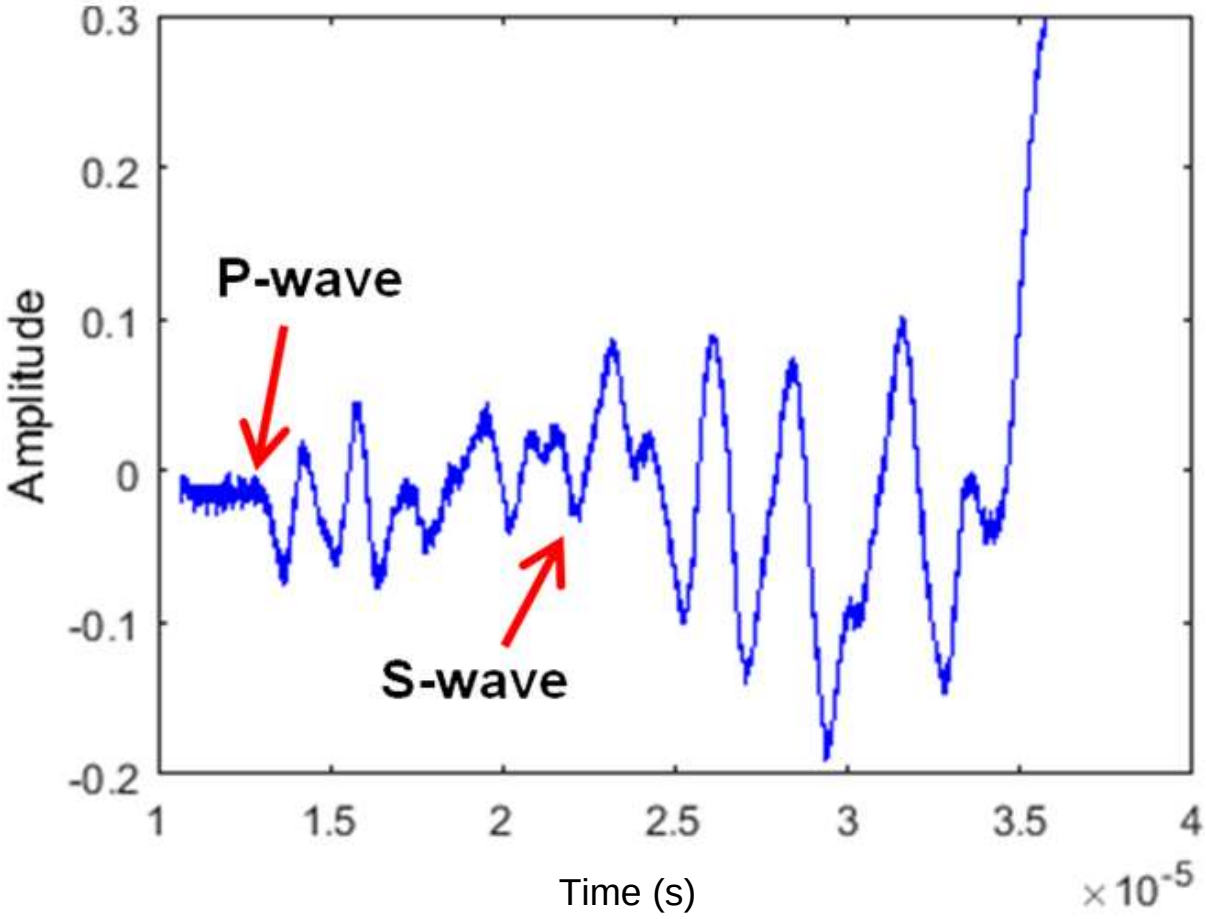

Figure A.33: The output waveform of sample W33

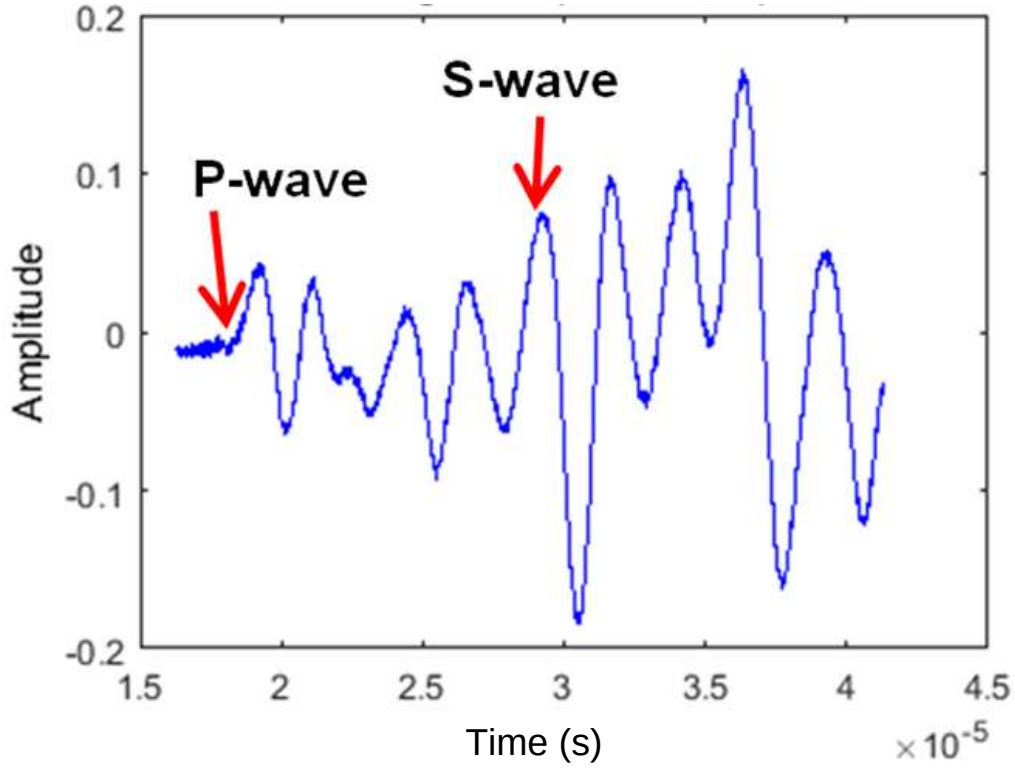

Figure A.34: The output waveform of sample W34

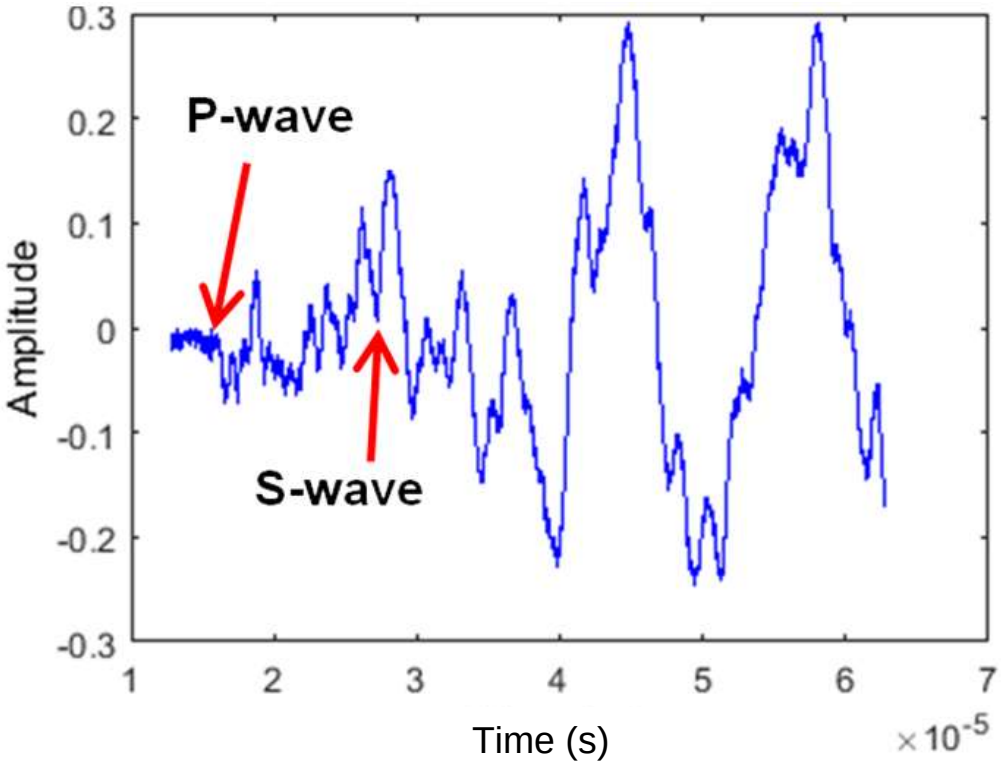

Figure A.35: The output waveform of sample W35

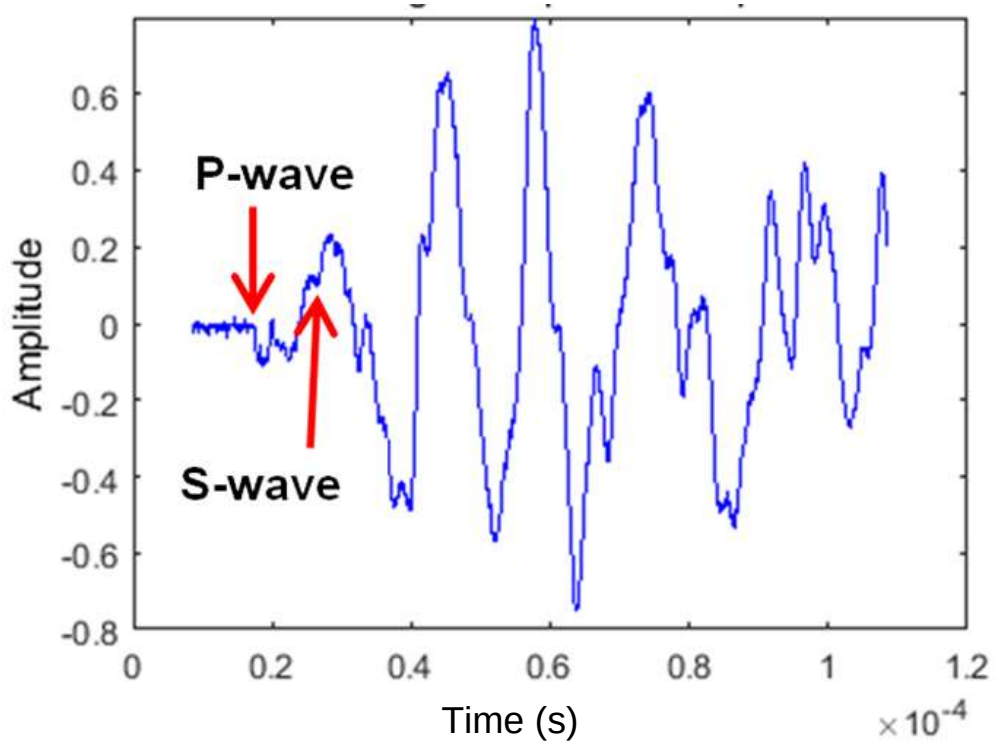

Figure A.36: The output waveform of sample W36

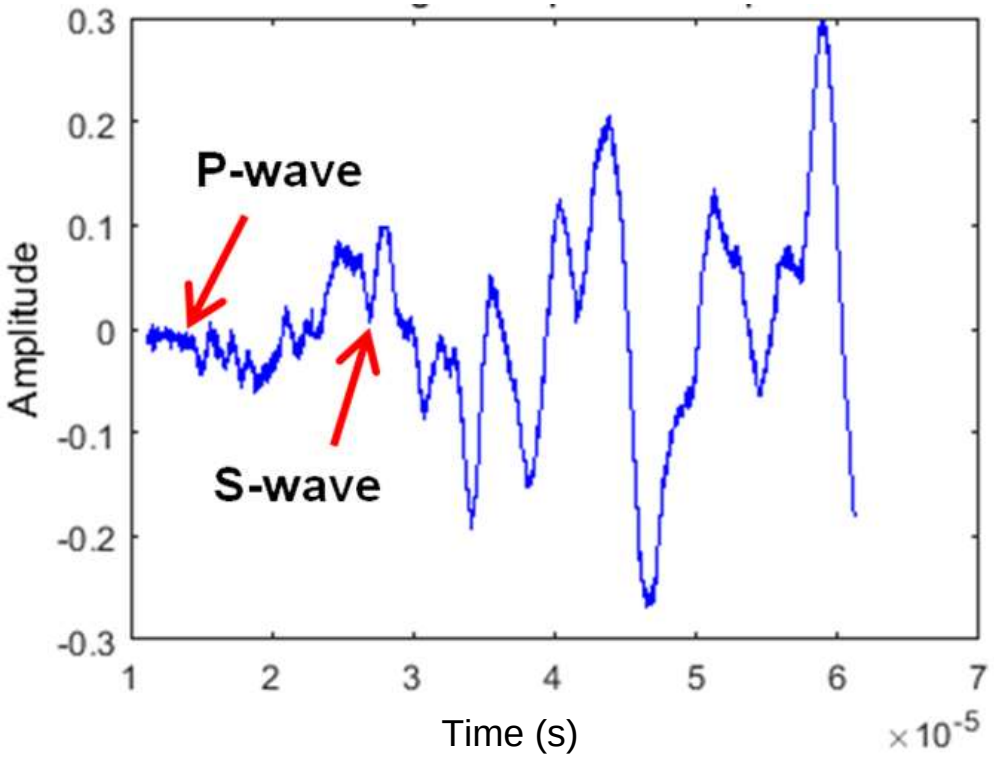

Figure A.37: The output waveform of sample W37

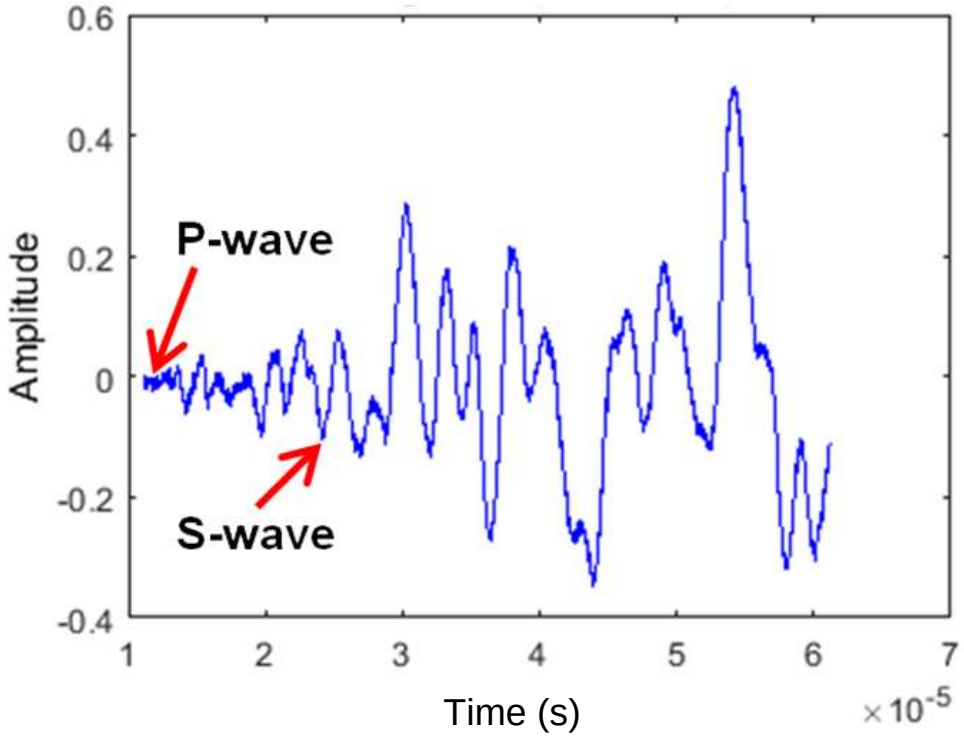

Figure A.38: The output waveform of sample W38

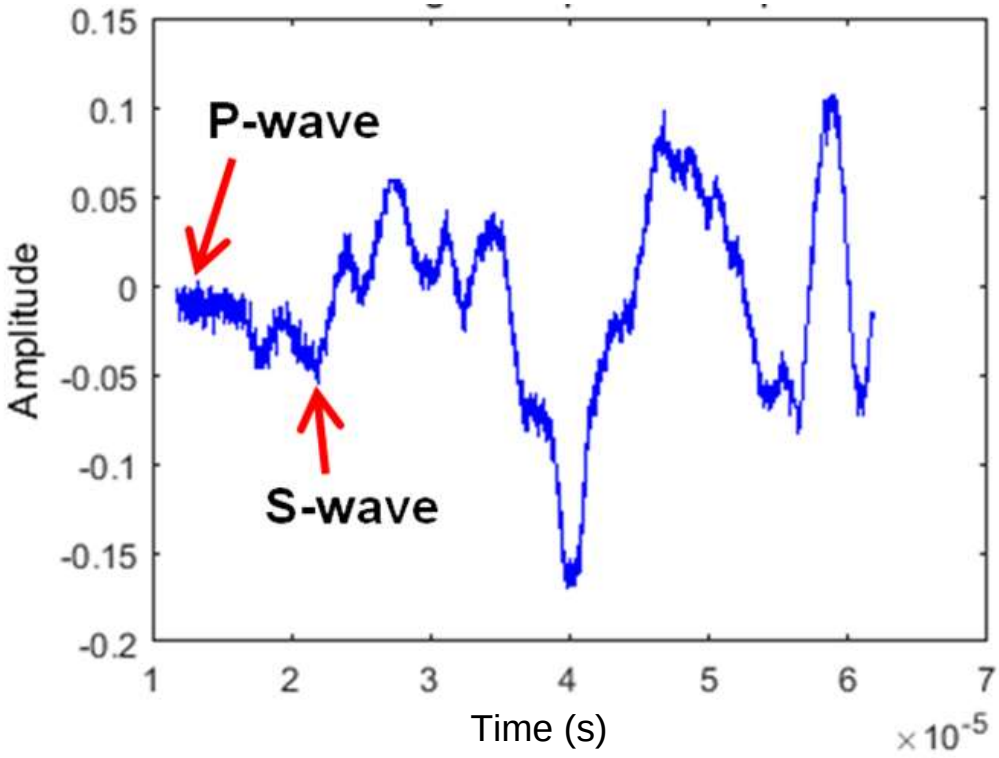

Figure A.39: The output waveform of sample W39

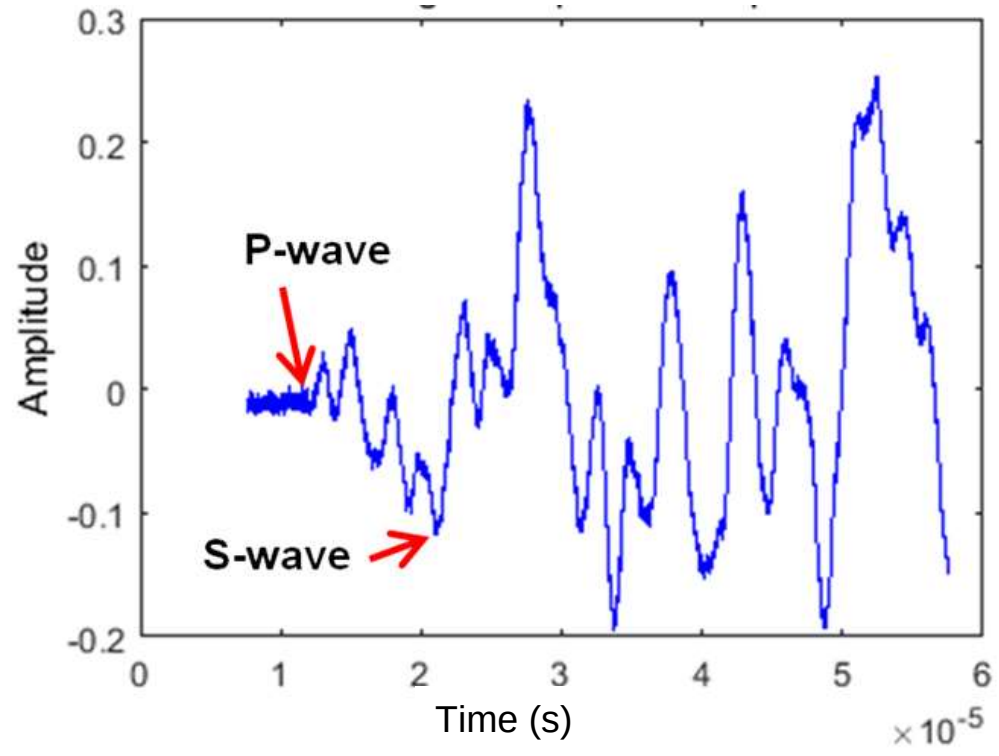

Figure A.40: The output waveform of sample W40

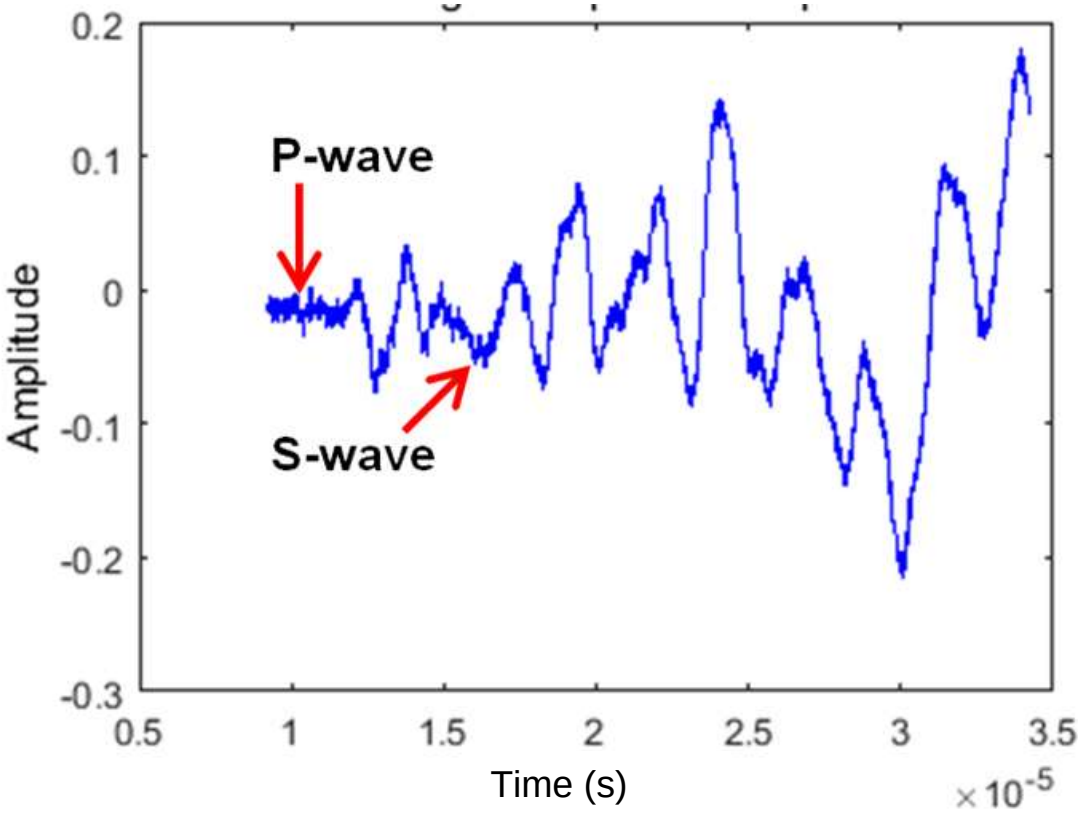

Figure A.41: The output waveform of sample W41

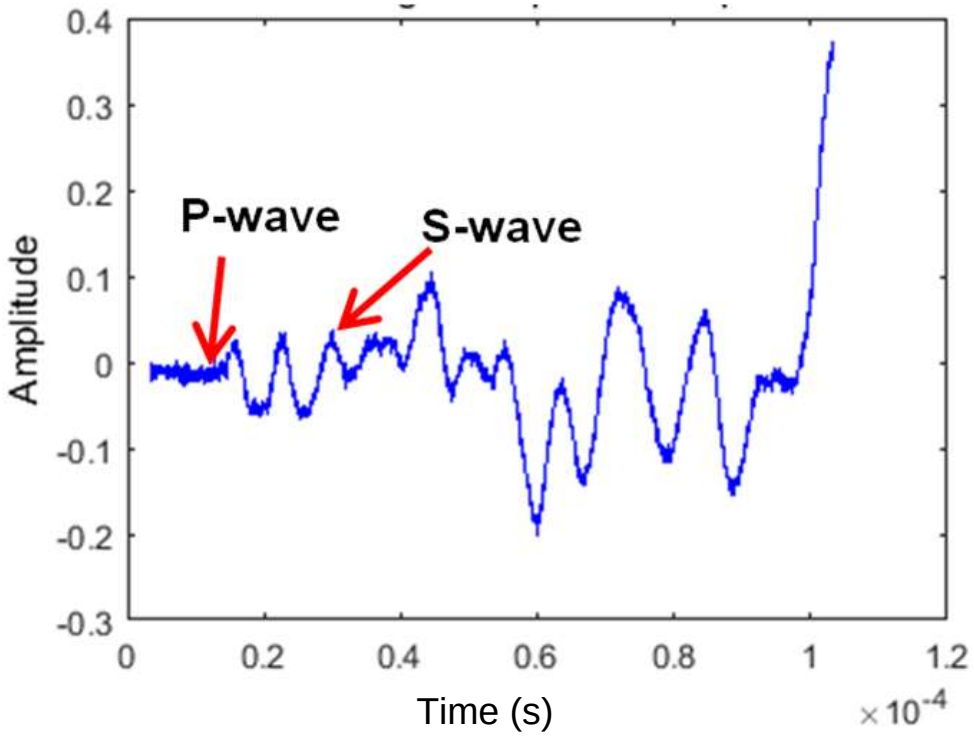

Figure A.42: The output waveform of sample W42

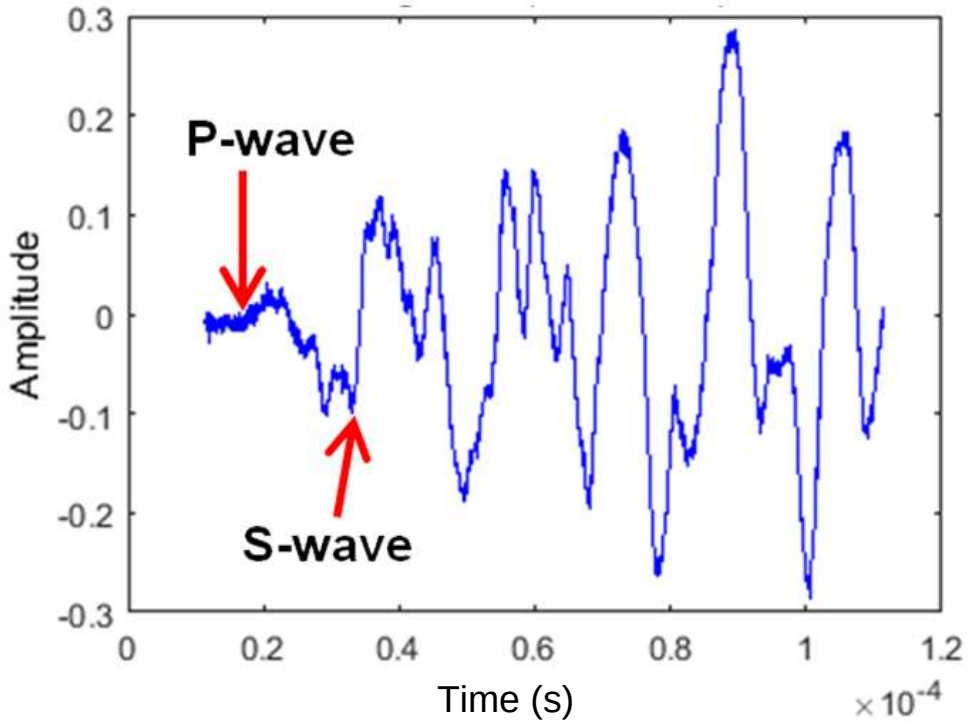

Figure A.43: The output waveform of sample W43

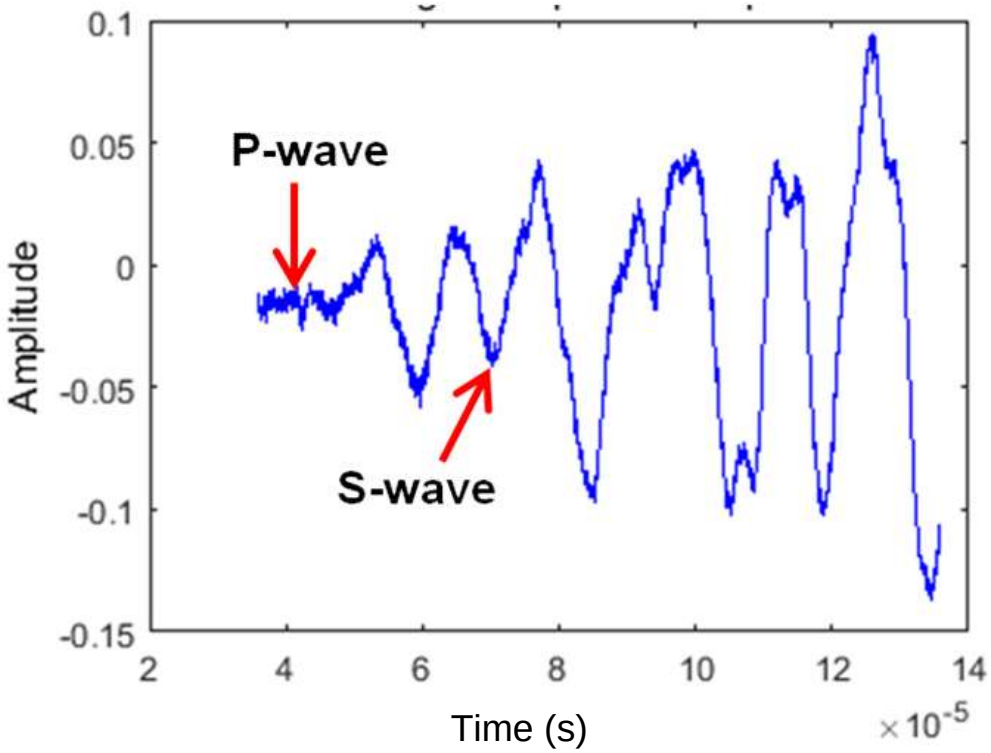

Figure A.44: The output waveform of sample W44

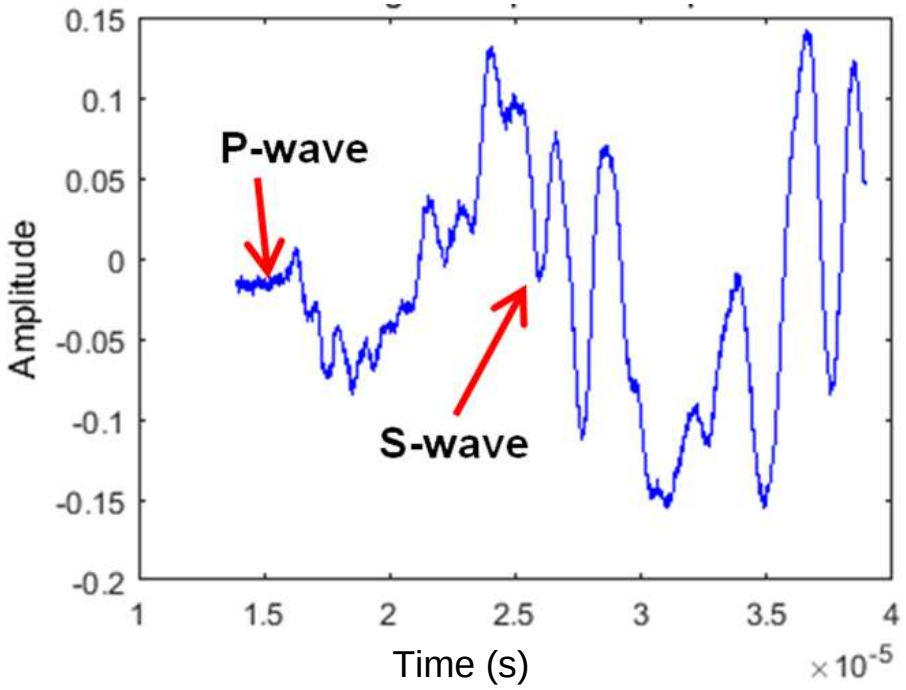

Figure A.45: The output waveform of sample W45

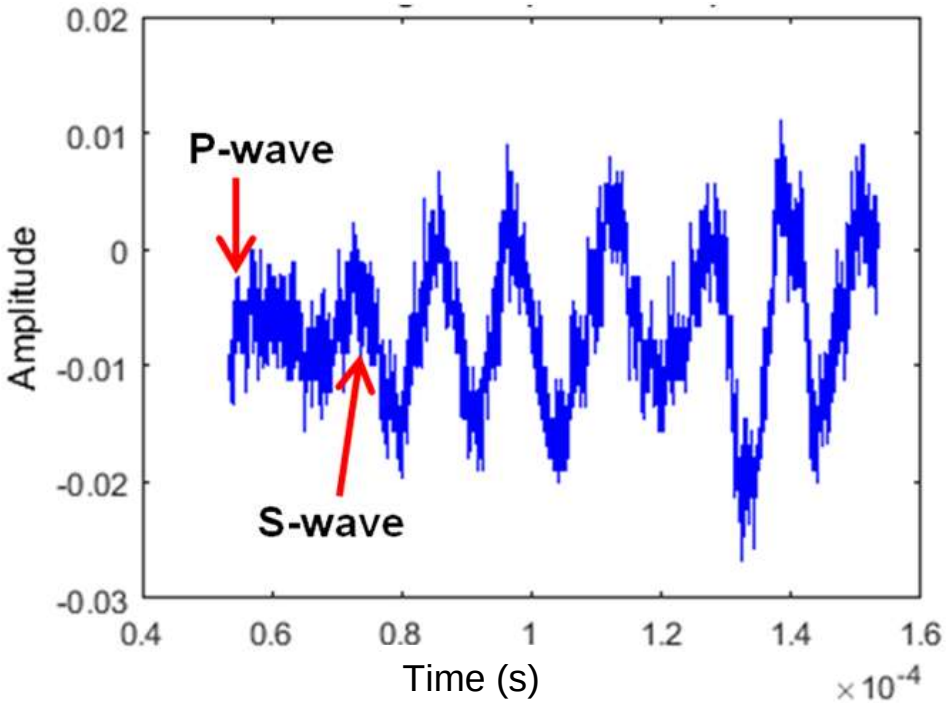

Figure A.46: The output waveform of sample W46

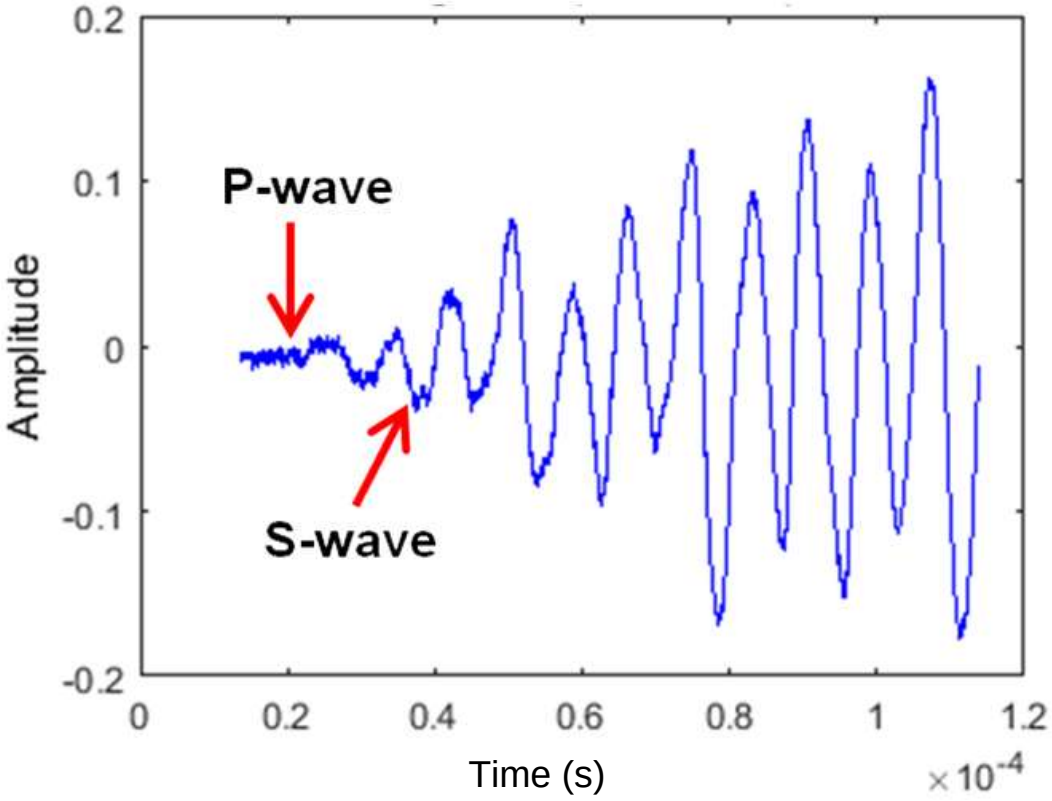

Figure A.47: The output waveform of sample W47

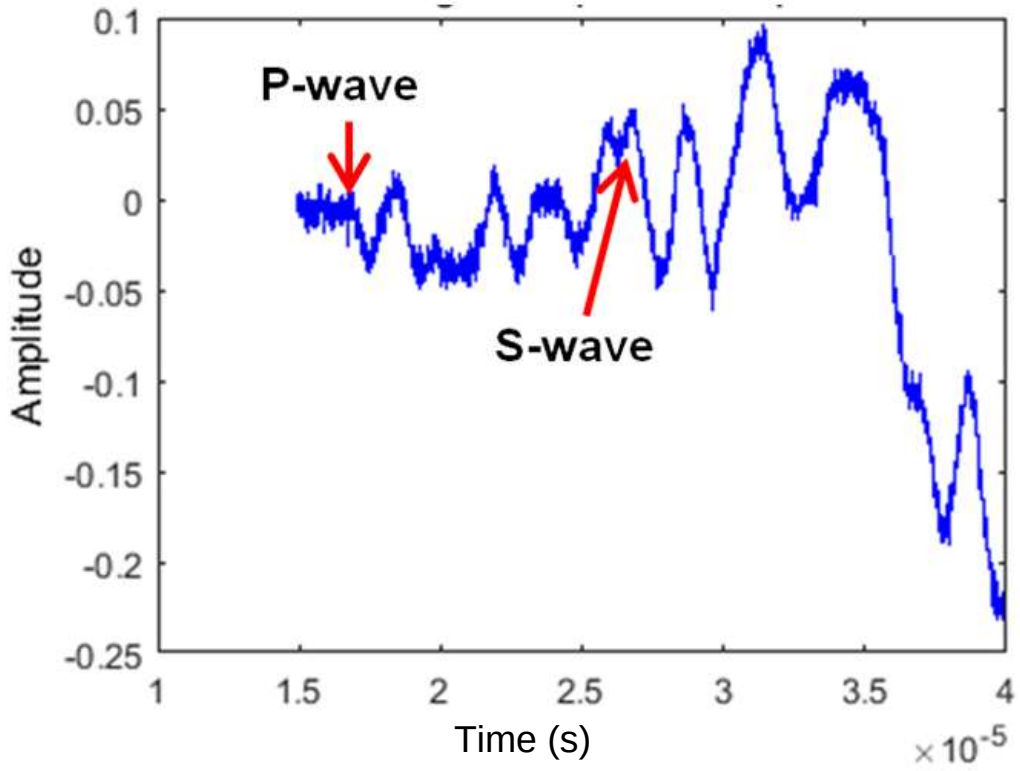

Figure A.48: The output waveform of sample W48

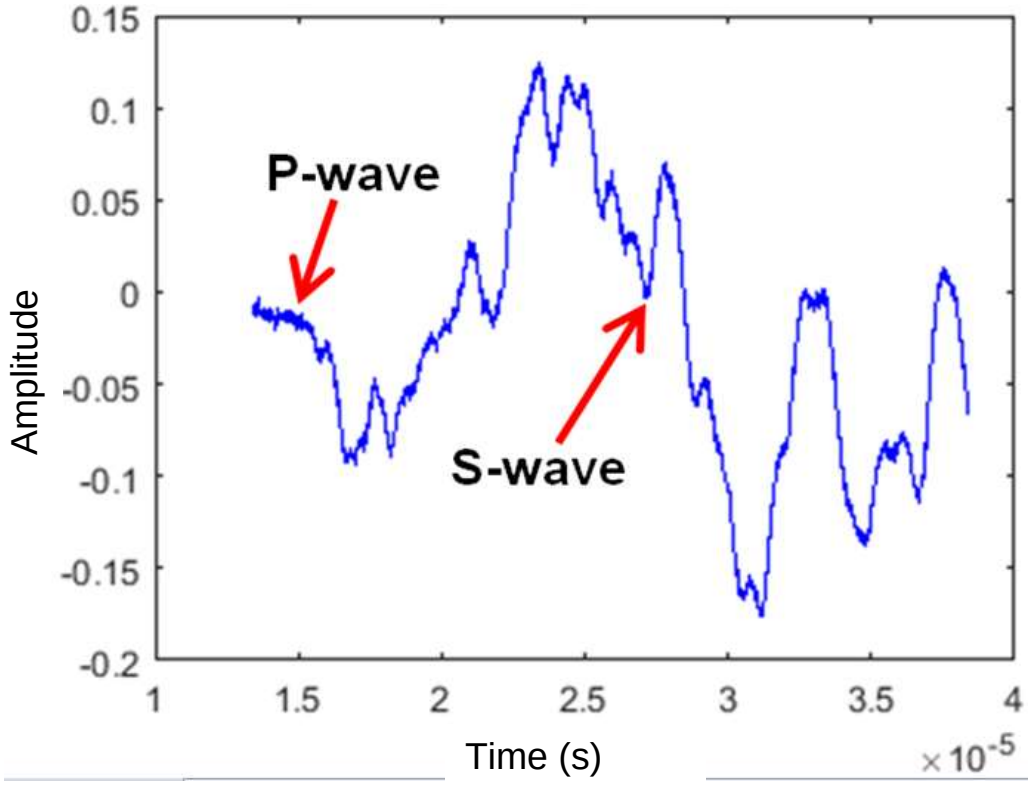

Figure A.49: The output waveform of sample W49

B. Appendix B – Signal processing

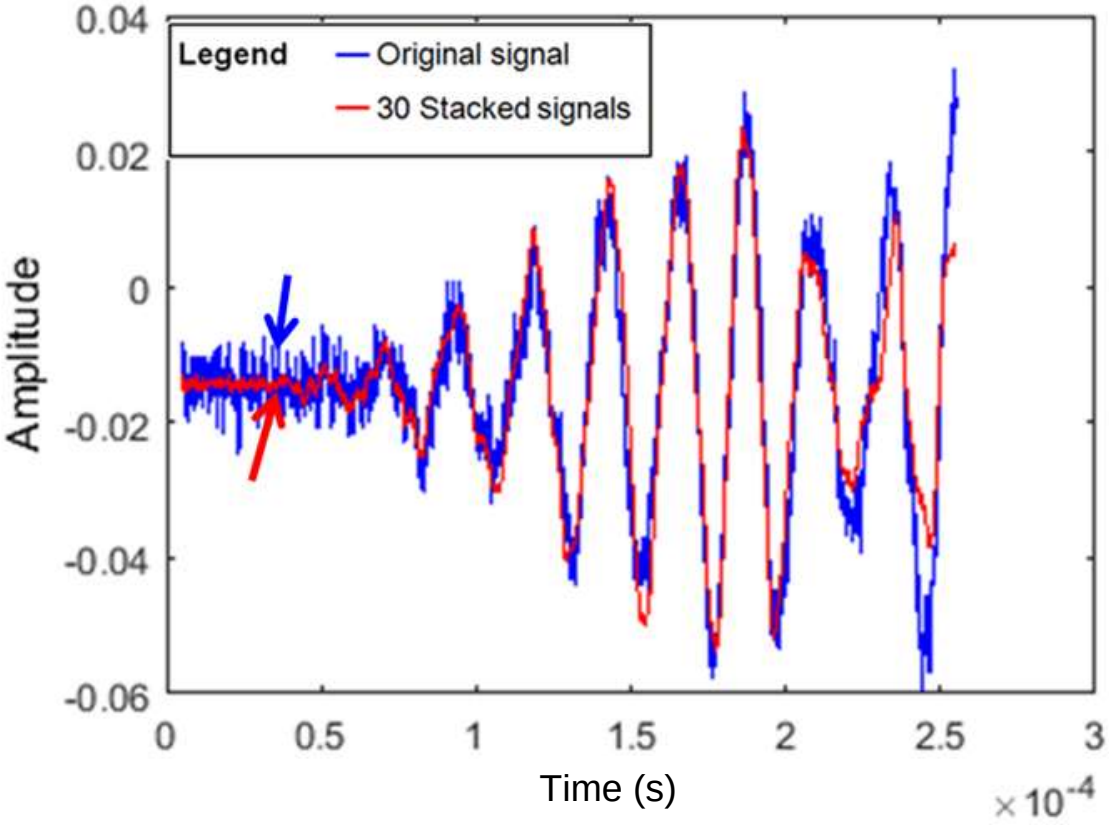

Figure B.1: The results of stacking several output waveforms for sample W2

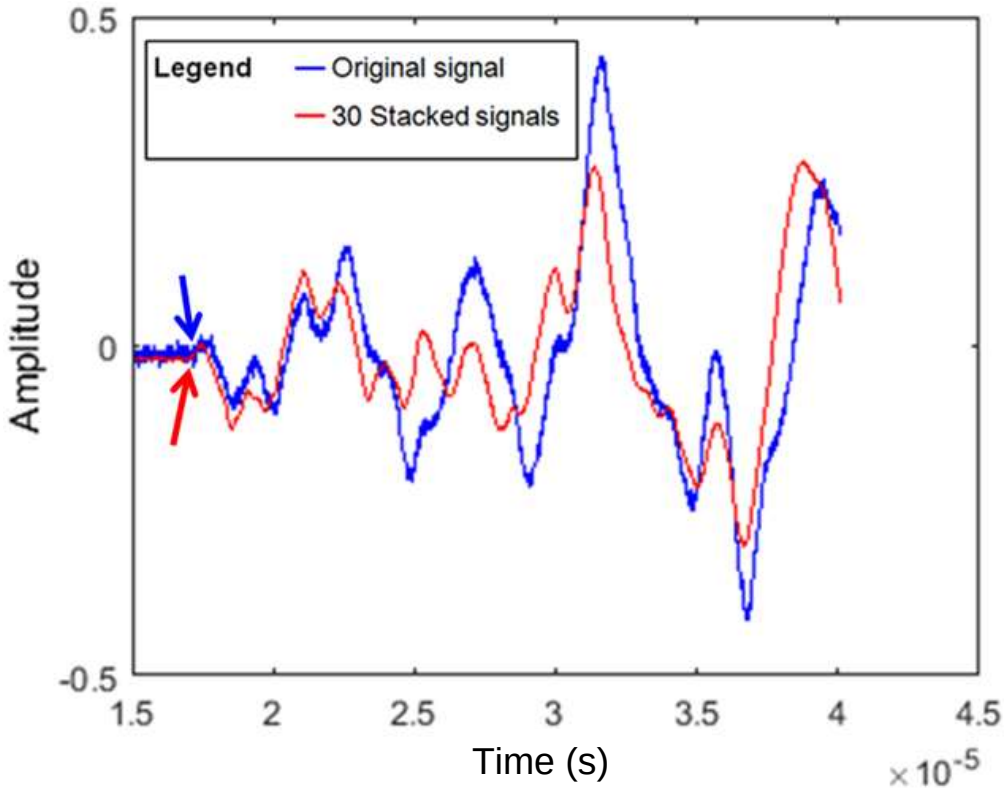

Figure B.2: The results of stacking several output waveforms for sample W8

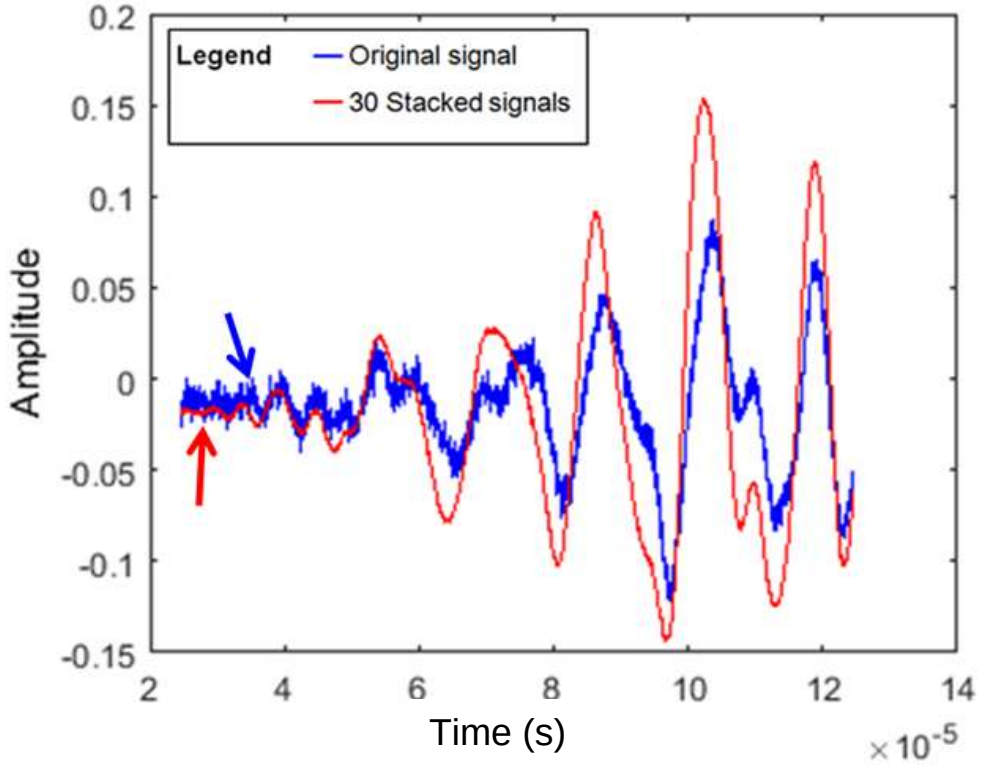

Figure B.3: The results of stacking several output waveforms for sample W9

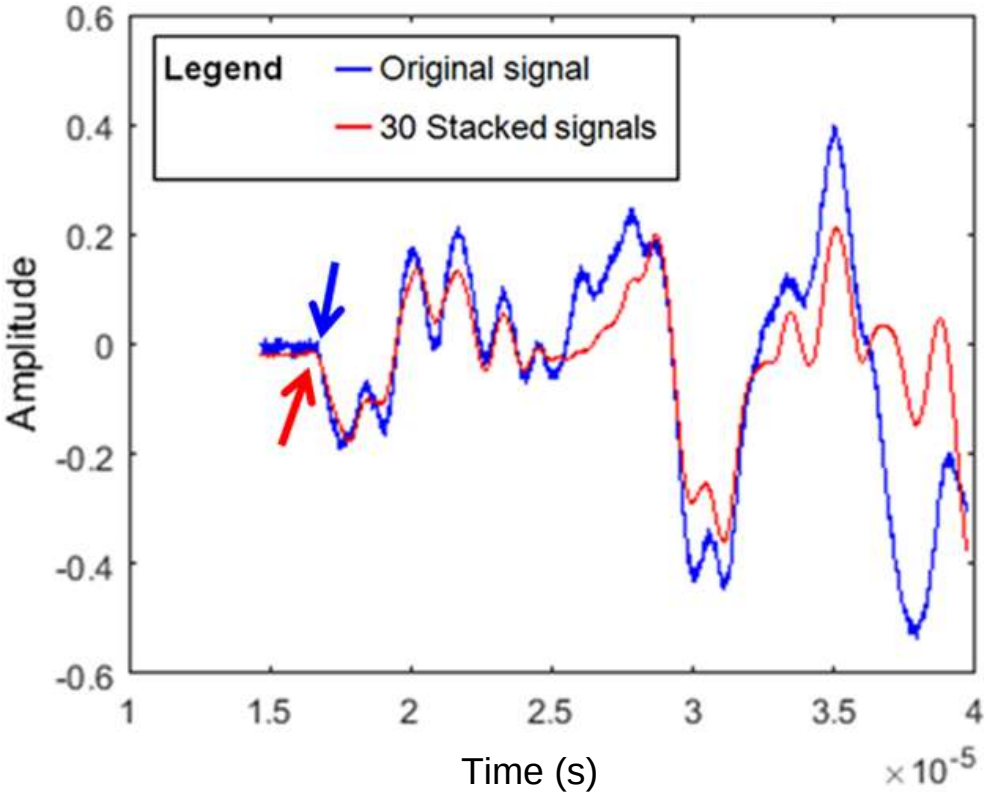

Figure B.4: The results of stacking several output waveforms for sample W16

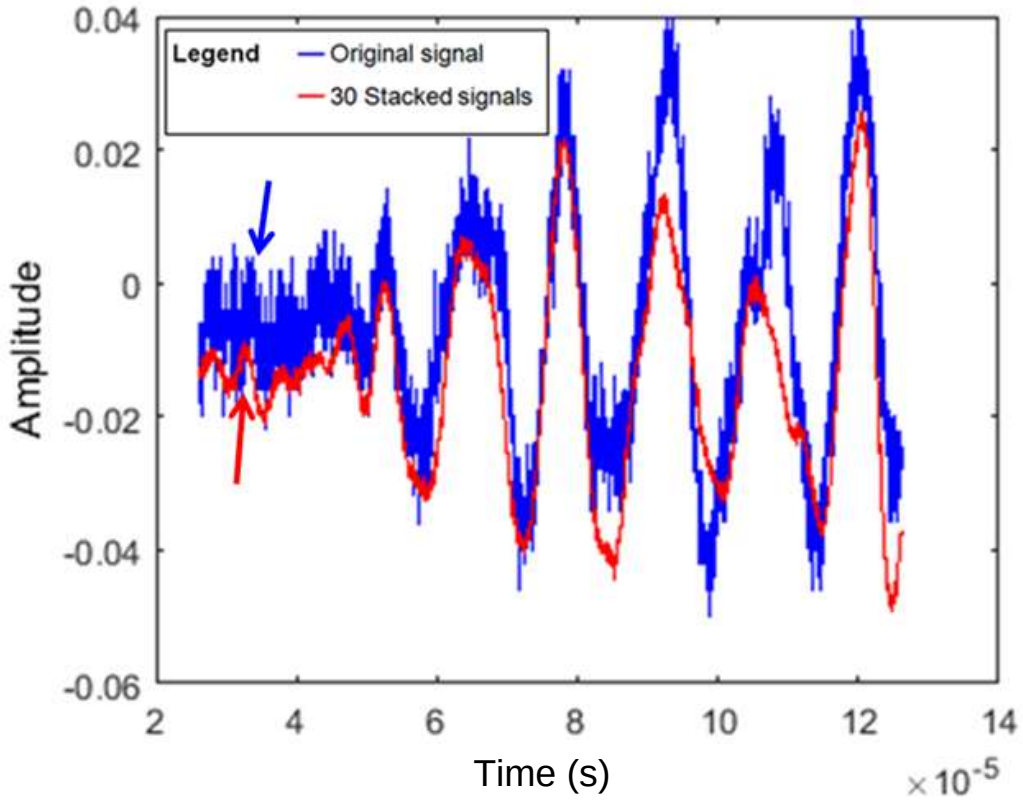

Figure B.5: The results of stacking several output waveforms for sample W17

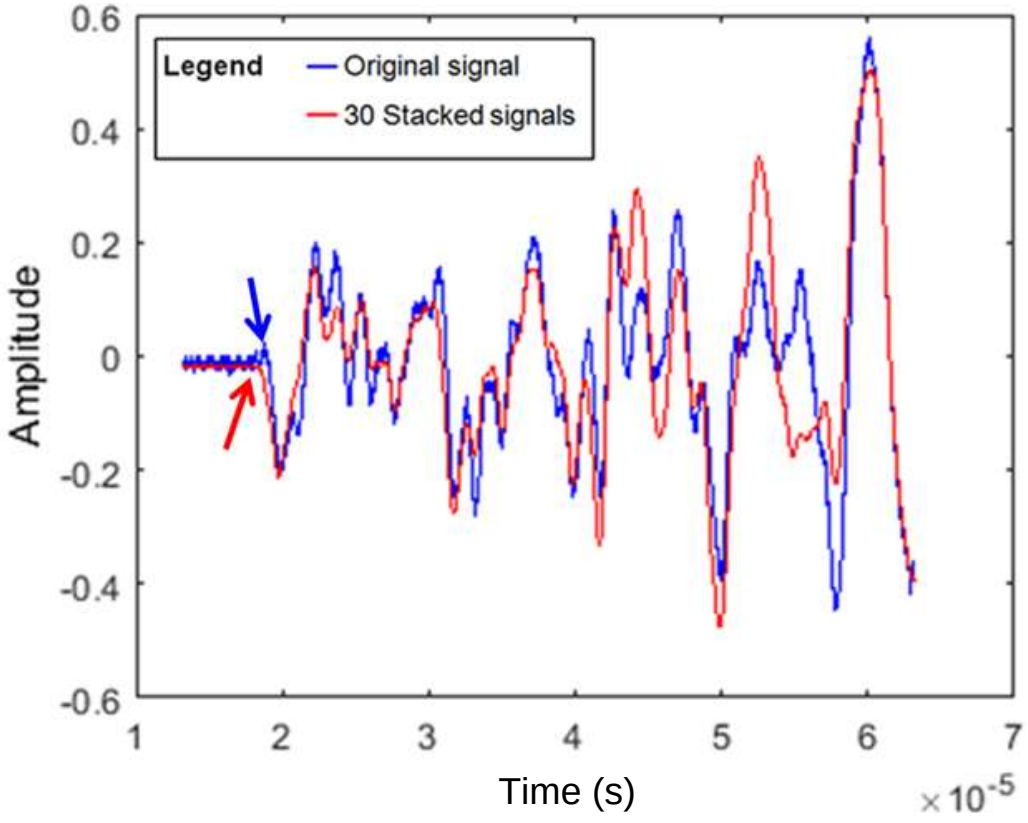

Figure B.6: The results of stacking several output waveforms for sample W18

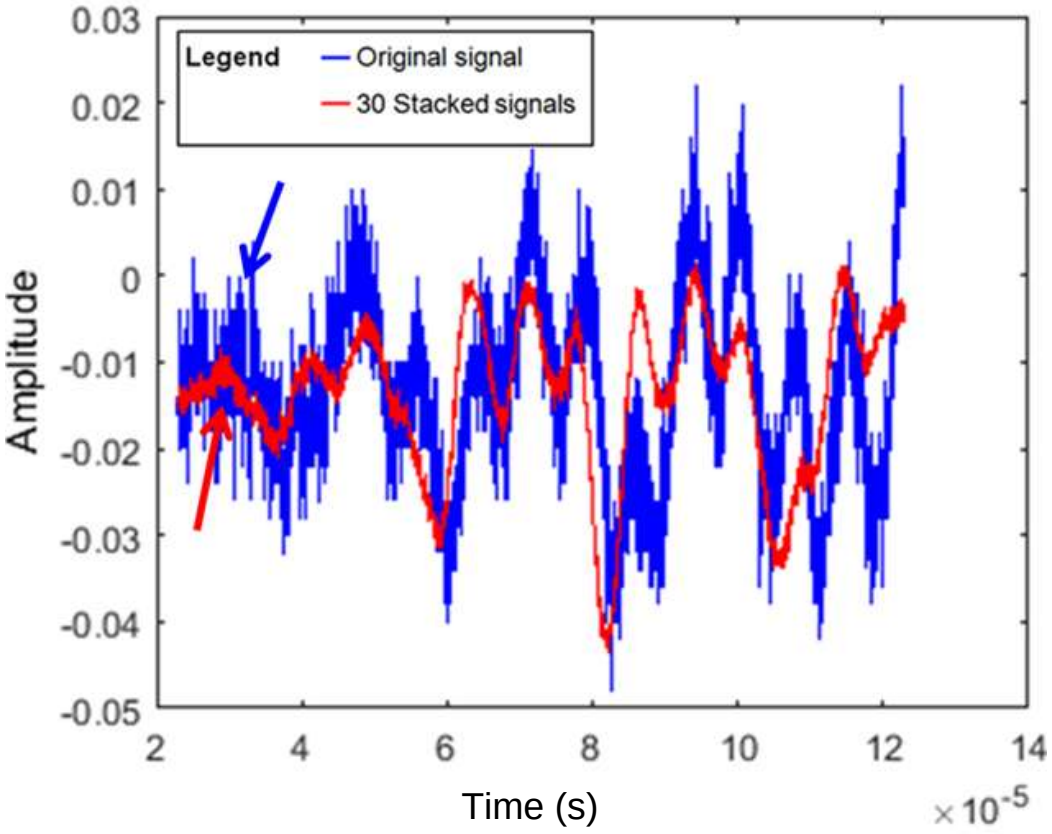

Figure B.7: The results of stacking several output waveforms for sample W19

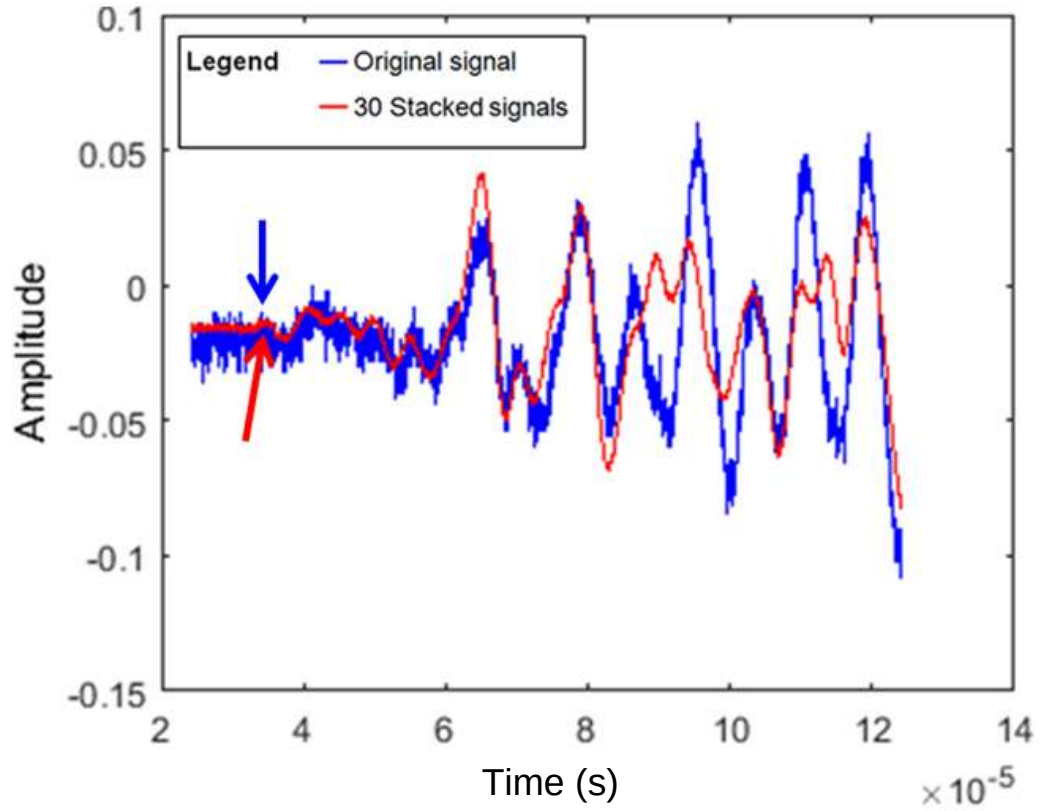

Figure B.8: The results of stacking several output waveforms for sample W24

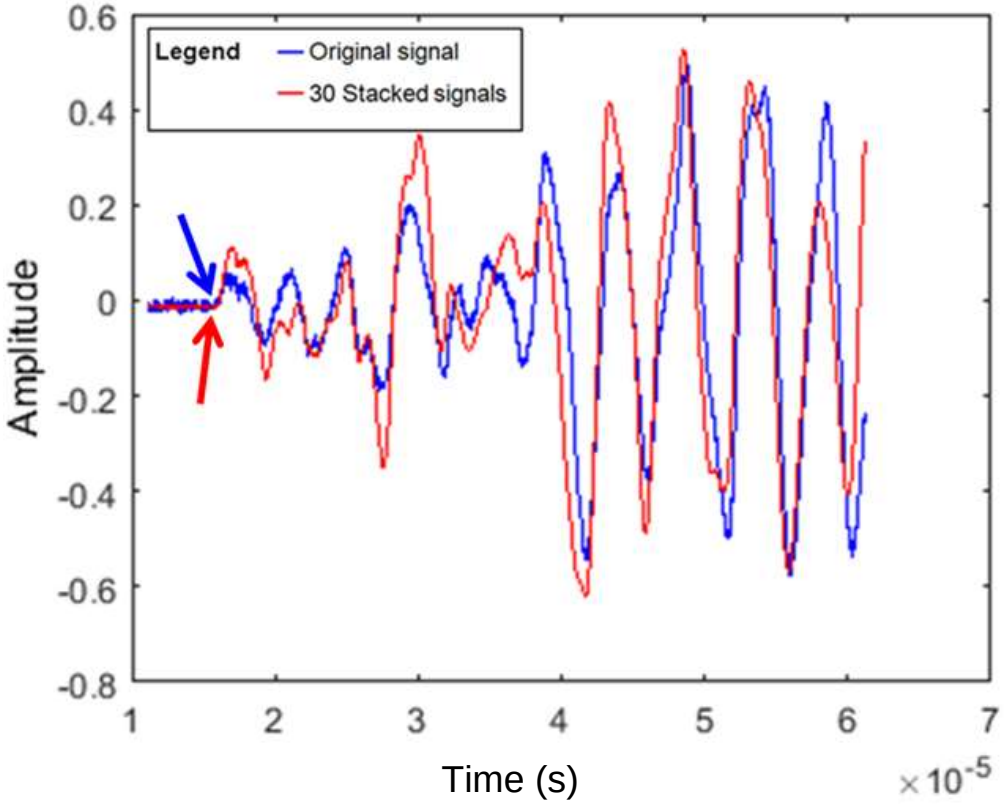

Figure B.9: The results of stacking several output waveforms for sample W25

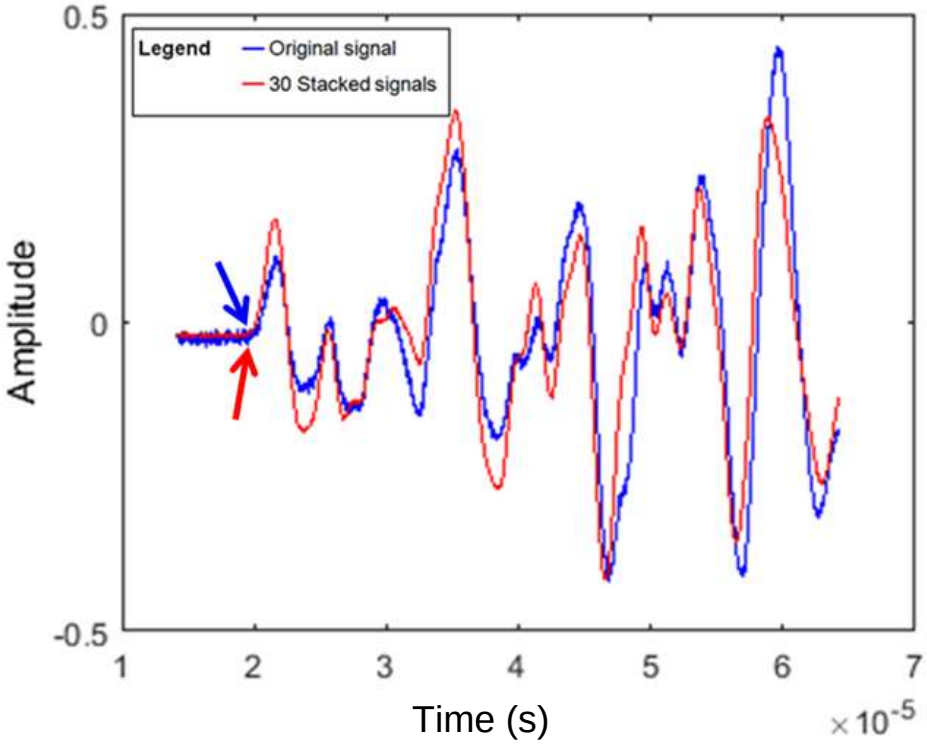

Figure B.10: The results of stacking several output waveforms for sample W26

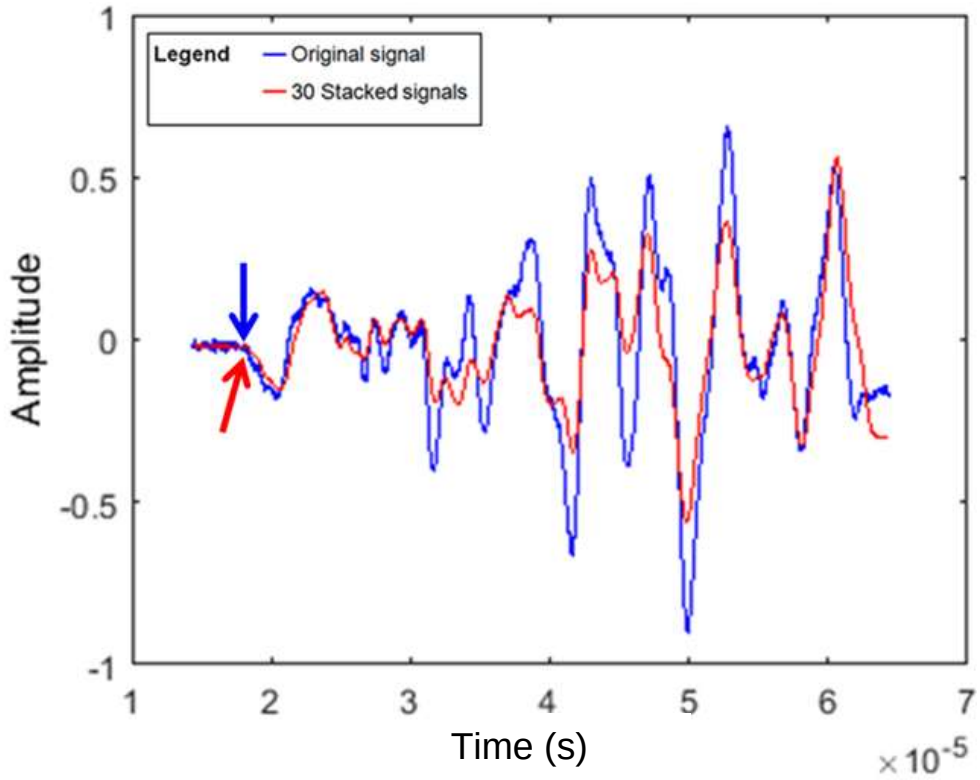

Figure B.11: The results of stacking several output waveforms for sample W30

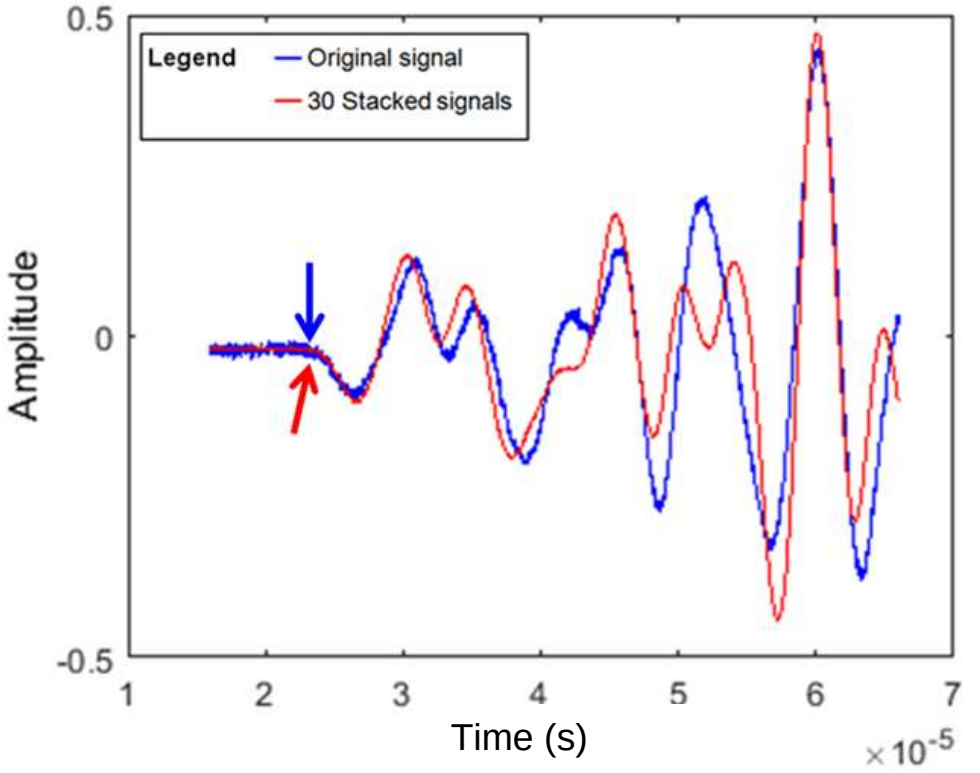

Figure B.12: The results of stacking several output waveforms for sample W31

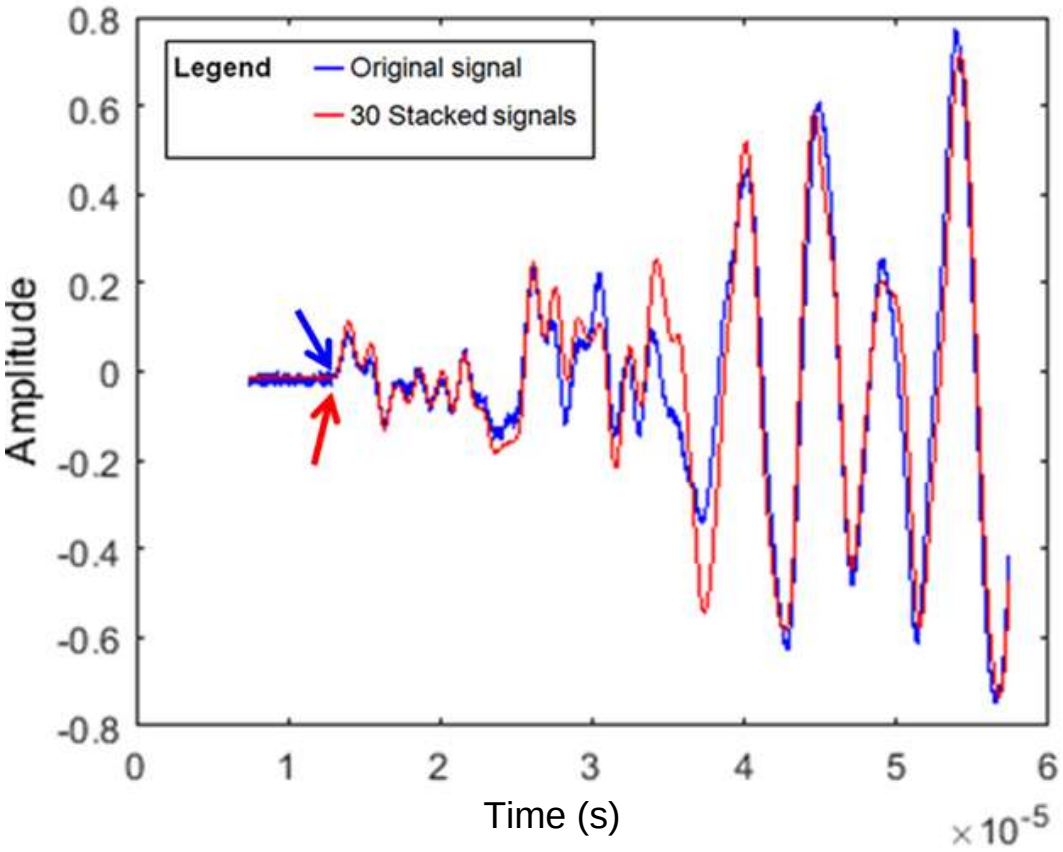

Figure B.13: The results of stacking several output waveforms for sample W33

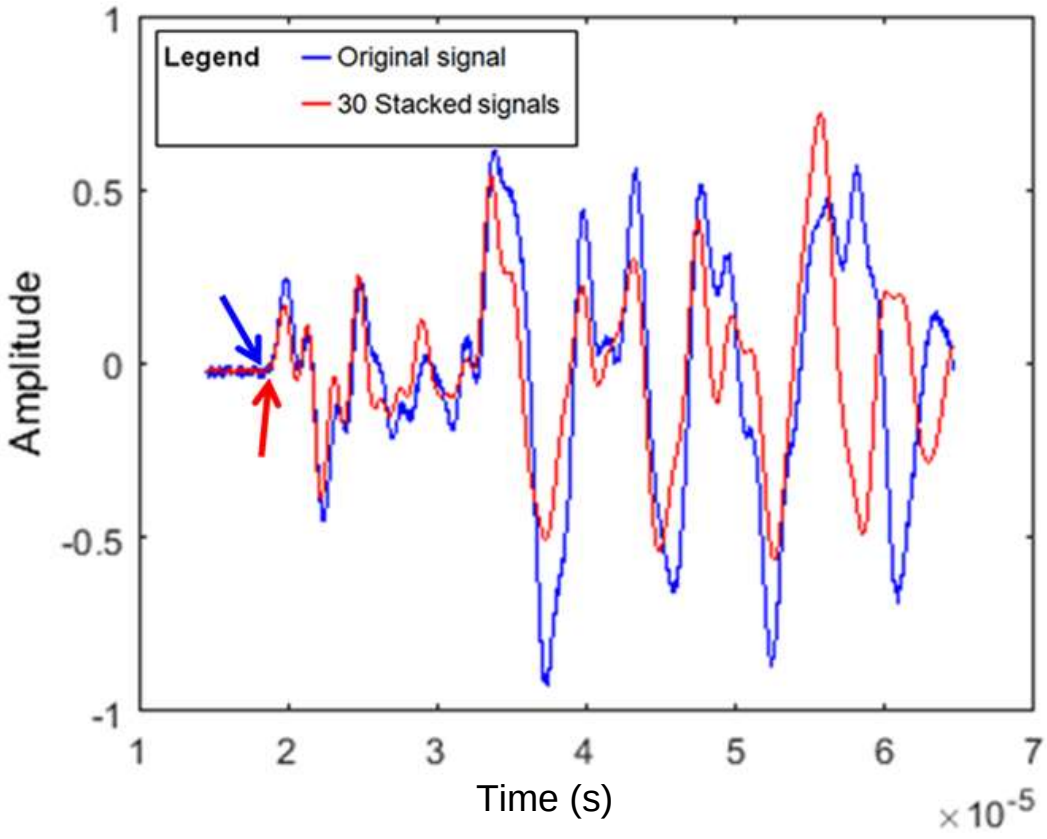

Figure B.14: The results of stacking several output waveforms for sample W34

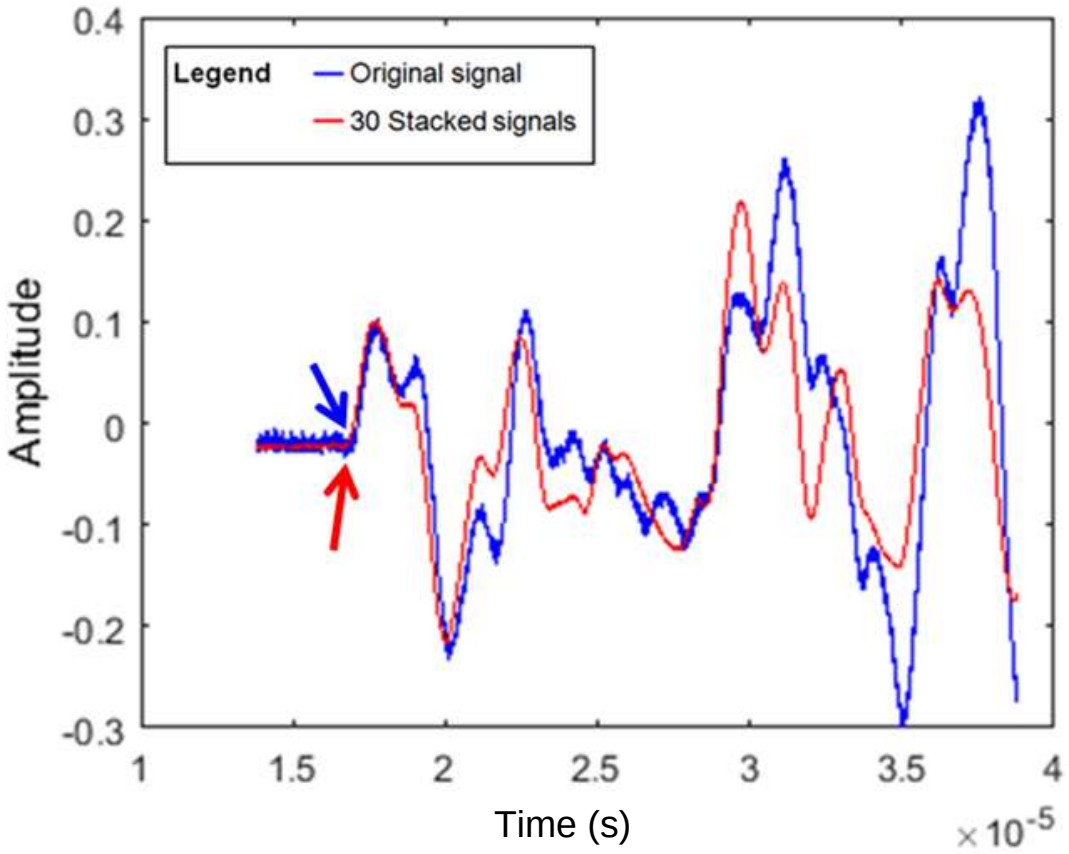

Figure B.15: The results of stacking several output waveforms for sample W36

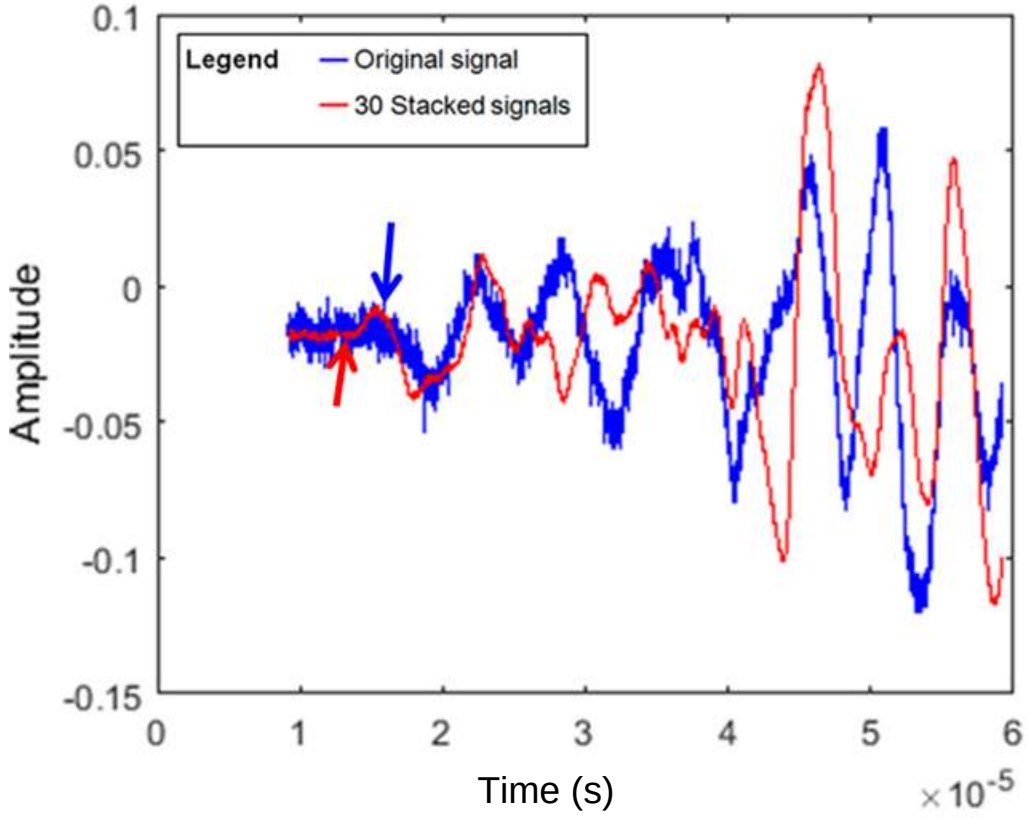

Figure B.16: The results of stacking several output waveforms for sample W39

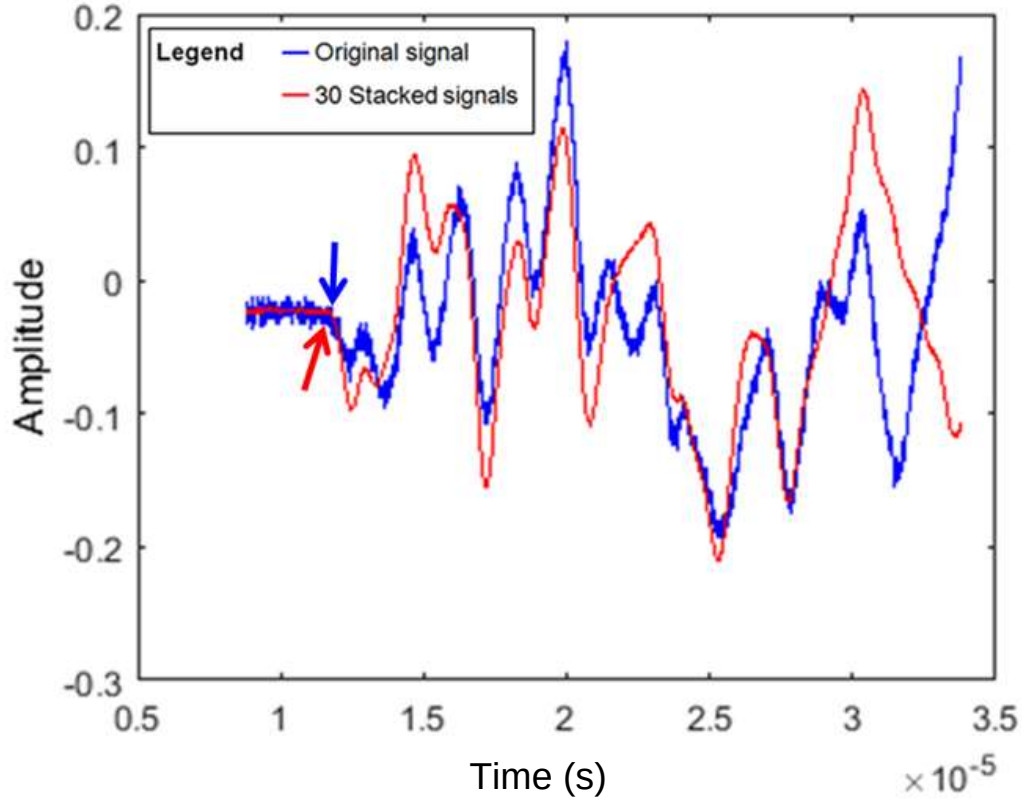

Figure B.17: The results of stacking several output waveforms for sample W40

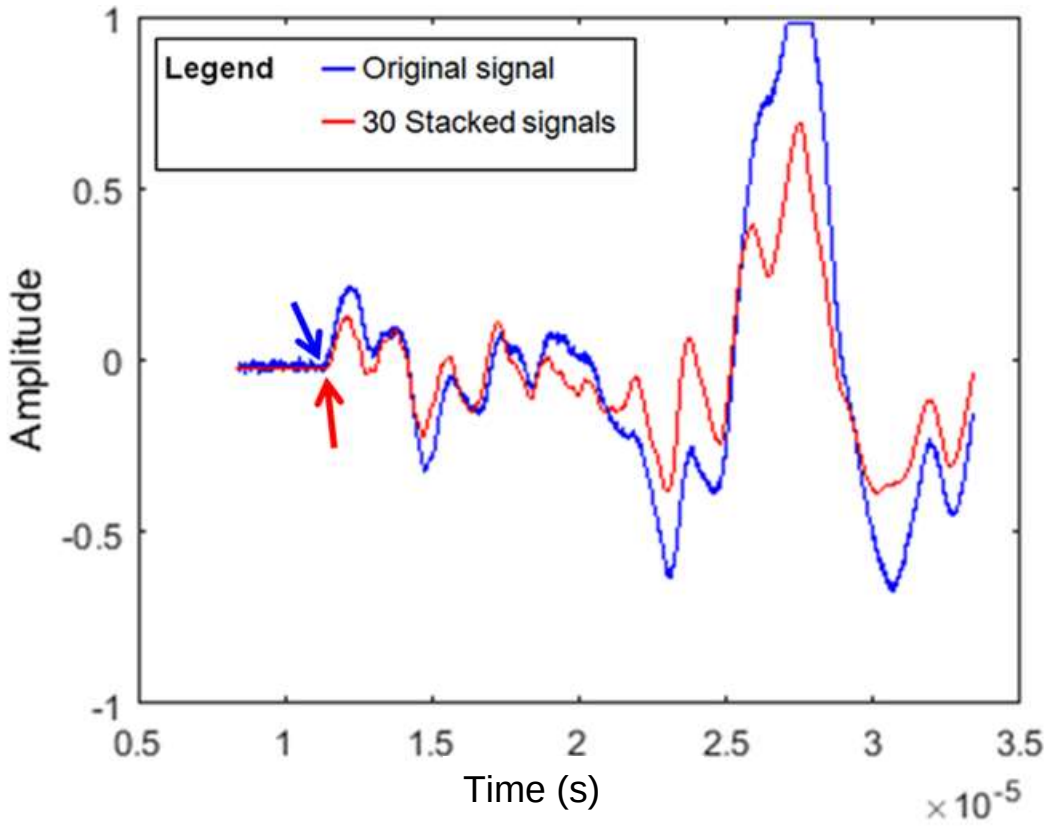

Figure B.18: The results of stacking several output waveforms for sample W41

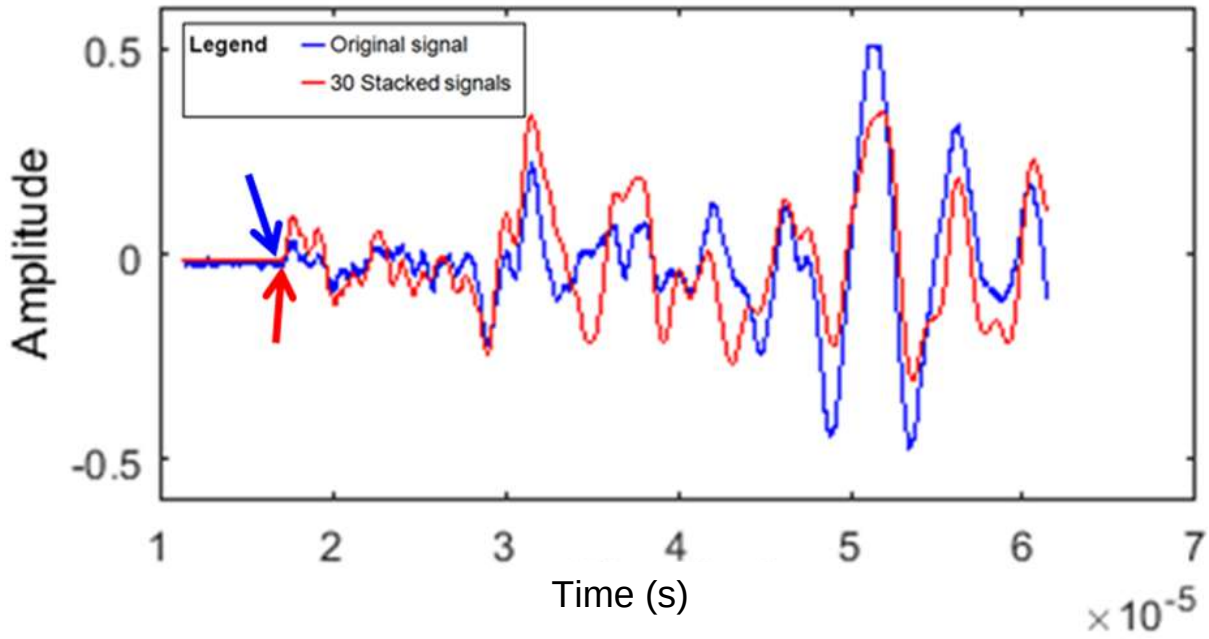

Figure B.19: The results of stacking several output waveforms for sample W42

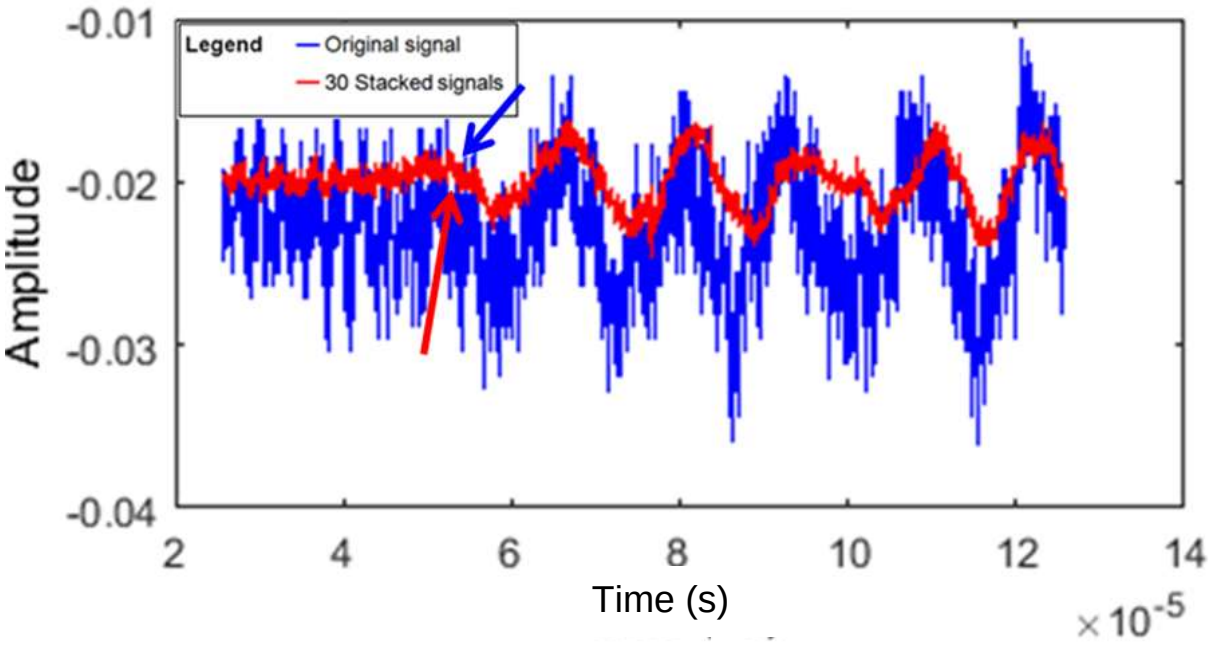

Figure B.20: The results of stacking several output waveforms for sample W46

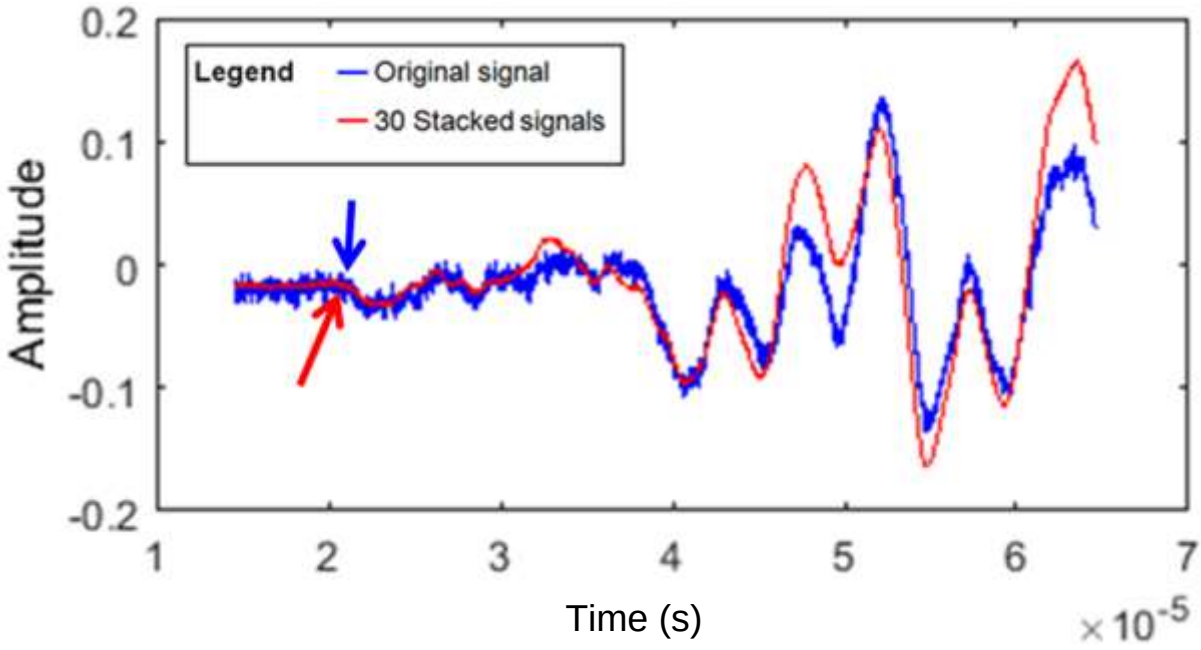

Figure B.21: The results of stacking several output waveforms for sample W47

C. Appendix C – Uniaxial stress

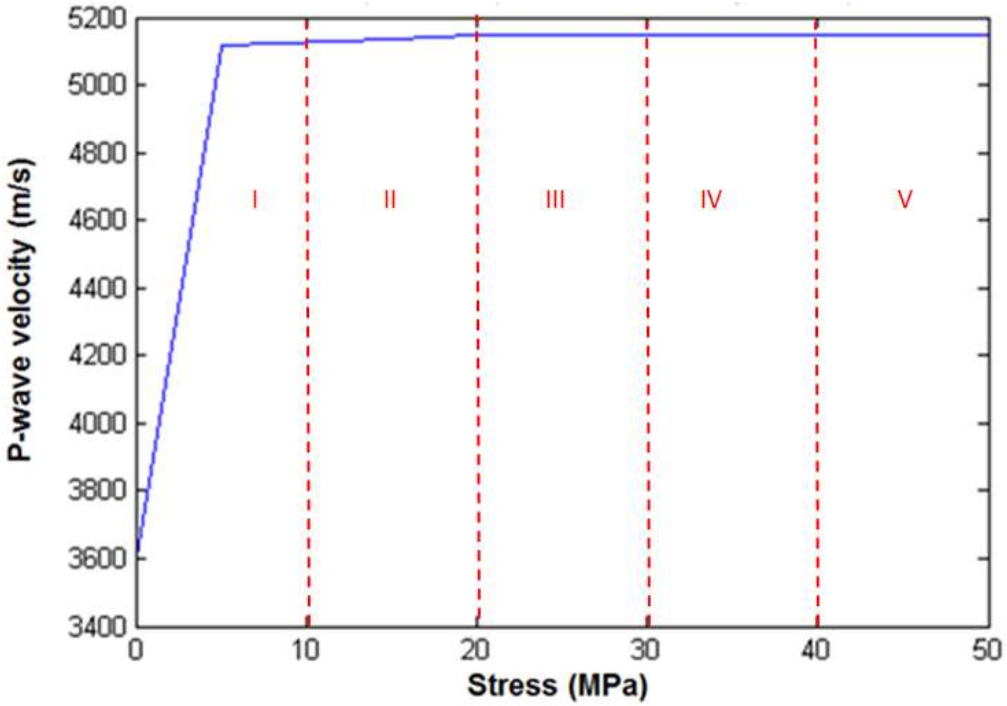

Figure C.1: The relationship between stress and seismic P-wave velocity of sample W5 (Shale)

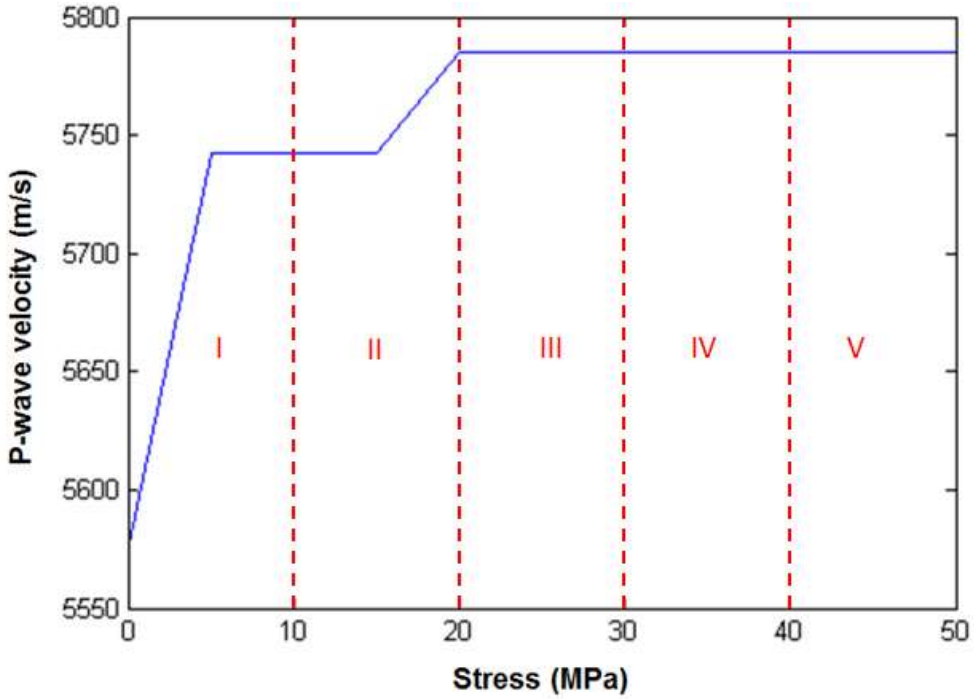

Figure C.2: The relationship between stress and seismic P-wave velocity of sample W7 (Dolerite)

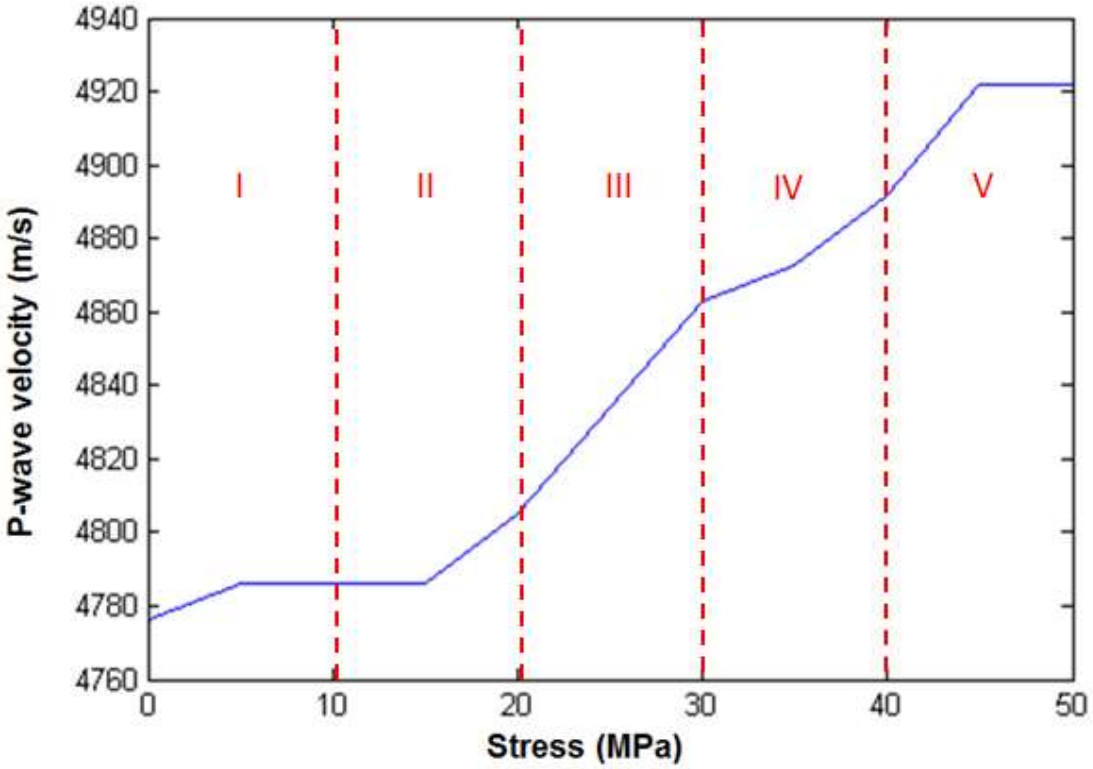

Figure C.3: The relationship between stress and seismic P-wave velocity of sample W8 (Sandstone)

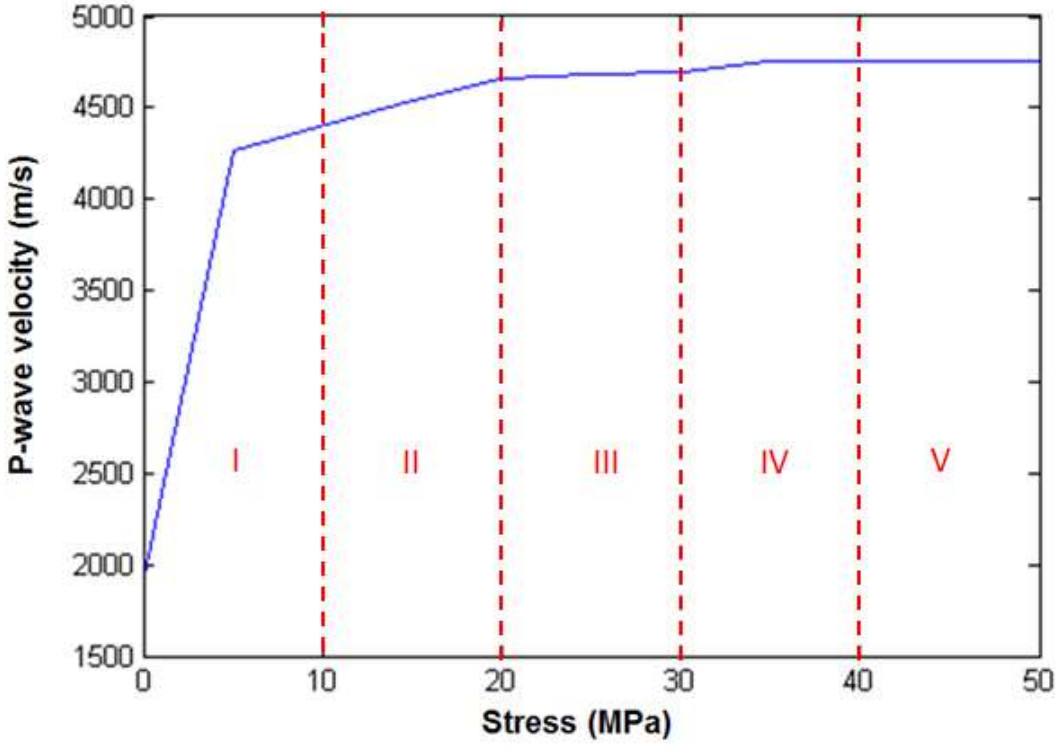

Figure C.4: The relationship between stress and seismic P-wave velocity of sample W9 (Carbonaceous shale)

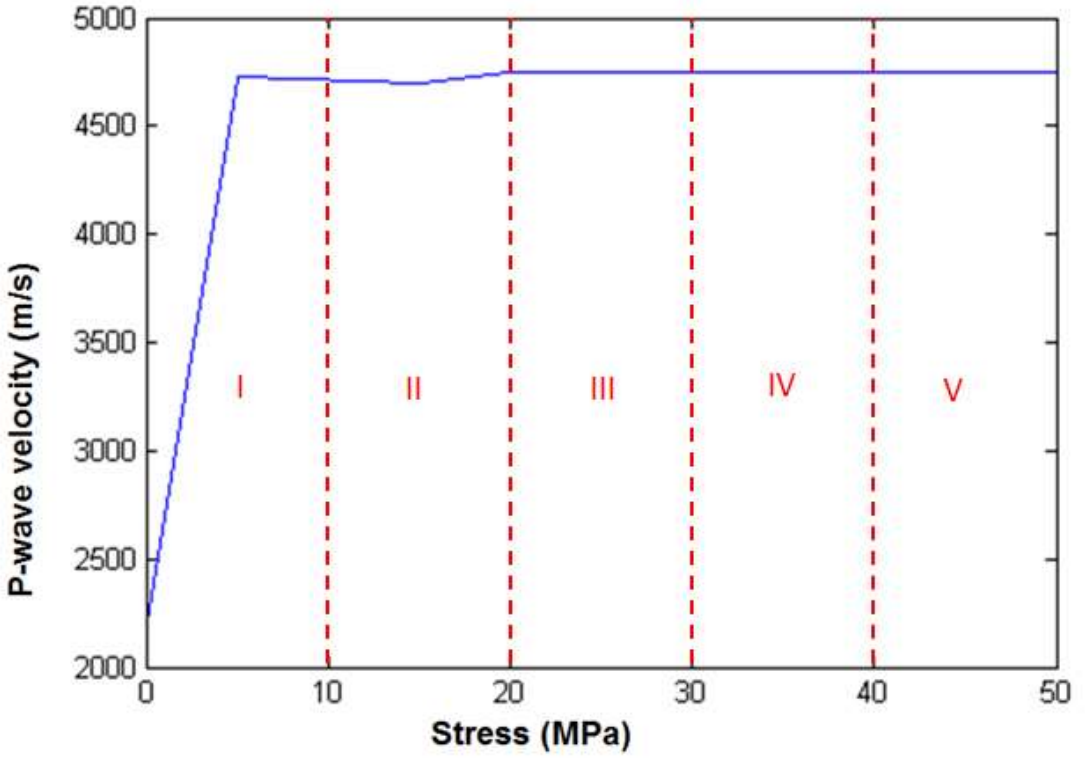

Figure C.5: The relationship between stress and seismic P-wave velocity of sample W10 (Sandstone)

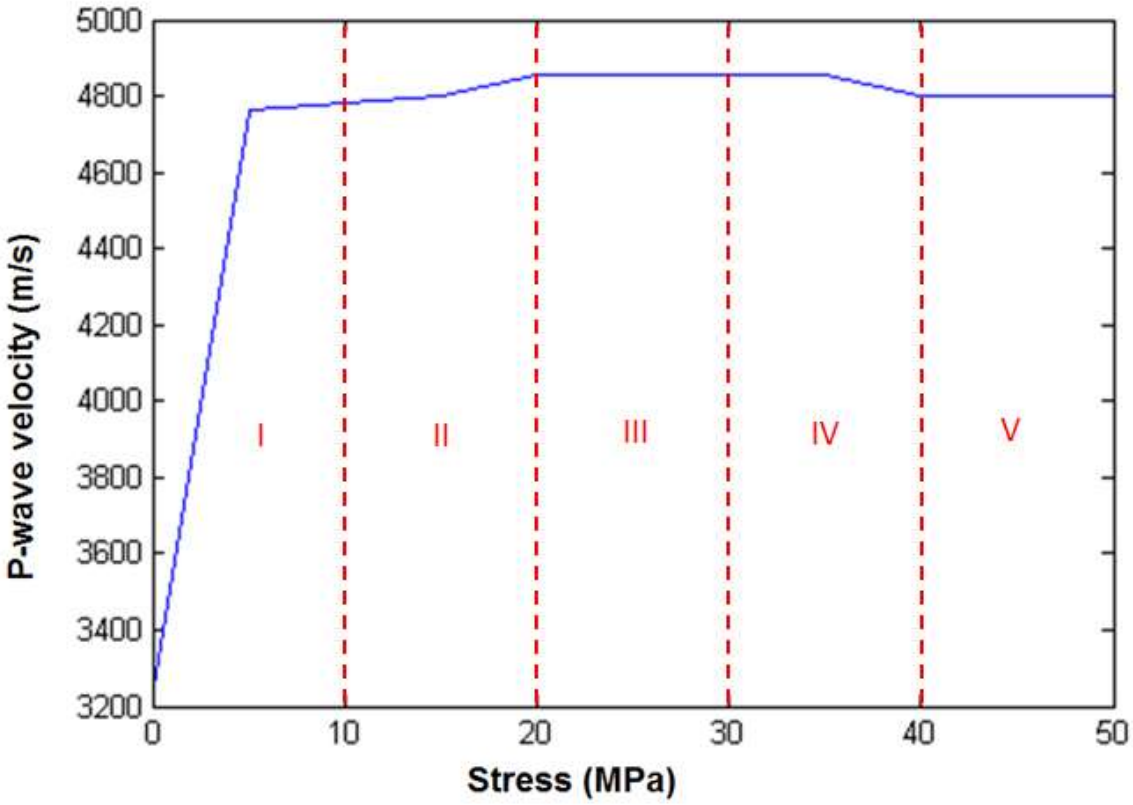

Figure C.6: The relationship between stress and seismic P-wave velocity of sample W11 (Shale)

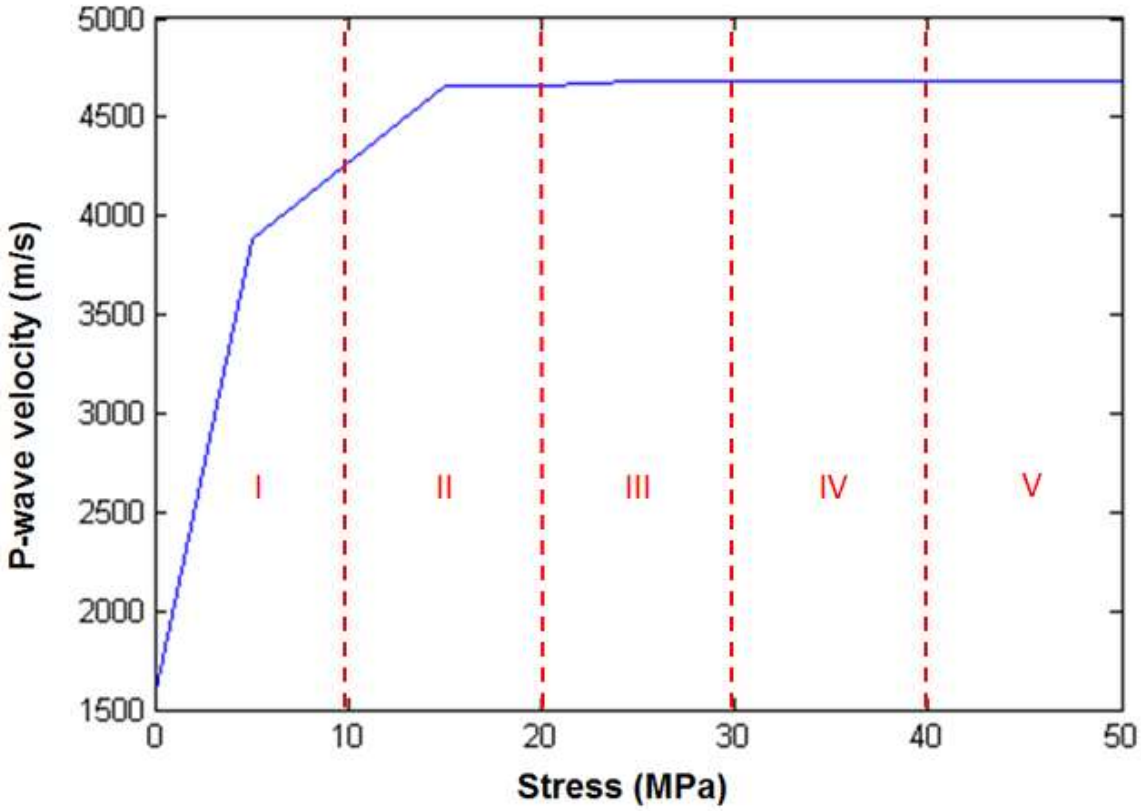

Figure C.7: The relationship between stress and seismic P-wave velocity of sample W13 (Sandstone)

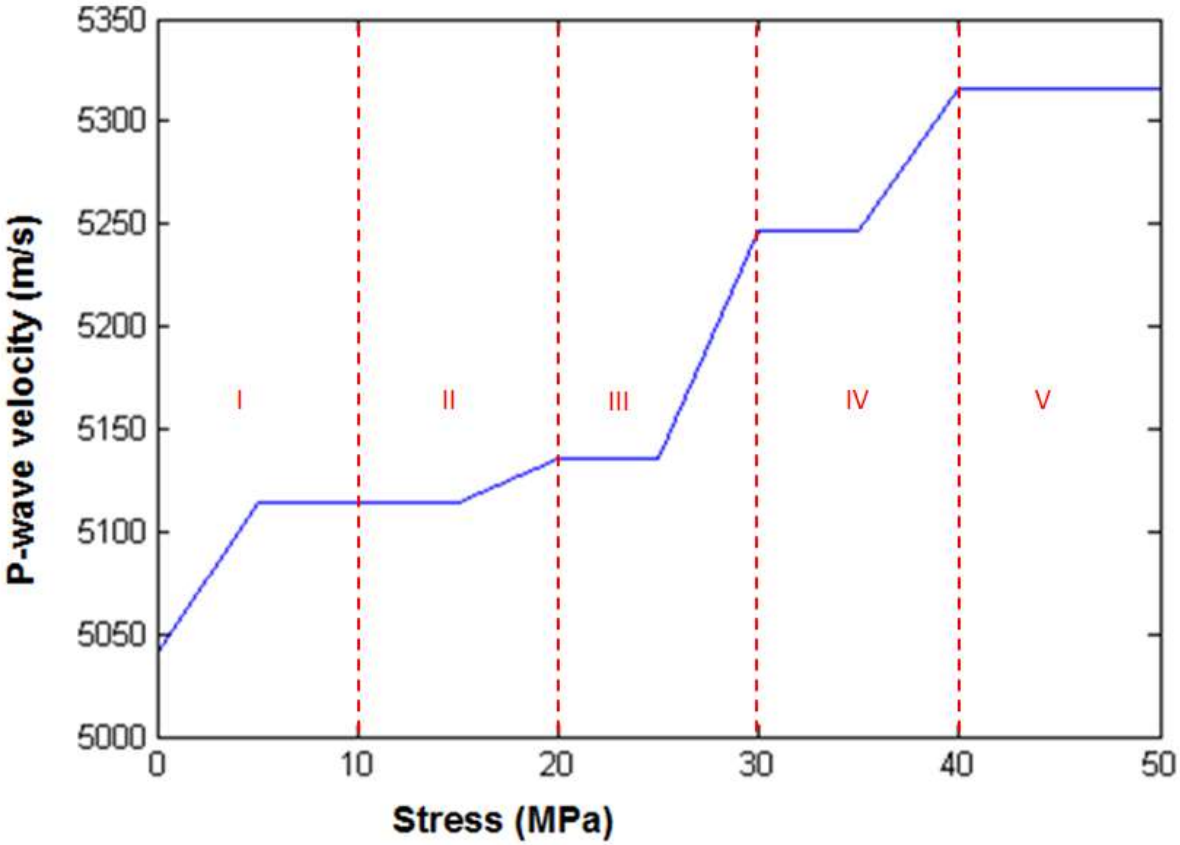

Figure C.8: The relationship between stress and seismic P-wave velocity of sample W16 (Dolerite)

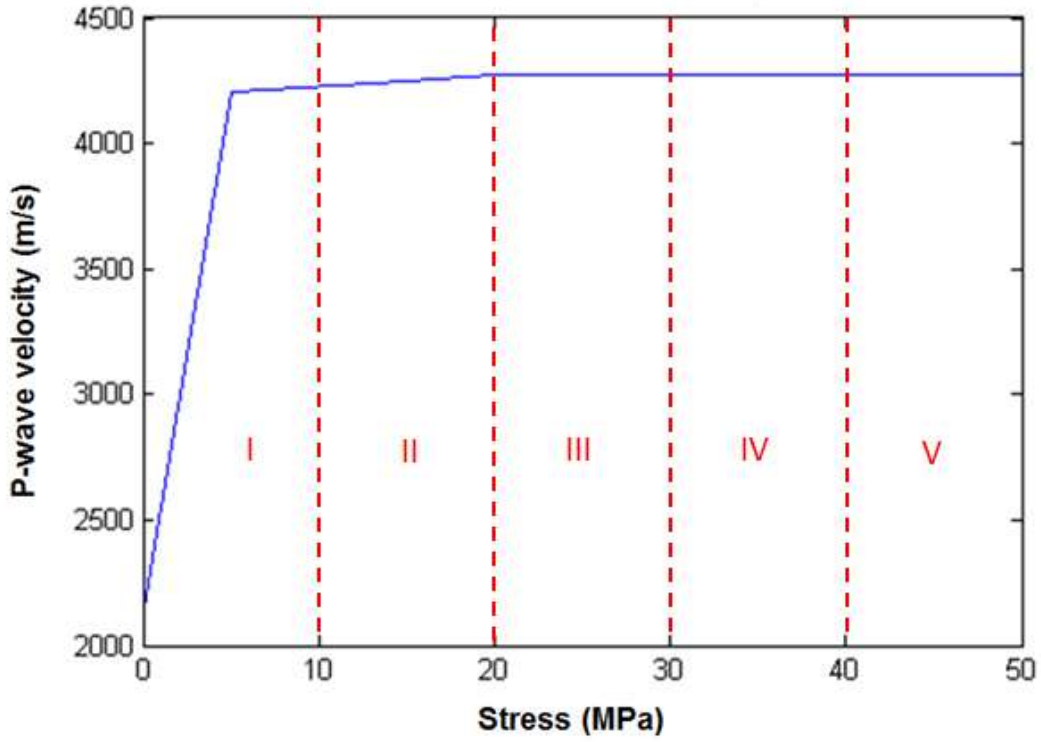

Figure C.9: The relationship between stress and seismic P-wave velocity of sample W17 (Black shale)

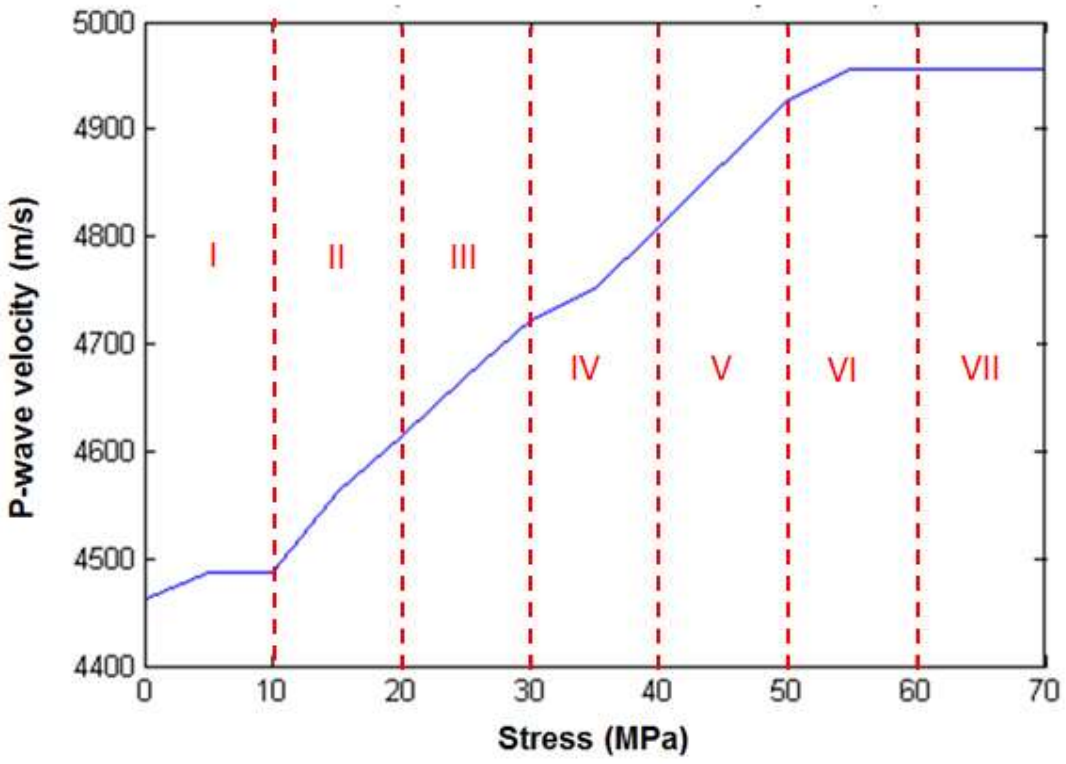

Figure C.10: The relationship between stress and seismic P-wave velocity of sample W18 (Sandstone)

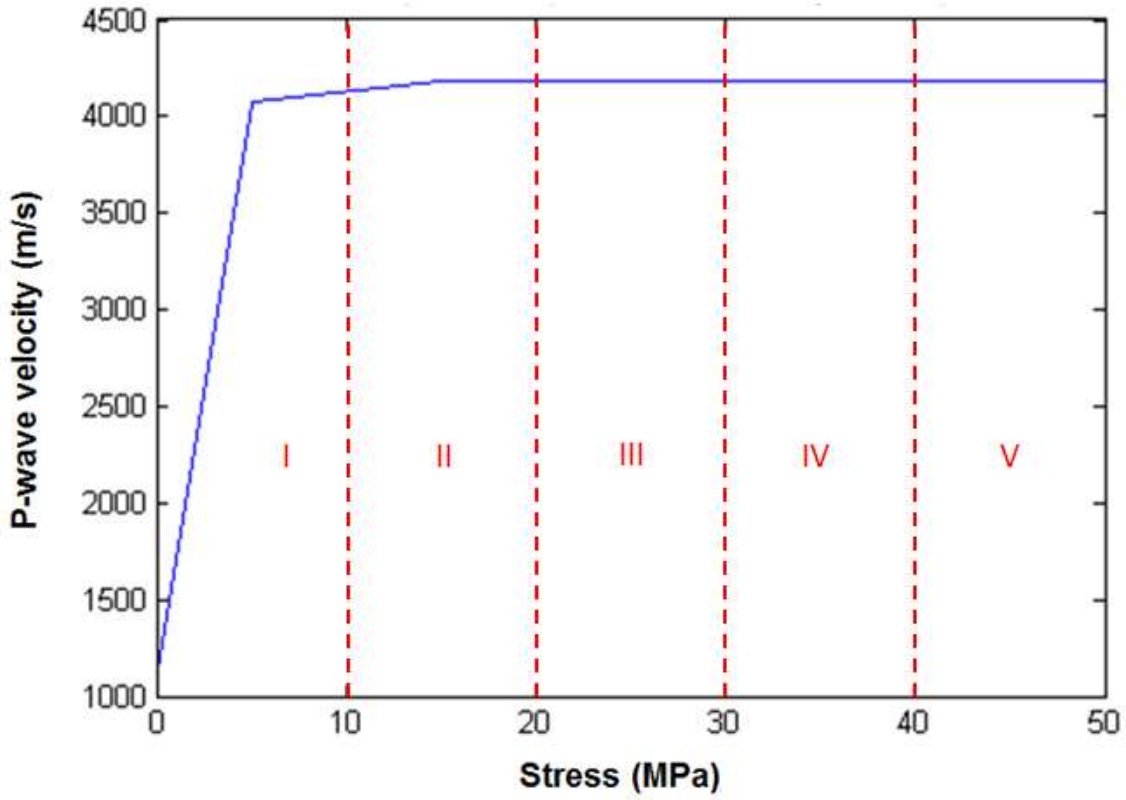

Figure C.11: The relationship between stress and seismic P-wave velocity of sample W19 (Carbonaceous shale)

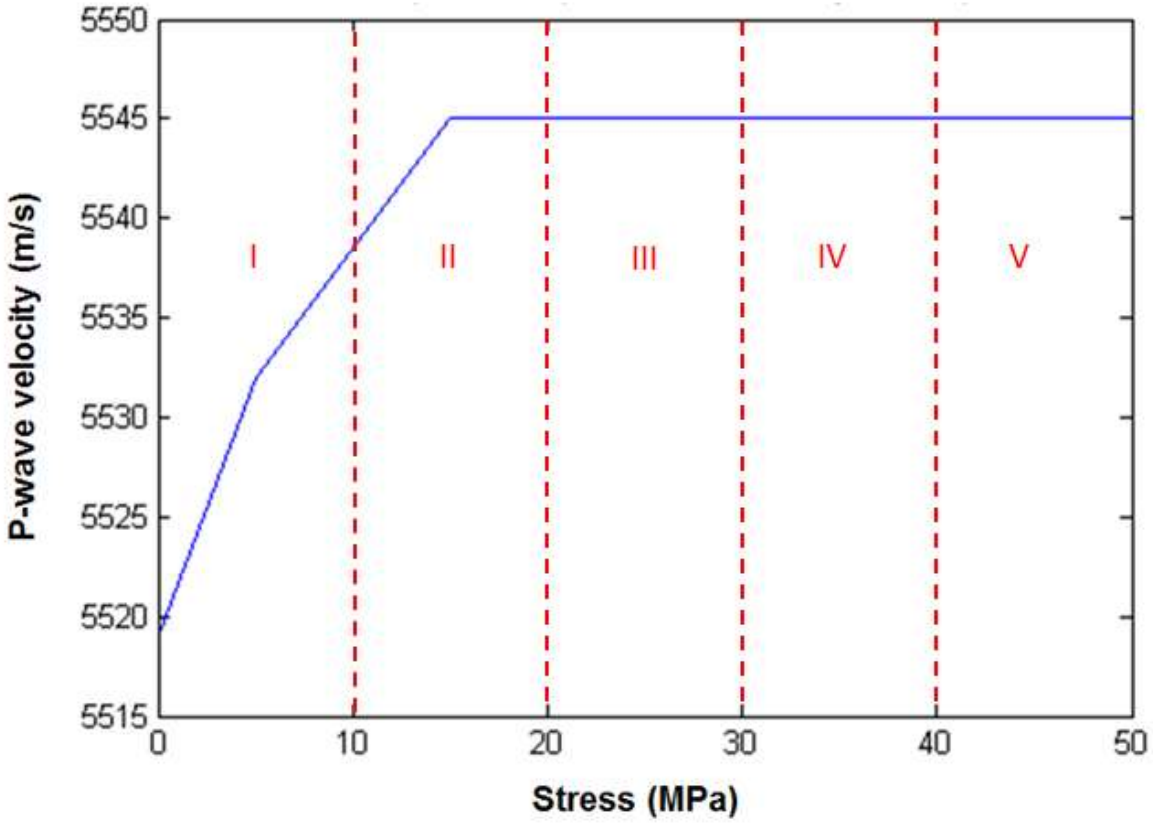

Figure C.12: The relationship between stress and seismic P-wave velocity of sample W21 (Sandstone)

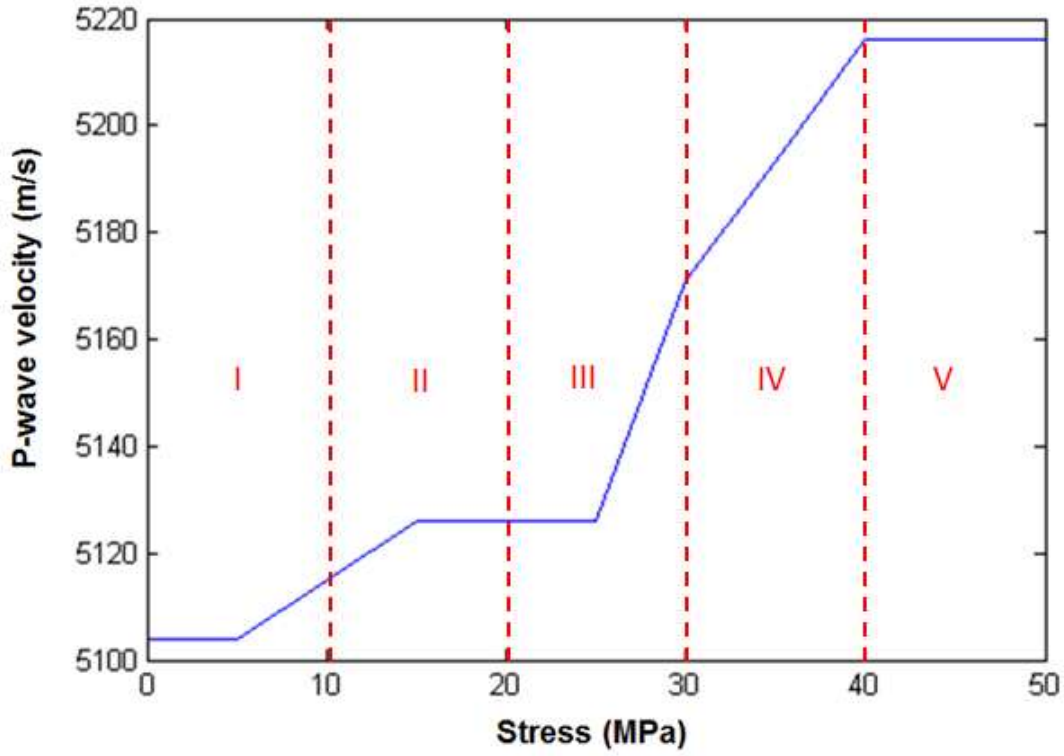

Figure C.13: The relationship between stress and seismic P-wave velocity of sample W25 (Shale)

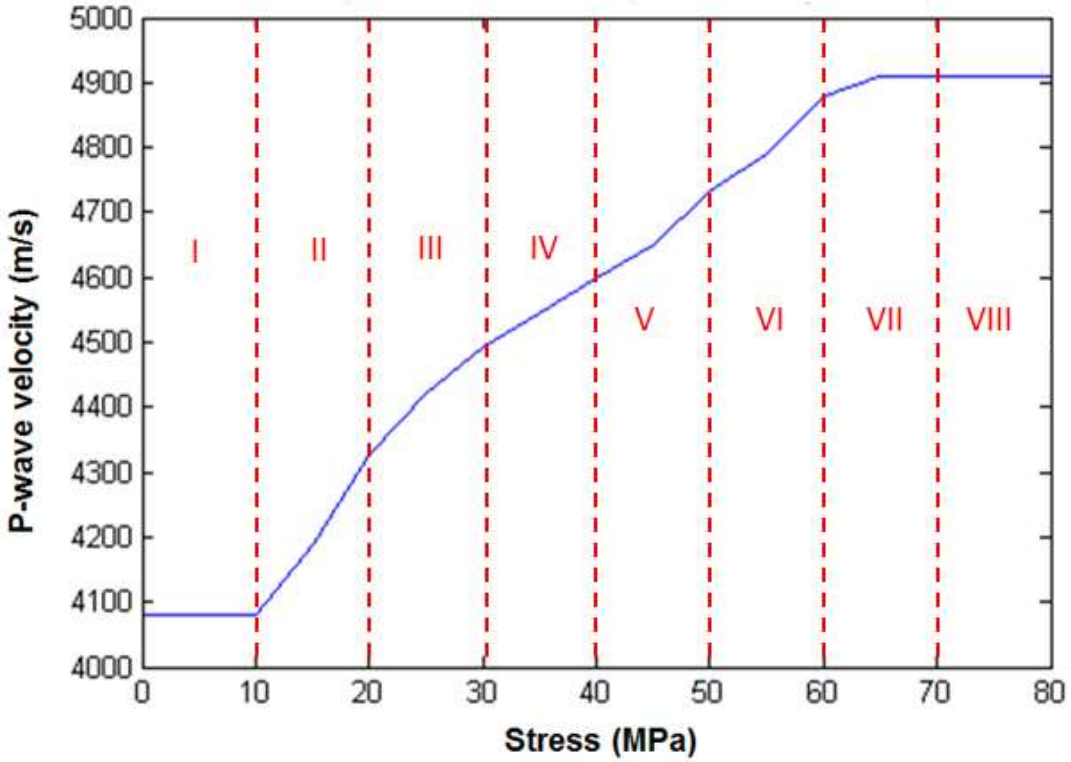

Figure C.14: The relationship between stress and seismic P-wave velocity of sample W26 (Dolerite)

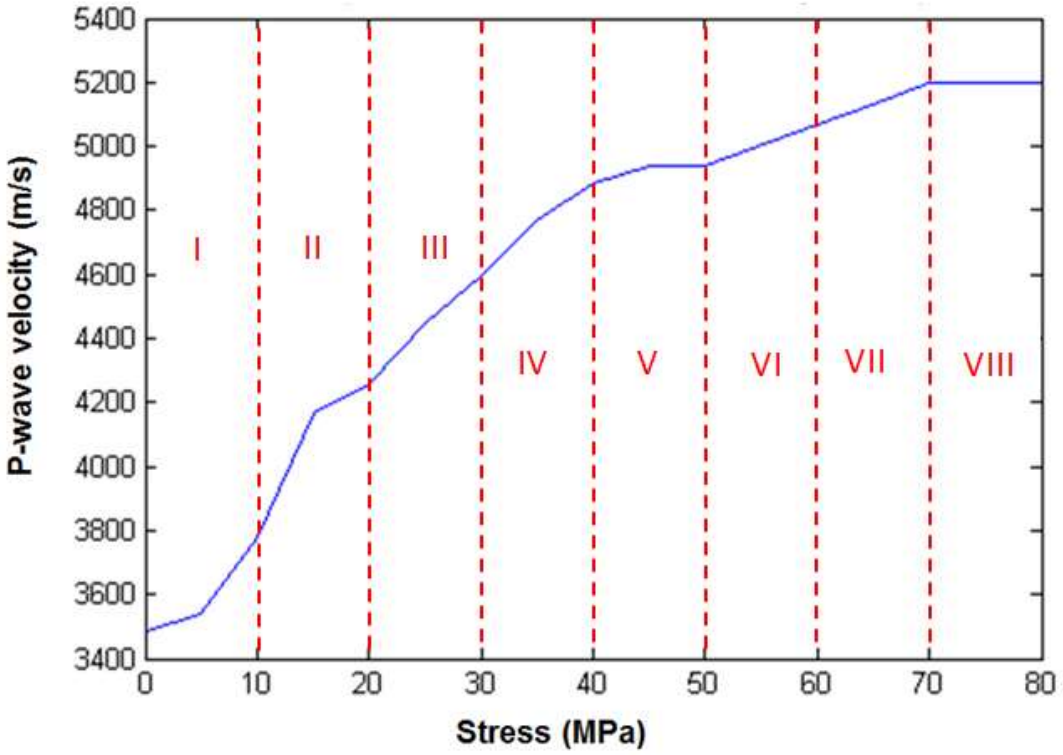

Figure C.15: The relationship between stress and seismic P-wave velocity of sample W31 (Dolerite)

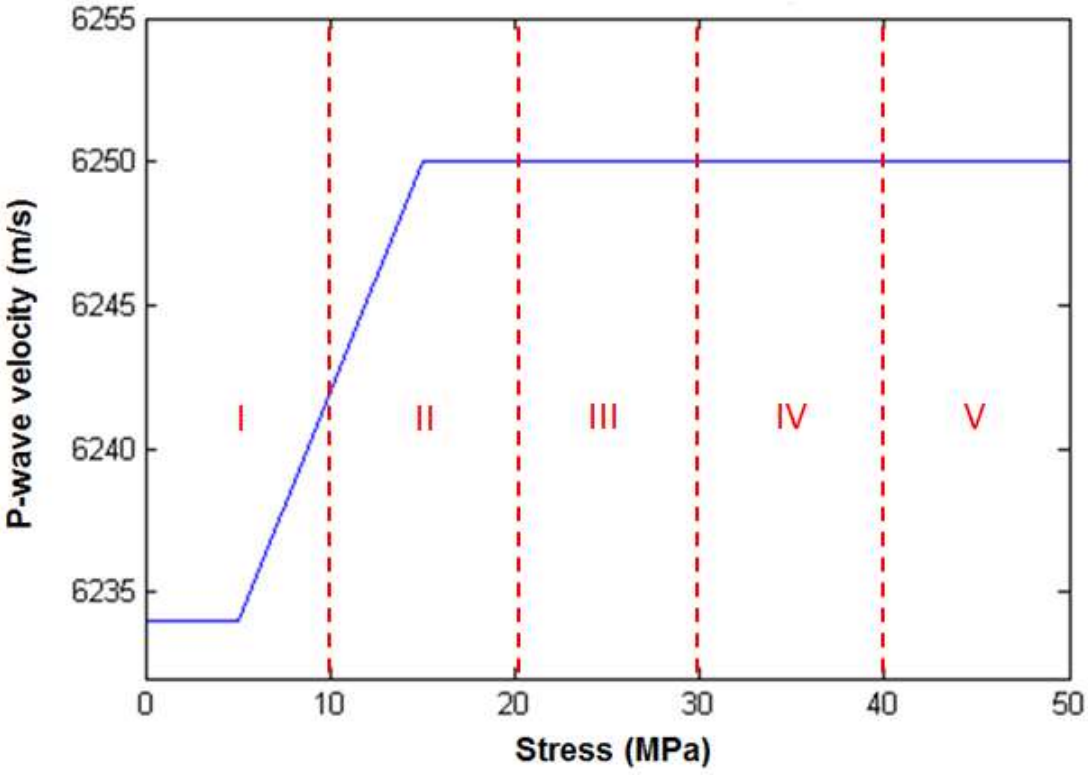

Figure C.16: The relationship between stress and seismic P-wave velocity of sample W33 (Dolerite)

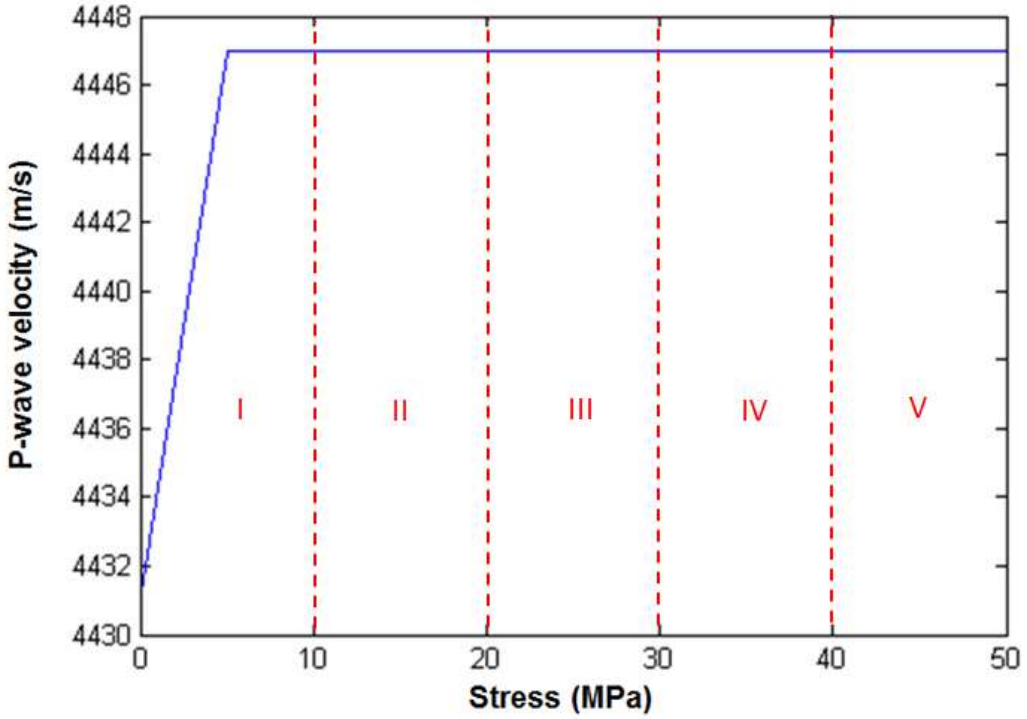

Figure C.17: The relationship between stress and seismic P-wave velocity of sample W34 (Dolerite)

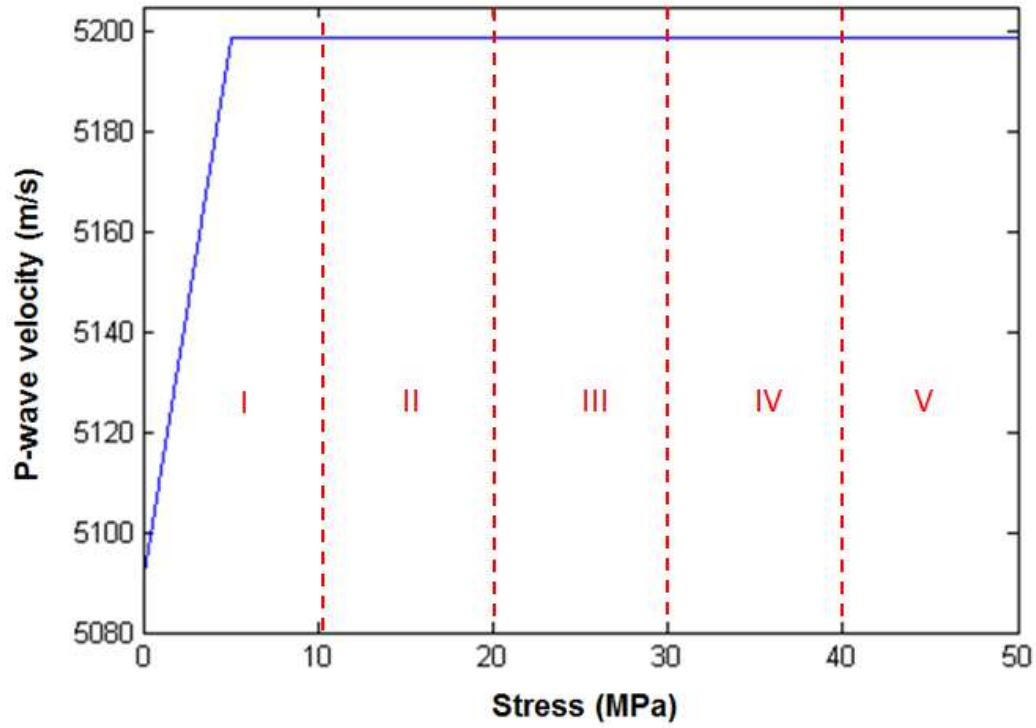

Figure C.18: The relationship between stress and seismic P-wave velocity of sample W37 (Dolerite)

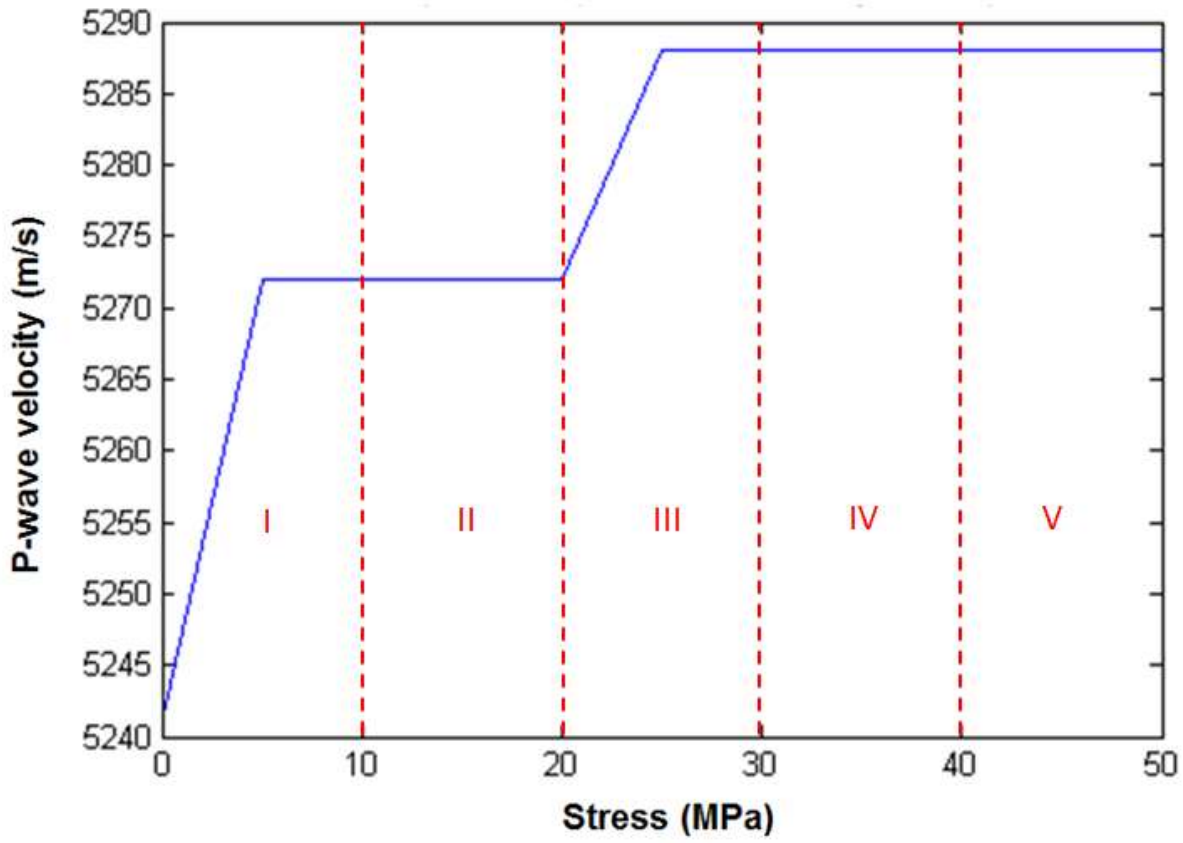

Figure C.19: The relationship between stress and seismic P-wave velocity of sample W41 (Carbonaceous shale)

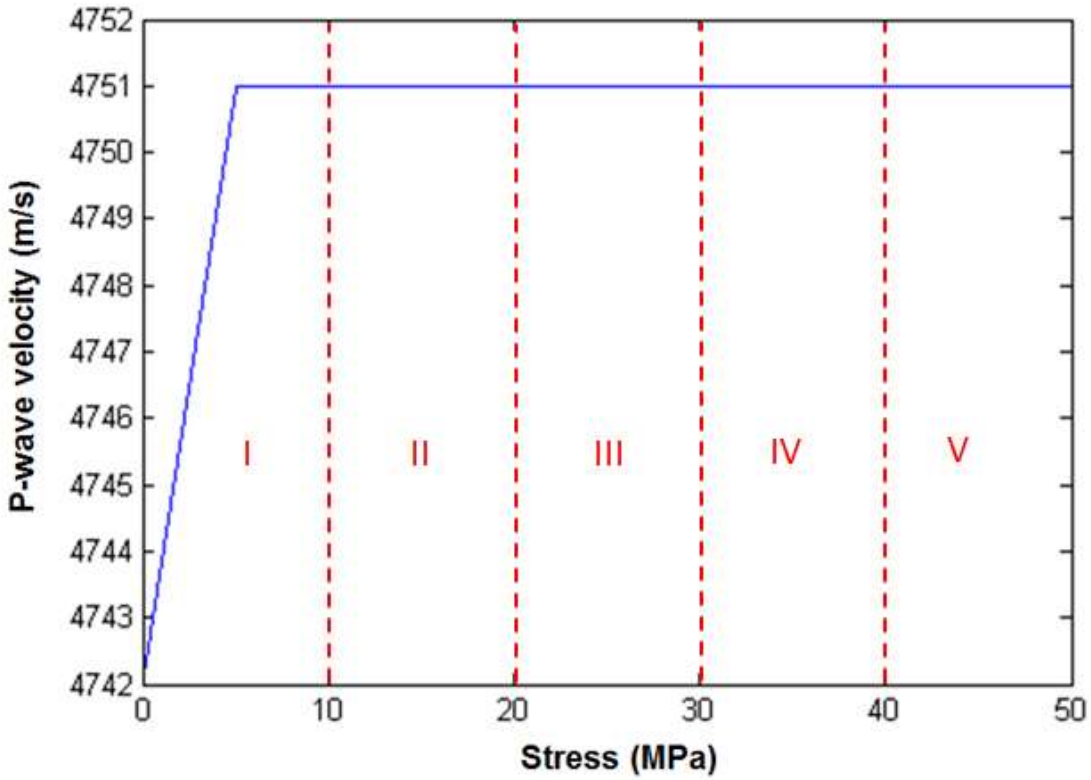

Figure C.20: The relationship between stress and seismic P-wave velocity of sample W42 (Carbonaceous shale)

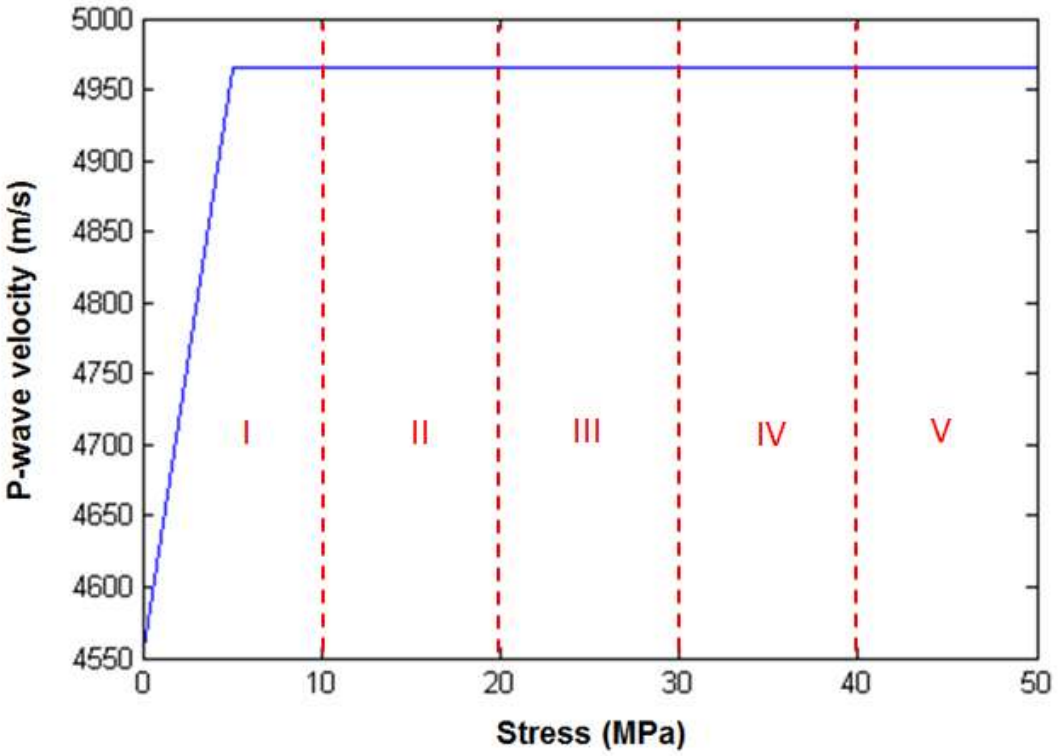

Figure C.21: The relationship between stress and seismic P-wave velocity of sample W43 (Shale)

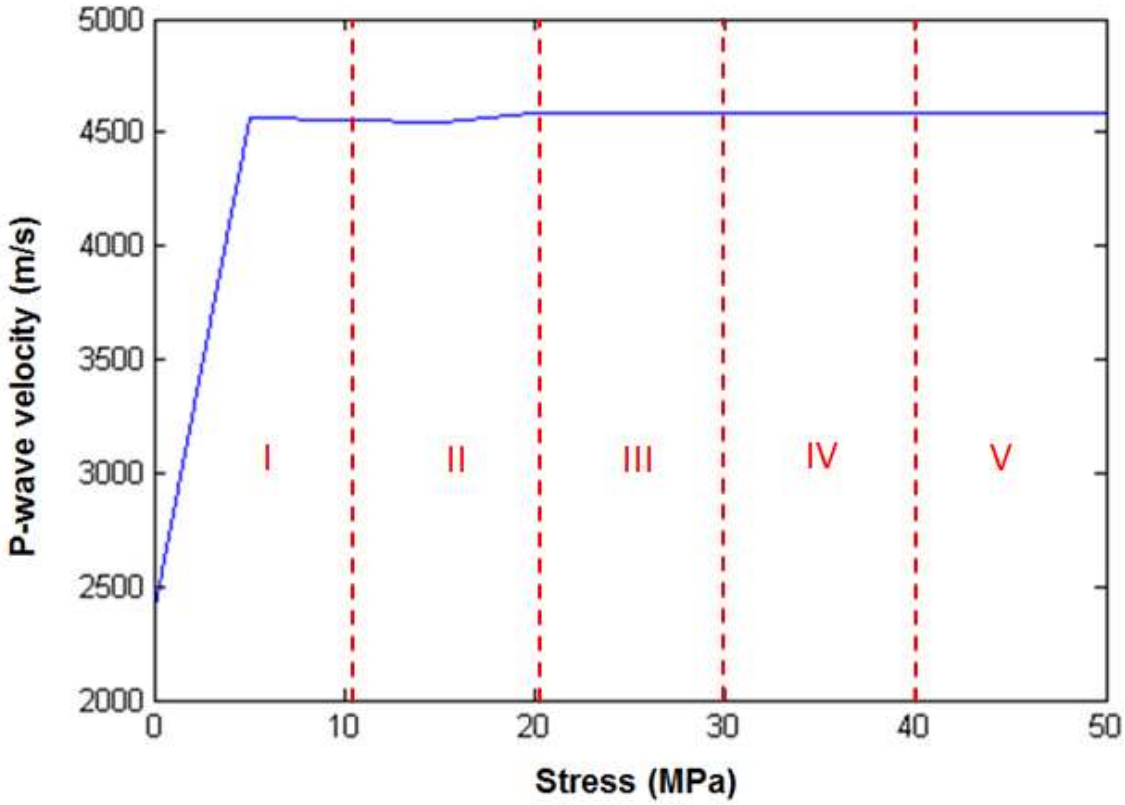

Figure C.22: The relationship between stress and seismic P-wave velocity of sample W44 (Shale)

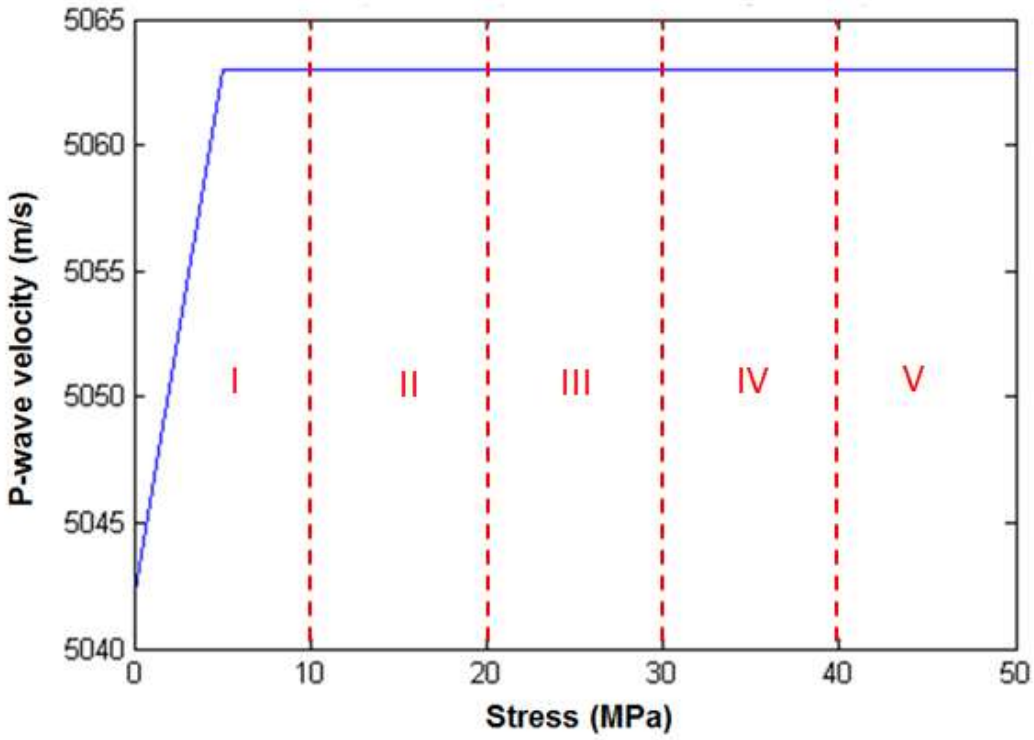

Figure C.23: The relationship between stress and seismic P-wave velocity of sample W45 (Shale)

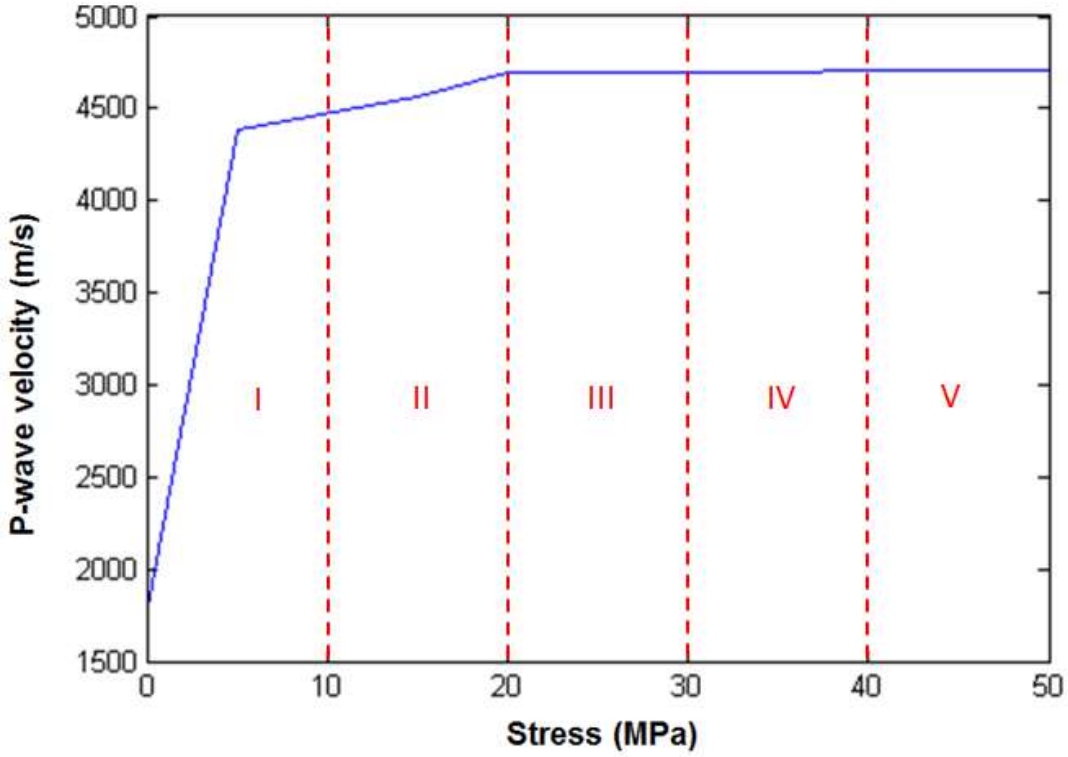

Figure C.24: The relationship between stress and seismic P-wave velocity of sample W46 (Rhythmite)

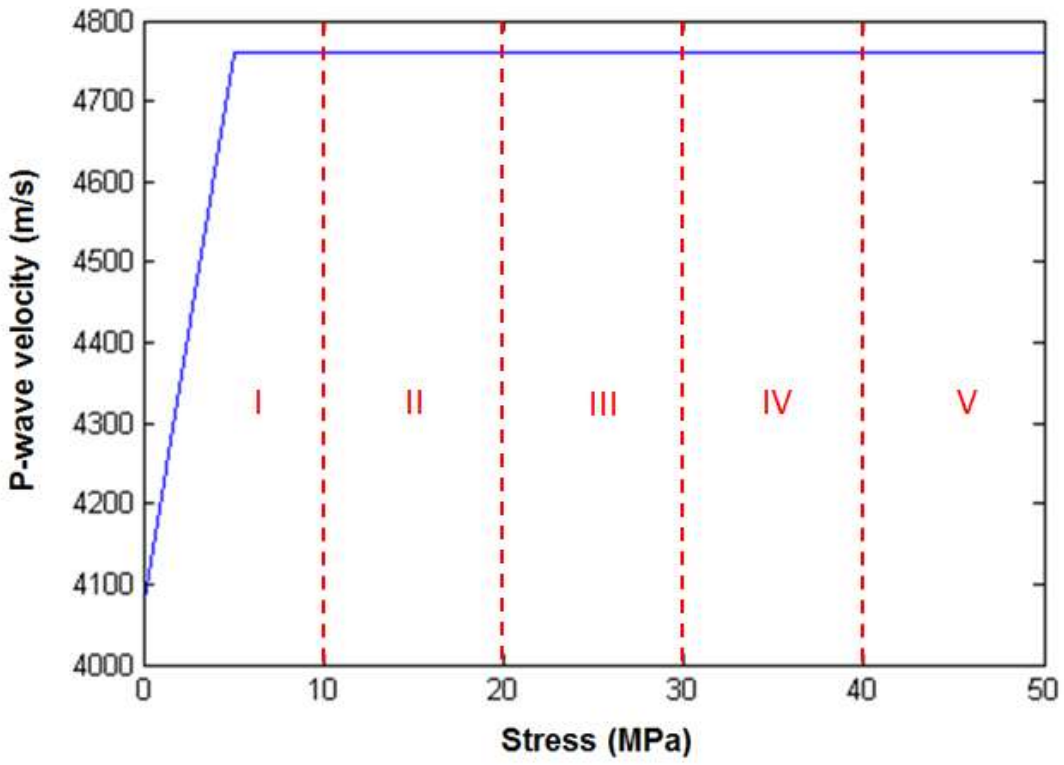

Figure C.25: The relationship between stress and seismic P-wave velocity of sample W47 (Rhythmite)

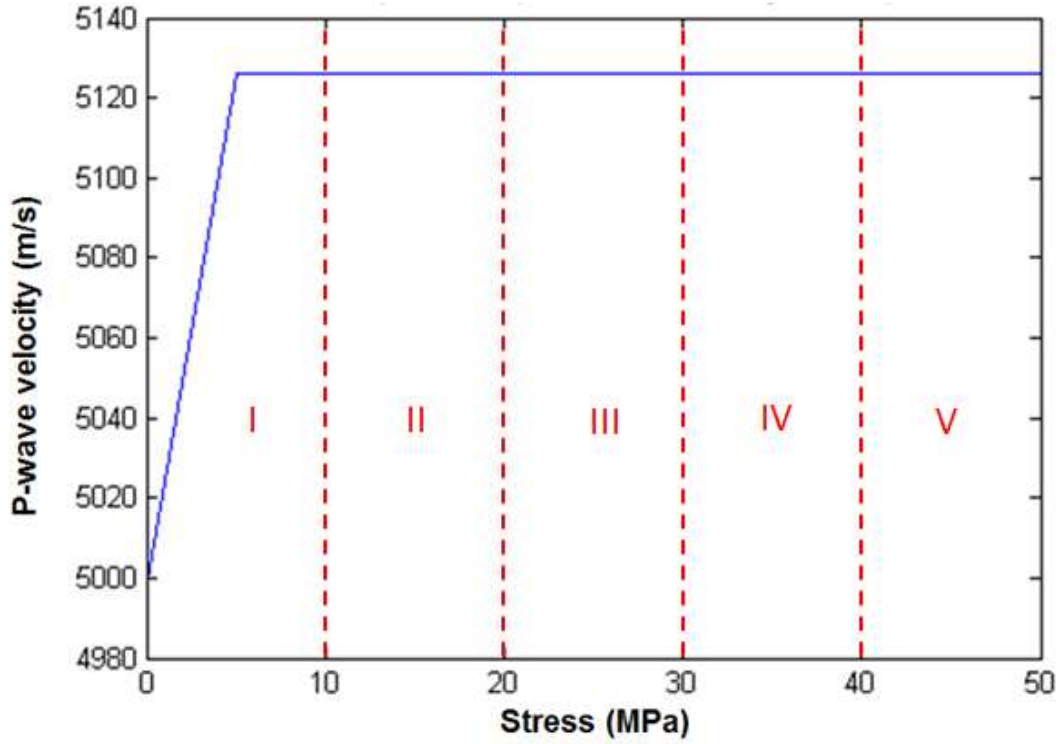

Figure C.26: The relationship between stress and seismic P-wave velocity of sample W48 (Tillite)

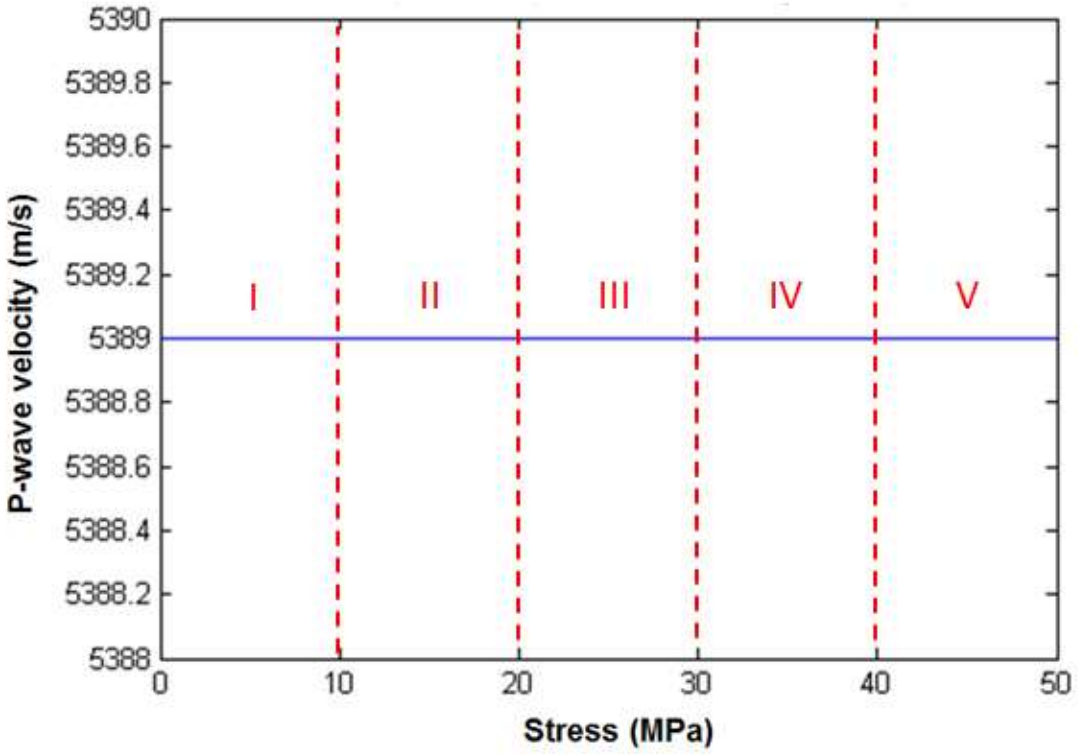

Figure C.27: The relationship between stress and seismic P-wave velocity of sample W49 (Tillite)

D. Appendix D – MATLAB code

Signal Stacking

```
function [time,s,stack] = SeisStack(list,p)
%_____________________________________________________________________
%SEISSTACK reads velocity signals that are indiviually grouped in folders
%with the naming convention FxxxxCH2.CSV, where xxxx is the signal number
%and produces a stack of the signals. The stacked signal is then plotted.
%INPUT:
% list: Cell list of signal identifiers xxxx.
% p: Path of parent folder of signals.
%OUTPUT:
% time: Time series data in microseconds.
% s: Matrix whose rows are the unstacked signals.
% stack: Final stacked signal.
%
% M. C. Westgate, 2017
% University of the Witwatersrand
%_____________________________________________________________________
l = length(list);

for j=1:l
path = [p, '\ALL',list{j},'\F',list{j},'CH2.csv'];
data = csvread(path,0,3,[0,3,2499,4]);
time(:,j) = data(:,1);
s(:,j) = data(:,2);
end

stack = sum(s,2)/l;
plot(time(:,1),stack); title('Stacked Signals'); xlabel(['Time \mu','s']);
ylabel('Amplitude');
end
```